Génération d'impulsions laser proches du cycle optique en durée pour l'interaction laser-matière relativiste à haute cadence

Marie Ouillé

INSTITUT POLYTECHNIQUE DE PARIS

NNT : 2022IPPAE007

Thèse de doctorat

ENSTA

IP PARIS

Generation of near-single-cycle duration pulses for relativistic laser-matter interaction at high repetition rate.

Thèse de doctorat de l'Institut Polytechnique de Paris
préparée au Laboratoire d'Optique Appliquée

École doctorale n°626 École doctorale de l'Institut Polytechnique de Paris (EDIPP)
Spécialité de doctorat : Optique, Laser et Plasma

Thèse présentée et soutenue à Palaiseau, le 11 Mai 2022, par

MARIE OUILLÉ

Composition du Jury :

Patrick Audebert Directeur de Recherche, École Polytechnique (Laboratoire pour l'Utilisation des Lasers Intenses)	Président
Éric Cormier Professeur des Universités, Université de Bordeaux (Laboratoire Photonique Numérique et Nanosciences)	Rapporteur
László Veisz Professor, Umeå University (Relativistic Attosecond Physics Laboratory)	Rapporteur
Marc Hanna Directeur de Recherche, CNRS (Laboratoire Charles Fabry)	Examinateur
Jérôme Faure Directeur de Recherche, CNRS (Laboratoire d'Optique Appliquée)	Directeur de thèse
Rodrigo Lopez-Martens Ingénieur de Recherche, École Polytechnique (Laboratoire d'Optique Appliquée)	Co-directeur de thèse
Mathias LePennec PDG, ARDoP Industrie	Invité

Acknowledgements

D'un professeur de Seconde qui a eu la merveilleuse idée de nous faire lire *Poussières d'étoiles* (Hubert Reeves) et de discussions sur *MSN* (oui, ça existait encore !) avec Samuel, Mohssen ou Matthieu sur la physique fondamentale à l'aboutissement d'un doctorat en physique, il y a beaucoup d'étapes et évidemment beaucoup de personnes impliquées, sans qui je ne serais certainement pas arrivée là où j'en suis...

En tout premier lieu, bien sûr, il y a Stefan et Rodrigo, qui m'ont accueillie dans l'équipe PCO. Je ne saurais comment les remercier de m'avoir soutenue pendant cinq ans et d'avoir cru en moi en me donnant l'opportunité de préparer ma thèse dans l'équipe. Je remercie Rod de m'avoir fait confiance avec la *Salle Noire 2* entière et de m'avoir laissée toucher littéralement à tout (pas toujours pour le meilleur ! j'en ai encore pour des années à rembourser mes dettes...). J'ai adoré cet aspect de ma thèse ! Merci également de m'avoir donné l'opportunité d'aller à plusieurs conférences (on s'est d'ailleurs bien amusés à Strasbourg !) et de rencontrer une partie de ton réseau infini à travers plusieurs campagnes *Laserlab*. Je crois que je n'aurais pu faire tout ça nulle part ailleurs. Rodrigo est un *group leader* jamais à court d'idées (et de bonne humeur), qui se soucie du bien-être de son équipe, et avec qui on peut parler franchement et simplement. Merci à Stefan pour ta patience et ta bienveillance... Sans ton aide, je n'aurais jamais pu reprendre la main sur les manipes, ou même l'analyse de données, après le départ des anciens thésards. Je n'aurais probablement pas non plus fini ce manuscrit... Tu es la personne vers qui on se tourne quand on a une question sur la physique ou la théorie. Une aide discrète mais totalement indispensable, le groupe PCO est chanceux de t'avoir ! Merci également à Jérôme qui a accepté d'être mon directeur de thèse, pour sa gentillesse et sa disponibilité. Merci à Mathias pour avoir accepté de mettre en place la convention CIFRE avec ARDOP, et d'avoir ainsi rendu tout cela possible.

Then, of course, I would like to thank Zhao, who joined the group a little later than me and has infinite know-how with Ti:Sa lasers. The optimization of the laser chain entered a new dimension with you! What a pleasure it was to observe the master tweaking the oscillator and the amplifiers after months of struggle almost on my own, and what an honor to learn from you! Je n'oublie évidemment pas Aline, qui a été d'une aide énorme au labo (surtout au début quand mon expérience avec les lasers était proche de zéro). Tu es hyper attentionnée, pleine de ressources, jamais à court d'anecdotes geek, et tu m'as soutenue dès le départ. Tu m'as montré comment être méthodique et agir avec précaution. With Zhao and Aline, it was the perfect balance between intuitive and methodical work. Then, of course, Jaismeen! You are the personification of efficiency itself, you make things happen, and quickly! During our last experiments together, our minds were perfectly synchronized, and your help was precious. You know just as much as I do now, if not more! Je n'oublie pas non plus Louis, notre expert post-compression jamais à court de blagues (ni de clopes) ! We had really fun times in Rome with Jaismeen. Et merci à Antoine, le nouveau venu dans le groupe, pour tous les repas partagés et les discussions sympathiques.

Merci au groupe APPLI: Igor, Neïl, Isa, Domynikas, Lucas, Julius et Joséphine pour leurs précieuses contributions à ce manuscrit par des simulations numériques ou par les résultats LWFA. Merci pour votre bonne humeur et pour les quelques soirées dans les bars et restaus. Merci à tous ceux qui m'ont aidée à un moment donné : Magali, Jean-Philippe, YBA, Pascal

pour la Haute Tension... Grosse pensée à tous les services annexes du labo : Charly et Bernard, l'âge d'or de l'atelier de méca, travail rapide et efficace, et toujours dans la bonne humeur ! Sébastien pour nous avoir sauvées d'une situation délicate de vis bloquée à la sueur de son front... Toutes les secrétaires sans exceptions (Sandrine, Patricia, Catherine, Magali) pour leur travail extrêmement rapide et efficace, ainsi bien sûr que l'organisation des petits événements qui font la vie du labo comme le barbecue annuel. Ce sont ces petites choses qui font que le LOA est un lieu si convivial !

Thanks to all those who contributed to this thesis through collaborations: Tamas Nagy, Ayhan Tajalli, Rosa Romero, Helder Crespo and Esmerando Escoto for the XPW d-scan experiments; Dan Lévy, Alessandro Flacco and Victor Malka for the protons measurements; Antoine Jeandet and Spencer Jolly for the STC campaign, Li Lu and Philippe Zeitoun for the XUV wavefront measurements... I had the chance to meet many inspiring great scientists during these few years!

I also want to thank the examiners Laszlo Veisz and Eric Cormier for carefully reading my thesis and for their very interesting questions and remarks, as well as Marc Hanna and Patrick Audebert for accepting to be part of the jury.

Pour finir sur un point de vue plus personnel, je ne peux écrire de remerciements sans un mot pour mes parents, qui sont la raison première de ma réussite, qui m'ont soutenue et poussée à faire ce que je voulais, même dans mes demandes les plus folles. Merci à mes amis, Dylan (qui m'a d'ailleurs initiée à LaTeX pendant notre stage à l'IAS) et Elsa, qui répondent toujours présents malgré la distance et avec qui on peut parler de tout, pour tous les bons moments. Merci Mehdi pour ces onze années passées à mes côtés et pour les nombreuses à venir. J'ai hâte de voir ce que l'avenir nous réserve. Tokyo, we're coming!

Contents

List of acronyms and abbreviations

AOFS: Acousto-Optic Frequency Shifter
AOM: Acousto-Optic Modulator
AOPDF: Acousto-Optic Programmable Dispersive Filter
A.U.: arbitrary units
BS: Beam Splitter
BSI: Barrier-Suppression Ionization
CCD: Charge Coupled Device
CEP: Carrier-Envelope Phase
CM: Chirped Mirror
CPA: Chirped Pulse Amplification
CWE: Coherent Wake Emission
DFG: Difference Frequency Generation
EMP: Electromagnetic Pulse
FOD: fourth order dispersion
FT: Fourier Transform
FTL: Fourier Transform Limited
FWHM: Full Width at Half Maximum
GD: Group Delay
GDD: Group Delay Dispersion
GVD: Group Velocity Dispersion
GRISM: Gratings and Prisms
HCF: Hollow-Core Fiber
HHG: High-order Harmonic Generation
LOA: Laboratoire d'Optique Appliquée
LPA: Laser Plasma Accelerator
LWFA: Laser WakeField Acceleration
MCP: MicroChannel Plate
OAP: Off-axis parabola
PBS: Polarizing Beam Splitter
PFT: Pulse Front Tilt
PIC: Particle-in-cell
PPLN: Periodically-Poled Lithium Niobate
PSD: Photosensitive Detector
ROM: Relativistic Oscillating Mirror
SDI: Spatial Domain Interferometer
SFG: Sum Frequency Generation
SF-HCF: Stretched-Flexible Hollow-Core Fiber
SHG: Second Harmonic Generation
SHHG: Surface High Harmonic Generation
SPM: Self Phase Modulation
SS: Self Steepening

STC: Spatio-Temporal Couplings
TGC: Transmission Grating Compressor
Ti:Sa: Titanium Doped Sapphire
TNSA: Target Normal Sheath Acceleration
TOD: third order dispersion
TOF: Time Of Flight
TPS: Thomson Parabola Spectrometer
WFR: Wavefront rotation
WFS: Wavefront Sensor
XFEL: X-ray Free Electron Laser
XPW: crossed-polarized wave

Résumé substantiel de la thèse en Français

Cette thèse expérimentale est le résultat de travaux de recherche menés au Laboratoire d'Optique Appliquée (Palaiseau, France) sur l'installation laser « Salle Noire 2 », en partenariat avec l'entreprise ARDOP Industrie. L'objectif de cette thèse est double : d'une part améliorer la stabilité et la fiabilité de la source laser, et d'autre part utiliser cette source laser pour mener des expériences d'interaction laser-plasma en régime relativiste. Les motivations derrière ces travaux de recherche sont nombreuses. D'une part, les accélérateurs laser-plasma ont été reconnus comme très prometteurs il y a plusieurs années déjà, notamment grâce à leur capacité à accélérer les électrons jusqu'à des vitesses proches de la lumière sur des distances extrêmement courtes, contrairement aux accélérateurs conventionnels qui s'étendent sur plusieurs kilomètres. D'autre part, lorsqu'une impulsion laser est réfléchie par une surface plasma oscillant à des vitesses relativistes, celle-ci peut voir sa durée raccourcie (notamment par effet Doppler) jusqu'à atteindre le régime attoseconde, ce qui correspond à élargir le spectre jusque dans le domaine XUV (par propriété des transformées de Fourier). L'efficacité de conversion et les propriétés spatio-temporelles des impulsions attosecondes ainsi produites sont extrêmement prometteuses, d'autant plus que, contrairement à la méthode traditionnelle qui consiste à générer des impulsions attoseconde par ionisation et recombinaison d'électrons dans des jets de gaz, il n'y a pratiquement pas de limite sur l'intensité de l'impulsion laser génératrice, ce qui permettrait de produire des impulsions attosecondes considérablement plus lumineuses. Ainsi, l'interaction laser-plasma en régime relativiste permet de produire de nouveaux outils (à savoir des paquets d'électrons de durée femtoseconde et des impulsions lumineuses de durée attoseconde) qui serviront la communauté scientifique au sens très large pour sonder la matière à des échelles temporelles inédites, ainsi que la société toute entière de manière générale, soit directement comme à travers la radiothérapie, soit indirectement en bénéficiant des retombées de l'étude des matériaux. Il y a bien sur de nombreuses autres applications envisagées, telles que l'utilisation de miroirs plasma comme intermédiaires vers l'atteinte d'intensités laser extrêmes qui permettront de sonder les fluctuations quantiques du vide à partir de lasers petawatt. Les nombreuses possibilités offertes par les miroirs plasma relativistes ont d'ailleurs convaincu la communauté scientifique européenne puisque la grande infrastructure de recherche ELI comprendra une ligne de lumière dédiée aux miroirs plasma au sein du centre ELI-ALPS basé à Szeged, en Hongrie. L'entreprise ARDOP Industrie a été chargée de la mission de concevoir, construire et installer cette ligne de lumière à l'horizon 2023. Mon travail de recherche au Laboratoire d'Optique Appliquée a donc contribué à finaliser la conception de la ligne de lumière et à transférer l'expertise du groupe Physique du Cycle Optique (PCO) du Laboratoire d'Otique Appliquée vers l'entreprise, afin que cela bénéficie à la communauté scientifique via ELI, puisque cette ligne de lumière devrait être rendue disponible aux utilisateurs par le biais d'appels à projets d'ici quelques années.

Bien qu'il reste des phénomènes à interpréter, la compréhension des mécanismes physique sous-jacents est aujourd'hui à un stade assez avancé. Néanmoins, la réalisation expérimentale de faisceaux de particules et de lumière aux propriétés stables et optimales compatibles avec les applications envisagées reste en partie à démontrer. Au cours de cette thèse, un travail d'amélioration de la source laser « Salle Noire 2 » développée au LOA a donc été fait dans

un premier temps. Cette source unique au monde produit des impulsions lumineuses de durée ajustable, allant de quelques ps à seulement 3.5 fs. A la longueur d'onde centrale de 800nm, cela correspond à moins de deux périodes d'oscillations du champ électromagnétique (dits « cycles optiques »). Grâce à cette durée particulièrement courte, lorsque nous focalisons ces impulsions pour concentrer la lumière spatialement sur une surface aux dimensions de l'ordre du micromètre (c'est-à-dire comparable à la longueur d'onde du laser), nous parvenons à atteindre des intensités suffisantes pour faire osciller les électrons à des vitesses relativistes avec relativement peu d'énergie par impulsion (de l'ordre du millijoule). Du fait de la faible énergie contenue dans chaque impulsion dans ce régime extrême, appelé le régime lambda cube, nous pouvons générer ces impulsions à la cadence de 1 kHz, contrairement à la majorité des systèmes laser capables d'atteindre des éclairements relativistes, qui sont de plus longue durée, plus forte puissance moyenne, et donc à fortiori avec un faible taux de répétition ($\sim$1 tir par seconde). Pouvoir générer 1 000 impulsions par seconde est un avantage considérable pour les applications futures de cette source car il devient alors possible d'effectuer des études statistiques ou de moyenner les résultats sur un grand nombre de mesures afin d'améliorer leur fiabilité.

Dans un deuxième temps, plusieurs expériences d'interaction laser-plasma on été réalisées avec cette source de lumière et ont permis notamment de démontrer l'influence prévalente du décalage de phase entre l'enveloppe et la porteuse (décalage de la « CEP ») des impulsions laser quasi mono-cycles à plusieurs reprises, grâce l'implémentation d'une boucle de rétro-action permettant son contrôle dans la chaine laser. En particulier, nous avons démontré que la CEP influence le spectre et la direction d'émission des faisceaux d'électrons accélérés dans le sillage du laser dans des jets de gaz. Nous avons également pu démontrer la génération stable et contrôlée (via la CEP) de continuums spectraux dans la gamme XUV en réfléchissant les impulsions laser sur un miroir plasma. D'après des simulations numériques et les travaux d'autres équipes sur le sujet, ces continuums seraient associés à des impulsions attosecondes isolées avec une phase spectrale plate et contenant un pourcentage d'énergie de l'impulsion incidente très élevé ($>$30%), ce qui est extrêmement prometteur pour les applications à la science des matériaux à des échelles ultra-rapides, d'autant plus que nous générons ces continuums à haute cadence. En outre, lorsque le faisceau laser incident est réfléchi par le miroir plasma, des paquets d'électrons provenant du plasma sont injectés en phase dans le champ laser réfléchi. Nous avons mesuré les propriétés spatio-spectrales de ces faisceaux d'électrons et observé des différences claires en faisant varier la CEP. Bien que ces résultats expérimentaux nécessitent une investigation théorique plus approfondie, ils pourraient potentiellement ouvrir la voie vers la production de paquets d'électrons attoseconde isolés. Ces résultats inédits, qui sont le résultat de progrès technologiques et d'une optimisation approfondie de la source laser, ainsi que de la conception d'un dispositif expérimental unique au monde permettant l'étude des miroirs plasma au kHz, offrent donc de nouvelles possibilités en terme de contrôle des propriétés des faisceaux d'électrons et de lumière XUV.

Plan du manuscrit

Le but premier de ce manuscrit est de rendre compte de mes travaux de recherche et les comparer à l'état de l'art, mais j'ai aussi voulu produire un document qui puisse servir aux futurs nouveaux arrivants (stagiaires, doctorants, post-doctorants) dans le groupe PCO de quelque nationalité qu'ils soient, tel que j'aurais aimé avoir en arrivant dans le groupe pour mon stage de Master. Ayant apporté une plus ou moins grande contribution à pratiquement tous les éléments du laser et de la chambre d'interaction pour l'étude des miroirs plasma, cela n'était en outre pas hors de propos. J'ai donc tenté de donner le plus de détails possibles sur les dispositifs expérimentaux et les concepts physiques dans les termes les plus simples possibles sans toutefois rendre ce manuscrit trop long ou trop ennuyeux pour les experts du domaine. Je laisse au lecteur le soin de juger de l'atteinte (ou non) de mon intention. Le manuscrit est divisé en sept chapitres, répartis comme suit :

Chapitre 1. Dans le premier chapitre, j'introduis des notions physiques générales pré-

requises pour la génération, le transport et la caractérisation d'impulsions laser de durée proche du cycle optique.

Chapitre 2. Dans le deuxième chapitre, j'introduis certaines des notions physiques sous-jacentes à l'interaction laser-plasma en régime relativiste.

Chapitre 3. Dans le troisième chapitre, je présente la chaine laser « Salle Noire 2 » bloc par bloc en décrivant toutes les améliorations apportées lors de ma thèse, à savoir :

- Amélioration de la stabilité (CEP, énergie) du premier étage d'amplification à dérive de fréquences à travers le remplacement du laser de pompe par un nouveau laser et augmentation du facteur d'étirement temporel des impulsions dans l'amplificateur multi-passage

- Modernisation du filtre « XPW » servant à l'amélioration du contraste temporel des impulsions laser

- Modification du compresseur à la sortie du deuxième étage d'amplification à dérive de fréquences dans le but de réduire les effets thermiques et non linéaires introduits par l'ancien compresseur, et ainsi rendre la source laser plus

- Ajout d'une extension au dispositif servant à post-comprimer les impulsions lumineuses (càd à raccourcir leur durée) dans une fibre creuse afin de limiter les dommages induits par le laser sur le miroir situé en sortie de la fibre

Chapitre 4. Dans le chapitre 4, je présente les mesures effectuées afin de caractériser les impulsions produites dans le domaine spatial et temporel (à différentes échelles de temps), ainsi que les couplages spatio-temporels. Ensuite, je décris les moyens mis en œuvre afin de mesurer, stabiliser et contrôler la phase enveloppe-porteuse. Finalement, des premiers résultats mettant en évidence l'influence de la CEP dans les mécanismes d'accélération d'électrons dans des jets de gaz sont présentés, afin de démontrer les capacités de la source et la performance atteinte.

Chapitre 5. Dans le chapitre 5, je fais une revue des différents mécanismes de génération d'harmoniques d'ordre élevé sur miroirs plasmas, ainsi que les mécanismes d'accélération d'électrons et de protons identifiés par la communauté scientifique, à travers les expériences, les simulations numériques et les modèles analytiques.

Chapitre 6. Dans le chapitre 6, je décris la chambre expérimentale dédiée à l'étude des miroirs plasma au kHz en Salle Noire 2. Je détaille les procédures d'alignement et les différents diagnostics, dont certains ajoutés au cours de cette thèse.

Chapitre 7. Dans le chapitre 7, je présente un résumé des résultats expérimentaux obtenus pendant la thèse en utilisant le dispositif décrit au chapitre 6. Je présente des résultats à intensité sous-relativiste dans un premier temps (notamment l'étude approfondie d'un régime d'accélération de protons), ensuite je présente les résultats à plus haute intensité (notamment la mesure des spectres d'électrons en régime longs gradients). Finalement, je présente les effets de CEP observés lors des expériences avec leurs interprétations.

General introduction

Discerning the physical world beyond our natural capabilities.

As Brian Cox elegantly writes: "Curiosity is the rocket fuel that powers our civilization". Over 150 years ago, questions such as "Does a running horse have all of its four legs in the air at some point in its motion?", to which a human eye could not answer, led to the development of fast cameras, a tool that allowed us to overcome our physical limitations by freezing motion in time and replaying it at a lower rate.

When opening and closing a shutter takes too long (the times it takes is limited by its own weight), the acquisition can be gated by activating the sensor electronically for a short period of time instead. Whereas a normal motion picture movie is played at 24 frames per second, high speed cameras can achieve speeds of over 25 million frames per second, using rotating mirrors instead of mechanical shutters. There are numerous fascinating super slow motion videos online that are made using commercial high speed cameras. When even this gets too slow for the considered motion time scale, a solution is to keep the shutter open, the detector active and place the scene in the dark. The scene is then illuminated by a flash of light for a very short time and all we have captured is the scene at the precise moment when the flash reached it. Even more interesting, we can illuminate the scene with a series of short flashes separated in time. This is the principle of a stroboscope and an example is shown in figure 1. This very interesting field called chronophotography made our understanding of the mechanics of human bodies and living animals much better. The fastest movements that can be resolved depend on the duration of the flash light and the time interval between two consecutive flashes, the latest being inherently limited by the charging time of the capacitor. A way to circumvent that is to use a series of flash lamps synchronized with electronic signals, although those signals have a limited resolution themselves. Be that as it may, it remains our best tool to study phenomena which are not reproducible and need to be captured in a single take.

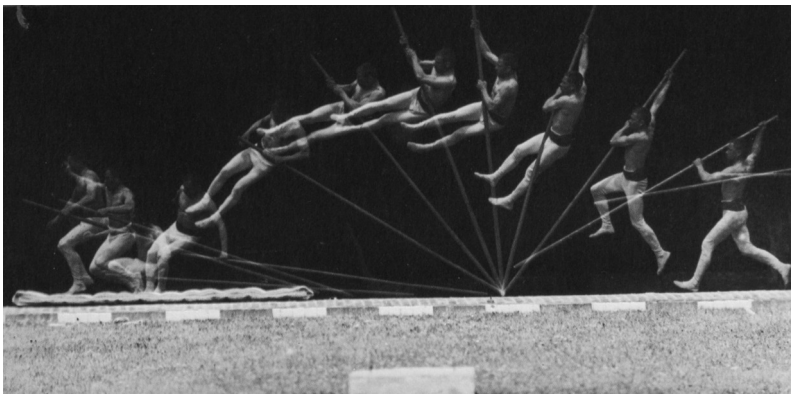

Figure 1: *Strobe shot of a pole vault, Etienne Jules Marey, Le mouvement, 1894.*

Nonetheless, going down on the time scale was made possible with the rapid progress of laser technology. From the first laser invented in 1960 by Theodore Maiman, it only took a few years to produce picosecond (1ps = 10^{-12}s) pulses, and ten more years to reach the femtosecond (1 fs = 10^{-15} s) scale in the mid 70's using dye lasers. In the late 1980s, Ahmed Zewail (Nobel Prize

of Chemistry in 1999) started using femtosecond laser pulses, which are now routinely produced, to study transition states of chemical reactions. This still very active field of science is known as femtochemistry. The femtosecond level is indeed the typical time scale for looking at molecules. In fact, the further down we go on the time scale, the further down we go on the length scale as well (see fig. 2 for examples), which makes sense because increasing an object's speed is much more difficult for large, often heavy objects, as it requires much more energy. Moreover, amongst the four fundamental forces that govern the physical world (gravity, electromagnetic, weak and strong force), the strongest ones are only efficient over very short distances. We are now naturally trying to enter the realm of attochemistry. The attosecond (1 as = 10^{-18} s, a billionth of a billionth of a second) is the typical time scale of electron motion. For instance, in a hydrogen atom, it takes 150 as for the electron to revolve around the nucleus. And if chemistry is the science of breaking and creating bonds between atoms and molecules, then attochemistry is its most fundamental form because it means controlling the electrons that form the bonds themselves. We thus progressively push the boundaries of what is within our grasp and gain some insight into ever faster phenomena.

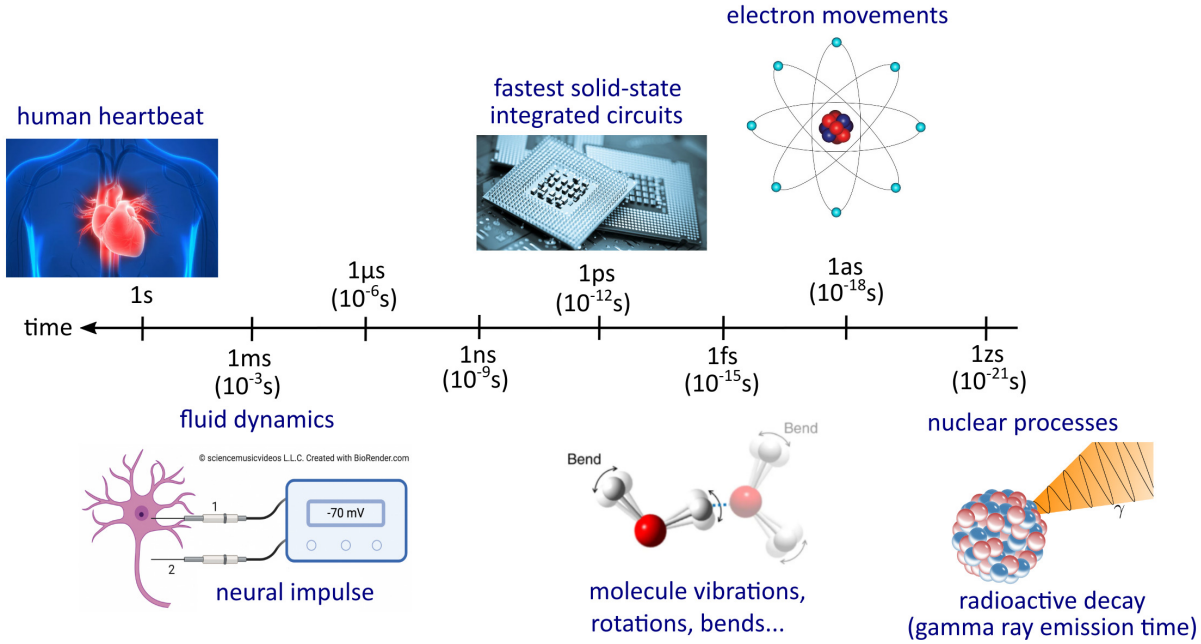

Figure 2: *Examples of phenomena occurring at different time scales.*

The most widely spread method to study phenomena on these extreme time scales, however only applicable to highly repeatable phenomena, is termed the optical "pump-probe" method and consists of triggering the event that one wants to look at with a pump pulse meanwhile observing it through a very narrow time window with a probe pulse, where both pulses are short on the time scale of the considered phenomenon. This operation is repeated for various time delays between the pump and the probe pulse, and we eventually obtain the movie of what happens during and after the event. Another similar method, ultrafast electron diffraction, combines an optical pump that triggers the event, with a fs electron bunch that probes the induced changes at different moments by looking at the electron diffraction pattern, which contains information about the sample structure. Although the tools already exist, many challenges remain to generate more suitable light pulses and electron bunches (duration, brightness, bunch charge, stability...) for various applications and widen access to these methods.

The need for short wavelengths, advantages and drawbacks.

A first indication on how to produce extremely short light pulses comes from the uncertainty principle, in its time-frequency form for Gaussian pulses: $\Delta t_{\mathrm{FWHM}} \Delta \nu_{\mathrm{FWHM}} \approx 0.441$. It tells us

that short pulses require broad spectra. For instance, a Δt_{FWHM}=1 fs pulse duration corresponds to a spectral bandwidth $\Delta\nu_{\mathrm{FWHM}}$ of 0.44 PHz. At the central visible wavelength (580 nm), this is equivalent to a 500nm broad spectrum (via eq. 1.15), so the entire visible spectrum (380 to 780nm) put together is not enough to achieve 1 fs. We need to extend to other spectral ranges.

Furthermore, the required spectral bandwidth to produce a ∼100 as pulse is so high that towards the low-frequency side of the electromagnetic spectrum, there is not enough energy/spectral density to supply the required bandwidth. For example, a 300 as Gaussian pulse requires a 1.47 PHz FWHM bandwidth, which simply cannot be centered at 500 nm (0.6 PHz). Therefore, such short pulses must have a central wavelength that is shorter than in the visible domain, and fall in the UV domain or further (fig. 3).

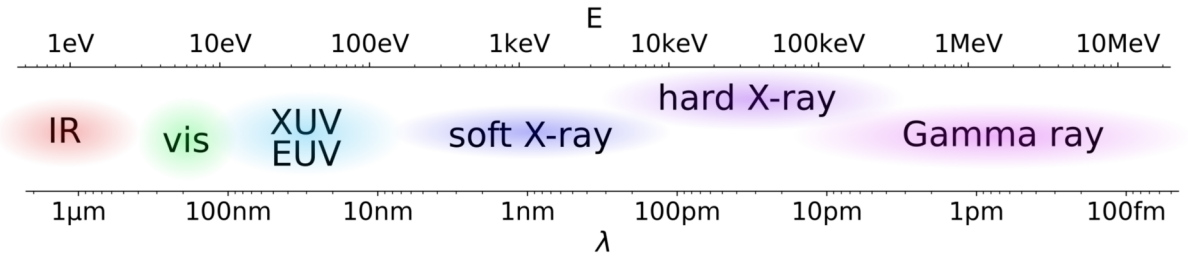

Figure 3: *Electromagnetic spectrum from IR to gamma rays.*

Additionally, short wavelengths have the advantage of being focusable into smaller diffraction spot sizes, thus also potentially increasing the spatial resolution of the probes. That is the reason why the most advanced chip-making processes (lithography) involve XUV lasers, now reaching down to a 2nm semiconductor node size. Amongst short wavelengths, the 2.3 to 4.4 nm range (the "water window") is particularly interesting for biological imaging because water is transparent, whereas organic molecules (carbon) are absorbing. Besides, the angstrom (10^{-10} m) is the characteristic length for atomic and molecular phenomena.

The drawback is that manipulating short wavelengths is extremely challenging because traditional optics don't work in the way we know. A fused silica convex lens focuses visible light but does not behave as a focusing lens at all for the XUV spectral range due to the wavelength dependence of its refractive index. Refractive optics are lacking in the XUV spectral region because most materials absorb XUV radiation, which was very useful for life to develop on earth, because the atmosphere protects us from these dangerous energetic rays, but becomes a problem for our research field. In fact, XUV optics is a field of research in its own right. Whereas new solutions like gas-phase prisms are proposed [67], the most common way to manipulate XUV beams currently consists in using reflective optics at grazing incidence angle.

Producing light at short wavelengths

Although it is not possible to produce such short pulses from a traditional laser system, as there is no gain medium able to produce a broad enough spectral bandwidth, short wavelength radiation, or equivalently energetic photons, can be produced in different ways to form attosecond pulses. A summary of different sources of photons with 10eV energy and more and the typical associated peak brightness is shown in figure 4.

One technique, known as "waveform synthesizer", consists of generating a super-continuum and then amplifying different spectral regions separately, either sequentially (*ie* the different co-propagating spectral regions are amplified one at a time in subsequent stages employing different phase-matching conditions) or in parallel (*ie* by spatially dividing the spectrum into different -typically three or four- spectral regions, which are amplified in parallel, and then carefully temporally and spatially recombining them) [284]. Pulses as short as 380 as were produced following this scheme [116].

Another method is to take advantage of the fact that accelerated charged particles can emit

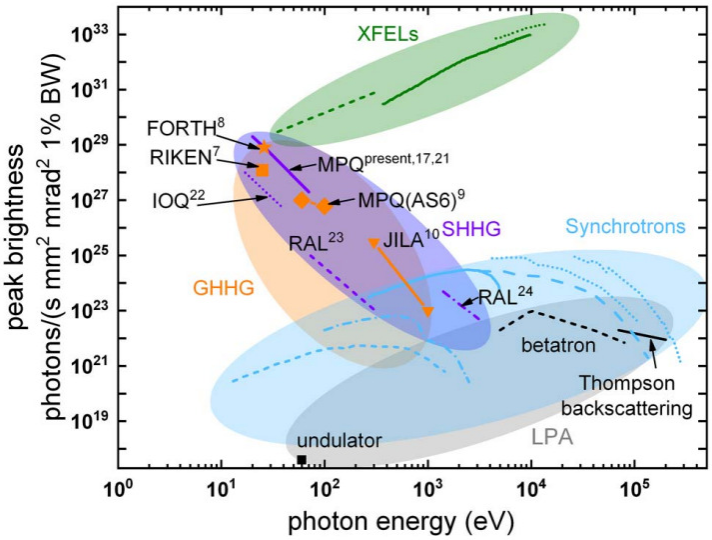

Figure 4: *Peak brightness for different types of x-ray sources. GHHG stands for gas harmonics, SHHG for solid harmonics (from plasma mirrors) and LPA for laser-plasma accelerators. Reprinted from [128].*

light. For instance, in cyclotrons or synchrotrons, electrons are accelerated by electric fields along a circular trajectory up to a few TeV kinetic energy, and generate X-rays. It is also possible to use a periodic structure of dipole magnets, called undulator, to force electrons to undergo several consecutive oscillations and coherently emit light. Oscillators and amplifiers in the IR domain using radiation from electrons propagating in an undulator were first experimentally demonstrated in the 1970s by John Madey, later leading to the proposal to build an X-ray Free Electron Laser (XFEL) by Claudio Pellegrini in 1992, followed by the construction of XFEL facilities all over the world (FLASH in Germany in 2005, LCLS in the USA in 2009, SACLA in Japan in 2011...), which combine very long linear electron accelerators (LINAC) with undulators. Nowadays, thanks to their ability to produce light with very short wavelengths below the angstrom, XFELs and synchrotrons are our most coveted tools to unravel the mysteries of materials science and those facilities receive more users proposals than they can accommodate for. However, they require a lot of space to accelerate the electrons over very long distances so that they can reach relativistic speeds (*ie* speeds close to the speed of light), and their typical sizes are of the order of one kilometer, whereas their cost is in billion dollars [205]. Moreover, the output radiation has limited temporal coherence because it all starts from incoherent spontaneous emission and the typical pulse duration falls in the femtosecond range. Nonetheless, realizing attosecond X-ray pulses from an XFEL is a quite active field of research and some efforts involving sophisticated injection schemes where an external infrared laser is used to modulate the electron bunch very recently led to the generation of isolated soft X-ray attosecond pulses (∼300 as) [73]. The remaining cost and size issue is also being addressed: a very promising alternative to LINAC is to use laser-plasma accelerators, a concept proposed by Tajima and Dawson in 1979 [242], to seed the undulators. Indeed, because of the extremely high electric field strengths achieved in laser-plasmas, they are able to accelerate electrons to relativistic speeds over extremely short distances.

Last but not least, the most widely used and extensively studied method to generate broad, coherent XUV spectra supporting as pulse duration is high-order harmonic generation (HHG). The first attosecond pulses [203, 121, 199] and the current record (measured) pulse duration of 43 as [97], as well as the first pioneering applications to attosecond pump-probe spectroscopy [68, 227, 43] are all attributed to harmonics generated in gaseous media.

Generation of XUV radiation via high-order harmonic generation

High-order harmonics in the XUV spectral domain can actually be generated from all sorts of media. The first observation of harmonics [42] was made in 1977, and resulted from the reflection of a CO_2 laser off a solid Al target in vacuum. The reflected beam contained up to the eleventh harmonic. It was then observed in gases for the first time in 1987 [172], which has been and still is extensively studied. The mechanism behind gas harmonics only works when the medium is not completely ionized, therefore imposing a limit on the driving laser intensity. With the advance of laser technology, reaching ever higher focused intensities, some researchers then naturally looked back towards plasma mirrors. More recently, HHG in solids, followed by liquids, began to draw attention because of all the possibilities they offer and because of their convenience. Generally, in order to extend to the XUV domain, the process becomes non-perturbative (meaning that it can no longer be explained by χ^n nonlinearities) but, as we will see, coherent VUV harmonics can also be generated by cascading many perturbative HHG processes.

Gases

In the late 1980s [84, 172], it was observed that when intense femtosecond laser pulses are focused into a dilute gas, the nonlinear interaction that takes place leads to the emission of a frequency comb of odd-order multiples of the driving laser frequency f_0, extending into the XUV spectral domain (fig. 5).

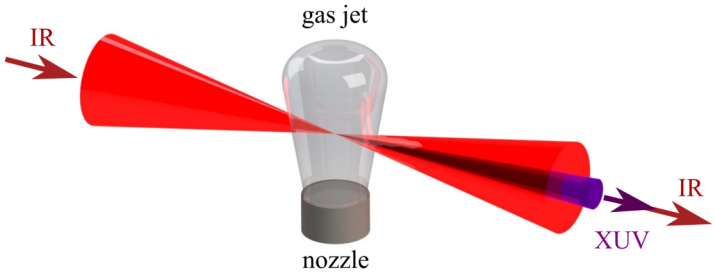

Figure 5: *Illustration of gas HHG.*

The surprise came from the shape of the spectrum. The harmonics were found to decrease rapidly in intensity at low orders, which was expected by the perturbative theory, but then they observed a plateau, with an approximately constant intensity over many orders, followed by an abrupt cut-off. This effect was named High-order Harmonic Generation (HHG) and drew a lot of attention because the broad generated spectrum was compatible with the production of an attosecond pulse train in the time domain [78].

A new model (the three-step semi-classical model [229, 59], see fig. 6) was proposed in 1993 to explain these spectral features through ionization, acceleration and recombination. During the first half-cycle of the femtosecond driving light wave, the laser electric field allows electrons to escape the atomic potential via tunnel ionization and gain kinetic energy. As the electric field sign is reversed, during the second half-cycle, electrons can recombine with their parent ions and

the excess kinetic energy is released as an XUV photon. Electrons born at different times gain a different amount of kinetic energy, therefore XUV photons are emitted with a broad range of energies, supporting attosecond duration.

As the process repeats itself every half-cycle, the XUV light bursts are emitted at the repetition rate $f_{rep} = 2f_0$ and spectral interferences lead to a comb of frequencies spaced by $2f_0$. Each subsequent XUV burst returns from a different direction, so the carrier-envelope phase flips from one attosecond burst to the next ($\Delta\phi = \pi$). Therefore the offset of the frequency comb will be $f_{ceo} = \Delta\phi f_{rep}/(2\pi) = f_0$ and we end up with odd harmonics only (see subsection 4.2.3).

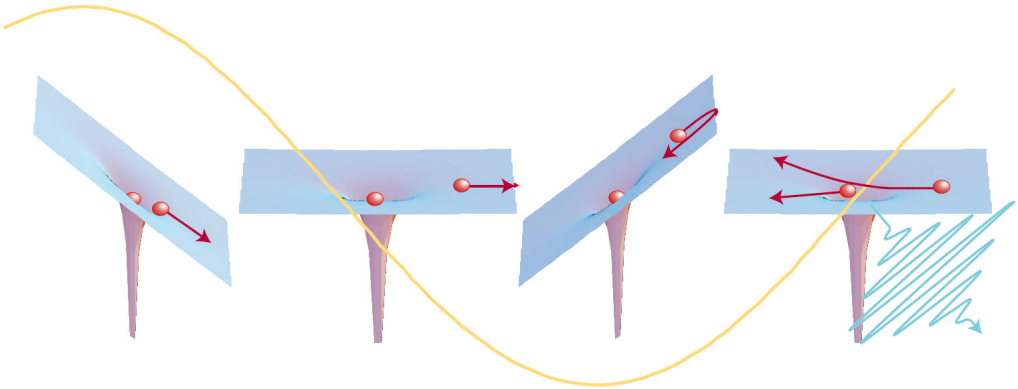

Figure 6: *Three step model describing the HHG mechanism in gaseous media. Reprinted from [60].*

The high frequency cutoff observed in the spectra depends on the laser intensity and wavelength: $\omega_{max} = 3.17U_p + I_p$, with U_p the ponderomotive energy, which scales as $I\lambda^2$, and I_p the ionization potential. Under normal conditions, the single atom HHG efficiency $\eta(\lambda)$ is proportional to λ^{-5}-λ^{-7} [233]. Thus, using driving lasers with longer wavelengths helps increasing the frequency cutoff (one of the reasons why more and more people turn to mid-IR lasers instead of Ti:Sa lasers) and reduces the ionization yield, but low order harmonic generation is more efficient when using higher frequency lasers [58].

A critical aspect of gas HHG is phase matching. At high repetition rates (>10MHz), phase-matching is prevented by steady-state plasma accumulation in the generation volume. For long pulses, such as those produced by ytterbium-doped fiber lasers, the phase-matching condition is not fulfilled during the whole pulse duration (hence the increasing interest in post-compression techniques to reduce the pulse duration).

Overall, gas-phase HHG has been extensively explored and has proven its capabilities [20]. It is now rather well understood and remains one of the privileged paths to reliably generate attosecond pulses. The main drawback of gas harmonics is the low conversion efficiency (the highest measured efficiencies are $\sim 10^{-4}$ [243] or maximum 10^{-3} [190]) and the limitation on the driving laser pulse intensity: it must be high enough to be in the strong-field regime (*ie* in a regime where the focused laser intensity is high enough to lower the barrier of the binding potential felt by the valence electrons so as to cause tunnel-ionization) but not become too high otherwise the mechanism breaks down due to plasma formation. Typically, the laser intensity in the gas medium must be $\sim 10^{14}$W.cm^{-2}.

Techniques [48] such as using very long focal length optics to increase the Rayleigh length or generating the harmonics in a gas-filled photonic crystal fiber can increase the effective interaction volume [269]. More sophisticated schemes also appeared to increase the average HHG power, like enhancement cavities [57]. Other parameters can be played with: for example, using hot gases, in which molecules move faster, helps reducing the steady-state plasma accumulation

in the laser focus [211] and allows working at high repetition rates.

Solids

More recently, high-harmonic generation from solids was also reported. In solids, the laser pulse promotes electrons from the valence to the conduction band. Harmonics can be emitted when electrons oscillate in the conduction band (intraband HHG), or when the electrons move back to the valence band (interband HHG). Non-perturbative HHG from solids was first observed in 2010 [101], using a mid IR (longer wavelengths correspond to a higher damage threshold of the crystal), few-cycle laser focused in a ZnO bulk crystal. The authors observed a spectrum of odd harmonics extending well beyond the bandgap of the crystal, which is evidence for the non-perturbative character of the process. Solid-state HHG was then observed from a wide variety of media [102]: dielectrics, common glass, or more sophisticated engineered structures like graphene, using a laser whose wavelength depends on the material's bandgap.

The advantage of HHG from solids is the compactness and the flexibility of the target design. Some researchers explore the possibility of using solids with tailored structures (e.g. nanostructures) and/or composition (e.g. ion-implanted semiconductors) in order to manipulate the XUV beam (spatial distribution, intensity and phase) at the same time as it is created [234]. One could for instance create XUV light carrying orbital angular momentum. HHG can also be enhanced by using semiconductors [92] or by taking advantage of plasmonic resonances in some materials [257]. This also opens up the path to the creation of compact all solid state EUV sources. However, it is quite limited in terms of driving laser intensity, because we want to remain below the intensity damage threshold of the bulk material.

Liquids

Using liquid targets, coherent HHG was first observed from laser-induced expansion of the droplets to lower densities [86, 147], so the scientific community argued that this was actually not from the liquid phase. Only more recently, in 2018, coherent HHG from the bulk of liquids reaching the XUV was observed. In [166], the authors used liquid water and ethanol flat microjets, and the dominant harmonic spectrum features could be explained by the width of the conduction and valence bands, the band gap and the peak electric field strength.

Cascading of many lower-order processes to generate high-order harmonics in the perturbative regime

It is also possible to generate high-order harmonics by cascading perturbative processes (*ie* processes described by $\chi^{(n)}$). In [225], the authors used PPLN crystals to generate coherent UV-visible light up to the ninth harmonic order and modeled the process with only $\chi^{(2)}$ nonlinearities. In [61], both odd and even harmonics in the VUV (spectral region from 6-15 eV) were produced in a microstructured, xenon-filled hollow-core fiber by focusing the fundamental and the frequency doubled components of an Yb:fiber laser. The intensity was only $\sim 10^{12}$W.cm^{-2}, offering the possibility to work at very high repetition rates, and the results were simulated by taking only four-wave ($\chi^{(3)}$) mixing processes into account. The advantage of cascaded HHG is the high conversion efficiency, resulting in flux levels comparable to that of synchrotrons in the VUV spectral range, but with a narrow spectral bandwidth.

Plasma mirrors

HHG with relativistic plasma mirrors is a totally different mechanism. It results from the reflection of a laser pulse off the interface between vacuum and an overdense plasma. The most practical way to obtain such an interface is to use polished solid targets, which are ionized by the leading edge of the incident pulse (or an auxiliary pulse). Using liquid targets (liquid sheets created by colliding two liquid jets) is also very promising as it would allow continuous operation by recycling the liquid, but it has been very little studied so far.

The main interest of plasma-based harmonic generation is that, contrary to all the other

interaction media mentioned above, there is almost no upper limit on the intensity of the driving laser. On the contrary, the more intense, the better. At very high intensities ($\sim 10^{19}$W.cm^{-2}), the laser triggers relativistic oscillations of the plasma reflective layer. This oscillatory motion induces a periodic frequency upshift of the reflected laser wave, or equivalently a temporal compression of the electric field (see fig.7). These new frequencies are generated periodically, every optical cycle, and the interferences lead to the observation of both odd and even harmonic orders of the incident laser.

When the interaction conditions are optimized, the reflected field contains field spikes which only last a few attoseconds each. An attosecond pulse train is thus created. In order for HHG to be efficient, the driving laser pulses must meet a lot of requirements. In addition to high intensity, which implies focusability (therefore high spatial quality) and femtosecond duration, we also need the pulses' temporal contrast to be extremely high. In other words, we want the ratio of light intensity near the peak of the pulse envelope to that a few ps before the peak to be over 10^{10}, so that the ionization of the target can be triggered by an auxiliary pulse at a controlled time before the peak of the driving pulse, thus allowing to customize the plasma density ramp at the surface of the target.

Although it is technologically very challenging, I hope to convince the reader of this manuscript that plasma-based HHG is a very promising way of producing bright attosecond pulses, and even isolated attosecond pulses, at high repetition rate.

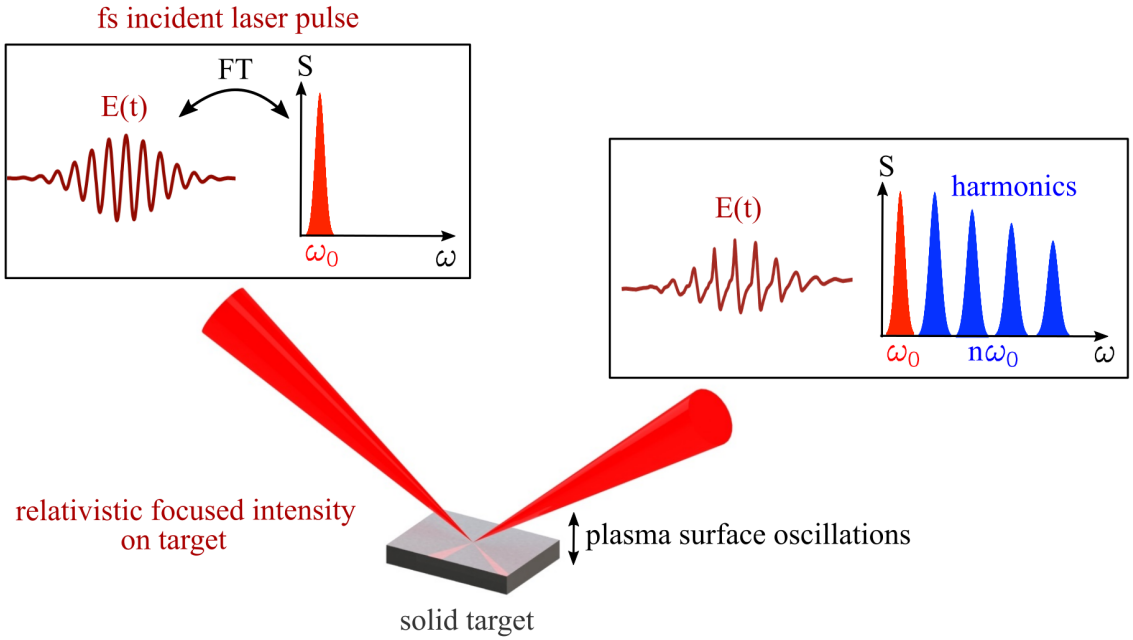

Figure 7: *Illustration of the attosecond pulse generation mechanism using relativistic plasma mirrors. A femtosecond laser pulse is obliquely incident on a solid target. A plasma is created at the surface of the target, which becomes a mirror for the incident light wave. Due to the relativistic oscillatory motion of the plasma surface, the reflected laser contains field spikes in the time domain, and high-order harmonics in the frequency domain.*

Electron and proton beams from laser-plasma interactions

Together with the generation of XUV harmonics from plasma mirrors, another motivation behind this thesis' work is the generation of charged particle (proton, electron) beams from relativistic laser-plasma interaction.

Laser-plasma electron acceleration

As an intense laser propagates in a gas jet, it ionizes atoms and turns it into a plasma. The laser beam pushes electrons away as it propagates, and triggers plasma waves in its wake (see fig. 8). Some electrons can be trapped inside the positively charged plasma cavities, which propagate at the same speed as the laser pulse, and thus gain huge amounts of kinetic energy. The accelerating gradients, up to ∼100 GeV/m, are several orders of magnitude higher than the typical gradients achieved in LINACs (∼10-100 MeV/m). Thus, laser-wakefield acceleration (LWFA) [74] promises to deliver compact, high energy particle accelerators.

Laser-plasma accelerators can produce electron beams with extremely interesting properties: high energy (MeV electrons can be obtained with mJ-class lasers, whereas energies up to 10GeV can be reached using PW-class systems), low divergence (few mrad), short duration (∼ fs [164]), high charge (∼ pC to nC), but also a low energy spread (∼ percent level). Moreover, the electron beam is perfectly synchronized with the laser source, thus both can be used for ultrafast pump/probe experiments.

Laser-plasma accelerated electrons can also be used as light sources [6]. X-rays [209] and gamma-rays can be produced when the electrons wiggle in the ion cavity as shown in fig. 8 (via Betatron radiation), in a counter-propagating laser beam (via Compton scattering), or in undulators. These radiation beams can be used in various fields: medical and biological applications, condensed matter and high energy density science, or even military applications [6].

Current research works aim at increasing the electron energy, further reducing the energy spread (e.g. for XFELs) or improving the shot-to-shot stability.

Laser-driven ion acceleration

The most common laser-driven ion acceleration mechanism is Target Normal Sheath Acceleration (**TNSA**) [271, 180]. In TNSA, the laser is focused to high intensities (typically well above 10^{18}W.cm^{-2}) on a thin ($\sim \mu$m) solid foil target. The interaction of the laser pulse with the preformed plasma and underlying solid target constitutes a source of hot electrons, which travel through the foil down to its rear side. Some of them are able to escape into the vacuum behind the target, whereas others are trapped and circulate back and forth through the target. The charge separation induced by the sheath of hot electrons coming out of the back side generates strong electric fields (∼ TV/m), which can ionize atoms and rapidly accelerate ions, thus emitted along the target normal direction (hence the name TNSA). Protons, originating from water vapor and hydrocarbon contamination, are lighter and come first, followed by heavier ions. It produces an ion beam with a broad, exponentially decaying energy spectrum, which is the main disadvantage of TNSA. However, the thus produced ion beams also have interesting

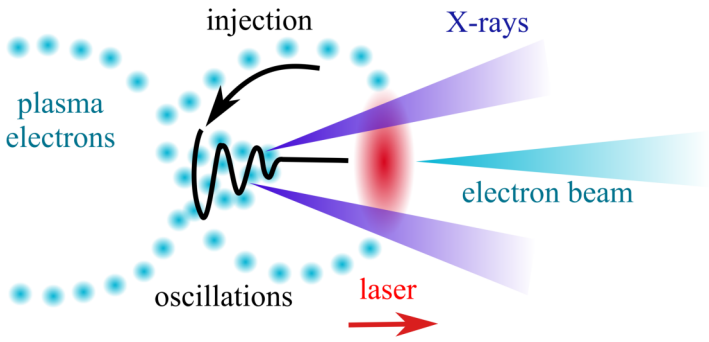

Figure 8: *Illustration of a laser-plasma accelerator. As a high-intensity laser (in red) propagates in a gas medium, it ionizes atoms and generates plasma waves in its wake. Electrons (blue dots) are injected in the positively charged plasma cavities in the laser wake (following the black solid lines), and thus accelerated. The electrons oscillate and can generate betatron radiation (X-rays, here in purple), before being ejected from the plasma accelerator in the form of an electron beam (blue cone).*

properties: energies up to tens of MeV, laser beam to ion beam energy conversion efficiency of up to ~ 10 %, and the proton beams are typically emitted with a $\sim 5°$ half opening angle (for the ones with highest energies only -this value increases for lower energy particles).

Other mechanisms exist, such as **radiation pressure acceleration** [76, 120]: a circularly polarized laser beam focused into a large focal spot is used so that the light pressure pushes the entire electron volume of a very thin foil forward instead of just exploding the foil. The ions are thus all accelerated by the same field and form a quasi mono-energetic beam. There are other advanced schemes like **Shock** acceleration or **magnetic vortex** acceleration, which can also be used to reduce the energy spread of the beam. Another approach is to shape the beam spatially and spectrally after its emission, using beam transport devices such as pulsed solenoid coils [35].

Due to their good spatial and temporal resolution, TNSA protons are used for imaging purposes (proton radiography) with stacks of proton-sensitive detectors, e.g. to spatially resolve the evolution of electric fields on a ps time scale [29], and also have the potential for medical applications [35]. Proton beams produced in cyclotrons have been used for decades for precision radiation therapy. The advantage of protons is that they experience less scattering as they go through the body and they deposit most of their energy in the Bragg peak *ie* at a certain depth, which depends on the proton energy. Therefore, they can be used to precisely target a tumor without causing collateral damages, contrary to conventional X-ray therapy or even electron radiotherapy, which makes them more suitable for treating sensitive body parts like eyes or brain tumors.

Electrons and protons from plasma mirrors

When a laser interacts with a plasma mirror, it can also accelerate protons, ions and electrons (fig. 9). Looking at these observables is interesting simply because it provides more information on the interaction dynamics, but those beams might actually be interesting for applications as well.

There are very few experimental studies on proton acceleration from plasma mirrors. There are only two papers [258, 125] reporting on the front-side (*ie* the side onto which the laser is impinged, rather than the target backside as in TNSA) emission of low-divergence, ~ 100 keV protons along the target-normal direction.

There has been more interest in the emission of electrons. Early on, the emission of attosecond electron bunches, synchronized with the harmonic generation, was predicted [188]. Different regimes and mechanisms for electron acceleration have now been identified experimentally and

theoretically, and will be detailed in Chapter 5. Electron beams have mostly been observed around the specular direction, sometimes more towards the target normal direction and sometimes at larger angles, depending on the gradient scale length and the angle of incidence of the laser on target.

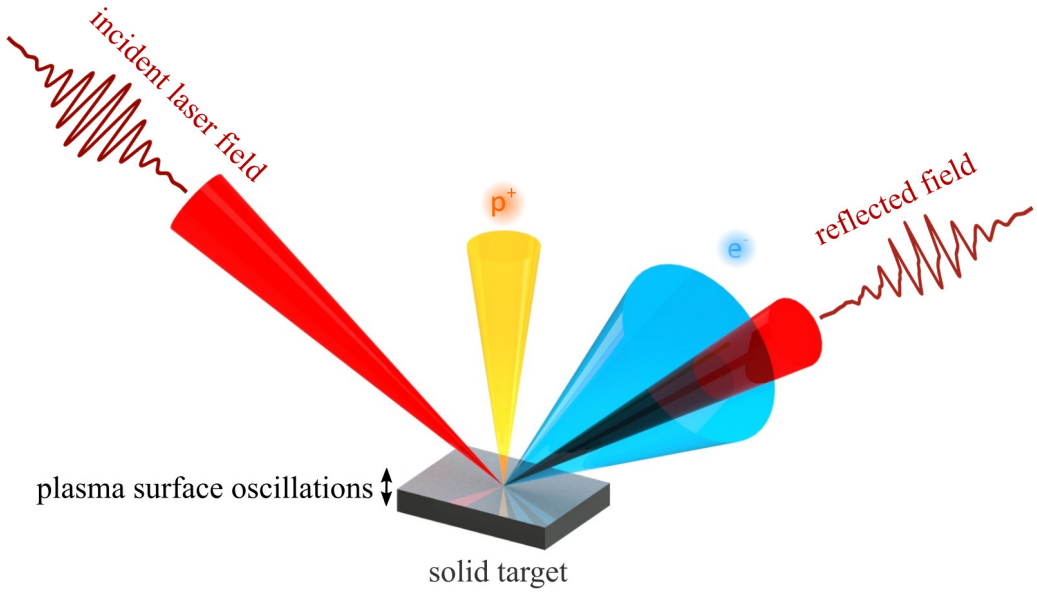

Figure 9: *Illustration of the typical emission of proton and electron beams from plasma mirrors.*

Outline of the manuscript

This thesis is the continuity of former experimental works in the PCO (led by Rodrigo Lopez-Martens) and APPLI (led by Jérôme Faure) groups at ***L**aboratoire d'**O**ptique **A**ppliquée* (LOA) in Palaiseau, France.

The first part of my thesis consists in the development of the existing *Salle Noire 2* laser system at LOA, designed by the PCO group to meet the afore-mentioned requirements for plasma mirrors. Efforts were made to make the system more stable and reliable. In particular, the main advance during my thesis was the stabilization and control of the carrier-envelope phase (the offset phase between the pulse envelope and the carrier wave below it) of the laser at its full repetition rate.

The second part of my thesis is the application of this laser source to relativistic laser-plasma interaction at kHz repetition rate. The APPLI group focuses on the acceleration of electrons in gas jets, while the PCO group focuses on the interaction with plasma mirrors. The carrier-envelope phase (CEP) stabilization and control allowed to produce laser-plasma accelerated electron beams exhibiting stable energy and direction, by controlling the electron injection within the laser-plasma accelerator through the CEP for the first time. During my thesis, I took part in several experimental campaigns to study plasma mirrors. Additions were made to the already existing experimental setups and different regimes of interaction were experimentally investigated. In particular, taking advantage of the carrier-envelope phase control, we could generate continuous XUV spectra supporting isolated attosecond pulses at kHz repetition rate, by forming a relativistic-intensity temporal gate at the surface of the plasma mirror.

This manuscript is divided into seven short chapters:

· **Chapter 1.** The first chapter will lay the theoretical background for femtosecond lasers and introduce the key concepts for understanding the *Salle Noire 2* laser system

· **Chapter 2.** The second chapter will introduce the fundamentals of relativistic laser-plasma physics

· **Chapter 3.** In the third chapter, I will describe the *Salle Noire 2* laser system and detail the changes that were made during my PhD

· **Chapter 4.** The fourth chapter will focus on the characterization of the laser pulses and the CEP stabilization of the laser system. The laser system capabilities will be demonstrated through laser-plasma electron acceleration in gas jets.

· **Chapter 5.** Finally, we will dive into the world of plasma mirrors: Chapter 5 will review the identified physical mechanisms leading to the emission of harmonics, protons and electrons in different regimes of interaction.

· **Chapter 6.** In this chapter, I will detail the experimental tools dedicated to the relativistic interaction with plasma mirrors at kHz repetition rate in *Salle Noire 2*, including new diagnostics.

· **Chapter 7.** In the last Chapter, experimental results with plasma mirrors that were obtained during my thesis will be presented.

The primary goal of this manuscript is of course to report on the research work that was done during my thesis, but I also tried to give enough details about the laser system and the experimental setup (which I spent most of my time working on), along with simple explanations of the underlying physical concepts, hoping it will be useful for the next newcomers in the PCO

group, while keeping the number of pages reasonable and the content not too simplistic for experts in the field. I will let the reader decide whether or not I reached this goal...

Chapter 1

Theoretical background for femtosecond lasers

"A laser is a solution seeking a problem".
Theodore Maiman

Both laser-plasma accelerators and plasma mirrors rely on femtosecond lasers. Thus, let me lay the theoretical background for femtosecond lasers in this first chapter.

1.1 Wave equations

1.1.1 Linear wave equation

Let us start from Maxwell's equations, which form the foundation of classical electromagnetism, expressed in SI units:

$$\vec{\nabla} \cdot \vec{E} = \frac{\rho}{\epsilon_0} \text{ (Maxwell Gauss)} \tag{1.1}$$

$$\vec{\nabla} \cdot \vec{B} = 0 \text{ (Magnetic flux)} \tag{1.2}$$

$$\vec{\nabla} \times \vec{E} = -\frac{\partial \vec{B}}{\partial t} \text{ (Maxwell-Faraday)} \tag{1.3}$$

$$\vec{\nabla} \times \vec{B} = \mu_0 \vec{j} + \mu_0 \epsilon_0 \frac{\partial \vec{E}}{\partial t} \text{ (Maxwell-Ampère)} \tag{1.4}$$

In vacuum, there are no current and charges: $\vec{j} = \vec{0}$ and $\rho = 0$, and we can obtain the wave equation [33] by using the curl of the curl identity $\nabla \times (\nabla \times \vec{A}) = \nabla(\nabla \cdot \vec{A}) - \nabla^2 \vec{A}$:

$$\boxed{\nabla^2 \vec{E} - \frac{1}{c^2} \frac{\partial^2 \vec{E}}{\partial t^2} = 0}, \tag{1.5}$$

with $c = (\mu_0 \epsilon_0)^{-1/2}$.

However, the propagation of linear waves in a **dielectric medium** is more conveniently described by introducing the polarization vector $\vec{P}$ (density of electric dipole moments), which can be expressed as a function of the electric field vector: $\vec{P} = \epsilon_0 \chi \vec{E}$, where χ is the electric susceptibility tensor. We also separate the contribution of free and bound charges in Maxwell-Gauss equation:

$$\vec{\nabla} \cdot \vec{E} = \frac{\rho_{\text{free}} + \rho_{\text{bound}}}{\epsilon_0} = \frac{\rho_{\text{free}} - \vec{\nabla} \cdot \vec{P}}{\epsilon_0}$$

and naturally introduce the auxiliary field $\vec{D} = \epsilon_0 \vec{E} + \vec{P}$. Finally, a dielectric medium is governed by the following set of equations:

$$\vec{\nabla} \cdot \vec{D} = \rho_{\text{free}} \qquad \vec{\nabla} \cdot \vec{B} = 0$$

$$\vec{\nabla} \times \vec{E} = -\frac{\partial \vec{B}}{\partial t} \qquad \vec{\nabla} \times \vec{B} = \mu_0 \left(\vec{J_{free}} + \frac{\partial \vec{D}}{\partial t} \right)$$

In the absence of free charges, the wave equation 1.5 becomes:

$$\boxed{\nabla^2 \vec{E} - \frac{1}{c^2} \frac{\partial^2 \vec{E}}{\partial t^2} = \mu_0 \frac{\partial^2 \vec{P}}{\partial t^2}} \tag{1.6}$$

1.1.2 Nonlinear wave equation

It is then very useful to develop the polarization vector into a power series of the electric field:

$$\begin{aligned}\vec{P} &= \epsilon_0(\chi^{(1)}\vec{E} + \chi^{(2)}\vec{E}^2 + \chi^{(3)}\vec{E}^3 + ...) \\ &= \vec{P}^{(1)} + \vec{P}_{\mathrm{NL}}\end{aligned}$$

with $\vec{P}^{(1)} = \epsilon_0\chi^{(1)}\vec{E}$. This will allow us to distinguish between linear (described by $\chi^{(1)}$) and nonlinear effects (described by $\chi^{(n)}$ with $n \geq 2$). The first order term of the susceptibility $\chi^{(1)}$ is related to the refractive index (real part) and the absorption (imaginary part).

The wave equation can be rewritten using $n^2 = 1 + \chi^{(1)}$ and decomposing the polarization vector:

$$\boxed{\nabla^2\vec{E}(r,t) - \frac{n^2}{c^2}\frac{\partial^2\vec{E}(r,t)}{\partial t^2} = \mu_0\frac{\partial^2\vec{P}_{\mathrm{NL}}(r,t)}{\partial t^2}} \tag{1.7}$$

Alternatively, equation 1.6 can be written in the frequency domain as follows:

$$\nabla^2\vec{E}(r,\omega) + \frac{\omega^2}{c^2}\vec{E}(r,\omega) = -\omega^2\mu_0\vec{P}(r,\omega) \tag{1.8}$$

Or, if we decompose the polarization vector:

$$\boxed{\nabla^2\vec{E}(r,\omega) = -\frac{\omega^2}{c^2}\epsilon(r,\omega)\vec{E}(r,\omega) - \omega^2\mu_0\vec{P}_{\mathrm{NL}}(r,\omega)} \tag{1.9}$$

with the relative permittivity defined as $\epsilon(r,\omega) = 1 + \chi^{(1)}(r,\omega)$.

1.2 Femtosecond pulses

One can show that the wave equation admits a general solution which is the sum of a progressive and a regressive plane wave. From Fourier decomposition, a progressive plane wave can be broken down into a linear combination of monochromatic progressive plane waves (a wave packet), which is better suited to describe femtosecond pulses. If we only consider a one-dimensional (z) propagation in space, a solution reads:

$$E(\vec{z},t) = \frac{1}{\sqrt{2\pi}}\int E(z=0,\omega)e^{i(\vec{k}.\vec{z}-\omega t)}d\omega. \tag{1.10}$$

1.2.1 Time-bandwidth product

For now, let us consider a Gaussian pulse at $\vec{z} = 0$ only (no propagation), with a central frequency ω_0 and a spectral width $\Delta\omega_0$ (corresponding to the half width at $1/e$ of the intensity profile):

$$E(0,\omega) = |E(0,\omega)|e^{i\phi(0,\omega)} = E_0 e^{-\frac{(\omega-\omega_0)^2}{2\Delta\omega_0^2}}e^{i\phi(0,\omega)} \tag{1.11}$$

If the spectral phase $\Phi(0,\omega)$ is constant or linearly depends on ω, the pulse is said to be Fourier-Transform limited, meaning it has the shortest pulse duration possible for a given spectrum. In the case of a constant phase $\Phi(0,\omega) = \Phi_0$, one can show that:

$$E(0,t) = \mathcal{FT}[E(0,\omega)] = \frac{1}{\sqrt{2\pi}}\int E_0 e^{-\frac{(\omega-\omega_0)^2}{2\Delta\omega_0^2}}e^{i\phi(0,\omega)}e^{-i\omega t}d\omega \tag{1.12}$$

$$= E_0 e^{i\Phi_0}e^{-i\omega_0 t}\Delta\omega_0 e^{-\frac{\Delta\omega_0^2 t^2}{2}}, \tag{1.13}$$

The Gaussian envelope $e^{-\frac{\Delta\omega_0^2 t^2}{2}}$ can be identified to $e^{-\frac{t^2}{2\Delta t_0^2}}$ and we find the time-bandwidth product

$$\boxed{\Delta t_0 \Delta\omega_0 = 1}. \tag{1.14}$$

If we consider the full width at half maximum of the intensity profile $\Delta t_{\mathrm{FWHM}} = 2\sqrt{\ln 2}\Delta t_0$, the product reads $\Delta t_{\mathrm{FWHM}}\Delta\nu_{\mathrm{FWHM}} = 2\ln 2/\pi \approx 0.441$. But the most accessible value in the lab is the FWHM of the intensity profile specified for wavelengths instead of frequencies:

$$\boxed{\Delta\lambda_{\mathrm{FWHM}} = \frac{\lambda_0^2 2\ln 2}{c\pi}\frac{1}{\Delta t_{\mathrm{FWHM}}}} \tag{1.15}$$

where λ_0 is the central wavelength. For example, if we consider a pulse centered at $\lambda_0 = 800$ nm, a duration of 28 fs requires $\Delta\lambda_{\mathrm{FWHM}} \approx 34$ nm, whereas a 3.5 fs pulse requires $\Delta\lambda_{\mathrm{FWHM}} \approx 269$ nm.

1.2.2 Spectral Phase

In order to optimize the pulse intensity, it is necessary to precisely control its temporal compression, especially for ultra short pulses. This information is contained in the spectral phase, which is rarely just a constant and can be expressed as a Taylor's series expansion around the central frequency:

$$\phi(0,\omega) = \sum_{n=0}^{\infty} \frac{1}{n!}\phi_n(\omega-\omega_0)^n \tag{1.16}$$

$$= \phi_0 + \phi_1(\omega-\omega_0) + \frac{\phi_2}{2!}(\omega-\omega_0)^2 + \frac{\phi_3}{3!}(\omega-\omega_0)^3 + \frac{\phi_4}{4!}(\omega-\omega_0)^4 + ... \tag{1.17}$$

with $\phi_n = \left(\frac{d^n\phi(\omega)}{d\omega^n}\right)_{\omega_0}$.

The first term ϕ_0 is the zeroth order spectral phase, and corresponds to a carrier-envelope phase (CEP) offset. If $\phi_0 \neq 0[2\pi]$, the maximum of the envelope and the maximum of the electric field amplitude are not in phase. This term does not modify the pulse duration and is usually negligible for a multi-cycle laser pulse, but it can dramatically affect the amplitude of the electric field for a few-cycle pulse, as shown in fig. 1.1. To be more precise, the final carrier-envelope phase of a pulse that is not Fourier-transform limited is not only defined by Φ_0, but will also be determined by higher order spectral phase terms.

A summary of the 1st to 4th order spectral phase effect on ultrashort pulses is represented in figure 1.2

GD. The first order phase ϕ_1 is expressed in fs and corresponds to a time shift of the pulse envelope, or group delay (red plot in figure 1.2). It does not modify the shape of the envelope either.

GDD. ϕ_2 [fs^2] is commonly called group delay dispersion (GDD) and expresses a linear variation of the group delay with the frequency, symmetric with respect to ω_0. As a consequence, the pulse duration can be drastically increased and the periods of the electric field are temporally chirped within the pulse envelope. For instance, a 3.5fs pulse will see its duration increased to 17fs after propagating over 1 meter in air (the GDD introduced by propagating through one meter of air is 21 fs^2 at 800nm) or to 29fs after propagating through 1mm of fused silica. It is therefore important to remain under vacuum and avoid

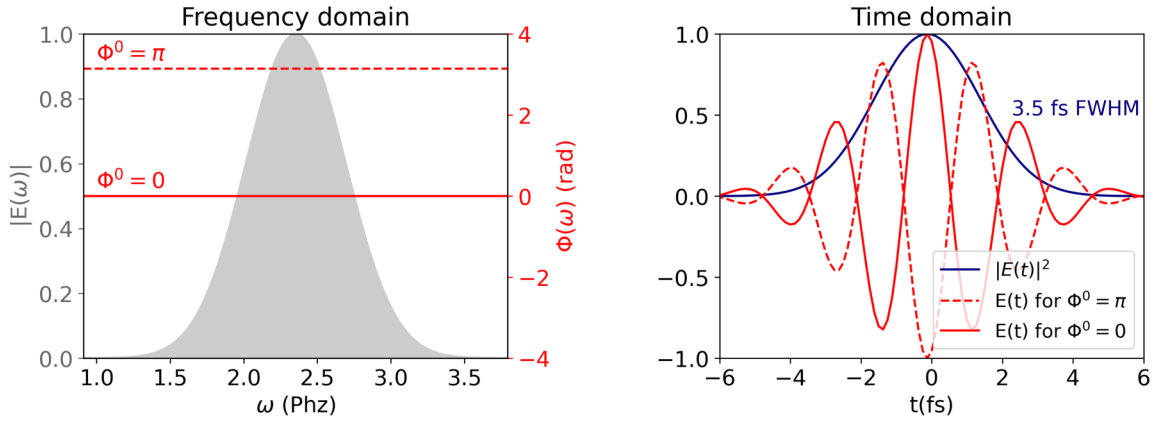

Figure 1.1: *Effect of 0 order spectral phase on the electric field of a Fourier transform limited 3.5fs pulse at the central wavelength of 800 nm*

transmissive optics when transporting sub-4fs pulses. The pulse elongation due to an amount of GDD Φ_2 is given by:

$$\Delta t'_{\mathrm{FWHM}} = \Delta t_{\mathrm{FWHM}} \sqrt{1 + \frac{16(\ln 2)^2 \Phi_2^2}{\Delta t_{\mathrm{FWHM}}^4}} \tag{1.18}$$

TOD. Third order dispersion Φ_3 [fs^3] will introduce some bounces in the temporal intensity profile. Because it is an odd order, it is not symmetric with respect to $t = 0$, and the bounces will appear on one side or the other of the pulse, depending on the sign. If third order can not be avoided, it is therefore better to introduce bounces on the tail of the pulse rather than the front, in order to keep a high contrast ratio on the front.

FOD. Fourth order dispersion Φ_4 [fs^4] is responsible for a symmetric pedestal and only changes the pulse duration for very significant amounts. In practice, we only consider up to the fourth order.

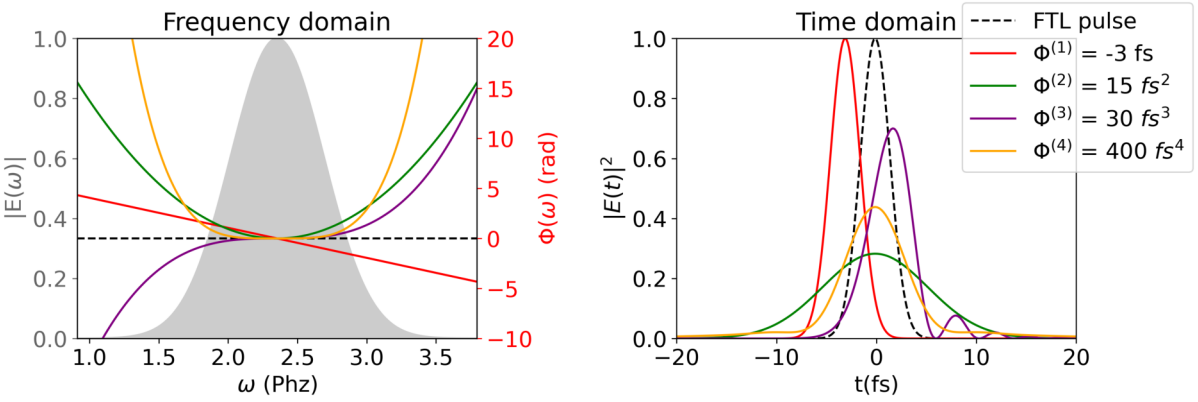

Figure 1.2: *Effect of adding arbitrarily chosen values of 1st, 2nd, 3rd and 4th order spectral phase on the temporal intensity profile of an initially Fourier transform limited 3.5fs pulse with a 800nm central wavelength.*

Interestingly, the pulse elongation due to one spectral phase order can be compensated for by another one. For instance, a pulse elongated due to 4th order phase can retrieve its initial FWHM duration by introducing some Φ_2 such that [51]:

$$\Phi_2 \approx 1.155 \frac{\Phi_4}{\Delta t_{\mathrm{FWHM}}^2}, \tag{1.19}$$

and similarly fifth and third order can compensate each other. However, the resulting high dynamic intensity profile will not be as clean as for a FTL pulse and the contrast ratio will be decreased. One must therefore be careful when optimizing spectral phase: for instance, making a plasma in air and optimizing compression by maximizing the brightness of white light and the volume of the kHz sound produced by the plasma spark is not precise enough. In order to avoid these inter-compensations, it is preferable to pre-calculate the theoretical values and optimize the compression while looking at the pulse intensity profile on a log scale with a high-dynamic range measuring device.

1.2.3 Propagation of a Gaussian pulse in a dispersive medium

We are now interested in the propagation of a Gaussian pulse in one dimension only, along the axis z. In particular, we consider propagation in dispersive media, for which the refractive index $n(\omega)$ depends on the frequency:

$$E(z,\omega) = E(0,\omega)e^{ik(\omega)z} = |E(0,\omega)|e^{i[\Phi(0,\omega)+k(\omega)z]} \tag{1.20}$$

where $k(\omega) = \omega n(\omega)/c$ is the wave number. The total spectral phase at z is now:

$$\Phi(z,\omega) = \Phi(0,\omega) + k(\omega)z \tag{1.21}$$

and the expression for the pulse in the time domain is:

$$E(z,t) = \frac{1}{\sqrt{2\pi}} \int_{-\infty}^{+\infty} E(0,\omega)e^{ik(\omega)z}e^{-i\omega t}d\omega. \tag{1.22}$$

We can also use a Taylor series expansion for the wave vector $k(\omega)$:

$$k(\omega) \approx k(\omega_0) + (\omega-\omega_0)\left[\frac{\partial k}{\partial \omega}\right]_{\omega_0} + \frac{1}{2}(\omega-\omega_0)^2\left[\frac{\partial^2 k}{\partial \omega^2}\right]_{\omega_0} + \frac{1}{6}(\omega-\omega_0)^3\left[\frac{\partial^3 k}{\partial \omega^3}\right]_{\omega_0} + ... \tag{1.23}$$

Far from resonances, the dispersion of a material can be approximated by Sellmeier's equation:

$$n(\omega) = \sqrt{1 + \sum_j \frac{A_j(10^6 2\pi c/\omega)^2}{(10^6 2\pi c/\omega)^2 - B_j}}, \tag{1.24}$$

where A_i and B_j are Sellmeier's coefficients, which are experimentally determined and tabulated. The n$^{\text{th}}$ order spectral phase accumulated upon propagation over a distance L reads:

$$\Phi_n = \left[\frac{\partial^n k}{\partial \omega^n}\right]_{\omega_0} \times L. \tag{1.25}$$

In particular, the term $\left[\frac{\partial^2 k}{\partial \omega^2}\right]_{\omega_0}$ is called the group velocity dispersion (GVD). A convenient way to determine the GDD, TOD and FOD introduced by common materials is to plot $k(\omega)$ $(=n(\omega)\omega/c)$ as a function of ω and make a polynomial fit. The derivatives are easily obtained and evaluated at any frequency. Examples are shown in Table 1.1.

1.2.4 CEP drifts upon propagation through dispersive media

Let us consider a Gaussian pulse propagating along the axis z. For simplicity, we assume that the initial spectral phase at $z = 0$ is constant and equal to zero: $\Phi(0,\omega) = \Phi_0 = 0$, and we only consider first order dispersion:

material	fused silica	SF57	TeO_2	sapphire	calcite
A_0	0.6961663	1.81651371	2.584	1.4313493	0.73358749
A_1	0.4079426	0.428893641	1.157	0.65054713	0.96464345
A_2	0.8974794	1.07186278	0	5.3414021	1.82831454
B_0	0.0684043^2	0.0143704198	0.1342^2	0.0726631^2	0
B_1	0.1162414^2	0.0592801172	0.2638^2	0.1193242^2	0.0194325203
B_2	9.896161^2	121.419942	0	18.028251^2	120
GDD	36	224	497	28	75
TOD	27	141	325	42	53
FOD	-11	51	188	-15	-10

Table 1.1: *Sellemeir's coefficients of materials commonly used in Salle Noire 2 and calculated GDD (fs^2), TOD (fs^3) and FOD (fs^4) at 800nm accumulated upong propagation over 1mm in different materials. The coefficients are taken from the website refractiveindex.info.*

$$E(z,\omega) = |E(0,\omega)|e^{ik_0 z + ik_1 \Delta\omega z}, \tag{1.26}$$

with $k_0 = k(\omega_0)$, $k_1 = \left[\frac{\partial k}{\partial \omega}\right]_{\omega_0}$ and $\Delta\omega = (\omega - \omega_0)$ (see section 1.2). We can compute the field $E(t)$ at a position z via a Fourier transform:

$$E(z,t) = e^{ik_0 z} e^{-i\omega_0 t} \mathcal{FT}\left[|E(0,\Delta\omega)|e^{ik_1 z\Delta\omega}\right] \tag{1.27}$$

$$= E_0|\Delta\omega_0| e^{-i(\omega_0 t - k_0 z)} e^{-\frac{(t-k_1 z)^2}{2\Delta t_0^2}} \tag{1.28}$$

We see that the maximum of the Gaussian envelope is now centered at $t = k_1 z$, therefore k_1 defines the group velocity $v_g = 1/k_1$. On the other hand, the carrier phase is now $\omega_0 t - k_0 z$, which defines the phase velocity $v_\phi = \omega_0/k_0$. The phase at the peak of the envelope, or carrier-envelope phase is thus

$$\Phi_{\text{CEP}}(z) = (\omega_0 k_1 - k_0)z = \omega_0 \left(\frac{1}{v_g} - \frac{1}{v_\phi}\right) z \tag{1.29}$$

We can define the characteristic length L_{CEP} for which the CEP has changed by 2π:

$$\Phi_{\text{CEP}}(L_{\text{CEP}}) = 2\pi \Leftrightarrow L_{\text{CEP}} = \frac{\lambda_0}{\frac{c}{v_g} - \frac{c}{v_\phi}} = \frac{\lambda_0}{n_g - n_\phi}. \tag{1.30}$$

According to Eq. 1.29, the CEP naturally drifts upon propagation whenever $v_\phi \neq v_g$. We have

$$\frac{1}{v_g} = \frac{\partial k(\omega)}{\partial \omega} = \frac{n(\omega)}{c} + \frac{\omega}{c}\frac{\partial n(\omega)}{\partial \omega} = \frac{1}{v_\phi} + \frac{\omega}{c}\frac{\partial n(\omega)}{\partial \omega}, \tag{1.31}$$

Therefore $v_\phi \neq v_g$ whenever $\partial n(\omega)/\partial\omega \neq 0$, which is the case for any material. We can re-write equation 1.31 in terms of wavelengths and refractive indices, which are easier to access:

$$n_g = n_\phi + \omega \frac{dn(\omega)}{d\omega} = n_\phi - \lambda \frac{dn}{d\lambda}. \tag{1.32}$$

The quantity n_ϕ is the refractive index at a given wavelength λ_0 and $dn/d\lambda$ is the chromatic dispersion at λ_0, both of which are easily found in the literature. The values in the case of fused silica and air are shown in Table 1.2.

material	fused silica	air
n_ϕ	1.453	1.000275
n_g	1.467	1.000280
$n_\phi - n_g$	0.014	5×10^{-6}
L_{CEP}	57 μm	16cm

Table 1.2: *CEP slippage length for fused silica and air. The values for n_g and n_ϕ are taken from the website refractiveindex.info whereas L_{CEP} is calculated from eq. 1.32.*

1.2.5 Laser parameters

Definitions

We define here important laser parameters. First, the peak amplitude of the electric field E_0 is expressed in TV/m. However, we more commonly talk in terms of peak intensity:

$$I_{\text{peak}} = \frac{1}{2} nc\epsilon_0 E_0^2. \tag{1.33}$$

The peak power is approximated as

$$P_{\text{peak}} = \frac{\pi \mathrm{w}_0^2 I_{\text{peak}}}{2}, \tag{1.34}$$

and the pulse energy is

$$E = \frac{P_{\text{peak}}\tau}{2\sqrt{\frac{\ln 2}{\pi}}} \approx P_{\text{peak}}\tau, \tag{1.35}$$

with τ the pulse duration at FWHM of the intensity profile.

Salle Noire 2.0 laser parameters

The final parameters of the *Salle Noire 2* laser are:

· repetition rate $f_{\text{rep}} = 1$ kHz

· pulse duration $\Delta t_{\text{FWHM}} = 28$ to 3.5 fs (tunable)

· central wavelength $\lambda_0 = 800$ to 720 nm (depending on the gas pressure in the hollow-core fiber used for post-compression)

· pulse energy E $\approx$ 2.5 mJ on target and 3.5 mJ compressed

· peak power P_{peak}: up to 1 TW (in the case of 3.5fs, 3.5mJ pulses)

· average power $P_{\text{av}} \approx 3.5$ Watt for the compressed pulses

1.3 Wave propagation

1.3.1 Spatial propagation

Considering only the spatial properties of the electromagnetic wave, one can solve Maxwell's equations (in vacuum) for a continuous, monochromatic Gaussian beam in 2 dimensions (see eq. 11.40 in [204]):

$$E(r,z) = E_0 \frac{\mathrm{w}_0}{\mathrm{w}(z)} \exp\left(-\frac{r^2}{\mathrm{w}(z)^2}\right) \exp\left(-i\left[kz - \tan^{-1}\left(\frac{z}{z_R}\right) + \frac{kr^2}{2R(z)}\right]\right) \tag{1.36}$$

where $\mathrm{w}(z)$ is the beam waist at a distance z from the focus:

$$\mathrm{w}(z) = \mathrm{w}_0\sqrt{1 + \left(\frac{z}{z_R}\right)^2}, \tag{1.37}$$

with z_R the Rayleigh length. It corresponds to the distance from the focus for which the beam intensity is divided by two:

$$\boxed{z_R = \frac{\pi \mathrm{w_0}^2}{\lambda}}, \tag{1.38}$$

and $\mathrm{w_0}$ is the beam waist in focus (see fig. 1.3). When focusing a collimated laser beam of waist $\mathrm{w_i}$ with an optic having a focusing length f, the minimum size that it can reach is given by:

$$\mathrm{w_0} = \frac{\lambda f}{\pi \mathrm{w_i}}. \tag{1.39}$$

And far from the focus, the beam divergence is given by:

$$\theta = \tan^{-1}\left(\frac{\lambda}{\pi \mathrm{w_0}}\right). \tag{1.40}$$

However, this is only true for perfectly aligned, ideal optical systems, called "diffraction-limited". In practice, aberrations tend to make it bigger.

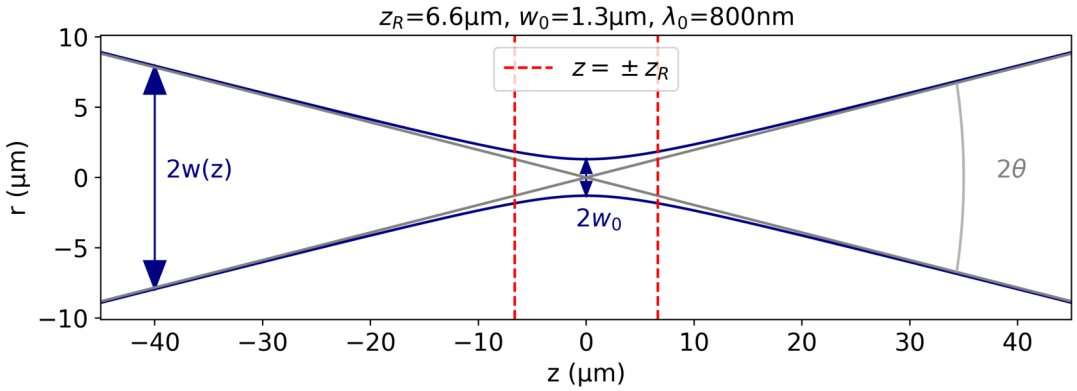

Figure 1.3: *Evolution of the beam waist* $\mathrm{w}(z)$ *around focus (z=0) for a Gaussian beam with* $\mathrm{w_0} = 1.3\mu\mathrm{m}$ *and a central wavelength* λ *=800nm, propagating along the axis z.*

1.3.2 Aberrations and spatio-spectral couplings

Geometric aberrations

Geometric aberrations are deviations from a plane wavefront for a monochromatic plane wave. These non-plane wavefronts can be expanded on the basis of Zernike polynomials. Each polynomial order corresponds to a particular geometrical aberration, similarly to spectral phase in the time domain. First order corresponds to tip and tilt, second order to defocus and astigmatism, third order to coma, fourth order to spherical aberrations... The most often seen aberration is astigmatism, and corresponds to misaligned (tilted) lenses, for example. A vertical tilt will induce 45° astigmatism whereas horizontal tilt will induce 0° and 90° elongations of the beam respectively before and after focus.

Spatio-spectral couplings

Whenever there are spatio-spectral couplings, the electric field can no longer be written as the product of a spatial and a temporal function [5]. Instead, we write:

$$E(x,y,\omega) = A(x,y,\omega)\exp(i\phi(x,y,\omega)) = \exp\left[\ln(A(x,y,\omega)) + i\phi(x,y,\omega)\right]. \tag{1.41}$$

Spatial chirp is probably the most well known coupling. For example, transverse spatial chirp corresponds to the situation where the different wavelengths co-propagate but are centered at different transverse positions in the beam, with a linear dependance of the position with respect to the wavelength.

If a spatially chirped pulse propagates through a dispersive medium, temporal chirp will be added, resulting in "pulse front tilt". Another case of pulse front tilt is angular dispersion, which corresponds to a wavelength dependent propagation direction. It may originate from tilted gratings or prisms, for example. When focusing a laser pulse exhibiting pulse front tilt, it will introduce wavefront rotation in focus (see fig. 1.4), an effect used for the attosecond lighthouse [268].

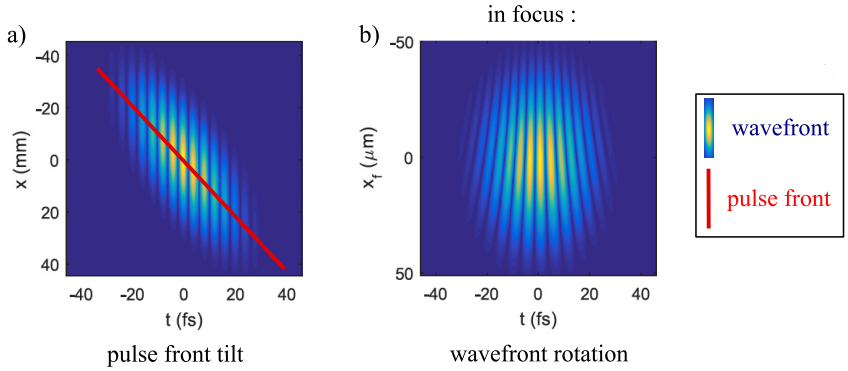

Figure 1.4: *a) Pulse exhibiting pulse front tilt b) The pulse exhibits WFR after being focused by a 250mm focal length convex lens. Adapted from [200].*

Another common coupling is pulse front curvature, which corresponds to the situation where the pulse arrival time depends quadratically on the beam radius. It can originate from the propagation of a broadband beam through a singlet chromatic lens, for instance.

1.3.3 Gouy phase

The term $\tan^{-1}(z/z_R)$ in eq. 1.36 is known as the Gouy phase and translates into a CEP shift around the focus. This is true for a continuous, monochromatic, Gaussian beam. However, for laser pulses, one needs to take the wavelength-dependent geometry of the beam into account, and the spatial phase dependence is found to be [123]:

$$\Delta\phi_{\text{Gouy}}(z,r) = -\tan^{-1}\left(\frac{z}{z_R}\right) + \frac{g_0\left[1-2\left(\frac{r}{\text{w}(z)}\right)^2\right]}{\frac{z}{z_R}+\frac{z_R}{z}}, \tag{1.42}$$

where

$$g_0 = \frac{dz_r(\omega)}{d\omega}\Big|_{\omega_0} \times \frac{\omega_0}{z_R(\omega_0)} \tag{1.43}$$

is a dimensionless geometry factor of the input beam, called the Porras factor. The evolution of the Gouy phase around the focus for a beam radius $\text{w}_0 = 1.3\mu\text{m}$ at $1/\text{e}^2$ is represented in fig. 1.5 for different values of the Porras factor. The case $g_0 = 0$ corresponds to a Gouy phase $\tan^{-1}(z/z_R)$. This spatial dependence was verified experimentally by a team in Jena [123].

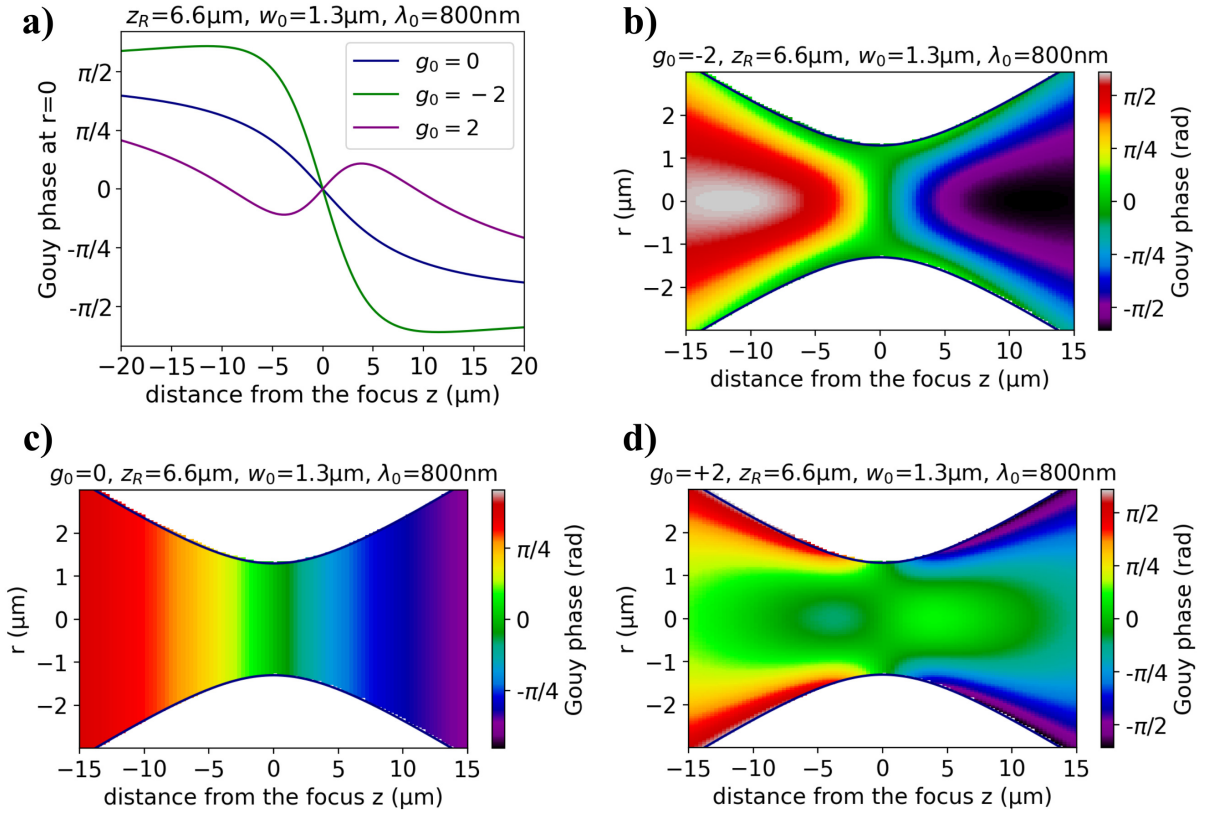

Figure 1.5: *Evolution of the Gouy phase around focus (z=0) for a gaussian beam with w_0 = 1.3µm, λ =800nm and z_R=6.6µm. a) Gouy phase along the optical axis (r=0) for different Porras factors g_0. 2D color plot of the Gouy phase for a Porras factor of b) -2, c) 0 and d)+2.*

1.3.4 Propagation and coupling of laser pulses inside hollow-core fibers

We use hollow-core fibers in our laser chain, for both spatial cleaning of the beam (in the XPW filter) and spectral broadening of the pulses (in the post-compression stage), therefore let us see how light couples into and propagates inside a hollow-core fiber.

Let us consider a linearly polarized input laser beam with radial symmetry propagating inside a thick, glass hollow-waveguide whose inner radius a is very large compared to the laser wavelength. The input beam mostly excites the EH_{1m} hybrid modes [194] (the first three modes are shown in fig. 1.6.b) and the radial intensity profile inside the hollow core is thus given by

$$I_{1m}(r) = I_0 J_0^2\left(\frac{u_{1m} r}{a}\right), \tag{1.44}$$

where J_0 is the zero order Bessel function of the first kind and u_{1m} its m^{th} root. For a linearly polarized laser, the overlap between a Gaussian input beam $E_g(r) = \sqrt{2/\pi \mathrm{w}_0^2}\exp(-r^2/\mathrm{w}_0^2)$ and the EH_{1m} mode is given by [2]:

$$\left|\int_0^a E_g E_{1m} 2\pi r dr\right|^2 = \frac{4\left[\int_0^a r J_0\left(\frac{u_{1m} r}{a}\right) e^{-r^2/\mathrm{w}_0^2} dr\right]^2}{\mathrm{w}_0^2 \int_0^a r J_0^2\left(\frac{u_{1m} r}{a}\right) dr}. \tag{1.45}$$

When $\mathrm{w}_0 = 0.64a$, the overlap (eq. 1.45) for $m = 1$ is maximized, i.e. a Gaussian input beam most efficiently couples into the fundamental EH_{11} waveguide mode, as shown in fig. 1.6.a [194].

The transmitted power at a distance L from the fiber entrance is $P(L) = P_0 \exp(-2\alpha_{1m} L)$

with the absorption coefficient

$$\alpha_{1m} = \left(\frac{u_{1m}}{2\pi}\right)^2 \frac{\lambda^2}{a^3} \frac{\nu^2+1}{2\sqrt{\nu^2-1}}, \tag{1.46}$$

where ν is the refractive index of the fiber cladding material ($\nu \approx 1.4533$ for fused silica at 800nm) [171].

The results are shown in fig 1.6.c and d, for an inner diameter ID=250μm, corresponding to our XPW fiber, and ID=536μm, corresponding our post-compression fiber (see further).

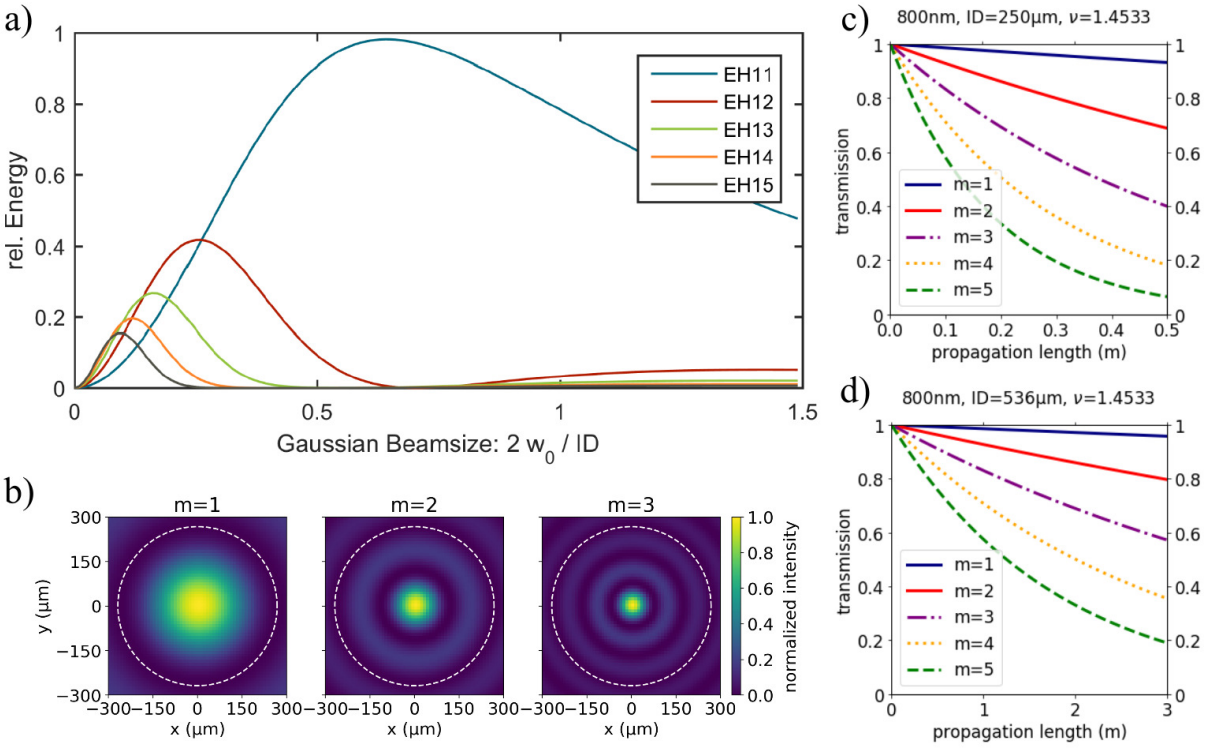

Figure 1.6: *a) Coupling coefficients between the hybrid modes EH_{1m} for a HCF and a Gaussian beam with the mode size of w_0, see Eq. 1.45. b) normalized intensity profiles of the EH_{1m} modes with m=1,2,3 for ID=536μm (the diameter is indicated by the white dashed circle) c) HCF transmission of the EH_{1m} modes depending on the fiber length, shown here for the case of a 536 μm inner diameter and d) for $ID = 250\mu$m. Subfigure (a) is reprinted from [25] and subfigures (b,c,d) were made with Python.*

1.4 Nonlinear effects

The terminology *nonlinear optics* was first introduced in 1942 [230]. It encompasses phenomena occurring when the response of a material system to an applied optical field nonlinearly depends on the strength of the applied field. Typically, only laser light is sufficiently intense to modify a system's optical properties in this manner.

1.4.1 Overview

Second order nonlinear terms are described by the polarization vector:

$$\vec{P}^{(2)}(\omega_3 = \omega_1 + \omega_2) = \epsilon_0 \chi^{(2)}(\omega_3; \omega_1, \omega_2)\vec{E}(\omega_1)\vec{E}(\omega_2),$$

where the frequency components can be either positive or negative. We can list some well known effects:

- $\omega_1 = \omega_2$: Second Harmonic Generation (SHG)
- $\omega_1 \neq \omega_2$ and $\omega_3 = \omega_1 + \omega_2$: Sum Frequency Generation (SFG) or $\omega_3 = \omega_1 - \omega_2$: Difference Frequency Generation (DFG)

Now let us inspect third order nonlinearities *ie* interactions between four waves (four-wave mixing):

$$\vec{P}^{(3)}(\omega_4 = \omega_1 + \omega_2 + \omega_3) = \epsilon_0 \chi^{(3)}(\omega_4; \omega_1, \omega_2, \omega_3) \vec{E}(\omega_1) \vec{E}(\omega_2) \vec{E}(\omega_3)$$

Many wave mixing processes are possible, among which:

- the optical Kerr effect: $\vec{P}^{(3)}(\omega) = \epsilon_0 \chi^{(3)}(\omega, -\omega, \omega) |E(\omega)|^2 E(\omega) \vec{e}\vec{e}\vec{e}$
- crossed-polarized wave generation (XPW): $\omega_\perp = \omega_\parallel + \omega_\parallel - \omega_\parallel$

1.4.2 Kerr effect

I will detail here the case of the optical Kerr effect as an example. Let us consider the propagation of a monochromatic wave at ω in a $\chi^{(3)}$ nonlinear material. The nonlinear polarization vector reads:

$$\vec{P}^{(3)}(\omega) = \epsilon_0 \chi^{(3)}(\omega, -\omega, \omega) |E(\omega)|^2 E(\omega) \vec{e}\vec{e}\vec{e},$$

and the total polarization vector is:

$$\begin{aligned} \vec{P}(\omega) &= \epsilon_0 \left(\chi^{(1)}(\omega) \vec{e} + \chi^{(3)}(\omega, -\omega, \omega) \vec{e}\vec{e}\vec{e} |E(\omega)|^2 \right) E(\omega) \\ &= \epsilon_0 \left(\chi^{(1)}_{\text{eff}} + \chi^{(3)}_{\text{eff}} |A(\omega)|^2 \right) A(\omega) e^{ikz} \end{aligned}$$

The real part of the third order effective susceptibility $\chi^{(3)'}_{eff}$ will induce a modification of the refractive index:

$$n^2(\omega) = 1 + \chi^{(1)}_{\text{eff}} + \chi^{(3)'}_{\text{eff}} |A(\omega)|^2 = n_0^2(\omega) + \chi^{(3)'}_{\text{eff}} |A(\omega)|^2 \tag{1.47}$$

$$\Leftrightarrow n(\omega) = n_0(\omega) \sqrt{1 + \frac{2\chi^{(3)'}_{\text{eff}}}{n_0^3 \epsilon_0 c} I(\omega)}.$$

This can be further simplified because $2\chi^{(3)'}_{\text{eff}} / (n_0^3 \epsilon_0 c) I(\omega) \ll 1$:

$$\boxed{n(\omega) \approx n_0(\omega) + n_2 I(\omega)}$$

with the nonlinear refractive index $n_2 = \chi^{(3)'}_{\text{eff}} / (n_0^2 \epsilon_0 c)$. A wave can thus modify the refractive index of a medium proportionnally to its intensity.

If we now consider a temporal or a spatial wave packet, the intensity varies in time or in space and the nonlinear refractive index leads to, respectively: an instantaneous phase shift called Self Phase Modulation (SPM) which is further detailed in the following subsection (see eq. 1.51), or to self-focusing of the beam (also called Kerr-lensing). This last effect is often used to mode-lock oscillators: for high intensities (when the modes of the cavity are in phase), the nonlinear refractive index $n(r) = n_0 + I(r) n_2$ in the crystal becomes intensity-dependent and varies radially, thus creating a focusing lens. The pulses are self-focused and can be spatially selected with a hard aperture while the continuous wave is mostly eliminated (Fig. 1.7).

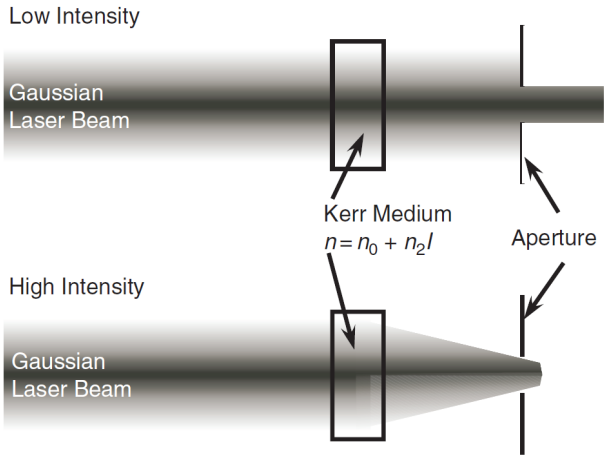

Figure 1.7: *Illustration of the Kerr lens mode-locking principle. Due to the Kerr effect, the Ti:Sa crystal refractive index becomes intensity-dependent and acts as a focusing lens for the pulses (because they have a higher intensity), which are then spatially selected with an aperture, whereas the continuous waves (because they have a low intensity) are not focused and experience losses. Reprinted from [62].*

1.4.3 Spectral broadening via Self Phase Modulation

In our laser chain, we also take advantage of the Kerr effect to broaden the spectrum of the pulses, which allows to shorten their duration. In order to simulate spectral broadening of a laser pulse in a hollow-core fiber differentially filled with gas (the pressure gradient is modeled according to eq. 3.8), the 1D nonlinear Schrödinger wave equation 1.7 can be re-written in the slowly-evolving-wave approximation [34, 33, 4], where we do not consider the transverse evolution of the pulse:

$$\frac{\partial}{\partial z}A(z,\tau) = -\frac{\alpha_0}{2}A + i\widehat{D}A + i\frac{2\pi\omega_0}{n_0 c}\left(1 + \frac{i}{\omega_0}\frac{\partial}{\partial \tau}\right)B_{nl}(z,\tau,A),$$

where $\tau = t - \beta_1 z$ is the retarded time, moving along with the pulse envelope. Using $B_{nl}(z,\tau,A) = n_0 n_2 |A|^2 A/(2\pi)$ in the case of Kerr nonlinearities, this becomes:

$$\boxed{\frac{\partial}{\partial z}A(z,\tau) = \left[-\frac{\alpha_0}{2} + i\widehat{D} + i\frac{\omega_0}{c}n_2\left(1 + \frac{i}{\omega_0}\frac{\partial}{\partial \tau}\right)|A(z,\tau)|^2\right]A(z,\tau)} \tag{1.48}$$

Let us now examine this equation term by term.

The first term

$$\frac{\partial}{\partial z}A(z,\tau) = -\frac{\alpha_0}{2}A \tag{1.49}$$

has a very simple solution: $A(z,\tau) = A(0,\tau)\exp[-\alpha_0 z/2]$ and accounts for the attenuation of the beam.

The second term

$$\frac{\partial}{\partial z}A(z,\tau) = i\widehat{D}A, \tag{1.50}$$

with

$$\widehat{D} = -\frac{1}{2}k_2\frac{\partial^2}{\partial \tau^2} - \frac{i}{6}k_3\frac{\partial^3}{\partial \tau^3} + ...$$

is a linear term which accounts for dispersion (GVD, TOD...). It can be solved in the frequency domain, where it simply consists of adding the spectral phase terms corresponding to the accu-

mulated linear dispersion (see section 1.2).

And finally, the last term accounts for the nonlinearities and can be decomposed into a self-phase modulation (SPM) term

$$\frac{\partial}{\partial z}A(z,\tau) = i\frac{\omega_0}{c}n_2|A(z,\tau)|^2A(z,\tau) \tag{1.51}$$

and a self-steepening (SS) term

$$\frac{\partial}{\partial z}A(z,\tau) = -\frac{n_2}{c}\frac{\partial}{\partial \tau}|A(z,\tau)|^2A(z,\tau). \tag{1.52}$$

For pure SPM, $|A(z,\tau)|^2 = |A(0,\tau)|^2$ and equation 1.51 has the following solution:

$$A(z,\tau) = A(0,\tau)e^{i\frac{\omega_0}{c}n_2|A(0,\tau)|^2z}, \tag{1.53}$$

where the nonlinear phase term $\phi_{nl}(\tau) = \omega_0 n_2 I(\tau)z/c$ is equivalent to a nonlinear refractive index n_2 such that the total refractive index reads:

$$\boxed{n = n_0 + n_2 I(\tau)}. \tag{1.54}$$

Thus, there is an instantaneous frequency shift:

$$\delta\omega = -\frac{d\phi_{nl}}{d\tau} = -\frac{\omega_0}{c}n_2\frac{dI(\tau)}{d\tau}z,$$

which corresponds to the time-dependent generation of new frequency components *ie* spectral broadening and temporal chirp.

The maximum accumulated nonlinear phase shift over a distance L is given by the B integral:

$$B = \frac{\omega_0}{c}\int_0^L n_2(z)I_{max}(z)dz,$$

where $I_{max}(z)$ is the maximum value of $I(\tau)$ at z.

In the case of pure SPM, the broadening ratio for a Gaussian FTL input pulse is [207]:

$$F = \frac{\Delta\omega_0}{(\Delta\omega)_0} = \sqrt{1 + \frac{4}{3\sqrt{3}}B^2}, \tag{1.55}$$

where $(\Delta\omega)$ is the rms spectral bandwidth:

$$(\Delta\omega) = \sqrt{\langle\omega^2\rangle - \langle\omega\rangle^2}. \tag{1.56}$$

On the other hand, equation 1.52 can be solved iteratively:

$$A(z+\Delta z,\tau) = A(z,\tau)\exp\left[i\frac{n_2}{cA}\frac{id}{d\tau}(|A(z,\tau)|^2A(z,\tau))\Delta z\right] \tag{1.57}$$

Overall, equation 1.48 can be numerically solved with a split step Fourier method [63]. I implemented such a numerical calculation in Python, using numerical recipes from a Matlab script by Stefan Haessler. An example of a simulation of the combined effect of SPM and SS is shown in figure 1.8. Pure SPM would give a perfectly symmetric broadening (with red components on the leading edge and blue components on the trailing edge). However, self-steepening of the trailing edge (physically understood as resulting from the higher group-index for the higher intensity pulse peak) leads to more SPM-broadening on the trailing edge, *ie* to the blue, and less on the leading edge.

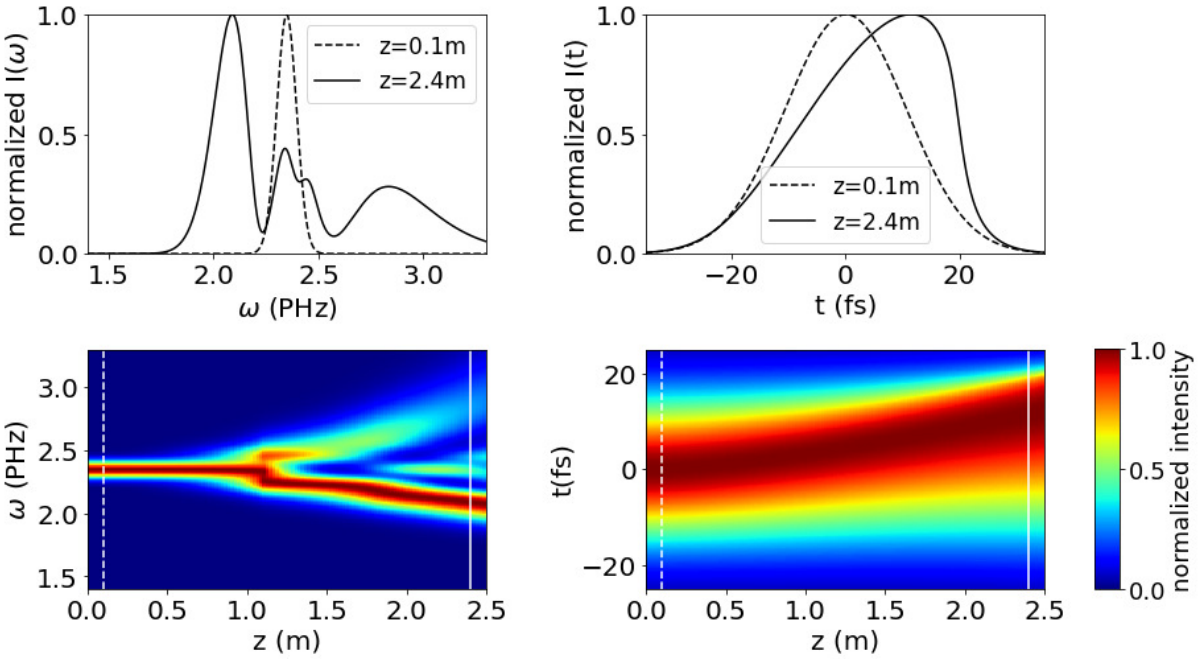

Figure 1.8: *1D simulation of the spectral and temporal evolution of a Gaussian 25 fs, 9 mJ pulse through a 2.5m long HCF with a 536µm inner diameter. The maximum helium pressure at the output was 1.3 bar. Only the effect of SPM and SS was considered, dispersion was neglected. The intensity profiles are normalized to unity at each position z along the fiber.*

1.4.4 XPW effect

Finally, there is one more key non-linear effect used in our laser system: crossed-polarized wave (XPW) generation. It is a third order nonlinear effect, thus the polarization vector reads $\vec{P}^{(3)}(t) = \epsilon_0 \chi^{(3)} \vec{E}^3(t)$. As the pulses propagate through a nonlinear crystal, a wave whose polarization is orthogonal to that of the incident wave (an "XPW wave") is generated and can be selected using a polarizer beam splitter (fig. 1.9).

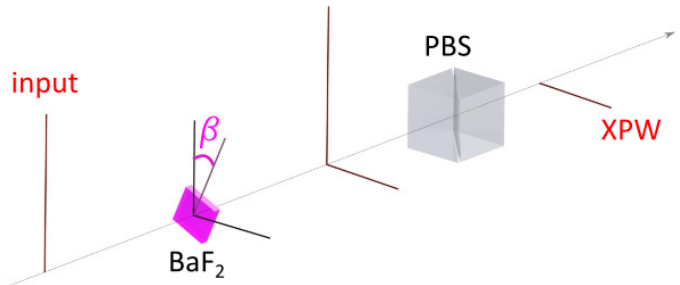

Figure 1.9: *Principle of the XPW generation in our laser chain.*

We use BaF_2 to generate the XPW wave, which is a centro-symmetric cubic crystal. Due to the centrosymmetry, the $\chi^{(3)}$ tensor (with 81 components) only has 21 non-vanishing components, which contain only 4 variables: $\chi^{(3)}_{xxxx}$, $\chi^{(3)}_{xxyy}$, $\chi^{(3)}_{xyxy}$ and $\chi^{(3)}_{xyyx}$ (see [133]). For an isotropic medium, we also have

$$\chi^{(3)}_{xxxx} = \chi^{(3)}_{xxyy} + \chi^{(3)}_{xyxy} + \chi^{(3)}_{xyyx} \tag{1.58}$$

but this relation is not fully satisfied in the case of a cubic lattice, such as that of BaF_2.

Therefore, we introduce the anisotropy coefficient to account for this difference:

$$\sigma = \frac{\chi^{(3)}_{xxxx} - \chi^{(3)}_{xxyy} - \chi^{(3)}_{xyxy} - \chi^{(3)}_{xyyx}}{\chi^{(3)}_{xxxx}} = \frac{\chi^{(3)}_{xxxx} - \chi^{(3)}_{xxyy} - 2\chi^{(3)}_{xyyx}}{\chi^{(3)}_{xxxx}}. \tag{1.59}$$

When the incident wave polarization is aligned with the crystal axis ($\beta = 0$), there is no generation of a crossed-polarized wave. For arbitrary crystal orientations, however, one can derive the following set of coupled nonlinear differential equations [44] for the amplitudes of the mutually orthogonally polarized waves A(z) and B(z):

$$\frac{dA(z)}{dz} = i(\gamma_1 A|A|^2 + \gamma_2 AAB^* + 2\gamma_2 B|A|^2 + 2\gamma_3 A|B|^2 + \gamma_3 BBA^* + \gamma_4 B|B|^2) \tag{1.60}$$

$$\frac{dB(z)}{dz} = i(\gamma_5 B|B|^2 + \gamma_4 BBA^* + 2\gamma_4 A|B|^2 + 2\gamma_3 B|A|^2 + \gamma_3 AAB^* + \gamma_2 A|A|^2) \tag{1.61}$$

where the γ_i coefficients depend on the orientation of the crystal and $\chi^{(3)}$. We see that the XPW conversion process from A to B and B to A is governed by γ_2 and γ_4. For low intensities, *ie* considering B=0, the efficiency is proportional to γ_2^2. The maximum conversion efficiency is obtained for holographic crystallographic orientation [011] (see [45]), and in that case γ_2 depends on β as follows:

$$\gamma_2 = -\frac{\sigma}{8}\sin(2\beta)[3\cos(2\beta) - 1] \times \frac{6}{8}\frac{\pi}{n_0\lambda}\chi^{(3)}_{xxxx}. \tag{1.62}$$

The XPW efficiency as a function of the crystal angle β is shown in figure 1.10. Subfigure (a) was obtained by solving the coupled differential equations with a numerical split-step Fourier method, whereas subfigure (b) simply corresponds to the parameter γ_2^2 (eq. 1.62). We see that as we vary β, *ie* as we rotate the crystal in the plane orthogonal to the incident beam, by 180°, we go through two strong maxima and two weaker maxima.

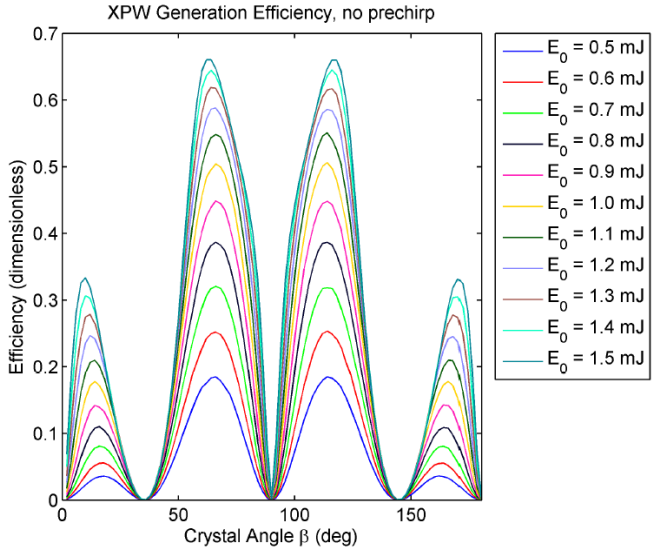

(a) XPW efficiency obtained by solving the coupled differential equations 1.60 and 1.61. Reprinted from [24].

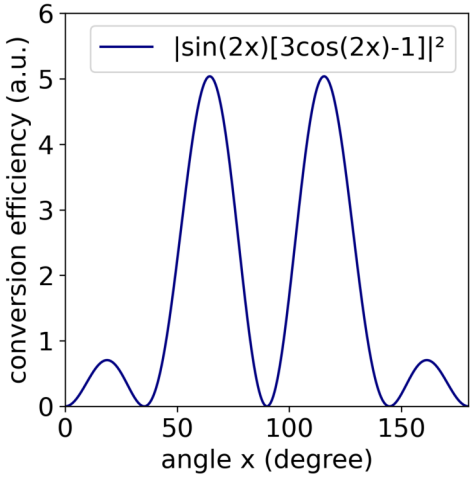

(b) XPW efficiency predicted by the γ_2 factor (Eq. 1.62).

Figure 1.10: *XPW generation efficiency as a function of the crystal orientation angle*

1.5 Light amplification in Ti:Sa crystals

LASER is the acronym for Light Amplification by Stimulated Emission Radiation. It is based on the discovery by Albert Einstein that a photon of the same energy as a radiative transition can stimulate the emission of another similar photon (same energy, direction, phase...) by de-excitation from the upper energy level to the the lower one of the considered transition. This copy mechanism is used to amplify light coherently.

1.5.1 Titanium-doped sapphire

A titanium-doped sapphire crystal, or Ti:Sa crystal for short, is a sapphire matrix in which some Ti^{3+} cations are inserted. These cations can be modeled as a 4 energy level system (fig. 1.11.a.), and transition from level 2 to level 1 corresponds to an energy loss, either in the form of a photon, or through non-radiative de-excitations (vibrations, heat dissipation...). The photon emission can be spontaneous or stimulated by another incident photon, whose energy $\hbar\omega$ corresponds to the energy gap between these two levels.

In order for the lasing transition to occur, the 4-level system must be first excited from its stable ground level to the third level, which is done by absorbing a more energetic photon. These more energetic photons ($\lambda_p \approx 450$ to 570 nm) come from a pump laser, generally a frequency-doubled Nd:YAG, Nd:YLF or Nd:YVO laser. The fast (~ 3.5 ps), non-radiative transition from the 3rd to the 2nd level then quickly populates the 2nd level, whose lifetime is much longer, typically ~ 3.2 μs. This gives plenty of time to stimulate the radiative decay. The first level also has a very short lifetime, and we can consider that only the ground level and the 2nd one are populated at all times.

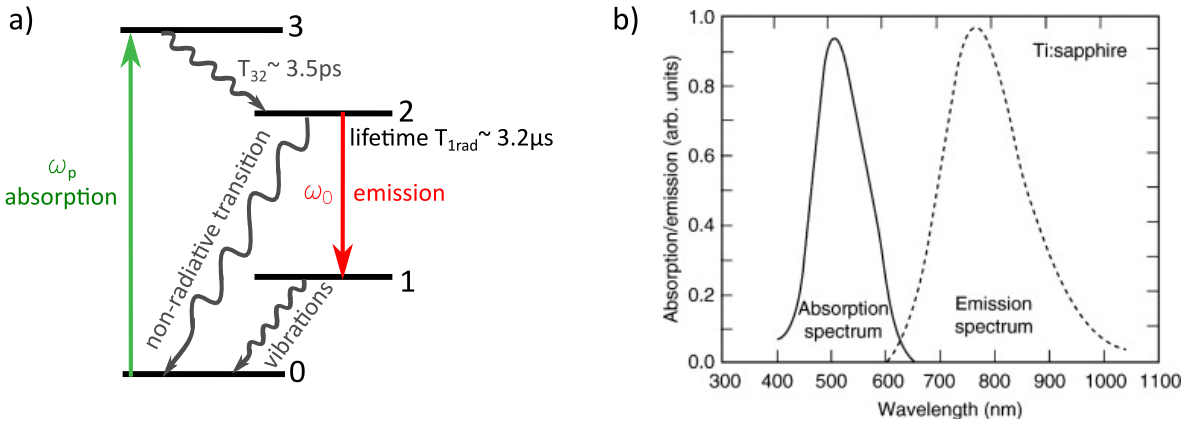

Figure 1.11: *a) Representation of the 4 energy levels of Ti3+ ions in titanium-doped sapphire crystals. b) Absorption and emission spectra of the* Ti^{3+} *ion in sapphire. Reprinted from [273].*

Ti:Sa is one of the preferred gain media because of its broad emission bandwidth (fig. 1.11.b.) capable of supporting 8fs pulses, high thermal conductivity, high saturation fluence ($J_{sat} \approx 0.8 - 1\text{J.cm}^{-2}$) and high damage threshold.

1.5.2 Influence of the temperature

Quantum efficiency

The rate of radiative transitions from level 2 to the ground level is given by the quantum

efficiency, which is temperature-dependent:

$$\eta_c(T) = \frac{T_1(T)}{T_{1rad}} = \left(\frac{1}{T_{1rad}} + \frac{1}{T_{nr}} \exp\left[-\frac{\Delta E}{k_B T}\right]\right)^{-1} \frac{1}{T_{1rad}} \tag{1.63}$$

with $\Delta E = 1794\text{cm}^{-1}$, $T_{nr} = 2.93$ ns the non-radiative lifetime, $T_{1rad} = 3.87\mu$s the lifetime for a purely radiative transition (*ie* at very low temperature) and $T_1(T)$ the lifetime on level 2. At 300 K, $\eta_c = 0.81$, whereas at 77 K, $\eta_c \approx 1$. This is one of the reasons why we maintain the Ti:Sa crystals at low temperature (T≈177 Kelvin) in our laser chain.

Thermal conductivity

The thermal conductivity K_1 varies a lot with the temperature: at T=77 K, $K_1 = 1000\text{W.m}^{-1}\text{.K}^{-1}$ whereas at T=300 K, $K_1 = 42\text{W.m}^{-1}\text{.K}^{-1}$ [264].

Index gradient

The refractive index gradient $\left[\frac{dn}{dT}\right]_{T=T_0}$ also more strongly depends on the temperature T at higher average temperatures T_0: for example, at 77 Kelvin $\partial n/\partial T = 0.34 \times 10^{-6}\text{K}^{-1}$, whereas at 300K, $\partial n/\partial T = 5.05 \times 10^{-6}\text{K}^{-1}$.

Absorption coefficient

The absorption coefficient of the Ti:Sa crystal $\alpha[\text{m}^{-1}]$ is also temperature-dependent and the pump is more efficiently absorbed at lower temperatures. For instance, $\alpha = 2.3\text{cm}^{-1}$ at 78K and $\alpha = 1.9\text{cm}^{-1}$ at 320K [85]. Thanks to the much higher quantum efficiency, this increase in absorption at low temperature is not entirely lost in heat but mostly converted into photons at λ =800nm.

Thermal lens

The refractive index gradient in the Ti:Sa crystal acts as a thermal lens, whose equivalent focal length is [208]

$$f_{th} = \frac{2\pi r_1^2 K_1}{P_{th}\left[\frac{dn}{dT}\right]_{T=T_0}}, \tag{1.64}$$

with r_1 the pump radius on the crystal at $1/\text{e}^2$ and P_{th} the pump power lost in heat, the latter being expressed as

$$P_{\text{th}} = (1 - \text{e}^{-\alpha L}) E_p (1 - \eta_c \eta_q) f_{\text{rep}}, \tag{1.65}$$

where $\eta_q = \lambda_{\text{pump}}/\lambda_{\text{laser}}$ is the quantum defect, E_p is the incident pump energy and f_{rep} is the repetition rate of the laser.

For example, if we calculate the thermal lens for r_1 =680μm, L=6mm, E_p=37mJ, f_{rep}=1kHz, λ_{pump}=532nm and λ_{laser}=790nm, we find a value $f \approx 945$m at 77K (negligible), whereas at 300K we find a much smaller value of ≈ 2.9m, which makes the design of the amplifier more complex.

1.5.3 Chirped Pulse amplification

Chirped Pulse Amplification (CPA) [237] is a technique invented in 1983 by G. Mourou and D. Strickland that was awarded half of the 2018 Physics Nobel Prize. It is based on the very simple idea that in order to amplify a pulse to very high energies, above the damage threshold of the optics used in the amplifiers (mirrors, lenses, crystals..), one could temporally stretch the pulses prior to amplification, and recompress them afterwards (fig. 1.12). This invention revolutionized laser technology and is responsible for numerous groundbreaking applications.

I will detail in the following the principles behind some key components in our laser chain which are used for temporal stretching or compression of the laser pulses.

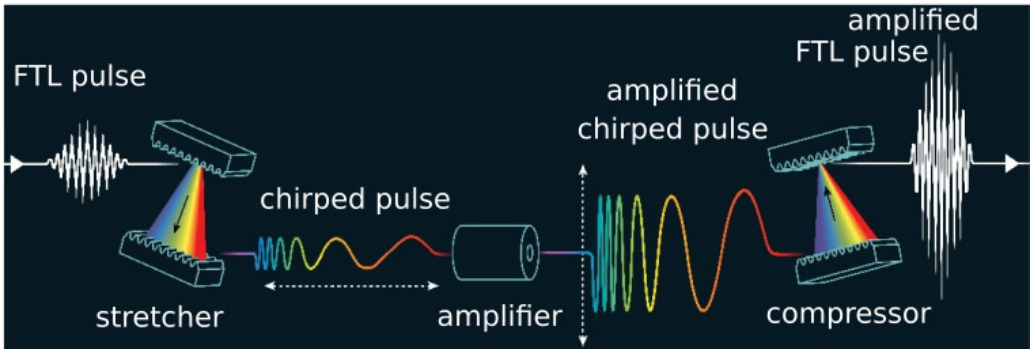

Figure 1.12: *Illustration of the CPA technique. Adapted from © Prix Nobel de Physique 2018 – Royal Swedish Academy of Sciences*

1.5.4 Dispersion introduced by a gratings compressor

The two compressors in our laser chain make use of diffraction gratings in transmission mode. The 2nd, 3rd and 4th order dispersion introduced by two pairs of transmission gratings can be calculated through basic geometric optics, knowing the gratings' parameters and the angle of incidence. We consider parameters corresponding to our final gratings compressor in the following. The pitch of the grating is $d = 1/1.282\mu$m, we take the refractive index of air equal to 1 ($n_1 = n_2 = 1$), and the distance between the two gratings is noted L. We only consider the $m = -1$ diffraction order. The angle of incidence on the first grating is the Littrow angle [115], for which the incident beam diffracts back on itself and the diffraction efficiency is maximum, defined by

$$\theta_{Littrow} = \sin^{-1}\left(\frac{\lambda_0}{2d}\right),$$

ie $\theta_i \approx 30.8°$ for $\lambda_0 = 800$nm. The frequency-dependent diffraction angle $\theta_d(\omega)$ is given by:

$$\theta_d(\omega) = \sin^{-1}\left[\frac{1}{n_2}\left(n_1 \sin\theta_i + \frac{m}{d}\frac{2\pi c}{\omega}\right)\right],$$

which leads to the frequency-dependent optical path length OPL(ω) for two pairs of gratings:

$$\mathrm{OPL}(\omega) = \frac{2\mathrm{L}}{\cos[\theta_d(\omega)]}\left(1 + \sin\theta_i \sin\theta_d(\omega)\right).$$

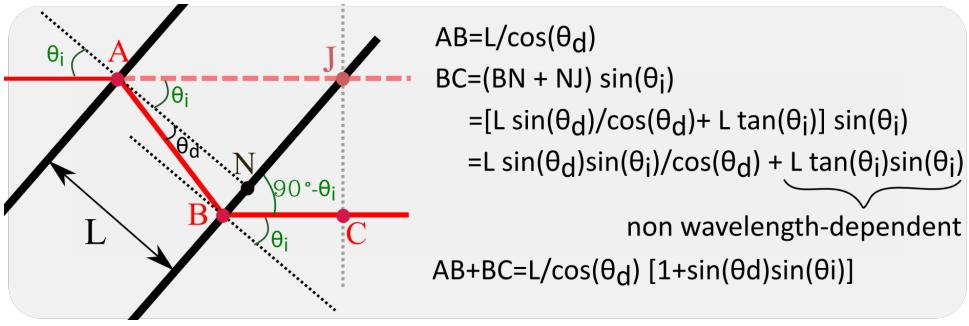

Figure 1.13: *Geometric considerations for calculation of the wavelength dependent optical path length (OPL) from A to C (in red). The solid black lines correspond to the transmission gratings, whereas the black dashed lines are orthogonal to the gratings.*

Finally, the accumulated spectral phase reads:

$$\phi(\omega) = \frac{\omega}{c}\mathrm{OPL}(\omega) - 2R(\omega),$$

where $R(\omega)$ is a correction term to account for the relative phase shift accumulated on the gratings, and can be expressed as 2π times the number of grooves between B and N (see fig. 1.13 for the notations), as explained by Treacy [254]. Therefore,

$$\phi(\omega) = \frac{\omega}{c}\mathrm{OPL}(\omega) - 2 \times 2\pi \frac{\mathrm{L}\,\tan[\theta_d(\omega)]}{d} \tag{1.66}$$

Finding the spectral phase orders is then easily done by plotting the spectral phase as a function of the frequency and fitting the curve to a fourth order (or more) Taylor series expansion, or alternatively by using analytical formulas for the GDD and the TOD [72]:

$$\mathrm{GDD}(\lambda) = -\frac{\lambda^3 \mathrm{L}}{\pi c^2 d^2}\left[1 - \left(\frac{\lambda}{d} - \sin(\theta_i)\right)^2\right]^{-3/2} \tag{1.67}$$

$$\mathrm{TOD}(\lambda) = -\mathrm{GDD}(\lambda) \times \frac{3\lambda}{2\pi c}\left[1 + \frac{\lambda}{d}\frac{\lambda/d - \sin\theta_i}{1 - (\lambda/d - \sin\theta_i)^2}\right] \tag{1.68}$$

1.5.5 Acousto-optic programmable dispersive filters

Acousto-Optic Programmable Dispersive Filters (AOPDF) are often used for a more precise control of the spectral phase. We have two AOPDFs in our laser chain, which are called *Dazzler* and commercialized by *Fastlite* [253]. It consists of a birefringent uniaxial crystal (TeO_2), a piezo-electric transducer and a radio-frequency generator. An acoustic wave is generated in the crystal by the oscillations of the transducer via piezo-electric effect. It propagates in the birefringent crystal, and diffracts the different frequency components of the incident laser beam (Bragg diffraction) from the ordinary to the extraordinary axis (fig. 1.14). For TeO_2, $n_e > n_o$, therefore the earlier a monochromatic wave is diffracted, the larger group delay it will experience.

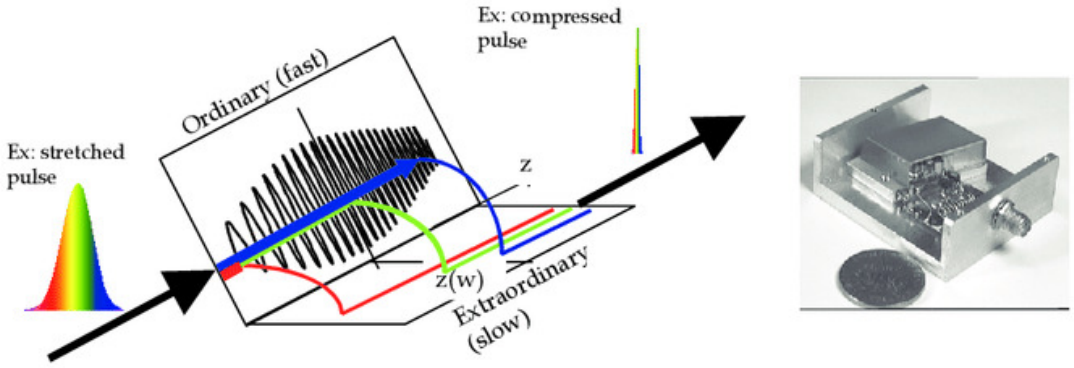

Figure 1.14: *a) Illustration of the AOPDF principle. b) Photograph of a Dazzler. Reprinted from [197].*

Through careful shaping of the acoustic wave, one can tailor the spectral phase by controlling the position z along the crystal at which each frequency contained in the light pulse is diffracted. The frequency-dependent group delay introduced by the Dazzler reads:

$$\tau_g(\omega, z) = \frac{n_0\omega}{c}z(\omega) + \frac{n_e\omega}{c}(L - z(\omega)),$$

with L the crystal length, n_e and n_0 the group indices of the extraordinary and ordinary axis respectively and $z(\omega)$ the wavelength-dependent position of diffraction in the crystal. The output optical signal is given by a convolution between the amplitude of the input signal and

the programmable acoustic signal $S(t/\alpha)$, with S(t) the electrical signal applied to the piezoelectric transducer:

$$E_{out}(t) = E_{in}(t) \otimes S(t/\alpha), \tag{1.69}$$

where α is the ratio of the acoustic frequency (in the MHz range) to the optical frequency. In the frequency domain, this corresponds to:

$$E_{out}(\omega) = E_{in}(\omega) \cdot S(\alpha\omega). \tag{1.70}$$

and thus the spectral phase at the Dazzler output is given by:

$$\Phi_{out}(\omega) = \Phi_{in}(\omega) + \Phi_{Dazzler}(\omega). \tag{1.71}$$

It can be shaped at will, by changing the 0 to 4th order on the software front panel or by providing a custom spectral phase in a text file, or both.

Moreover, the spectral amplitude can be modulated by changing the diffraction efficiency for each wavelength. Typically, during amplification, the gain saturates over time and the front of the chirped pulse is better amplified than the trail, therefore the central wavelength shifts towards the red. This effect is called **gain shifting**. Another effect occurring during amplification is the narrowing of the spectrum or **gain narrowing** due to the fact that the central frequency experiences a higher gain than the edges of the spectrum. The Dazzler located in the first amplifier in our laser system is used for dispersion management but also to mitigate these effects by adding a hole in the amplitude profile around the central wavelength. The shape of the output spectrum is optimized by finely adjusting the hole position, width and depth, so as to obtain a $\approx$ 47 nm FWHM Gaussian spectrum.

1.5.6 Chirped mirrors

Chirped mirrors are stacks of dielectric layers with varying thicknesses capable of introducing negative GDD [239], as illustrated in fig. 1.15.

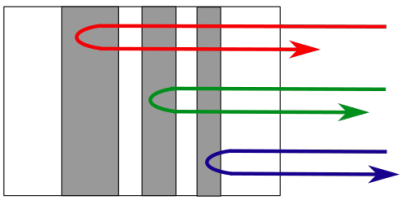

Figure 1.15: *Schematic representation of a chirped mirror. Its principle is based on wavelength-dependent penetration depths.*

1.6 Pulse train and associated frequency comb structure

At the output of an oscillator, the pulses are temporally spaced by the cavity roundtrip time $t_{rt} = 2L/c$, where L is the cavity length. The electric field of the pulse train can be written as [62]

$$E(t) = \sum_n E_p(t - nt_{rt}) \tag{1.72}$$

where each pulse is made of a CW sinusoidal carrier at the frequency ω_c multiplied by a Gaussian envelope A(t):

$$E_p(t) = A(t)e^{i(\omega_c t)} \tag{1.73}$$

In the frequency domain:

$$E(\omega) = \int \sum_n A(t - nt_{rt})e^{i\omega_c(t-nt_{rt})}e^{-i\omega t}dt \tag{1.74}$$

$$= \sum_n e^{-in\omega_c t_{rt}} \int A(t - nt_{rt})e^{-i[\omega-\omega_c]t}dt \tag{1.75}$$

And then we use the Fourier shift theorem $\int f(x-b)e^{-i\alpha x}dx = e^{-i\alpha b}\int f(x)e^{-i\alpha x}dx$:

$$E(\omega) = \sum_n e^{-in\omega t_{rt}} \int A(t)e^{-i(\omega-\omega_c)t}dt \tag{1.76}$$

$$= \sum_n e^{-in\omega t_{rt}} A(\omega - \omega_c) \tag{1.77}$$

We can recognize the Fourier series of a Dirac comb function δ in the last expression, which can thus be re-written as:

$$E(\omega) = A(\omega - \omega_c)\sum_m \delta(-\omega t_{rt} - 2\pi m). \tag{1.78}$$

Therefore, the output spectrum of the oscillator is a comb of discrete frequencies ω_n spaced by $f_{rep} = 1/t_{rt}$:

$$\omega_m = \frac{2\pi m}{t_{rt}} = 2\pi m f_{rep}. \tag{1.79}$$

Then, it is very useful to show that the information of the pulse-to-pulse CEP change $\Delta\phi_{\text{cep}}$ is connected to the offset of the frequency comb in the spectral domain [280]. This result can be retrieved by adding a phase term $\phi_{\text{cep}} = n\Delta\phi_{\text{cep}} + \phi_0$ to the expression of the nth pulse (eq. 1.73), as was done in [62]:

$$E(t) = \sum_n A(t - nt_{\text{rt}})e^{i(\omega_c t + n[\Delta\phi_{\text{cep}} - \omega_c t_{rt}] + \phi_0)} \tag{1.80}$$

Following the same derivation as before, we obtain the following expression in the frequency domain:

$$E(\omega) = e^{i\phi_0}A(\omega - \omega_c)\sum_m \delta(\Delta\phi_{cep} - \omega t_{rt} - 2\pi m) \tag{1.81}$$

Therefore the frequency comb components are

$$\omega_m = \frac{2\pi m}{t_{rt}} - \frac{\Delta\phi_{cep}}{t_{rt}} \Leftrightarrow \boxed{f_m = m f_{\text{rep}} + f_{\text{ceo}}} \tag{1.82}$$

where the comb offset f_{ceo} is

$$\boxed{f_{\text{ceo}} = \Delta\phi_{\text{cep}}\frac{f_{\text{rep}}}{2\pi}.} \tag{1.83}$$

The structure of the frequency comb and its time-domain equivalent are represented in fig. 1.16.

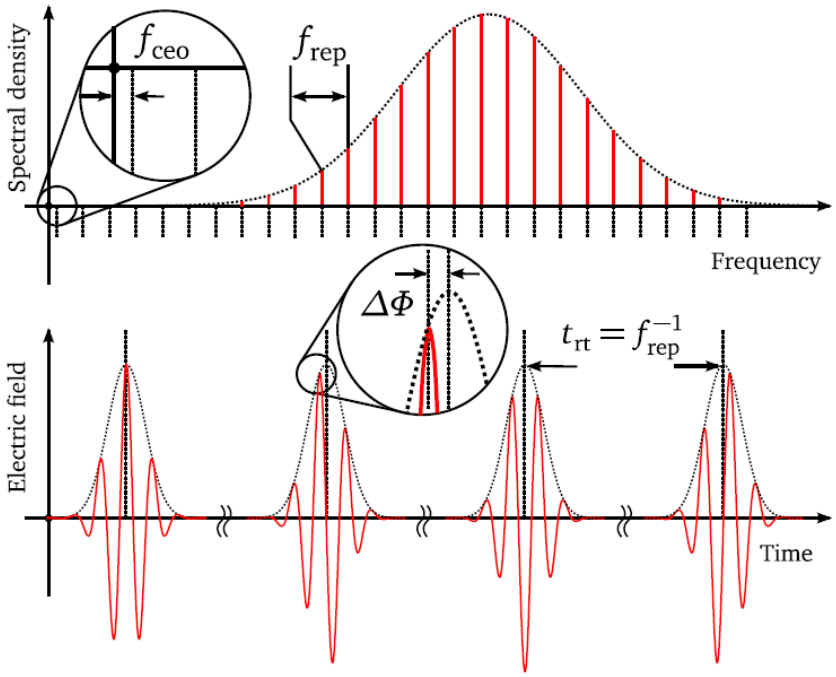

Figure 1.16: *Representation of a pulse train in the frequency (upper graph) and time (lower graph) domains. Reprinted from [161].*

Chapter 2

Theoretical background for laser-plasma physics

"If you have any questions, you can call my friend Tajima".
Gerard Mourou

2.1 Wave propagation in plasmas

99% of the visible universe is made of plasma. By definition, a plasma is a quasi-neutral gas of charged particles showing collective behaviour. Quasi-neutrality simply means that the overall charge densities of electrons and ions cancel each other, or in other words that the plasma electronic density n_e and the ion density n_i are linked by the expression $n_e = Z^* n_i$, with Z^* the degree of ionization. The collective behavior term arises from the fact that the macroscopic fields usually dominate over the microscopic, short-term fluctuations. Any disturbance of the equilibrium, for example a charge imbalance $\rho = e(Z^* n_i - n_e)$, immediately gives rise to an electrostatic field according to Gauss's law. And likewise, the motion of those charged particles will introduce a current density $J = e(Z^* n_i v_i - n_e v_e)$, which in turn will induce a magnetic field according to Ampère's law. These electric and magnetic fields largely determine the plasma dynamics, including its response when external fields are applied.

2.1.1 Plasma frequency

Let us consider the propagation of a sub-relativistic-intensity, monochromatic electromagnetic plane wave $E = E_0 \exp[i(\omega t - kz)]$ in a homogeneous plasma with a density n_e. Because of their much greater mass, we consider ions as immobile compared to electrons and we assume the plasma to be non-collisional. We use the fluid equation of motion:

$$\frac{\partial v_e}{\partial t} + (v_e.\nabla)v_e = -\frac{e}{m_e}(E + v_e \times B), \tag{2.1}$$

with v_e the fluid electrons velocity. This equation can be linearized for small perturbations:

$$\frac{\partial v_e}{\partial t} = -\frac{e}{m_e}E \tag{2.2}$$

And we can rewrite it for the current density $J = -en_e v_e$:

$$\frac{\partial J}{\partial t} = \epsilon_0 \omega_p^2 E, \tag{2.3}$$

with

$$\boxed{\omega_p = \sqrt{\frac{n_e e^2}{m_e \epsilon_0}}} \tag{2.4}$$

the plasma frequency. It corresponds to the frequency of electron oscillations around their position of equilibrium, or plasma waves frequency.

2.1.2 Maxwell's equations

In the beginning of this manuscript we saw that Maxwell's equations are written differently whether we consider propagation in vacuum or in a dielectric medium. When dealing with plasmas, one must consider Maxwell's equations for dielectric media, including charges and currents.

We distinguish two types of plasmas: cold ones and hot ones. A cold plasma is a plasma for which the electrons have a greater temperature or kinetic energy than the ions, which are not very responsive. On the contrary, a hot plasma is a plasma in which the ions have enough energy to influence the overall behavior of the plasma and are highly reactive.

If we now consider the case of a cold, noncollisional plasma, with no space charge separation (1st order approximation), Maxwell's equation becomes:

$$\nabla^2 E - \frac{1}{c^2}\left(\frac{\partial^2 E}{\partial t^2} + \omega_p^2 E\right) = 0 \tag{2.5}$$

2.1.3 Critical density

This equation admits a solution of the form $e^{i(\omega t - kz)}$, where

$$k = \frac{\omega}{c}\sqrt{1 - \frac{\omega_p^2}{\omega^2}}. \tag{2.6}$$

The refractive index of the plasma is given by

$$N(\omega) = \sqrt{1 - \frac{\omega_p^2}{\omega^2}} \tag{2.7}$$

and is less than 1. If $\omega_p < \omega$, the wave can propagate, whereas $\omega_p > \omega$ corresponds to an evanescent field. The case where the electromagnetic wave frequency ω is equal to the plasma frequency ω_p defines the critical electron density

$$\boxed{n_c = \frac{m_e \epsilon_0 \omega_p^2}{e^2}} \approx 1.1 \times 10^{21} \mathrm{cm}^{-3} \frac{1\mu\mathrm{m}^2}{\lambda_0^2}. \tag{2.8}$$

In the regions where the electronic density is less than n_c, the plasma is called under-dense, whereas in the regions where $n_e > n_c$, the plasma is called overdense.

2.2 Ionization

2.2.1 Mechanisms

The energy of a photon at the wavelength λ_0 is

$$E = \frac{hc}{\lambda_0[\mathrm{m}]}[\mathrm{J}] = \frac{1.2398}{\lambda_0[\mu\mathrm{m}]}[\mathrm{eV}] \tag{2.9}$$

where h is Planck's constant ($h = 6.62607015 \times 10^{-34}[\mathrm{m}^2\mathrm{kgs}^{-1}]$). Therefore the energy of a single photon at $\lambda_0 = 800$ nm is only $E \approx 1.5$ eV. Even an atom of cesium, with the lowest ionization energy of $E_i = 3.9$ eV [1], cannot be ionized by one photon alone. However, ionization can be achieved in different ways (represented in fig. 2.1): several photons can be absorbed at a time (multiphoton ionization), electrons can tunnel through the Coulomb potential barrier when it is bent enough by the laser electric field (tunnel ionization) or even classically escape when the electric field amplitude is high enough to suppress the Coulomb potential barrier (barrier-suppression ionization).

When an atom is placed in a homogeneous external electric field $\vec{E} = E\vec{e_x}$, a (single active) electron in the atom feels the sum of the Coulomb nucleus potential (potentially shielded by the other electrons) and the electric field potential, which reads along the x-axis:

$$V = \frac{-Z^* e^2}{4\pi\epsilon_0 x} + (-e)Ex \tag{2.10}$$

Barrier-suppression ionization corresponds to the case when $\forall x > 0$, $|V| < E_i$, which yields the barrier-suppression ionization intensity [288]:

$$I_{BSI} = \frac{\pi^2 c \epsilon_0^3 E_i^4}{2e^6 Z^{*2}} = 4 \times 10^9 \frac{E_i^4[\mathrm{eV}]}{Z^{*2}}[\mathrm{W.cm}^{-2}] \tag{2.11}$$

To identify the dominant mechanism, one can use the Keldysh parameter γ_K:

$$\gamma_K = \frac{\omega_0}{eE}\sqrt{2m_e E_i} = \sqrt{\frac{E_i}{2U_p}}, \tag{2.12}$$

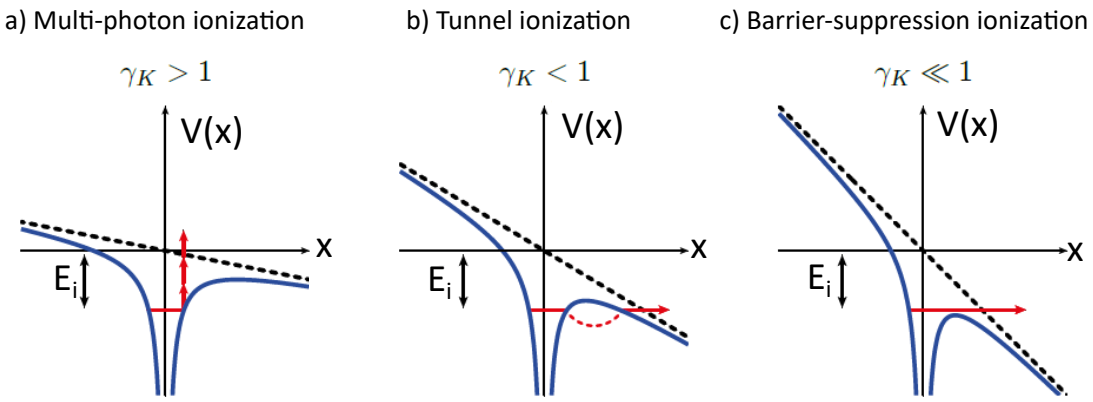

Figure 2.1: *Different ionization mechanisms. Reprinted from [53]*

where U_p[eV] is the laser ponderomotive energy (see 2.5). If $\gamma_K > 1$, MPI dominates whereas if $\gamma_K < 1$, tunnel ionization or even BSI ($\gamma_K \ll 1$) becomes the dominant mechanism. Thus, for a given wavelength and target material, the regime clearly depends on the laser intensity. The tunnel ionization probability and rate of the different species can be calculated for different laser intensities using the ADK theory [64, 19].

2.2.2 Ionization of solid fused silica targets

We are now interested in the ionization of solid glass targets by focused laser beams with intensities ranging from $\sim 10^{14}$ to $\sim 10^{19}$W.cm^{-2}.

Fused silica

We use solid fused silica (SiO_2) as target material. The ionization intensities are given in Tab. 2.1. A silicon atom contains 14 protons and electrons whereas an oxygen atom contains 8 electrons and protons, therefore each molecule contains 30 electrons. The density of fused silica is 2.2g.cm^{-3} and its molar mass is 60.08 g.mol^{-1}, thus we have 0.0367 mol.cm^{-3} *ie* a molecular density of 2.2×10^{22}cm^{-3}. Consequently, a fully ionized fused-silica target corresponds to a plasma electron density of $n_{e,max} = 30 \times 2.2 \times 10^{22} = 6.6 \times 10^{23}$cm^{-3}, or equivalently:

$$\boxed{n_{e,max} = 330 n_c}. \tag{2.13}$$

Ionization by the laser

In the experiments with plasma mirrors, we use an auxiliary pulse, also called prepulse, to ionize the solid target at a precise moment before the arrival of the pulse peak. The typical intensity of the prepulse is $\sim 10^{14}$W.cm^{-2}. It thus creates a plasma, called preplasma, at the surface of the target, which expands towards vacuum. A few picoseconds later, the main pulse is focused on this preplasma to relativistic intensities. The plasma density gradient scale length seen by the pulse peak therefore depends on the time interval τ between the prepulse and the main pulse, as well as on the temporal intensity profile of the main laser pulse around the peak, *ie* its temporal contrast.

For prepulse intensities $\sim 10^{14}$W.cm^{-2}, the initial plasma or preplasma contains at least Si^{2+} and O^+, which come from barrier suppression ionization. As the main pulse reaches the target, for a typical laser intensity $\sim 10^{18} - 10^{19}$W.cm^{-2}, we clearly suppress the potential barrier ($\gamma_K \ll 1$) until we arrive at Si^{12+} and at least 0^{6+}. Then, the intensity is too low to get Si^{13+} and Si^{14+} in the tunneling regime ($\gamma_K \approx 0.14$-0.15 for 10^{18}W.cm^{-2}, but the tunnel ionization probability is practically zero according to the ADK model). However, collisions with fast electrons can also certainly further ionize those Si^{12+} and Si^{13+} ions: it would take ≈ 2.5

keV energy to do that, and we detect plenty of electrons with hundreds of keV energy, up to ≈ 1 MeV. At the peak of the main pulse, the target is thus fully ionized.

2.2.3 Ionization tables

The laser intensities and energies required for ionization of the different ions considered in this manuscript are given here. Silicon and oxygen are the constituents of the solid target; hydrogen and carbon (from which accelerated protons originate) are considered to take the contamination of the target surface into account; finally, gas jets used in the laser wakefield acceleration experiments are made of nitrogen.

Silicon

atomic orbital	ionization	E (eV)	I_{BS} (W.cm^{-2})
$3p^2$	Si to Si^{+}	8.15	1.76×10^{13}
	Si^{+} to Si^{2+}	16.3	7.06×10^{13}
$3s^2$	Si^{2+} to Si^{3+}	33.5	5.60×10^{14}
	Si^{3+} to Si^{4+}	45.1	1.03×10^{15}
$2p^6$	Si^{4+} to Si^{5+}	167	1.24×10^{17}
	Si^{5+} to Si^{6+}	205	1.96×10^{17}
	Si^{6+} to Si^{7+}	247	3.04×10^{17}
	Si^{7+} to Si^{8+}	304	5.34×10^{17}
	Si^{8+} to Si^{9+}	351	7.50×10^{17}
	Si^{9+} to Si^{10+}	401	1.03×10^{18}
$2s^2$	Si^{10+} to Si^{11+}	476	1.70×10^{18}
	Si^{11+} to Si^{12+}	523	2.08×10^{18}
$1s^2$	Si^{12+} to Si^{13+}	2440	8.39×10^{20}
	Si^{13+} to Si^{14+}	2670	1.04×10^{21}

Oxygen

atomic orbital	ionization	E (eV)	I_{BS} (W.cm^{-2})
$2p^4$	O to O^{+}	13.6	1.37×10^{14}
	O^{+} to O^{2+}	35.1	1.52×10^{15}
	O^{2+} to O^{3+}	54.9	4.04×10^{15}
	O^{3+} to O^{4+}	77.4	8.97×10^{15}
$2s^2$	O^{4+} to O^{5+}	114	2.70×10^{16}
	O^{5+} to O^{6+}	138	4.03×10^{16}
$1s^2$	O^{6+} to O^{7+}	739	2.43×10^{19}
	O^{7+} to O^{8+}	871	3.60×10^{19}

Table 2.1: *Ionization energies of silicon and oxygen (from [1]) and corresponding barrier-suppression ionization intensities (using eq. 2.11).*

Carbon

atomic orbital	ionization	E (eV)	I_{BS} (W.cm^{-2})
$2p^2$	C to C^+	11.3	6.5×10^{13}
	C^+ to C^{2+}	24.4	3.5×10^{14}
$2s^2$	C^{2+} to C^{3+}	47.9	2.3×10^{15}
	C^{3+} to C^{4+}	64.5	4.3×10^{15}
$1s^2$	C^{4+} to C^{5+}	392.1	3.8×10^{18}
	C^{5+} to C^{6+}	490.0	6.4×10^{18}

Hydrogen

atomic orbital	ionization	E (eV)	I_{BS} (W.cm^{-2})
$1s^1$	H to H^+	13.6	1.4×10^{14}

Table 2.2: *Ionization energies of carbon and hydrogen (from [1]) and corresponding barrier-suppression ionization intensities (using eq. 2.11).*

Nitrogen

atomic orbital	ionization	E (eV)	I_{BS} (W.cm^{-2})
$2p^3$	N to N^+	14.5	1.8×10^{14}
	N^+ to N^{2+}	29.6	7.7×10^{14}
	N^{2+} to N^{3+}	47.4	2.2×10^{15}
$2s^2$	N^{3+} to N^{4+}	77.4	9.0×10^{15}
	N^{4+} to N^{5+}	97.9	1.5×10^{16}
$1s^2$	N^{5+} to N^{6+}	552.1	1.0×10^{19}
	N^{6+} to N^{7+}	667.0	1.6×10^{19}

Table 2.3: *Ionization energies of nitrogen (from [1]) and corresponding Barrier Suppression laser intensity (according to Eq. 2.11).*

2.3 Preplasma expansion

After ionization of the solid target by the prepulse, the preplasma starts expanding into vacuum. I explain in the following how we model the evolution of the plasma density ramp at the surface of the target over time and show at which depth the laser is reflected.

2.3.1 Isothermal model

For the preplasma expansion, we use an isothermal model (1D fluid-model) in which there are no collisions, the only field considered is the electric field due to charge separation in the plasma $E = -\partial V/\partial x$, the ion fluid temperature is zero and the electron fluid is isothermal with a temperature T_e. Let $x = 0$ be the target surface and x the distance from the target along the normal direction. At $t = 0$, before the interaction, the ion density is piecewise constant (see fig.2.2):

$$n_i = \begin{cases} n_{i0}, & \text{for} \quad x \leq 0 \\ 0, & \text{for} \quad x > 0. \end{cases}$$

At $t > 0$, the preplasma expands towards vacuum due to the charge separation. We assume that this plasma is quasi-neutral ($n_e = Zn_i$) and that the electrons are at thermal equilibrium, so that the electron density follows a Boltzmann distribution:

$$n_e = n_{e0} \exp\left(\frac{eV}{k_B T_e}\right), \tag{2.14}$$

where $n_{e0} = Zn_{i0}$ and k_B is Boltzmann's constant. Solving the equations of conservation of mass and momentum leads to the following expression for the electron density at $t > 0$ [288]:

$$n_e = Zn_i = \begin{cases} n_{e0} \exp\left(-\frac{x}{c_s t} - 1\right), & \text{for} \quad x \geq -c_s t \\ n_{e0}, & \text{for} \quad x < -c_s t. \end{cases} \tag{2.15}$$

where $c_s = \sqrt{Zk_B T_e / m_i}$ is the ion sound velocity. The plasma density profile is exponential and the gradient scale length $L = c_s t$ increases linearly with time.

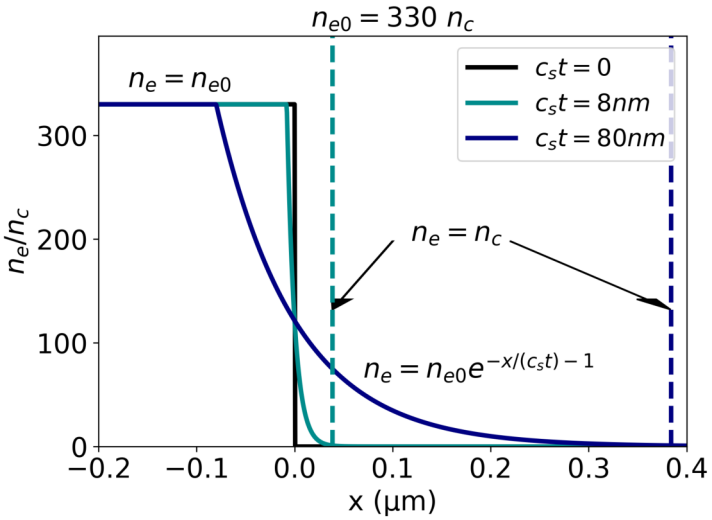

Figure 2.2: *Plasma density gradient profile according to the isothermal model for an initial electronic density of 330 n_c, plotted for three different gradient scale lengths: $L = 0$, $\lambda/100$ and $\lambda/10$, with $\lambda = 800nm$.*

2.3.2 Total reflection condition

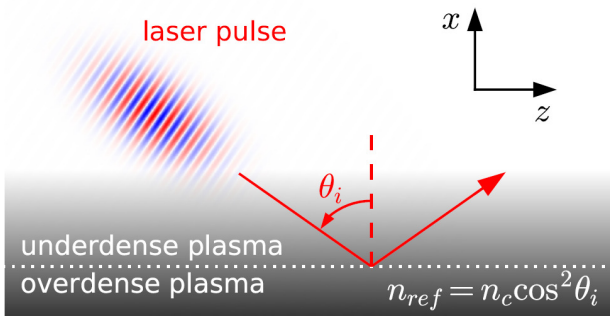

Figure 2.3: *Illustration of the reflection of a laser pulse with oblique incidence off an overdense plasma surface. The plasma density gradient is along the x axis. Taken from [288].*

An obliquely incident laser beam on a target, with an angle of incidence θ_i with respect to the target normal direction (see fig. 2.3), will be refracted according to Snell-Descartes' law:

$$\sin\theta_i = n(x) \sin\theta_R, \tag{2.16}$$

where $n(x)$ is the refractive index of the plasma at a depth x: $n(x) = \sqrt{1 - n_e(x)/n_c}$ and θ_R is the angle of refraction. The laser is totally reflected by the plasma when $\sin\theta_R = 1$, *ie* at the depth x_{ref} where the electron density is

$$\boxed{n_e(x_{\text{ref}}) = n_c \cos^2\theta_i}. \tag{2.17}$$

2.4 Relativistic thresholds

If we consider a non-relativistic electron (charge e, mass m_e) in a laser field (amplitude E_0), it will experience the Lorentz force:

$$m_e \frac{dv}{dt} = -eE_0 \sin(\omega t) \tag{2.18}$$

and thus have a velocity:

$$v = \frac{eE_0}{m_e\omega} \cos(\omega t) = v_{\text{osc}} \cos(\omega t). \tag{2.19}$$

The quantity

$$\boxed{a_0 = \frac{v_{\text{osc}}}{c} = \frac{eE_0}{cm_e\omega}} \tag{2.20}$$

is called the normalized field amplitude and allows discerning the limit between the classical regime ($a_0 < 1$) and the relativistic regime ($a_0 \geq 1$). For a 800nm central wavelength and considering $n = 1$, the limit case corresponds to a laser intensity:

$$a_0 = 1 \Leftrightarrow I_{peak} = \frac{nc\epsilon_0}{2} \left| \frac{cm_e\omega}{e} \right|^2 \approx 2.14 \times 10^{18} \text{W.cm}^{-2} \tag{2.21}$$

or equivalently $E_0 \approx 4.02$ TV/m. The quantity a_0 is linked to the laser peak intensity I_{peak} as follows:

$$a_0 = 8.52 \times 10^{-10} \lambda_0[\mu\text{m}] \sqrt{I_{\text{peak}}}[\text{W.cm}^{-2}], \tag{2.22}$$

or equivalently:

$$\boxed{a_0 = \lambda_0[\mu\text{m}] \times \sqrt{\frac{I_{\text{peak}}[\text{W.cm}^{-2}]}{I_0[\text{W.cm}^{-2}]}}}, \tag{2.23}$$

with $I_0 \approx 1.37 \times 10^{18} \text{W.cm}^{-2}$.

Electrons are considered relativistic when their kinetic energy $E_{\text{kin}} = (\gamma - 1)mc^2$ is comparable to the electron rest mass energy $mc^2 \approx 0.5$ MeV, with $\gamma = 1/\sqrt{1 - v^2/c^2}$ the Lorentz factor. The limit case $E_{\text{kin}} = mc^2$ corresponds to an electron velocity $v = \sqrt{3/4}c \approx 0.87c$.

The proton rest mass energy is much higher, ≈ 938.3 MeV. The difference between the classical and the relativistic momentum $p = \gamma m_p v_p$ becomes $\geq 1\%$ only when $\gamma = 1.01 \Leftrightarrow v = 0.14c \Leftrightarrow E_{\text{kin}} = 0.01 m_p c^2 \approx 9.4$ MeV. Thus, protons with energies ∼few MeV can be treated classically.

2.5 Ponderomotive force

We are now interested in how the plasma interacts with the laser. One of the most important effects when a laser propagates in an underdense plasma is the radiation pressure or ponderomotive force.

Simple case of a 1D non-uniform electric field oscillating at ω

Let us consider the simple case of a 1D electric field directed along the x-axis with a field gradient along x: $E_x(x,t) = E_{0x}(x)\sin(\omega t)$. The motion of an electron interacting with this field is given by the equation:

$$m[\partial_t v + (v \cdot \nabla)v] = -eE_x(x,t). \tag{2.24}$$

At first order, we only look at the linear term and obtain

$$v = \frac{eE_{0x}(x)}{m\omega}\cos(\omega t), \tag{2.25}$$

indicating that the electron oscillates in the field. At second order, a nonlinear force term appears:

$$F_{\mathrm{NL}} = -m(v \cdot \nabla)v = -mv\partial_x v = -\frac{1}{2}m\partial_x v^2. \tag{2.26}$$

Plugging expression 2.25 into this yields:

$$F_{\mathrm{NL}} = -\frac{1}{2}m\cos^2(\omega t)\frac{e^2}{m^2\omega^2}\partial_x E_{0x}^2(x) \tag{2.27}$$

Averaged over one oscillation period of the laser, this force becomes:

$$\langle F_{\mathrm{NL}} \rangle = -\frac{e^2}{4m\omega^2}\partial_x E_{0x}^2(x) \tag{2.28}$$

and pushes the electrons away from the high field region in the plane of polarization.

Relativistic particle in a 3D laser pulse

If we now consider a relativistic particle in a three-dimensional laser pulse, the full expression of the ponderomotive force was derived in [215]. The authors separated each quantity q into an average contribution over the laser oscillations $\bar{q}$ and a high frequency contribution $\tilde{q}$. Since the derivation is quite long, I will only give here the result:

$$\frac{d\bar{\mathbf{p}}}{dt} = -\frac{1}{2m\bar{\gamma}}\nabla\overline{|q\tilde{\mathbf{A}}_{perp}|^2}, \tag{2.29}$$

with

$$\bar{\gamma^2} = 1 + \frac{1}{m^2c^2}\left[|\bar{\mathbf{p}}_{perp}|^2 + \overline{|q\tilde{\mathbf{A}}_{perp}|^2} + \bar{p_z^2}\right] \tag{2.30}$$

and $\mathbf{A}$ the vector potential in Coulomb gauge ($\nabla \cdot \mathbf{A}$ =0).

The result is similar to Eq. 2.28, but we see that eventually the ponderomotive force does not depend on the polarization direction of the laser and pushes the electrons away from the high field region isotropically. We can also note that it inversely depends on the particle mass. Thus, it is much stronger for electrons than ions.

Ponderomotive energy

Finally, it is useful to define the cycle-averaged quiver energy of a free electron in the electromagnetic field or ponderomotive energy U_p:

$$U_p = \frac{e^2E_0^2}{4m\omega^2} = \frac{2e^2}{c\epsilon_0 m}\frac{I}{4\omega^2}, \tag{2.31}$$

which can also be expressed more conveniently as:

$$\boxed{U_p[\mathrm{eV}] = 9.33I[10^{14}\mathrm{W.cm^{-2}}]\lambda^2[\mu\mathrm{m}]}. \tag{2.32}$$

To give the reader an order of magnitude, for a laser intensity of $10^{19}\mathrm{W.cm^{-2}}$, $U_p \approx 0.6\mathrm{MeV}$ whereas for a laser intensity of $10^{14}\mathrm{W.cm^{-2}}$, $U_p \approx 6\mathrm{eV}$.

Chapter 3

Generation of TW peak power, near-single-cycle laser pulses at 1kHz repetition rate with high contrast

"Insanity is doing the same thing over and over and expecting different results".
Albert Einstein

The *Laboratoire d'Optique Appliquée* (LOA), founded in 1972, was a precursor in the use of titanium doped sapphire crystal amplifiers, which have been the main workhorse of ultrafast laser science for decades. The *Salle Noire 2* laser system was developed in this context, in the PCO group, under the lead of Rodrigo Lopez-Martens, with the installation of the first optical tables [255] in 2006. The goal was to reach the relativistic lambda-cubed regime, a concept introduced by G. Mourou and N. Naumova [182, 187], where light is temporally concentrated in a single period of the oscillations of the electric field, and spatially focused down to a $\sim \lambda$ spot size, where λ is the pulse central wavelength. In this regime, laser intensities

$$I = \frac{E}{\tau A} = \frac{Ec}{\lambda^3},$$

with τ the pulse duration, and A the beam surface area, capable of driving relativistic motion of electrons can be reached with pulse energies E of only about a few millijoule [7]. Compared to traditional PW or multi-TW lasers delivering multi-cycle, Joule-level pulses that are used in most relativistic laser-matter interaction experiments, this approach allows working at higher repetition rates because lower energy pulses reduce problems related to heat dissipation, thus making the laser more stable, but also allowing to accumulate statistics in applications downstream. Moreover, the laser system can remain quite compact as no large-size optics are needed.

Following this approach, efforts were made in the group towards reducing the pulse duration down to the near-single-cycle regime and controlling the waveform of the pulses, while ensuring the stability of the source properties and the focussability of the beam, so as to reach relativistic intensities on target. Furthermore, in order to efficiently drive HHG from plasma mirrors, the group developed methods to increase the contrast ratio, thus enabling plasma density gradient control at the target surface. Following the work of my predecessors, I took over the laser system in 2017 for an internship, and contributed to new developments, while also using it for applications to laser-plasma interaction.

In this first chapter, I will present the laser system in details, and describe the latest developments.

3.1 Global architecture and summary of the laser upgrades

Salle Noire 2 global architecture

The *Salle Noire 2* laser system consists of two CPA stages using Ti:Sa crystals as a gain medium, with a nonlinear XPW filter in between for contrast enhancement. The output of this double CPA is then post-compressed in a stretched-flexible hollow-core-fiber (SF-HCF) to reach the few-cycle regime. The global diagram of the system in its current state is shown in fig. 3.1.

Latest developments

All along its History, *Salle Noire 2* has been constantly under development. Compared to the laser system at the time I arrived at LOA (a detailed description of its previous states can be found in [255], [218], [25] or in [220]), the following changes were made during my thesis:

1) We started by replacing the first amplifier's pump laser with a more stable one in terms of pulse energy and spatial mode, which improved the overall laser stability (CEP, energy, duration).

2) We doubled the amount of glass to stretch the pulses further before the first amplifier in order to avoid damaging the Ti:Sa crystal, and we changed the compression (acousto-optic programmable dispersive filter and transmission-grating compressor) parameters accordingly.

3) Then, I had to adapt the XPW filter setup to the new input beamsize and upgraded the optomechanics for more convenient maintenance operation.

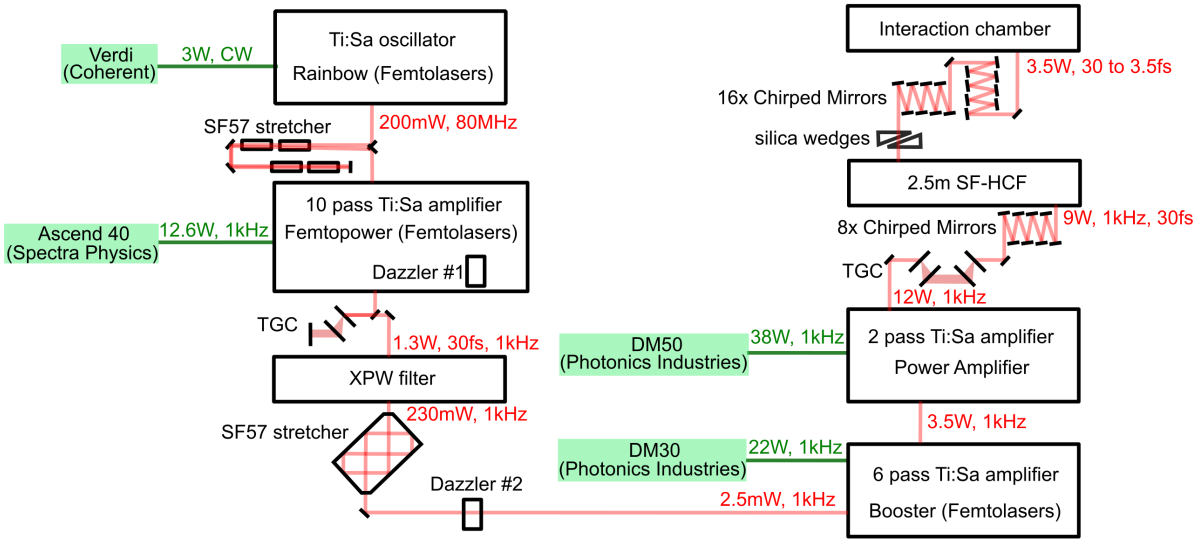

Figure 3.1: *Global architecture of the Salle Noire 2 laser chain.*

4) After that, we decided to change the second CPA compressor from a GRISM to a grating compressor, which also implied changing the second acousto-optic programmable dispersive filter configuration from double pass to single pass. The main motivation was to decrease the energy losses due to the non-zero reflectivity of the prisms, increase the post-compression fiber transmission by improving the spatial quality of the beam at the entrance (the prisms degraded the spatial beam quality due to thermal lensing and B-integral) but also to make the daily alignment of the laser much faster by avoiding having to wait for slow thermalisation of the prisms before seeding the fiber.

5) The resulting increase in power induced very frequent (about every other week) damages on the first mirror after the post-compression hollow-core fiber. We therefore added an extension (a tube and a little extra vacuum chamber) to place this mirror further from the fiber exit. The refocusing optics had to be changed accordingly.

I also characterized the pulses with various devices and implemented a feedback loop for CEP control and stabilization at 1 kHz repetition rate, but this will be detailed in the next chapter. In this chapter, the laser chain will be described block by block and I will detail those changes in each section.

3.2 Front-end

The front-end is what we call the oscillator and the first CPA.

3.2.1 Oscillator

The first brick of the laser is a commercially available Ti:Sa oscillator (*Rainbow, Femtolasers*) operating at a repetition rate $f_{rep} \approx 80$ MHz. It is pumped by 3 W of a continuous-wave frequency doubled Nd:YVO4 laser (*Verdi, Coherent*) at 532nm, corresponding to the maximum absorption wavelength of Ti:Sa.

To obtain pulses, the oscillator is mode locked by Kerr lensing (see 1.4.2): pulses are preferentially amplified due to a better overlap with the pump volume in the Ti:Sa crystal which acts like a soft aperture [281, 282]). The initial pulses are generated out of noise, by just quickly moving a mirror. More details about Ti:Sa ultrafast oscillators can be found in [281].

The average power at the output of the oscillator is ≈ 200 mW. To compensate for the GDD, broadband intra-cavity chirped mirrors are used, allowing to obtain a pulse duration $\approx$

10fs. Moreover, the output coupler is wedged to prevent unwanted reflections, so there is a compensating plate to eliminate the angular dispersion. Therefore, additional extra-cavity chirped mirrors are needed to compensate for their dispersion as well.

3.2.2 First CPA

The second brick of the laser chain is the first CPA (see figure 3.2). The beam goes through a Faraday isolator (to prevent back-reflections from propagating back into the oscillator), then the pulses are stretched in bulk glass (SF57) and amplified in a commercially available 10 pass Ti:Sa amplifier (*Femtopower Compact Pro CE-Phase, Femtolasers GmbH*), in which the repetition rate is reduced to 1kHz. Temporal recompression is achieved using a double-pass transmission grating compressor.

Two major changes were made during my PhD: first, we replaced the amplifier's pump laser (*JADE, Thales*) with a new one (*Ascend 40, Spectra Physics*) to significantly increase the pulse-to-pulse energy stability, from 2 % fluctuations rms (over 3 minutes) to 0.2 %. Secondly, we doubled the amount of glass to further stretch the seed pulses and lower the risk of damaging the Femtopower Ti:Sa crystal.

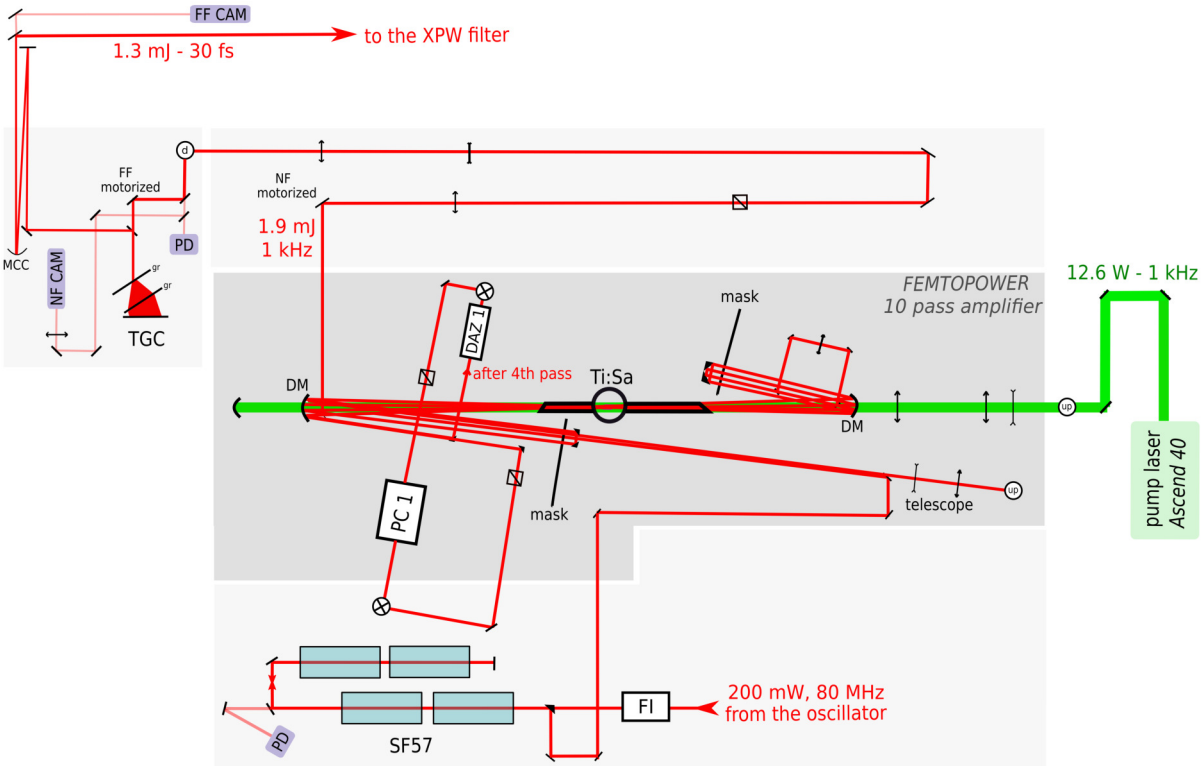

Figure 3.2: *First CPA schematic drawing. FI: Faraday Isolator, PC 1: Pockel's Cell 1, DAZ 1: Dazzler 1, DM: dichroic mirror, TGC: transmission gratings compressor, PD: photodiode used for energy monitoring, NF CAM: near field camera, FF CAM: far field camera, NF and FF motorized: motorized mirrors for active beam stabilization using the references provided by NF and FF CAM.*

Femtopower

The Ti:Sa crystal dimensions in the Femtopower are 3 x 6 x 8 mm. The crystal is placed inside a small vacuum chamber (inside of which the pressure is $\approx$ 0.1 mbar) with silica windows at Brewster angle on both sides, and maintained at a 180K temperature. It is optically pumped by 12.6 Watt at 1kHz repetition rate. The MHz pulse train coming from the oscillator

is amplified in the first four passes. After the 4th pass, the pulses are sent into an acousto-optic programmable dispersive filter (*Dazzler*, see 1.5.5), and then the first order diffracted beam from the AOPDF is sent into a Pockels' cell to reduce the repetition rate. Indeed, the repetition rate of 80 MHz needs to be reduced in order to reach the mJ-level with the pump power available. A Pockels' cell consists of a birefringent material (in our case, a KD*P crystal), which acts as a half wave plate whenever a high voltage is applied. A pair of crossed polarizer beam splitters are placed before and after the Pockels cell to eliminate light whose polarization is unchanged (when no voltage is applied). Therefore, by applying a 7kV pulsed voltage every 1 ms to the KD*P crystal, we reduce the repetition rate down to 1 kHz, which is our final repetition rate. The thus obtained kHz pulse train is then further amplified up to 2 mJ in the subsequent passages through the crystal.

Increasing the temporal stretching of the seed pulses

We initially had 2 pieces (which were 5cm long each, and used in double pass) of SF57, whereas we now have 4 pieces, corresponding to 40cm propagation length in total. After doubling the path length in the stretching material, which corresponds to adding (using values in Table 1.1):

$$\Phi_{2,SF57} \approx 44.8 \times 10^3 \text{fs}^2, \Phi_{3,SF57} \approx 28.2 \times 10^3 \text{fs}^3, \Phi_{4,SF57} \approx 10.2 \times 10^3 \text{fs}^4,$$

the compression was optimized by focusing the beam in air and visually optimizing white light generation in focus (*ie* increasing the spectral bandwidth and the light intensity in the diverging beam), by varying the gratings' spacing first and then changing the spectral phase on the Dazzler front panel.

The gratings' spacing was increased by approximately 13mm, which was actually the maximum allowed by the translation on which one of the gratings stands. Knowing the angle of incidence (30.8°) and the groove density (1280 per mm), we can estimate the dispersion thus added (see subsection 1.5.4 for more details):

$$\Phi_{2,g13mm} \approx -61 \times 10^3 \text{fs}^2, \Phi_{3,g13mm} \approx 133 \times 10^3 \text{fs}^3, \Phi_{4,g13mm} \approx -446 \times 10^3 \text{fs}^4.$$

The Dazzler 1 settings were changed from

$$\Phi_{2,Daz} = -25.5 \times 10^3 \text{fs}^2, \Phi_{3,Daz} = -180 \times 10^3 \text{fs}^3, \Phi_{4,Daz} = 450 \times 10^3 \text{fs}^4$$

to

$$\Phi'_{2,Daz} = -8.7 \times 10^3 \text{fs}^2, \Phi'_{3,Daz} = -335 \times 10^3 \text{fs}^3, \Phi'_{4,Daz} = 480 \times 10^3 \text{fs}^4,$$

which corresponds very well to the theoretical predictions for the grating compressor and the stretching material for the second and third order.

The compression was then finely tuned with a self-referenced spectral interferometric measurement (Wizzler, see 4.1.1), which can generate a text file containing the precise remaining spectral phase that needs to be compensated for, and send it to the Dazzler. Eventually, the correction applied by the Dazzler is the combination of this text file and the values set on the front panel.

Since we added those extra pieces of SF57, we have not had any damage on the Femtopower Ti:Sa crystal. Together with the new pump laser, this results in a very stable pulse train at the output of the first CPA, except for a very slow drift which only implies optimizing the amplifier alignment every few weeks.

3.3 XPW filter

The temporal contrast of a laser is defined as the ratio of the peak intensity and the intensity at n ps from the peak $C = I/I_{n\,\text{ps}}$. The typical contrast of a Ti:Sa CPA amplifier is $\sim 10^6$ on

the ns time scale, and can reach values up to 10^3 on a ps time scale. The typical pulse structure is represented in fig. 3.3: the finite incoherent contrast at long delays (on the ns time scale, corresponding to the pump pulse duration) is mostly due to Amplified Spontaneous Emission (ASE) whereas the coherent contrast (on the ps time scale) results from imperfect temporal compression (residual spectral phase) [15] and modulations of the spectral amplitude. On top of that, there are often post-pulses, originating from the back-reflection of the laser inside windows or lenses, which can convert into prepulses in the next amplification stages [65, 159]. The typical intensity on target in our experiments is $\sim 10^{18} - 10^{19}$W.cm^{-2}, thus the intensity of such a pedestal is high enough to ionize the target material in an uncontrolled manner. To efficiently drive plasma mirrors, it is critical to control the plasma density ramp at the surface of the target, therefore we need to enhance this contrast ratio.

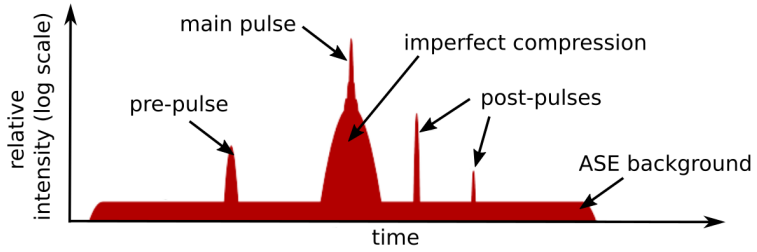

Figure 3.3: *Typical contrast of a CPA laser.*

A contrast-enhancement technique base on the XPW effect (detailed in 1.4.4) was developed at LOA a few years ago [134], and is now widely spread. The intensity of the generated wave is proportional to the cube of the incident wave intensity so it can potentially increase the contrast ratio from C to $C' = C^3$. In practice, the contrast enhancement is limited by the extinction ratio of the polarizer used to select the crossed-polarized wave, which is $\sim 10^4$ with our calcite polarizer-beam splitter, but can now reach up to 10^6 using higher-quality polarizers.

3.3.1 XPW setup

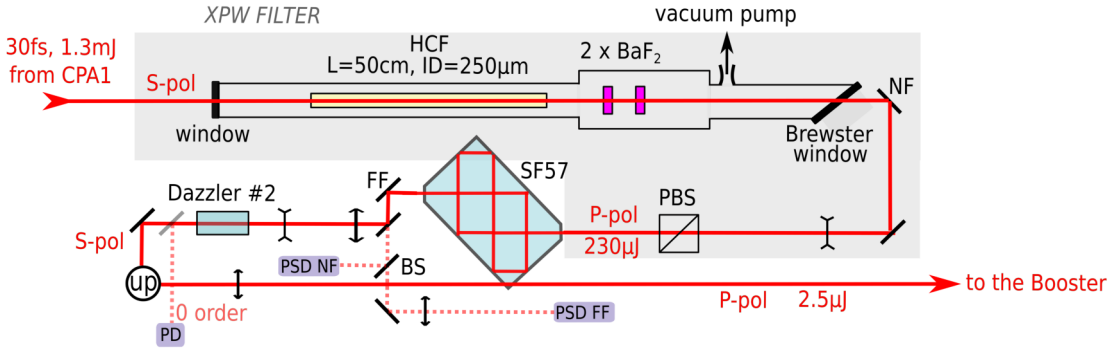

Figure 3.4: *XPW filter setup. The mirrors labeled 'NF' and 'FF' are motorized to ensure active beam pointing stabilization, using references PSD NF and PSD FF.*

After the transmission grating compressor, the spatial beamprofile is cleaned by focusing the beam into a fused silica hollow-core fiber with a $f = 1.75$m focal length, 2 inch, dielectric concave mirror. The focal spot diameter is $\approx 160\mu$m at $1/e^2$, which corresponds to the optimum beamsize for our fiber, with a 250μm inner diameter (ID) (the outer diameter is 1.6mm). Indeed, when the beamsize is $0.64 \times ID$, most of the light is coupled into the fundamental spatial mode

as explained in 1.3.4. The fiber length is 50 cm, which corresponds to a size available off-the-shelf so we can avoid the delicate operation of cutting the fibers with a Sapphire blade. Increasing the fiber length helps obtaining a cleaner mode as the higher spatial modes get more attenuated (see fig.1.6.c), but also reduces the transmission efficiency and makes the setup less compact.

At the fiber output, two square 10 x 10mm, 1.5mm thick BaF_2 crystals generate the XPW wave, changing the polarization from s to p. It was found that using two crystals can help increasing the conversion efficiency from about 20 % to 30 % [135]. We tried using a single thicker (2mm) crystal but to extract the same energy, it would systematically get damaged. The first crystal is placed at a distance $z \approx 28$cm from the fiber exit and the second crystal is located ≈4cm further.

A home-made active slow beam-stabilizer (shown in fig.3.2) ensures long-term operation of the filter. The whole setup is placed under vacuum ($P \approx 10^{-4}$ mbar) to avoid pollution of the crystals, which must however be replaced every few months, and pulse distortions due to ionization and plasma formation around the focus. The entrance window is a 0.5mm thick (thicker might induce nonlinear effects, which are visible in the spectrum), AR coated fused silica window, with quasi-normal orientation with respect to the beam (it is slightly titled to avoid back reflections, which can reduce the amplifier output by depleting the gain medium before the pulses get amplified), whereas the output window is oriented at Brewster angle to preferentially select the XPW (p-polarized) beam and avoid back-reflections.

With 1.3mJ per pulse entering this XPW filter, we obtain ≈ 650 μJ at the output (measured right after the Brewster window), with about 230 μJ contained in the XPW wave (measured after the PBS). The fiber transmission is typically ≥ 80 %, which can be verified by removing the crystals and placing a normal incidence window at the output. The difference with the measured 650 μJ comes from Fresnel reflection losses at the BaF_2 crystals/vacuum interfaces and the orientation of the output window.

Spectrum

The FTL duration FWHM of the XPW pulse Δt_{XPW} is shorter than the FTL duration of the initial pulse Δt, with a ratio:

$$\Delta t_{\mathrm{XPW}} = \Delta t/\sqrt{3}. \tag{3.1}$$

Equivalently, the spectral bandwidth is expected to increase by a factor $\sqrt{3}$. In practice, we may obtain a slightly broader spectrum (see fig 3.5) due to a little bit of SPM (described by the first terms $\propto \gamma_1$ and $\propto \gamma_5$ in Eqs. 1.60 and 1.61) [217] and depending on the Dazzler hole parameters.

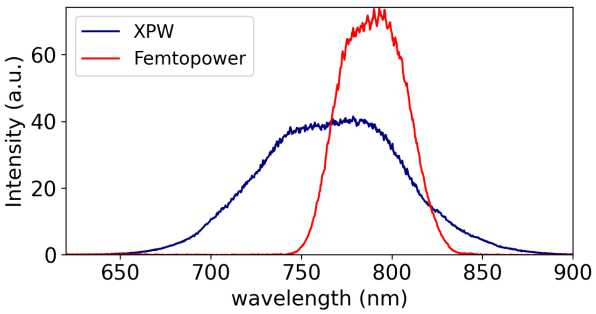

Figure 3.5: *Typical spectrum before and after the XPW filter. The input spectrum is 47nm FWHM whereas the XPW spectrum is 95nm FWHM.*

XPW filter upgrade

When replacing BaF_2 crystals, one must carefully determine the angle β of each crystal individually, for which the maximum XPW efficiency is obtained. The same maxima must be chosen for both crystals. At the time I started my PhD, this was a very time-consuming operation, as

there was no way to rotate the crystals under vacuum. I thus upgraded the opto-mechanics by implementing a different design, which allows rotating the crystals from outside the chamber using small magnets positioned around the crystal mount inside the vacuum chamber and a rotating external ring with magnets.

3.4 Second CPA

The second CPA is made of a SF57 bulk stretcher in snooker design, a second AOPDF (Dazzler), a commercial Booster amplifier (from *Femtolasers*) and a home-made 2 pass power amplifier. Temporal compression is currently achieved using a transmission grating compressor and a set of chirped mirrors.

We used to have a combination of gratings and prisms, called a GRISM compressor, but we decided to remove the prisms and turn it into a traditional transmission grating compressor (see fig. 3.6) during my thesis, as will be detailed in this section.

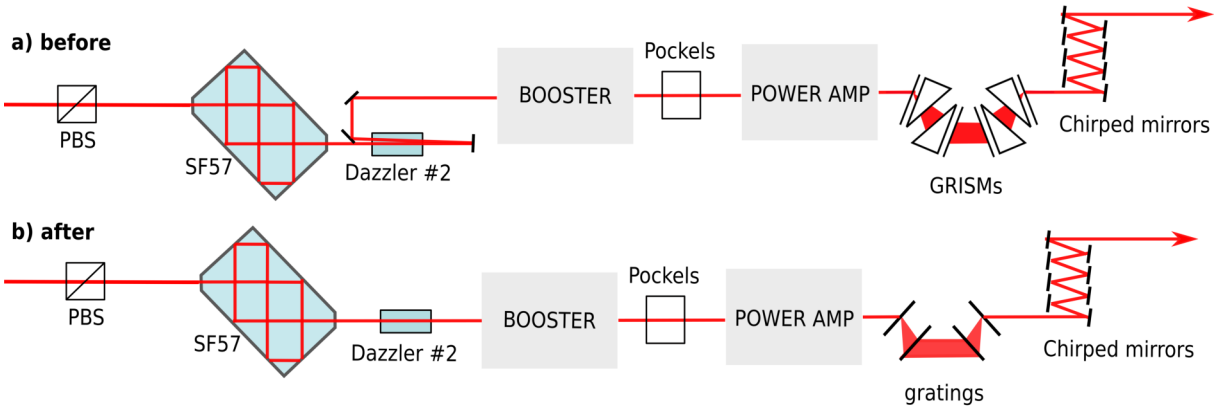

Figure 3.6: *Global architecture of the second CPA in Salle Noire 2.0. a) before b) after removal of the prisms.*

3.4.1 Stretcher

After the 6cm long polarizing beam splitter (PBS), the ≈ 20 mm diameter beam propagates through the stretcher, which is a 182.7 x 109.6 x 25 mm glass block (*Schott, SF57 ultra* from *Fichou*) used in snooker configuration with six total internal reflexions. Although the beam is already diverging at the output of the XPW filter, we added a diverging lens before the PBS (f=-700mm) in order to avoid damages inside the stretcher due to self focusing (see fig. 3.4). The propagation length through the stretcher is 75cm, which corresponds to a dispersion amount ≈ 168,000 fs^2 (see Table 1.1), thus stretching the pulses to ≈ 20ps. The transmission is 70 %.

Then, there is a pair of fused silica, AR coated lenses ($f = +300$ mm and $f = -75$ mm) to collimate the beam into a ≈ 1.8 mm beamsize at $1/e^2$ (and ≈ 750μm FWHM). This is followed by a second identical HR45 Dazzler (45mm TeO_2 crystal), which further stretches the pulses by adding ≈ 40,000 fs^2 and compensates for the third and fourth order dispersion mismatch between the stretcher and the compressor.

After the Dazzler, which changes the polarization to s when used in single-pass, we put a crossed periscope (to change the polarization back to p and elevate the beam to the appropriate height for the subsequent Booster amplifier) and a slightly converging lens (f=+3m) so as to obtain the right beamsize at the entrance of the Booster amplifier and on the Ti:Sa crystal.

3.4.2 Booster amplifier

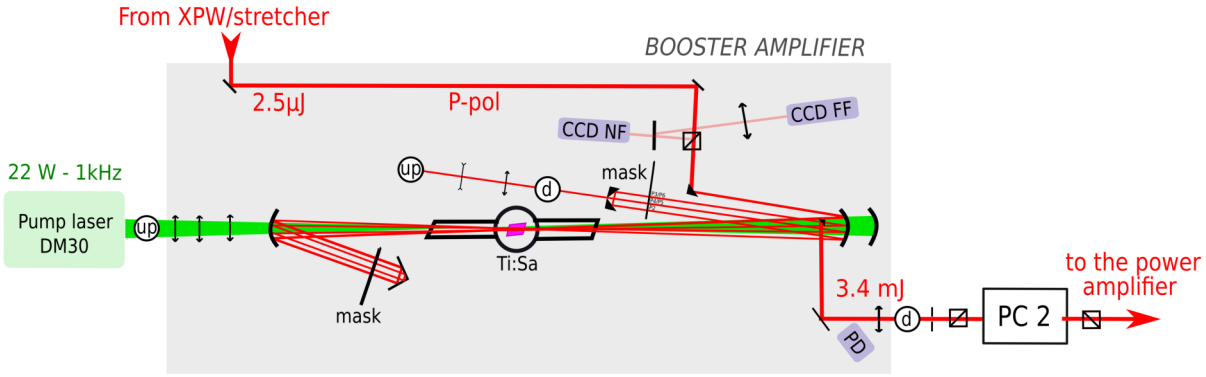

Figure 3.7: *Schematic drawing of the Booster*

The Booster amplifier is schematically represented in fig. 3.7. This amplifier is almost the same as the Femtopower, except there are only six passes. The Ti:Sa crystal has the same dimensions as in the Femtopower and is placed inside a similar small vacuum chamber.

The crystal is pumped by a commercial laser (*DM30, Photonics Industries*), which delivers 22mJ per pulse, with a pulse duration of 180ns, at 1 kHz repetition rate. The central wavelength is 527 nm and the emission is temporally synchronized with the seed using a delay generator (*Thales* Master Clock). The pump beam is focused using a triplet of lenses ($f_{cc} = +150$mm, $f_{cx} = -75$mm and $f_{cc} = +273$mm) so as to obtain a 800 μm diameter at $1/e^2$ (400 μm FWHM) on the crystal.

A polarizing beam splitter is placed at the entrance of the Booster to clean the polarization of the seed beam, while the leak (the light rejected by the PBS) is used for position (near field) and angle (far field) references. The two focusing confocal mirrors have a ROC of -800 and -600mm respectively. For the first pass, the beam diameter on the Booster crystal is $\approx 180\mu$m FWHM and 300μm at $1/e^2$, while the crystal is located $\approx$3 cm before the focal plane, with a beamsize in focus $\approx 160\mu$m at $1/e^2$. The size on crystal is increased after the fifth pass with a telescope to extract all the gain and saturate the amplifier, meaning that increasing the seed energy does not result in an increase of the output energy. We obtain 3.4mJ per pulse after amplification.

At the output of the amplifier, there is a second Pockels' cell placed between two crossed polarizer beam splitters, which rotates the polarization during a short time window. The purpose is to prevent back reflexions inside the power amplifier from propagating back to the Booster.

3.4.3 Power amplifier

The last amplifier, represented in fig. 3.8, is a two-pass, home-made amplifier. The pump laser (*DM50, Photonics Industries*) delivers 38mJ, 150ns pulses at 1 kHz repetition rate with a central wavelength of 527 nm. The pump beam is shaped with a pair of cylindrical lenses ($f = \pm 1$m) to make the beamprofile more circular in the crystal plane. Then it is focused with lenses into a $2w \approx 1100$ by 950 μm spot at $1/e^2$ (700μm FWHM).

The Ti:Sa crystal is slightly bigger (6 x 6 x 8mm) than in the previous two amplifiers and placed inside a similar vacuum chamber with temperature regulation. Bigger elliptical UVFS windows are also glued on both sides of the chamber, oriented downwards at Brewster angle to reject the p-polarized components.

The IR seed beam is focused approximately 15cm before the Ti:Sa crystal into a $2w = 215$ by 185 μm at $1/e^2$ spot, which corresponds to a beamsize on the crystal $2w = 820$ by 900 μm at $1/e^2$. For the second pass, we use a concave mirror (ROC=+1.4m) placed 835mm away from

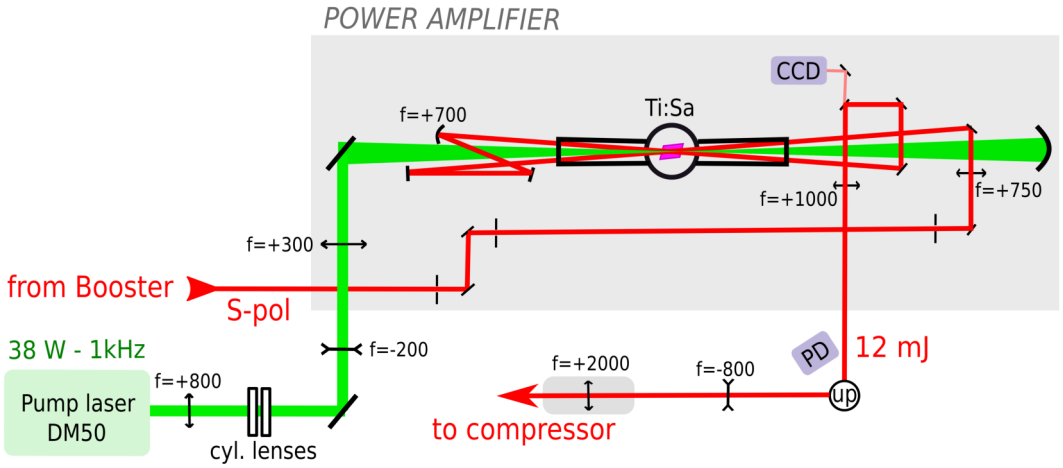

Figure 3.8: *Schematic drawing of the Power Amplifier.*

the crystal. The focal plane is located about 15cm after the crystal, and the beam diameter on the crystal is ≈1200 by 900 μm at $1/e^2$.

The amplifier delivers around 12mJ per pulse for this pump power setting. The output beam is collimated with a $f = 1$m convex lens, then expanded with a telescopic combination of two lenses (f=-800 and f=+2000 mm), with the last one placed on a translation stage for fine optimization of the beamprofile at the entrance of the post-compression hollow-core fibre.

3.4.4 Compressor

The initial compressor was a combination of 4 transmission gratings (*Ibsen*, fused silica substrate, groove density 1282 lines/mm, AR coated on the back side) and 4 prisms (SF57, α=43.5° apex angle, AR coated on both faces), called GRISM, which was designed by *Fastlite* [90].

It had been chosen over a traditional grating compressor because of its ability to compensate for both second and third order dispersion introduced by SF57 bulk stretchers, while maintaining a small footprint for more efficient CEP stabilisation [136, 219]. Indeed, contrary to transmission grating compressors introducing negative GDD and positive TOD, the GRISM can introduce both second and third order negative dispersion. Therefore, the AOPDF does not need to compensate for TOD (only FOD) and we can increase the stretching ratio by using the AOPDF at its maximum capacity. The advantage is that it reduces the nonlinear effects in the amplifiers.

The settings of the GRISM were chosen so as to leave a residual GDD of +2,000fs^2 at the output, which is compensated for a little bit further, using chirped mirrors placed inside a vacuum chamber.

However, we decided to remove the prisms and change it into a traditional 4 transmission grating compressor.

3.4.5 From GRISM to gratings compressor

Motivations behind this modification

The first reason is that there were high losses from the many reflexions on the prisms. Then, the prisms introduced a thermal lens, as well as some B-integral, which had the effect of distorting the spatial profile of the beam at the entrance of the hollow-core fiber used for post-compression. Any change in alignment at the input induced some drastic changes in the beamprofile and we often had to optimize it by slightly tilting the last prism, which made the

laser output vary quite a lot from day-to-day. The wavefront of the laser beam before and after the GRISM had even been characterized by [25] (p.51), and the measured rms value of wavefront aberrations was three times higher at the output. Last but not least, we had to wait everyday for about half an hour for the prisms to thermalize after aligning the laser, otherwise the beamsize would slowly vary at the fiber entrance and damage it.

Dispersion introduced by the different elements in the second CPA

In the initial configuration, the total amount of GDD, TOD and FOD accumulated from the entrance of the XPW filter, where the pulses are temporally compressed, to the chirped mirrors can be estimated using values in Table. 1.1. This is summarized in figure 3.9.

The total dispersion is approximately $\Phi_{2,\text{tot}} \approx 254,300\text{fs}^2$, $\Phi_{3,\text{tot}} \approx 72,100\text{fs}^3$ and $\Phi_{4,\text{tot}} \approx 2,137,400\text{fs}^4$, which is very close to what was compensated for by the GRISM (see fig. 3.9), as had been calculated in [24]. The remaining difference can be explained by the fact that we neglected the Pockels cell material, the lenses, the BaF_2 crystals, the fused silica windows, air and dispersion from the mirrors...

		polarizer	stretcher SF57	Dazzler #2			Ti:Sa	GRISMs L=62.82mm	gratings L=50mm	8xCM HD58
				TeO_2	polynomial	phase.txt				
length (mm)		60	750	45 / 90			64			
before	GDD (fs^2)	**4,500**	**168,000**	**44,800**	**34,200**	**3,000**	**1,800**	**-255,953**		**-2,000**
	TOD (fs^3)	3,200	106,000	29,200	-70,000	3,000	2,700	-76,330		
	FOD (fs^4)	-2,600	38,000	17,000	2,200,000	-112,000	-1,000	-2,193,341		
after	GDD (fs^2)	**4,500**	**168,000**	**22,400**	**17,000**	**68**	**1,800**		**-236,000**	**-2,000**
	TOD (fs^3)	3,200	106,000	14,600	-656,000	-21,319	2,700		514,000	
	FOD (fs^4)	-2,600	38,000	8,500	670,000	-392,940	-1,000		-1,777,000	

Figure 3.9: *GDD, TOD and FOD introduced by the different elements in the second CPA, before and after removal of the prisms.*

Dispersion introduced by the gratings compressor and conclusion for the prisms removal

The purpose of the prisms was to reduce the amount of TOD that the Dazzler had to compensate for. In order to verify how much could be compensated for by the Dazzler when removing the prisms, we estimated the 2nd, 3rd and 4th order dispersion introduced by the two pairs of transmission gratings alone (see 1.5.4).

For the initial gratings spacing (L=62.82mm), we found that the gratings alone would result in higher absolute dispersion amounts than the AOPDF could compensate for. Indeed, the Dazzler capabilities are limited by the length of the TeO_2 crystal, and when we tried to change the polynomial settings on the software so as to compensate for the dispersion that would be introduced in that case, we obtained an acoustic waveform that was too long and thus truncated.

Instead, we found that L≈50mm would be the maximum acceptable. The GDD, TOD and FOD calculations (by making a polynomial fit of the spectral phase and using analytical formulas for GDD and TOD, see 1.5.4) for L=50mm are represented in fig. 3.10. We estimated the dispersion to be: GDD ≈ -236,000 fs^2, TOD ≈ +514,000 fs^3, and FOD ≈ -1,777,000 fs^4.

Due to the big difference in the GDD to TOD ratio that we needed to compensate for, compared to the GRISM configuration, the acoustic waveform sent into the Dazzler crystal was modified a lot (fig. 3.11), resulting in a much lower diffraction efficiency. Thus, we had to use it in single pass instead of double pass.

We first set the Dazzler polynomial settings according to our calculation, seeded the amplifiers and the hollow-core fiber, and then we finely optimized the settings by making a plasma in air and a duration measurement (Wizzler, see further). The final results after optimization

are summarized in fig. 3.9. The second and third order positive values correspond very well to the negative ones, however the experimentally determined optimum for fourth order is very different from what we expected from the gratings' dispersion calculation.

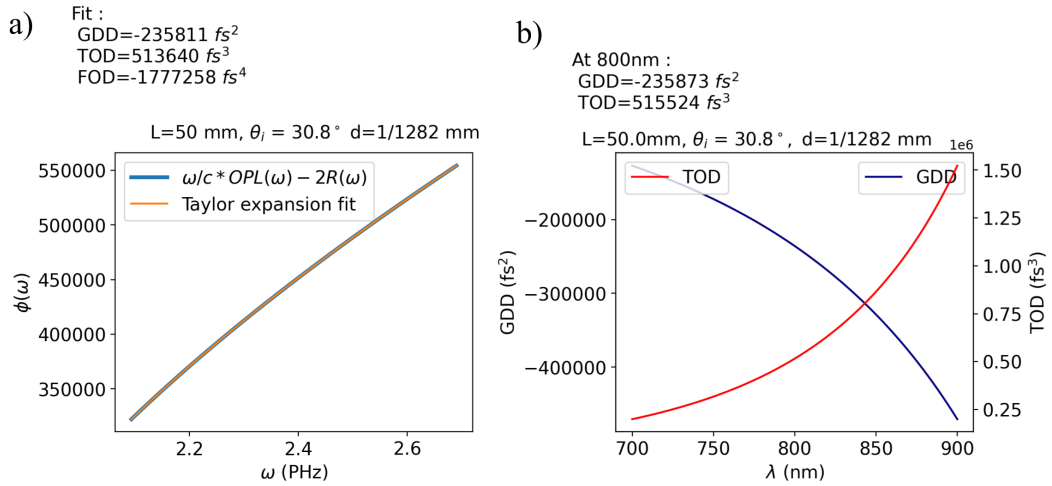

Figure 3.10: *a) Spectral phase (eq. 1.66) as a function of the frequency and curve fitting with a 5th order Taylor series expansion. b) GDD and TOD curves according to the analytical formulas in Eqs. 1.67 and 1.68.*

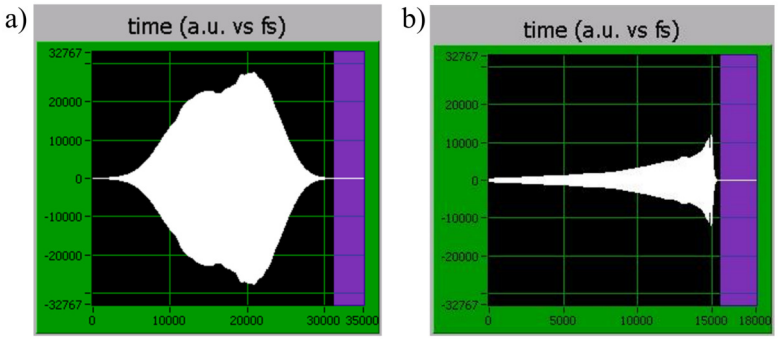

Figure 3.11: *Screenshot of the Dazzler software showing the simulated optical impulse time response of the filter (in fs) with a) the GRISM and b) the grating compressor.*

Outcome

Removing the prisms increased the compressor transmission from 77% to 85% and we typically obtain a pulse energy of 9 to 10 mJ after the grating compressor. Temporal contrast measurements revealed a massive temporally-stretched prepulse, which we found was coming from the direct transmission of the first grating. It was eliminated by simply adding beam-blockers for all the transmitted and reflected beams from the four different gratings. Removing the prisms also modified the beamsize (there was a thermal lens coming from the prisms) at the entrance of the HCF and we had to adapt the lenses at the output of the power amplifier as well as the distances between the concave and convex mirrors used to focus the beam into the hollow-core fiber. The spatial quality of the beam improved a lot on average: whereas we used to have to spend time tweaking the GRISM in order to get a nice beamprofile at the fiber entrance, we now have a very reproducible beam without doing anything from day to day. Another advantage, which we expected, is that we can now seed the HCF immediately after seeding the second CPA. The only waiting time that remains when turning on the laser system is for the thermalization of the different amplifiers after switching on the pump lasers and the chillers (about 30min).

3.5 Post-compression

The output pulses of the double CPA system have a 24 to 30fs duration, which corresponds to approximately 10 optical cycles at 800nm. Therefore, in order to reach the single-cycle regime, we need to shorten the duration by adding new spectral components in phase. This is what we call "post-compression". Many techniques exist and a complete review can be found in [185]. In *Salle Noire 2*, spectral broadening is achieved through Self Phase Modulation in a stretched-flexible hollow-core fiber filled with helium gas [193, 228]. This technique, which is the workhorse of most ultrafast optics labs for post-compression, has the advantage of preserving the high contrast ratio and the CEP stability [162] of the pulses while cleaning the beamprofile, which is of critical importance for our applications to plasma mirrors. Stretched-flexible hollow-core fibers (SF-HCFs) [184] were patented by Tamas Nagy and Peter Simon from the *Institute for Nanophotonics* in Göttingen and are commercially available through the company *Ultrafast Innovations*, but similar fibers can now also be purchased from *Few Cycle Inc*, for example.

The post-compression stage was implemented by Frederik Böhle [25] before I arrived, and only a few changes were made during my thesis (mostly adding an extension to increase the beamsize on the output mirror), which will be described here.

3.5.1 Power scaling laws

The mathematical description of spectral broadening in hollow-core fibers was done in 1.4.3. However, we did not consider the transverse spatial evolution of the beam, but of course the Kerr effect also translates into a spatially dependent refractive index, and thus self focusing. When scaling this post-compression scheme for higher powers, one must carefully determine the fiber dimensions and the type of nonlinear material in order to avoid ionization and self-focusing [263], which can be detrimental for the beam coupling into the fiber and the temporal coherence of the pulse.

In fact, ionization can also induce spectral broadening: under the pulse envelope, the electronic density increases, therefore the induced variations of the instantaneous frequency are always positive, corresponding to the generation of new high frequencies. This effect is called plasma blue shift and is sometimes desirable but makes the pulse temporal compression more difficult. We thus seek to avoid photo-ionization and remain below the intensity threshold I_{th}. For a given laser power P, this sets a lower limit for the effective beam area A_{eff} in the fiber:

$$P/I_{\text{th}} \leq A_{\text{eff}},$$

meaning that we have to use a fiber whose inner diameter is large. Then, self-focusing is avoided when the power is below the critical power

$$P_{\text{cr}} = \frac{\lambda^2}{2\pi n_2}. \tag{3.2}$$

Now that we have set the beam area, this means that the intensity must remain lower than $P_{\text{cr}}/A_{\text{eff}}$, which limits the B integral to:

$$B \leq \lambda \frac{L_{\text{eff}}}{A_{\text{eff}}}. \tag{3.3}$$

Thus, the only way to power-scale a HCF-based post-compression stage is to use long fiber lengths L_{eff} and large inner diameters.

Regarding the nonlinear medium, it is preferable to use a gas with a low nonlinear refractive index n_2 in order to increase the critical power threshold, whereas ionization can be avoided

by choosing a material with a high ionization intensity threshold. We use helium, which has a higher ionization threshold ($I_{\mathrm{BSI}} = 8.27 \times 10^{17}\mathrm{W.cm}^{-2}$), as well as a lower nonlinear index ($n_2 \approx 4.2 \times 10^{21}\mathrm{cm}^2.\mathrm{W}^{-1}$ [151]) compared to argon and neon.

Additional tricks

There are two additional tricks that we use, which help increasing the stability. The first is to change the laser polarization to circular before going into the fiber [50, 103]. This way, the laser electric field amplitude is divided by $\sqrt{2}$ and the ionization yield is reduced by one order of magnitude while the nonlinear refractive index n_2 is only reduced by a factor 2/3 [168], *ie* $n_2^{circ} = 2/3 n_2^{lin}$. It also leads to a more defined mode beating, and therefore to a more stable broadening [170].

The second trick consists in using a pressure gradient [238], where the pressure at the fiber entrance is close to 0 mbar and the pressure at the output around 1 bar (see eq. 3.8). Gas continuously flows through the fiber and is pumped at the entrance, therefore establishing a stable pressure gradient along the waveguide. The point is to avoid ionization or self-focusing induced distortions of the input beam and ensure a more efficient coupling into the fiber. The downside is that the effective interaction length L_{eff} is reduced by 33%, thus to compensate for the decrease in B integral, the HCF length or the gas pressure at the output needs to be increased [26].

3.5.2 Experimental setup

Hollow-core fibre

The post-compression stage is detailed in figure 3.12. After the gratings compressor, the 9 to 10 mJ, 30fs pulses are not perfectly compressed yet. A crossed periscope sends the beam into a vacuum chamber through a thin transparent window for final temporal compression using a set of 8 chirped mirrors (*HD58, Ultrafast Innovation*), introducing a GDD ≈ -250 fs^2 per mirror *ie* -2000 fs^2 in total. Then, there is an ultra-broadband quarter wave plate (*Bernhard Halle*) that changes the polarization to circular, followed by a telescopic arrangement of a concave and a convex mirror. The concave mirror (f_{cc}=1.25m) is placed d_{cc-cx}=55 cm before the convex mirror (f_{cx}=-1m), which corresponds to an effective focal length:

$$\mathrm{EFL} = \frac{f_{cc} f_{cx}}{f_{cc} + f_{cx} - d_{cc-cx}} = \frac{1.25 \times -1}{1.25 - 1 - 0.55} \approx 4.2\mathrm{m}. \tag{3.4}$$

With a $w_0 = 6.9$ mm beam radius at $1/e^2$ entering the chamber, in theory this corresponds to a focused beam of radius:

$$w_f = \frac{\lambda_0 \mathrm{EFL}}{\pi w_0} \approx 160\mu\mathrm{m}. \tag{3.5}$$

The angles of incidence on the curved mirrors θ_{cc} and θ_{cx} are chosen so that the tangential and saggital focal lengths (see fig. 3.13.a.) are equal, in order to minimize astigmatism (these are sometimes called "magic angles"). Let us consider a curved mirror with a focal length f. The focal lengths in the tangential plane (plane of incidence) and in the saggital plane depend on the angle of incidence θ on the mirror as follows:

$$f_{tan} = f\cos\theta \text{ and } f_{sag} = \frac{f}{\cos\theta} \tag{3.6}$$

Therefore θ_{cc} and θ_{cx} can be chosen by solving the equation:

$$EFL_{tan} - EFL_{sag} = 0. \tag{3.7}$$

The results are displayed in fig. 3.13.b.

Between the convex mirror and the HCF entrance, there is a 1 inch diameter, plane, dielectric mirror at 0° (from *Manx Precision Optics*). The distance from the convex mirror to this plane

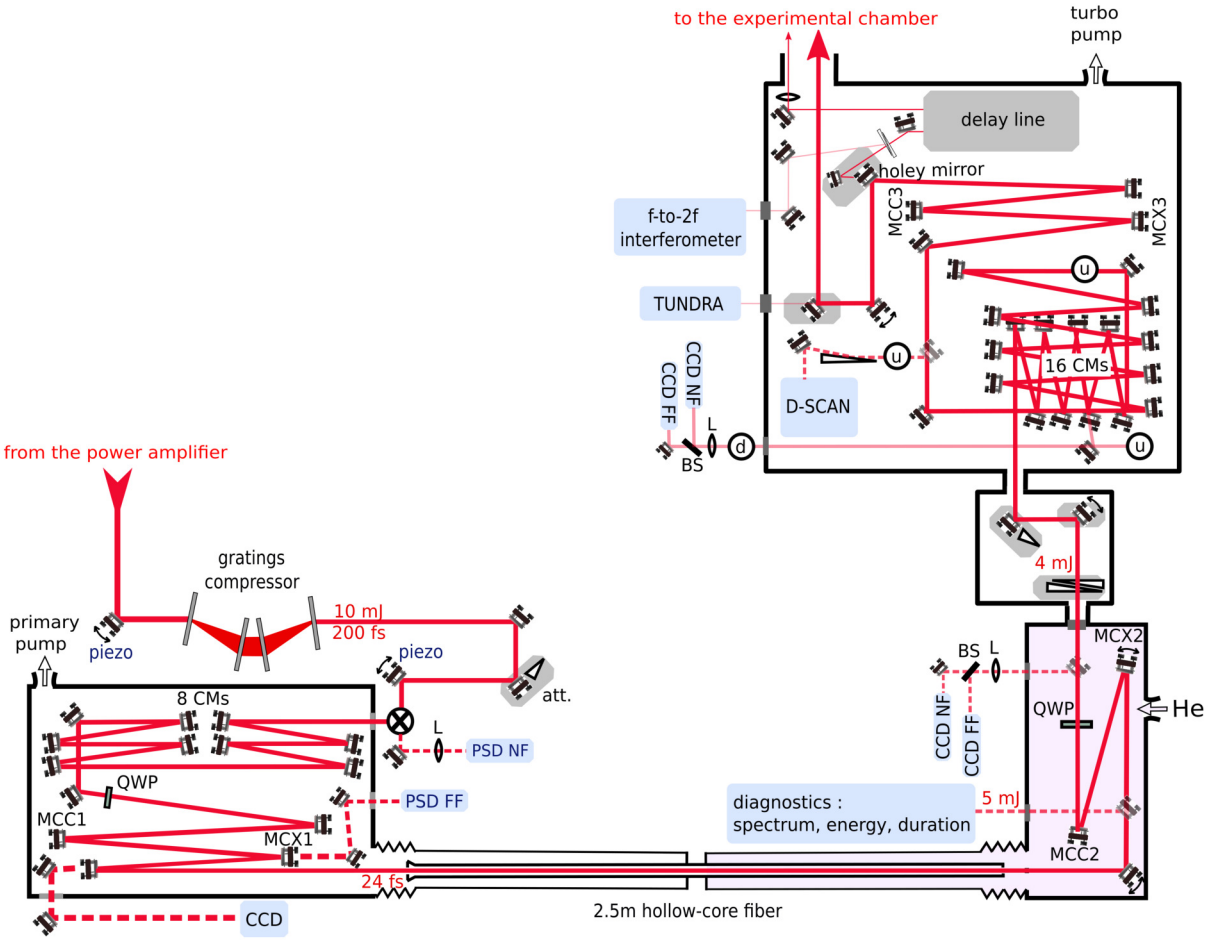

Figure 3.12: *att: half silver-coated, half un-coated wedge on a translation stage, MCC1 (ROC=2.5m), MCX1 (ROC=-2m), MCX2 (ROC=-1m), MCC2 (ROC=+2m), MCX3 (ROC=-1.7m), MCC3 (ROC=3m).*

mirror is $d_{cx-M} \approx 80$ cm, and then the distance from the plane mirror to the HCF entrance is $d_{M-HCF} \approx 113$ cm. The beamsize at the HCF entrance is verified by sending a leak of the last zero degree dielectric mirror out on a camera placed at the same distance from the mirror as the fiber entrance (an example of beamprofile is shown in fig 3.13.c). The ideal beamsize to seed the hollow-core fibre corresponds to $0.64 \times ID$ (see subsection 1.3.4), *ie* $2w_0 \approx 343\mu$m for our 536 μm inner diameter.

A fast beam stabilizer (*TEM Messtechnik Aligna*) is used to compensate for the beam pointing instabilities and ensure long-term operation of the laser. The Near Field (position) reference corresponds to the image of the periscope's lower mirror on a photosensitive detector (PSD), whereas the Far Field (angle) reference is taken as the focal spot of the leak through the convex mirror, sent outside the chamber through a transparent window onto a second PSD (fig. 3.12). To further prevent the laser from damaging the fibre, a conical glass taper is coaxially installed at the entrance.

The helium gas is introduced and regulated with a solenoid control valve in the chamber located at the exit of the fiber, whereas the incoupling chamber is continuously pumped with a primary vacuum pump. The first mirror in the output chamber is a plane protected silver mirror (EKSMA) at 45° and is located 1.65m away from the fibre exit. The beam is recollimated with a convex ($ROC = -1m$) and a concave mirror ($ROC = +2m$), while the polarization is changed back to linear (p) with a second quarter wave plate, identical to the one used in the incoupling chamber for making the polarization circular.

Additionally, two insertable mirrors are used to send the beam outside of the chamber for

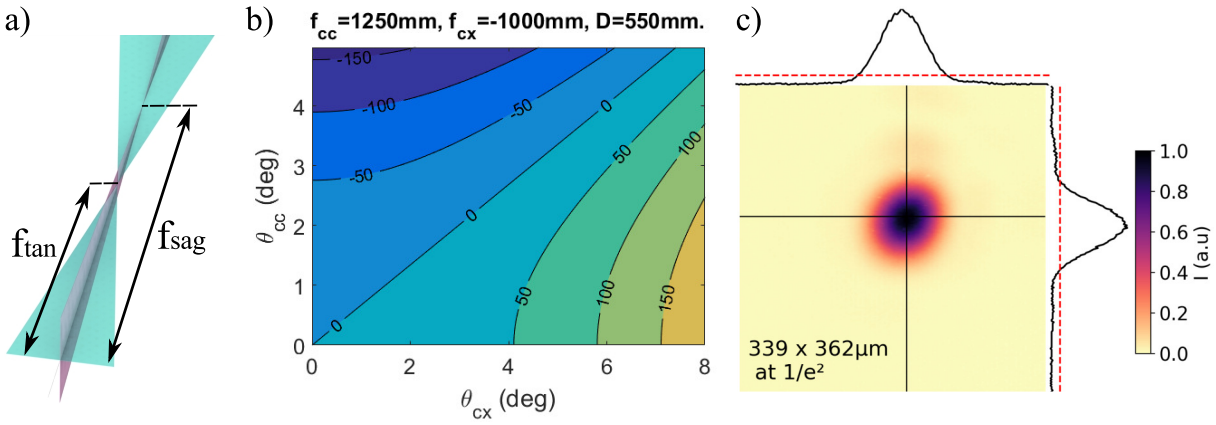

Figure 3.13: *a) Illustration of the tangential and the saggital focal length. b) Plot showing the values of $EFL_{tan} - EFL_{sag}$ depending on the angles of incidence of the focusing telescope mirrors before the hollow-core fiber, made with a Matlab script written by Stefan Haessler. The solutions of equation 3.7 correspond to the line marked as 0. c) Typical beamprofile at the HCF entrance. The red dashed lines show the 13.5 % signal level.*

diagnostics, through transparent windows. The first output is used to optimize the beamprofile, by tweaking the fiber entrance manually, and to measure the pulse energy. It is also used to measure the pulse duration by making a Wizzler measurement (with the fiber completely under vacuum, and the beam attenuated), which is minimized via a Wizzler/Dazzler feedback loop (see subsection 4.1.1). The second output serves as position and angle references for the beam: the NF camera images the plane of MCX2, whereas the far field looks at the beam focus.

The pulse to pulse energy stability measured after the fiber (fig. 3.14) is the same as before the fiber, ≈0.4 % rms and 4% peak-to-peak, measured over five minutes. Then, the beam exits this gas-filled output chamber through a transparent window to enter the subsequent vacuum beamline.

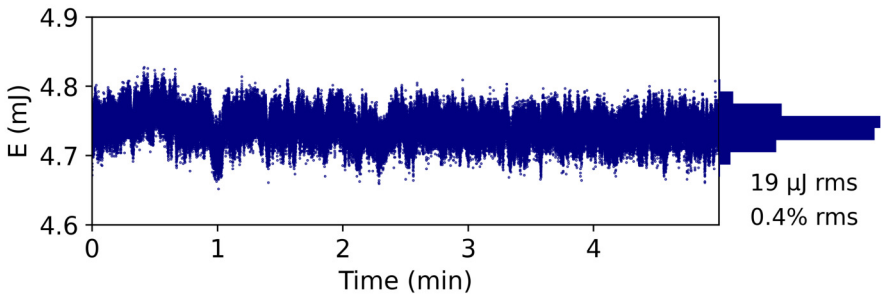

Figure 3.14: *Shot-to-shot energy measurement (left), measured at the output of the hollow-core fibre and histogram (right) with a Gentec energy-meter.*

Compression with chirped mirrors

The dispersion introduced by the helium gas, the output window and the quarter wave plate, but also by SPM and SS, needs to be compensated for in order to re-compress the pulses temporally. For that, we have a set of 16, 1.5 inch diameter chirped mirrors (*PC70, Ultrafast Innovations*), installed on two layers inside the compression chamber (see fig. 3.12). Each pair compensates for 40 fs^2, so the full set introduces -320fs^2 in total. They are designed to be used in pairs, at two different angles of incidence (5 and 19 °), so as to compensate for the introduced spectral phase oscillations, which are inherent to their production. The chirped

mirrors' reflectivity is >99% per bounce for the specified bandwidth (500-1050 nm).

The number of chirped mirrors was chosen to slightly over-compensate for the positive GDD and a pair of motorized fused silica wedges is used to perfectly compress the pulses. This pair of wedges is also used to measure the pulse duration by making a dispersion scan (d-scan, see subsection 4.1.1).

3.5.3 Tunable duration

A very nice advantage of this post-compression setup is that the duration can be tuned from 30fs to 3.5fs by varying the gas pressure, without any change in the output power. The output spectrum was recorded and the pulse duration was measured using a d-scan device (see section 4.1.1) for different gas pressures at the fiber exit.

The spectral bandwidth, defined as twice the rms bandwidth (eq. 1.56) obtained from the experimentally measured spectra, was compared to the width predicted by numerically solving the one-dimensional nonlinear Schrodinger equation for Kerr nonlinearity (eq. 1.48), which accurately reproduced the measurements (fig. 3.15.b, c, d and e).

In the simulations, the pressure gradient along the HCF was modeled as

$$p(z) = p_L\sqrt{z/L}, \tag{3.8}$$

with p_L the pressure at the exit (located at $z = L = 2.5$ m), which is displayed on along the x-axis of fig.3.15. a and b.

The output energy was also experimentally measured for different gas pressures, and compared to the output energy measured with chirped pulses, by adding +275 fs^2 with the second AOPDF (fig. 3.15.a), so as to keep the laser intensity well below the ionization threshold. We found that the energy is constant over the whole pressure range, except for 1.2 bar and more, in the case of compressed pulses, where we start seeing a slight energy drop, probably due to ionization. This indicates that our setup was correctly scaled for our laser power. Usually, at P=1.1bar, we already routinely obtain a 4 or sub-4 fs pulse duration, thus the effect of ionization is negligible.

Finally, the duration can even be increased up to a few picoseconds using the second AOPF (see fig. 3.1, Dazzler number 2), so that our laser source is tunable over a very broad range of pulse durations.

3.5.4 Extension

Fluence on the mirror at the output of the HCF

A serious issue that we faced was the high fluence on the first mirror after the HCF. There are currently no dielectric mirrors with a bandwidth broad enough to support our sub-4 fs pulses, therefore we use a metallic, enhanced silver mirror (from *EKSMA*). The specified laser-induced damage threshold (LIDT) is > 0.21 J.cm^{-2} at 800nm for 50fs pulses, whereas our peak fluence is estimated as

$$F_{peak} = \frac{2E}{\pi w_M^2} \approx \frac{2 \times 0.006[\mathrm{J}]}{\pi 0.21[\mathrm{cm}]^2} \approx 0.09\mathrm{J.cm}^{-2},$$

where 0.21cm is the experimentally measured beam radius at $1/e^2$. This corresponds to 43% of the specified damage threshold, but clearly it was too much because we very frequently damaged those mirrors (once a week). As the beam diverges after the HCF, the simplest solution was to increase the propagation length from the fiber exit to this mirror, which meant adding a little extension to the vacuum-integrated setup.

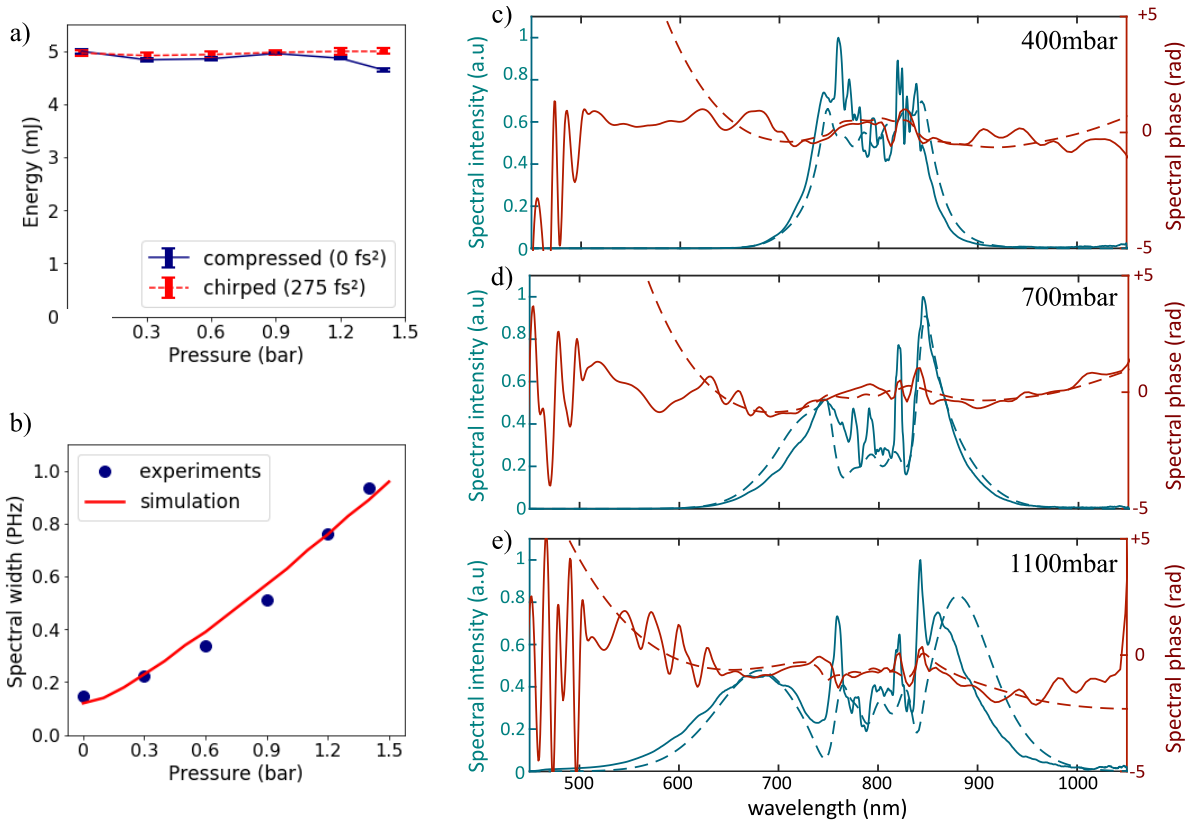

Figure 3.15: *a) Energy at the output of the HCF for different pressure values, in the case of chirped (red) and compressed (blue) pulses. b) Measured (blue dots) and simulated (red line) RMS spectral bandwidths. Panels (c), (d) and (e) show the spectral phase (red) and intensity (blue) for three different gas pressures at the fiber output, which give, respectively, compressed pulse durations of 9 fs, 6 fs, and 4 fs. The solid lines correspond to the experimentally measured data with the d-scan while the dashed lines correspond to simulated data. Subfigures (c), (d) and (e) were made by Stefan Haessler.*

Determination of the right focal lengths for re-collimating the beam after the HCF

The maximum distance from the fiber exit to the mirror, with the extension, is ≈3.5m, simply determined by the size of the room in which the laser system is. In order to find the right combination of convex and concave mirrors to re-collimate the beam after the hollow-core fiber while keeping the same output beam size (*ie* a ≈7mm beam waist), it is very convenient to use matrix optics. Let h_i be the initial beam radius at $1/e^2$ and θ_i the initial beam divergence. The ray transfer matrix for free space propagation over a distance L is:

$$P(L) = \begin{pmatrix} 1 & L \\ 0 & 1 \end{pmatrix}, \tag{3.9}$$

and the ray transfer matrix corresponding to a lens with focal length f is:

$$M(f) = \begin{pmatrix} 1 & 0 \\ -1/f & 1 \end{pmatrix}. \tag{3.10}$$

The initial beam waist, at the exit of the HCF, is determined by the inner diameter of the fiber $h_i = 0.343/2$mm. The theoretical divergence (at a distance much greater than the Rayleigh length) is ≈ 1.48mrad, but we also verified the actual beam divergence by imaging the plane of the first mirror after the HCF on a CCD camera and found $\theta_i \approx 1.17$mrad with 1.5bar of He in the output chamber and 1.39mrad in the absence of gas.

The distance from the HCF exit to first mirror MCC2 $d_{HCF-cc2}$ is determined by the position of the new chamber and must be around 3500 mm (see fig. 3.16). The third mirror MCX2 should ideally remain at the same position (*ie* as far as possible from the second plane mirror at 45°) in order to minimize the incidence angle: $d_{cc2-cx2} \approx 550$ mm, and the same argument yields $d_{cx2-cc3} \approx 550$mm as well.

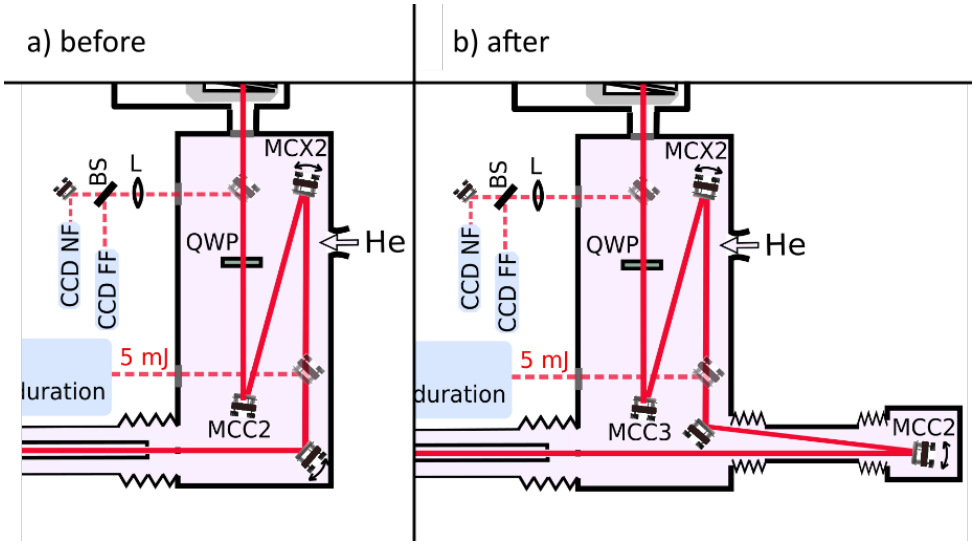

Figure 3.16: *HCF setup before (a) and after (b) adding the extension. a) MCX2 (ROC=-1m), MCC2 (ROC=2m). b) after: MCC2 (ROC=7m), MCX2 (ROC=-2m), MCC3 (ROC=3m)*

The beam after these three mirrors $\begin{pmatrix} h_f \\ \theta_f \end{pmatrix}$ can be evaluated for different ROCs for the three mirrors using the equation:

$$\begin{pmatrix} h_f \\ \theta_f \end{pmatrix} = M(f_{cc3}) \times P(d_{cx2-cc3}) \times M(f_{cx2}) \times P(d_{cc2-cx2}) \times M(f_{cc2}) \times P(d_{HCF-cc2}) \times \begin{pmatrix} h_i \\ \theta_i \end{pmatrix}.$$

We tried different mirror focal lengths and verified the beam size and collimation at the output of the chamber using this equation. Eventually, we converged towards the solution presented in fig. 3.16.b.

3.6 Future laser developments and perspectives

I will present here the next upgrades planned in *Salle Noire 2* and potential ways to further improve its performance.

3.6.1 Post-compression: HCF entrance shift

Regarding the post-compression stage, now that we have fixed the issue of the fluence on the output mirror, the input mirror has become the weak element and we are thinking of shifting the fiber entrance by 50cm so as to balance the constraints.

Flux on the input mirror

Let us first estimate the flux on the last plane mirror before the HCF. We verified the beamsize at the entrance of the vacuum chamber by imaging the plane of the lower mirror of the crossed periscope sending the beam into that chamber on a CCD camera. We measured a beam radius w_0 of 6.9mm at $1/e^2$ (and 4.2mm FWHM). The beamsize on the last zero degree plane mirror before the HCF w_M can be calculated as follows (see fig. 3.17 for the notations):

$$w_M = \frac{d_{M-HCF}}{EFL} \times w_0 \approx \frac{1.13[\text{m}]}{4.2[\text{m}]} \times 6.9[\text{mm}] \approx 1.9\text{mm}. \tag{3.11}$$

Therefore, with about 11 mJ per pulse, assuming a Gaussian profile, the peak fluence is

$$F_{peak} = \frac{2E}{\pi w_M^2} \approx \frac{2 \times 0.011[\text{J}]}{\pi 0.19[\text{cm}]^2} \approx 0.19\text{J.cm}^{-2}. \tag{3.12}$$

The manufacturer estimates the LIDT of our mirror (from *Manx Precision Optics*) to be about 0.45 J.cm^{-2} for a 30 fs pulse. The peak fluence is only about **42%** of this threshold but we still observe regular damages or pollution, which could be due to imperfect spatial intensity distribution in the beam, or errors in the estimation of the LIDT itself.

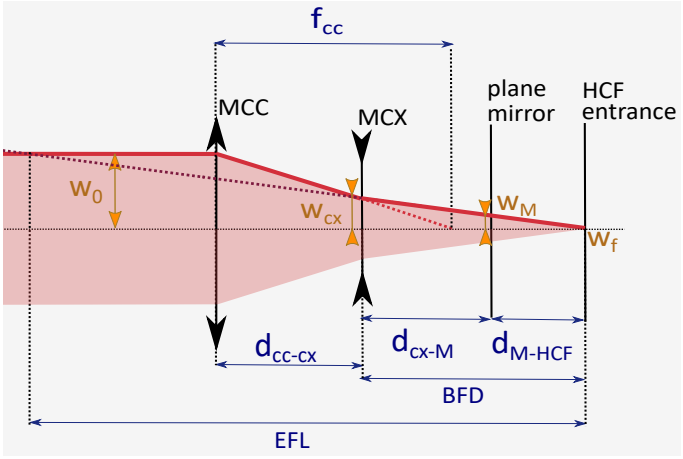

Figure 3.17: *Schematic drawing showing the relations between the effective focal length (EFL), the Back Focal Distance (BFD), the concave and convex mirrors focal lengths and the distances.*

Flux on the output mirror

This is to be compared with the flux on the output mirror. With the extension, the HCF exit is currently 3.5m away from the output mirror and the pulse energy is approximately 6 mJ. The pulse duration should not be less than 30 fs, even in the case of high pressure, precisely because of the dispersion introduced by the gas and SPM.

We consider the beam radius at $1/e^2$ at the exit of the HCF to be $\approx 171.5\mu$m and we use the average measured beam divergence previously determined $\theta \approx 1.28$mrad. Thus, the beam waist on the first mirror after the HCF is $w(3.5\text{m}) \approx \theta_i \times 3.5\text{m} \approx 4.48$mm and the peak fluence is

$$F_{peak} = \frac{2E}{\pi w_M^2} \approx \frac{2 \times 0.006[\text{J}]}{\pi 0.45[\text{cm}]^2} \approx 0.02\text{J.cm}^{-2}.$$

This is only **10%** of the specified LIDT of our silver mirrors (0.21J.cm^{-2}). Therefore, it is clear that shifting the fiber towards the output chamber would be beneficial.

Suggested choice of optics for the modification

Without changing too many things (we do not want to replace or remove any of the chambers located at the output of the HCF), the maximum possible shift of the fiber is approximately 90cm. Indeed, there is 135cm from the HCF exit to the entrance of the first chamber, but we need to leave some space $\approx$ 40cm for mechanical components. Another limitation comes from the dimensions of the incoupling chamber: it is 100cm long and 55cm large, thus the maximum distance d_{cc-cx} between MCC and MCX, and d_{cx-M} between MCX and M is $\approx$ 80cm (space is needed to pick off the leaks for references). Moreover, the effective focal length should remain the same as we want to change the beamsize neither at the entrance of the incoupling chamber nor at the fiber entrance.

Trying different focal lengths and distances while remaining within these limits, I converged towards the solution shown in fig. 3.18: f_{cc}=2.25m, d_{cc-cx}=67cm, f_{cx}=-3.5m, d_{cx-M}=80cm and d_{M-HCF}=207cm, corresponding to a fiber shift of 52cm and an effective focal length of 4.1m. This will result in a beam radius of 3.5mm (using eq. 3.11) on the last zero degree plane mirror before the HCF, therefore a peak fluence of 0.06J.cm^{-2} or **13%** of the LIDT.

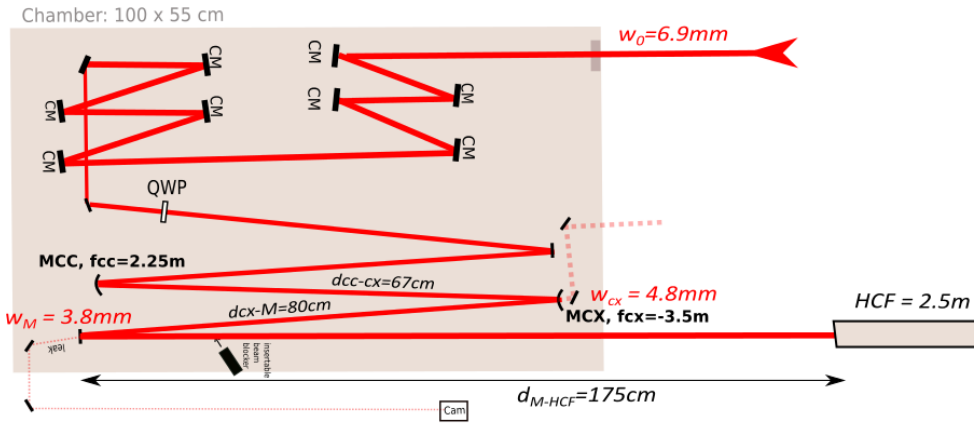

Figure 3.18: *Proposed future configuration for the post-compression setup near the fiber entrance.*

The resulting propagation distance from the HCF exit to the first mirror would be decreased to 298cm. Thus, the beam waist on the mirror (assuming it will remain at its current position) would be 3.8mm, resulting in a peak fluence $\approx 0.03\text{J.cm}^{-2}$ *ie* **14%** of the LIDT. This situation seems ideal, as we would be equally far from the LIDT on both sides of the fiber.

A new configuration for the beam re-collimation at the output can be determined using matrix propagation as previously described. For example, one could use a concave mirror f=+3m

placed 300cm away from the HCF, then a convex mirror f=-75cm placed 2.4m from the first mirror, and finally a f=+1.25m concave mirror 50cm further (see fig. 3.19). This should result in a collimated beam with a 6.4mm waist at the output of the chamber, *ie* no change compared to the current situation.

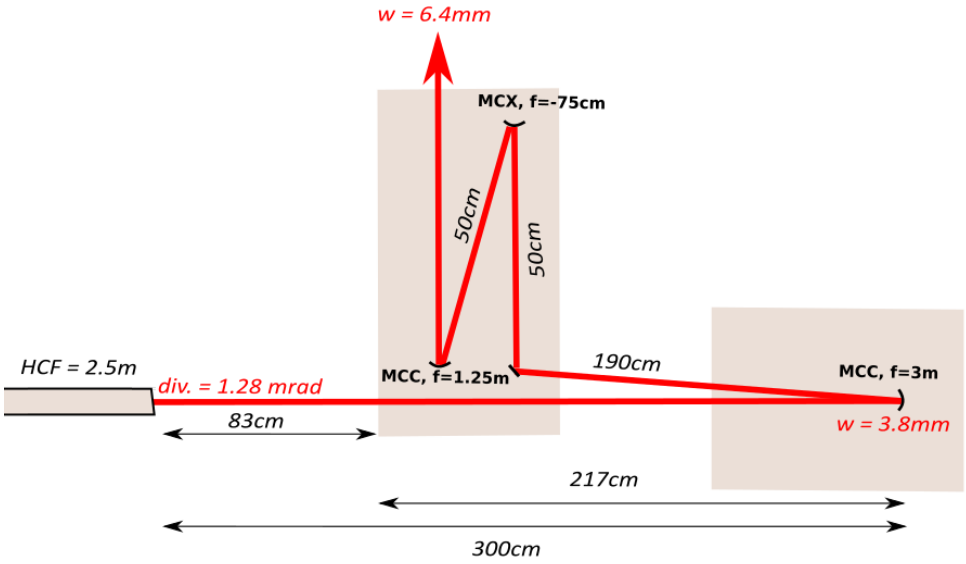

Figure 3.19: *Proposed future configuration for the post-compression setup near the fiber exit.*

Alternatively, very recently, ion beam sputtered dielectric ultrafast mirrors with a 0.8J.cm^{-2} LIDT were reported [272], which are compatible with our bandwidth. This would already help relaxing the constraint on the input mirror.

3.6.2 Cryo-cooled amplifier

In order to increase the laser stability, the two amplifiers in the second CPA of *Salle Noire 2* are going to be replaced with a single, cryo-cooled (T≈140 Kelvin) multipass amplification stage. We have already received the chamber and the ion-getter vacuum pump (capable of reaching a pressure of the order of 10^{-7} mbar), and started developing it. The goal is to obtain ≈ 12mJ in 6 passes.

In a Ti:Sa amplifier, roughly one third of the pump power is converted into heat. The heat load creates very strong temperature gradients inside the crystal that distort the amplified pulses (see subsection 1.5.1). The benefits of cryo-cooling and low temperatures in general are huge: it increases the spatial beamprofile quality, the thermal conductivity and the quantum efficiency *ie* the absorption of the pump energy by the crystal. It also reduces the thermal lens, making the design of the amplifier much easier. We can naturally expect the energy and the CEP stability to improve by reducing the crystal's temperature.

Chapter 4

Characterization of the laser and CEP control

"Perfect is the enemy of good.".
Voltaire

This chapter focuses on the spatio-temporal characterization of the pulses, the stabilization of their carrier-envelope phase (CEP), and their validation through the first observations of CEP effects in laser wakefield electron acceleration. Compared to previous work in *Salle Noire 2*, new diagnostics were used (XPW dscan, Tundra autocorrelator, TERMITES) and a good residual shot-to-shot CEP noise level of ≈ 400 mrad was achieved by implementing a kHz feedback loop.

In the first section, I will briefly describe the different methods used for measuring the temporal intensity profile of the pulses from the femtosecond to the nanosecond time scale, as well as spatio-temporal couplings, and show some measurements.

In the second section, I will explain why the carrier-envelope phase of a light pulse train is normally unstable at the output of a CPA laser. Then, I will describe the methods for the CEP stabilization of our laser, which is done in two loops: a fast loop (MHz) to stabilize the pulse train coming out of the oscillator, and a slower one (kHz) to compensate for additional noise accumulated all along the laser chain. I will also show some measurements of the final achieved stability.

In the third section, we will see that the laser upgrades allowed to observe CEP effects for the first time on the generation of relativistic electron beams through laser-wakefield acceleration in gas jets.

4.1 Characterisation of the pulses

4.1.1 Femtosecond temporal intensity profile

The temporal profile of a pulse is only fully characterized when both the spectral phase and the spectral intensity distribution are known.

Wizzler for measuring $\approx$ 30 fs pulses

A Wizzler (commercial product by *Fastlite*) is used to measure the pulse duration with a dynamic range $> 10^4$ before post-compression. It is a commercial device based on self-referenced spectral interferometry [196] that requires $\approx$10 μJ energy per pulse.

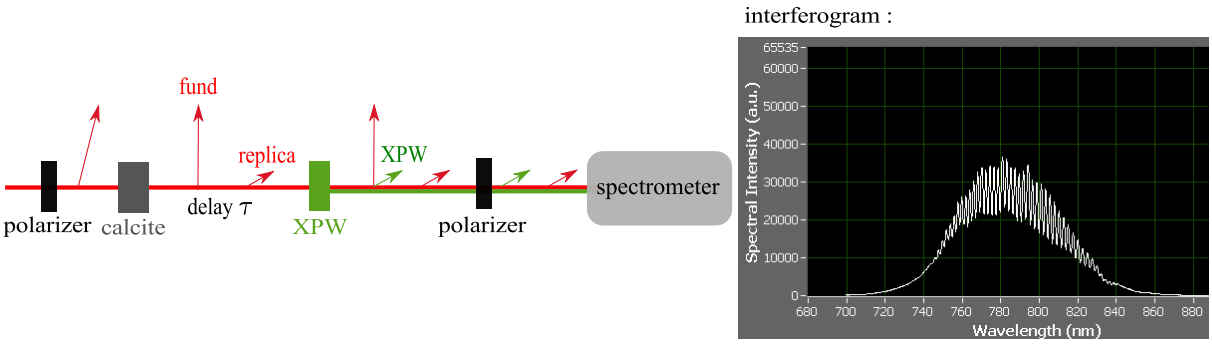

Figure 4.1: *Principle of the Wizzler measurement*

First, a weak, orthogonally polarized, time-delayed replica of the fundamental pulse is generated with a birefringent crystal (calcite), as shown in fig. 4.1. Then, a reference pulse is generated from the fundamental one via XPW (it acts as a reference since XPW produces a pulse with a flat spectral phase). The XPW and the replica, which have the same polarization, are finally selected with a polarizer and the interferogram is recorded with a spectrometer. The phase and amplitude of the fundamental pulse are obtained via Fourier Transform and numerical filtering of this interferogram [181].

The measurement is usually done after the evacuated hollow-core fiber, because it is much more convenient to install the Wizzler there than around the fiber entrance. An example is shown in fig. 4.2.a. Occasionally, we also use it at the output of the first CPA (fig. 4.2.b), e.g. after re-aligning the first amplifier, due to a slow, gradual power decrease.

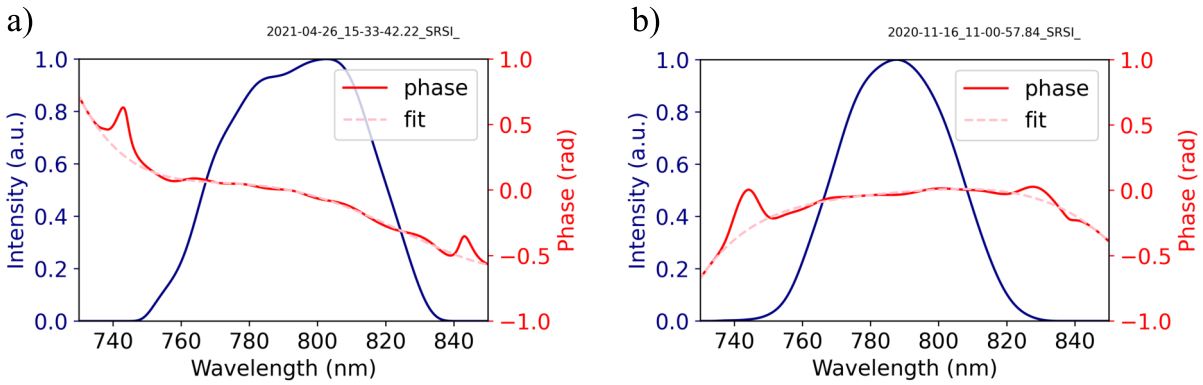

Figure 4.2: *Wizzler measurement a) at the output of the evacuated SF-HCF. The retrieved pulse duration is 25.9 fs FWHM, with a residual dispersion of -34*fs^2*, 229*fs^3 *and 11,076*fs^4 *estimated by the Wizzler. The central wavelength is 792nm and the bandwidth 54nm FWHM. b) at the output of the first CPA, before the XPW filter. The retrieved pulse duration is 28.2 fs FWHM, with a residual dispersion of -10*fs^2*, 274*fs^3 *and -8,793*fs^4 *estimated by the Wizzler. The central wavelength is 787nm and the bandwidth 41nm FWHM.*

SHG D-scan

An adapted version of the Wizzler can now work for durations as short as 4 fs, using reflective polarizers. However, for sub-4fs pulses, we need to use something else. We use a vacuum-integrated, customized d-scan (commercial product by *Sphere Photonics* [177, 176]) to measure the pulse duration after post-compression on a daily basis. The idea is to generate the second harmonic of the laser in a BBO crystal and measure the spectrum as a function of GDD by varying the insertion of a pair of motorized thin fused silica wedges. The fundamental spectrum is also recorded, and a retrieval algorithm [75] allows to obtain the spectral phase.

A typical measurement is shown in fig 4.3, where a 3.4fs FWHM duration was retrieved. Overall, the spectral phase is quite flat and we are not too far from the FTL duration (2.9fs, which would result in a 60% higher peak power). For this measurement, we found that a very small amount of TOD (-5fs^3) could help increasing the peak power by 15 % and reduce the pulse duration to 3.2fs.

However, the main peak intensity losses are due to higher order spectral phase terms. Oscillations are always observed in the blue part of the spectrum, between 700 and 550nm (fig. 4.4), which are very reproducible from day to day. These are most likely due to the chirped mirrors, and could eventually be smoothed by using complementary-pair chirped mirrors instead of our set of double-angle PC70s.

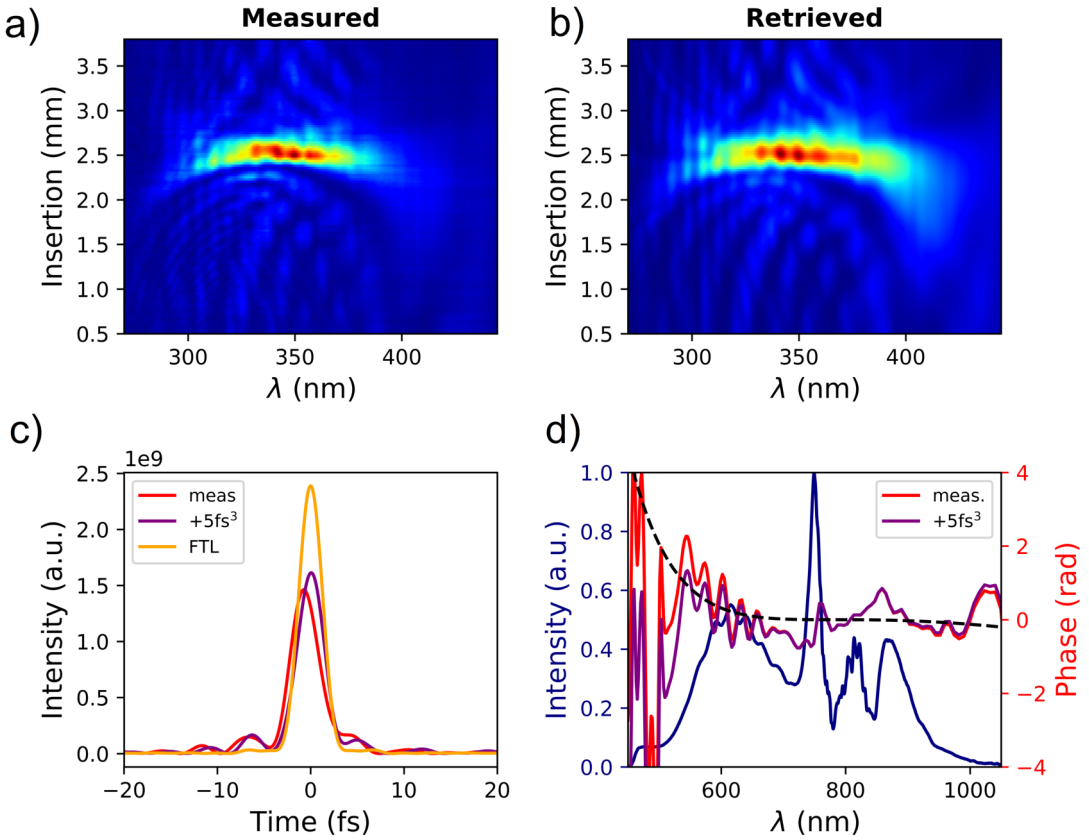

Figure 4.3: *D-scan measurement of the few-cycle pulses typically produced with this laser system. a) measured d-scan trace b) retrieved d-scan trace c) retrieved temporal intensity profile (red), FTL profile (orange) and profile obtained by adding 5fs^3 to the retrieved spectral phase (purple). d) fundamental spectrum (blue) and retrieved spectral phase (red). Spectral phase with an additional 5fs^3, represented by the black dashed line (purple).*

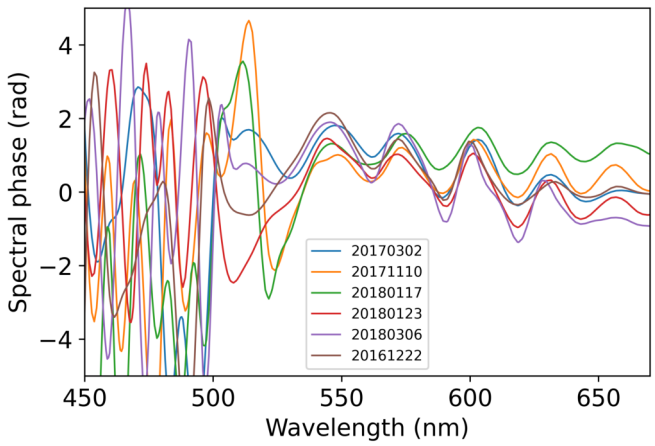

Figure 4.4: *Spectral phase oscillations on the blue side of the spectrum, retrieved from d-scan measurements. Data from different days are superimposed, all corresponding to sub-4fs duration pulses. Below 500nm, the signal is too low for the d-scan to properly retrieve the spectral phase, but the phase oscillations between 540 and 660nm are very reproducible.*

XPW D-scan

One can also use the XPW effect instead of SHG for measuring the pulse duration via a dispersion-scan. The method for the XPW d-scan is described in [240]. It was used in *Salle Noire 2* in the frame of a *Laserlab* campaign, aiming at studying the role of propagation effects in the characterization of few-cycle pulses [241]. The experiments were performed by Tamas Nagy, Ayhan Tajalli, Janos Csontos, Rodrigo Lopez-Martens and myself, with help from Aline Vernier. We put an XPW crystal, wedges at Brewster angle, and a spectrometer inside the compression chamber (see fig. 4.5) in order to compare the two techniques (SHG and XPW-based d-scans) with the same few-cycle pulses from our laser.

The main advantage of this method is that XPW is a third order nonlinear process that only involves photons of the same frequency (*ie* it is degenerate), therefore it is intrinsically phase-matched over extremely broad bandwidths. For example, BaF_2 is transparent from 0.2 to 9 μm. On the contrary, for BBO in the case of SHG dscan, the phase-matching is only achieved over a limited bandwidth. If one wants to measure extremely short pulses, with spectra spanning over an octave, it will require several BBOs with different cuts and/or very thin crystals, therefore limiting the conversion efficiency.

However, this can also lead to some confusion as the nonlinear signal is at the same wavelength as the fundamental one. One must therefore carefully avoid leakage of the fundamental through the polarizer which selects the XPW signal. For that reason, we put the XPW crystal on a motorized stage and acquired the background signal, which was later substracted.

The conversion efficiency of XPW is also weaker compared to SHG, therefore thicker crystals may be needed. The purpose of the campaign was to investigate the effect of material dispersion in the pulse retrieval by trying different BaF_2 thicknesses.

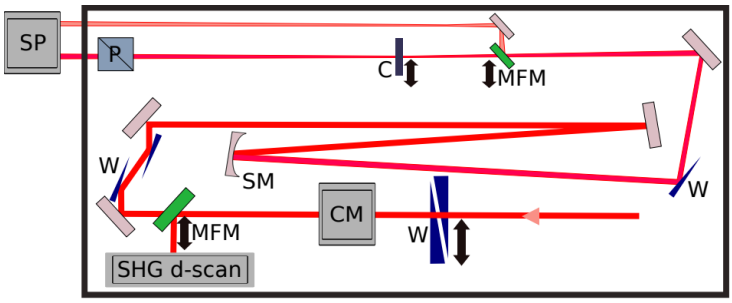

Figure 4.5: *Setup for the XPW dscan measurement. CM: chirped mirrors, W:silica wedges (the CM and the first pair of wedges are the ones we normally have in our compression chamber, whereas the other wedges were added to attenuate the beam and clean the polarization), SM:concave mirror to focus the beam in the XPW crystal with a ROC of 3m, MFM: motorized flip mirror, C:* BaF_2 *crystal on a motorized translation stage, P: polarizing beam splitter, SP: spectrometer.*

Starting from a measured 3.9fs pulse (intensity profile and spectral phase), Esmerando Escoto first simulated the d-scan traces that would be obtained using different crystal thicknesses (1 to 1000 μm). As the crystal becomes thicker, two effects are observed: i) the optimum wedge insertion for temporal compression decreases and ii) the trace is more extended along the y-axis (the dispersion axis), because the overall XPW signal is an accumulation of signals generated at different depths inside the crystal. This started affecting the retrieval for a 200μm thickness, for which a 4.3fs pulse duration was retrieved by the algorithm. Nonetheless, by including dispersion in the algorithm, the initial temporal profile was successfully retrieved for all thicknesses, in spite of the distorted dscan trace. This was verified experimentally, by measuring the XPW trace obtained in the case of a 50 and a 200 μm thick crystal: in both cases, although the trace was significantly different, the same durations and intensity profiles were retrieved.

With this improved algorithm, the XPW dscan measurement was also compared with a tra-

ditional SHG dscan measurement made immediately after. The results are shown in fig. 4.6. There is no noticeable difference in the retrieved spectral phase or the temporal profile. Pulse durations of 3.9 and 4.1fs were obtained for XPW and SHG techniques at FWHM, respectively. The difference is below the uncertainty, which is ≈ 0.3fs, estimated by making five consecutive retrievals for both techniques.

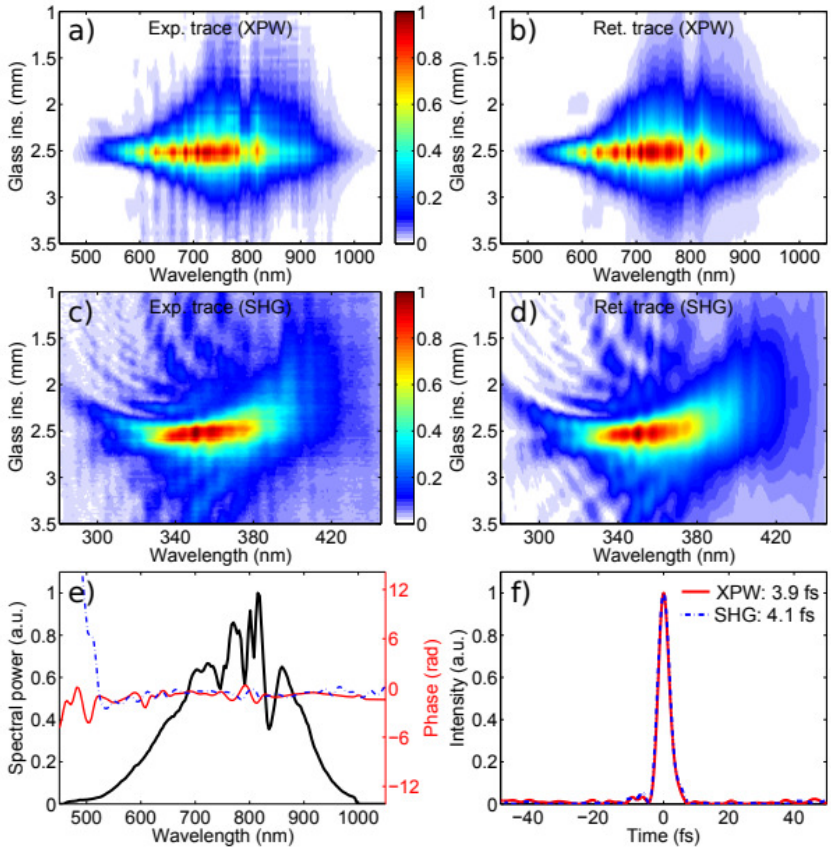

Figure 4.6: *Comparison of the XPW and SHG-based d-scan measurements. a) Measured and b) Retrieved XPW d-scan traces. c) Measured and d) retrieved SHG d-scan traces. e) Measured spectral intensity (black) and reconstructed spectral phase, from the XPW trace (red line) and from the SHG trace (dashed blue line). f) Reconstructed pulse shape at the optimum glass insertion from the XPW trace (red) and the SHG trace (dashed blue). Published in [241].*

We thus verified the robustness and the accuracy of the XPW-based d-scan measurement for measuring 1.5 optical cycle pulses from our laser chain, with crystal thicknesses up to 200 μm, paving the way for characterization of even the shortest possible light pulses.

4.1.2 Picosecond temporal contrast using a third order autocorrelator

3ω autocorrelator

The contrast level near the pulse peak was verified with a third order autocorrelator (*TUNDRA, Ultrafast Innovation*), which has a very high dynamic range of up to 12 orders of magnitude (provided a good input peak signal strength), over a 4ns time window. More recent versions can even detect signal down to 10^{-14}. The schematic drawing of the device is shown in fig. 4.7.a: a 6 mm diameter, s-polarized pulse with 300μJ is sent into the Tundra, where it can be attenuated with a variable neutral density (3 levels of attenuation), and then split

into two arms with a beam splitter. One arm contains an SHG crystal and a chromatic filter to select the second harmonic. The other arm consists of a very long motorized delay stage. The two beams recombine on a concave mirror to be focused into an SFG crystal, where the 3ω component is created instantaneously: $\omega + 2\omega = 3\omega$. The third harmonic beam is then spatially selected with a pinhole and detected with a photodiode. The measured trace is the intensity on the photodiode as a function of the introduced delay τ. The minimum step-size of the motorized delay line allows for a $\approx$ 2fs temporal resolution. However, in practice, a measurement from -2 to +2ns with this resolution takes several hours so we rarely use such a high resolution.

The only ambiguity in the measurement comes from the fact that each pre or post-pulse will generate a weaker replica (see fig. 4.7.b.), symmetric with respect to t=0. Ideally, one should avoid using beam-splitters, lenses, wave plates or windows to do the measurements, as they will introduce post-pulses, and prefer wedges, curved mirrors or crossed periscopes to obtain the right beam characteristics for the Tundra (energy, size, polarization). For example, propagation through a 1 mm thick fused silica ($n \approx 1.4533$ at 800nm) window at normal incidence will result in a post-pulse located $\Delta\tau = 2\Delta x n/c \approx 9.7$ ps after the main pulse due to reflection from the back surface.

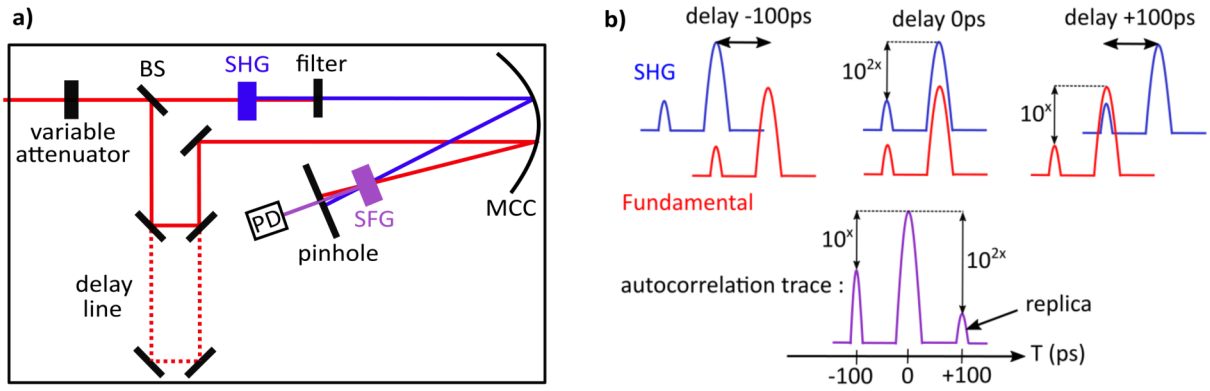

Figure 4.7: *a) schematic drawing of the TUNDRA measurement principle. The signal we are interested in is the intensity of the 3ω component as a function of the delay τ introduced by the motorized delay line. b) Illustration of the generation of symmetric replicas of post and pre-pulses.*

CPA 1 contrast

The contrast at the output of the first CPA is shown in fig. 4.8 at two different dates. We do not observe any pre-pulse, only post-pulses, and the contrast ratio is in both cases $> 10^7$ for $\tau < -15$ ps, which is typical of a *Femtopower* Ti:Sa CPA laser. In the most recent measurement, there is a strange step-like signal increase around -12ps, which we do not understand. We tried varying the trigger delays for the AOPDF and the pulse picker (Pockels) inside the amplifier, shifted the Ti:Sa crystal laterally, tilted lenses between the amplifier and the TGC, but the contrast trace always remained the same. Thus, we think it might come from damaged optics inside the Tundra. These optics have recently been replaced, and this should be measured again.

XPW contrast

The contrast trace before and after the XPW filter is shown in fig. 4.9. Measuring the contrast after the XPW filter is not trivial, because of the low power ($E_{\mathrm{XPW}} \approx 230\mu$J), and also because of the bad temporal compression (dispersion due to the crystals, the window and the polarizer), which result in a low nonlinear conversion (SHG, THG) efficiency. This low signal limits the dynamic range of our measurement, as indicated by the absence of signal decrease when we block the SHG and fundamental arms of the Tundra far from the peak. The overall contrast ratio on the ns scale is nonetheless increased by at least 3 orders of magnitude.

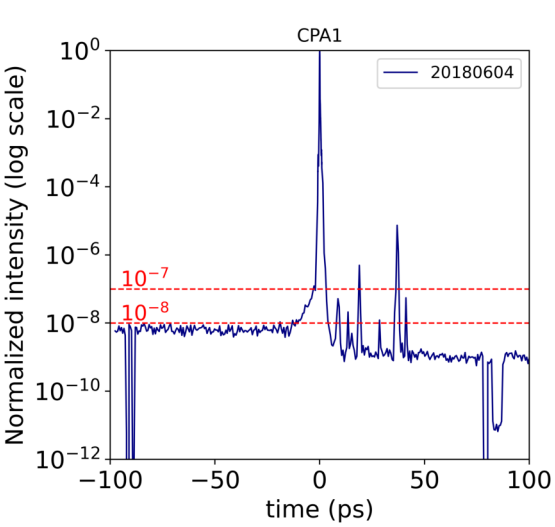

(a) Resolution of 600 fs, increased to 10fs from -1 to +1ps, with an average over 5 acquisitions per delay. The two arms of the autocorrelator were blocked around +90 and -90ps to show the dynamical range of the measurement.

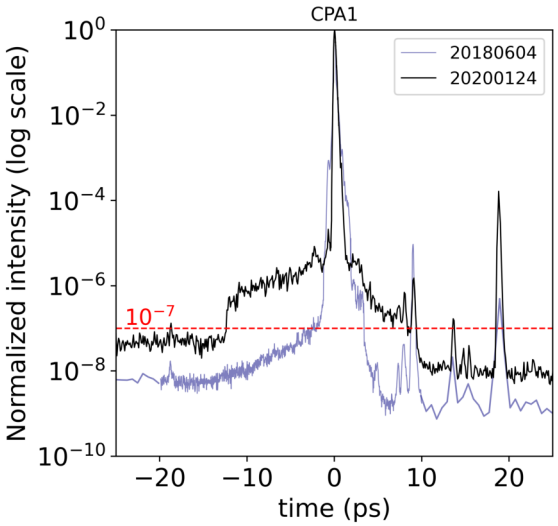

(b) Contrast traces on two different days. Solid black line: resolution of 100fs, increased to 10fs from -0.5 to +0.5ps, with an average over 5 measurements per delay. Light blue line: same measurement as shown in subfigure a, with an increased resolution (30fs step size) between -20ps and +10ps.

Figure 4.8: *Contrast measurement after the first CPA.*

Compression Chamber contrast

The next measurement (fig. 4.10) is performed at the output of the laser chain with 27fs pulses (*ie* without gas in the hollow-core fiber). It is preferable not to broaden the spectrum for the measurement, because in the case of sub-4 fs pulses, the fundamental spectrum already contains components at 2ω, which makes the signal optimization ambiguous.

For this measurement, we bypassed the telescope inside the compression chamber and sent the beam out after the mirror next to the holey mirror (see fig. 3.12). The compression chamber was vented and we removed the exit window to avoid adding a post-pulse. However, we did add a half-wave plate to rotate the polarization by 90°, as required by the Tundra. We could have put a crossed periscope instead, but it was much more convenient to use a wave plate at that time. Then, we used a telescopic combination of a concave (f=1m) and convex (f=-0.5m) mirror to reduce the beamsize, as well as a fused silica wedge (AOI $\approx$ 60 °) for attenuation to 320 μJ.

The prepulse that appears around -30ps with a 10^{-8} relative intensity is most likely a replica from the stronger, symmetric post-pulse at +30ps with a 10^{-4} signal level (visible in the "mirrored trace"). Thus, the contrast ratio at τ<-15ps before the peak is $>10^{10}$, whereas closer to the peak, for τ<-3ps, the contrast ratio is $>10^{7}$. The origin of the step-like increase at 15ps is again quite mysterious. It was also not observed in previous measurements.

Although the contrast is certainly not perfect and results in some ionization a few ps before the peak, the achieved temporal contrast is sufficient to control the plasma density gradient with an auxiliary pulse whose peak intensity is $\sim 10^{-4}$ times that of the main pulse.

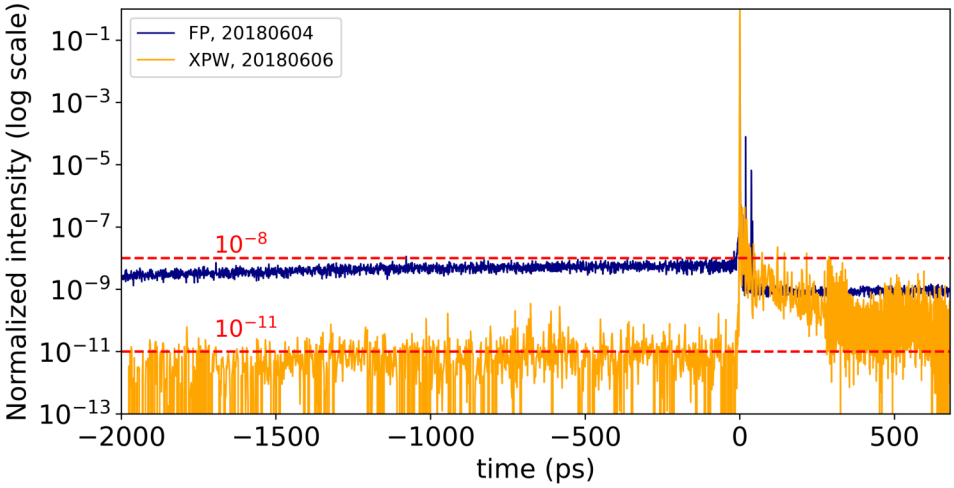

Figure 4.9: *Contrast measurement before (blue line) and after (orange line) the XPW filter.*

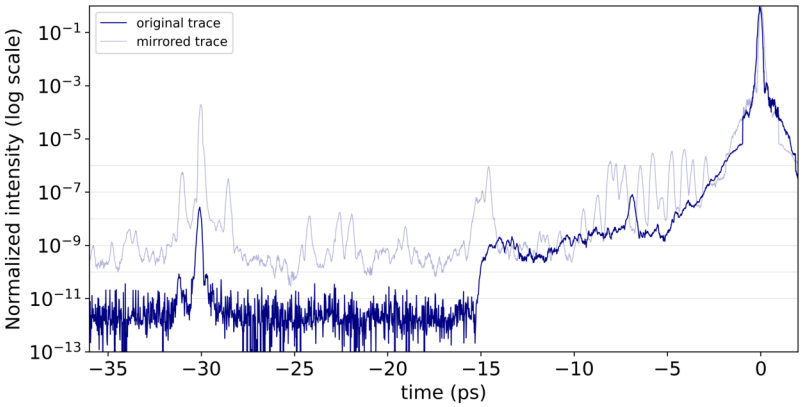

(a) *Steps of 20fs from -40 to +40ps and in steps of 10fs from -1 to +1ps (from 2020.07.07).*

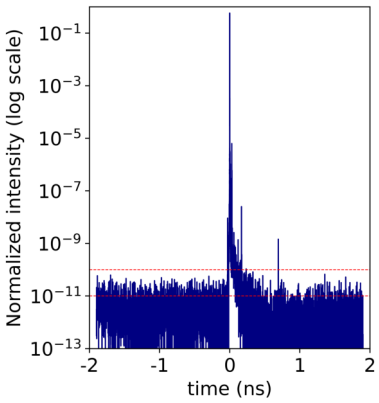

(b) *Steps of 500fs from -1.9 to +1.9ns, steps of 20fs from -40 to +40ps and steps of 10fs from -0.5 to +0.5ps (from 2020.07.08).*

Figure 4.10: *Contrast measurement of the 27fs pulses at the end of the laser chain. For each delay, the data is averaged over 10 measurements.*

4.1.3 Nanosecond temporal contrast using a fast oscilloscope

There is a simple, complementary device used to characterize the pulses on a longer time scale: a fast oscilloscope (*Keysight, MSOS804A*) with 8 GHz of analog bandwidth, a sampling rate of 20GSa/s (using 2 channels) with a 10 bit analog-to-digital converter, and up to 800 million points of memory. We use it in combination with an ultrafast photodiode (UPD-200-UP from *Alphalas*), which has a risetime <175ps and works for the wavelength range 170-1100 nm.

It can be conveniently used to verify the ns-scale temporal contrast. In particular, at the output of the first CPA, close to the peak of the pulse, we can see the MHz pulse train from the oscillator, which is amplified in the first four passes of the *Femtopower*, before the Pockels' cell reduces the repetition rate.

It results in a forest of pre and post-pulses spaced by 1/80MHz $\approx$ 12.5ns, which can be seen when the photodiode is saturated. The amplitude ratio of the main pulse with respect to this forest of ns pulses can be measured with calibrated neutral density filters. An example is shown in fig. 4.11: the maximum amplitude of the MHz train signal is 82mV, whereas the main pulse has an amplitude of 289mV, measured with a 10^{-4} neutral density filter. Therefore, the contrast ratio is $\approx 3.5\times10^4$.

If the ratio is too low, it can be enhanced by carefully aligning the Pockels cell crystal and the polarizer beam splitters before and after it. In practice, we always measured a typical ratio of 10^4 and never really had to do anything about it.

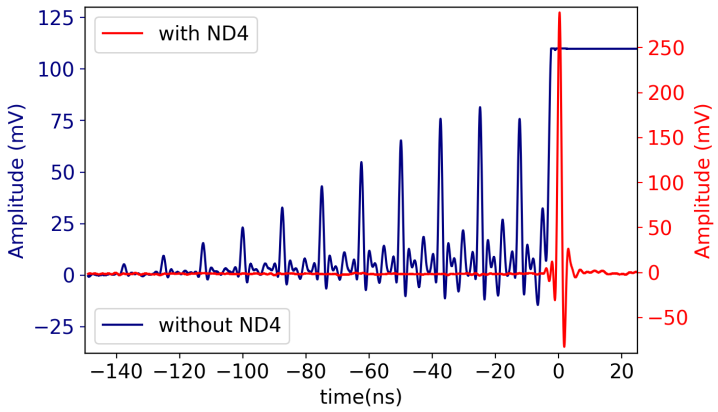

Figure 4.11: *Measurement of the laser temporal contrast at the output of the first CPA, using an oscilloscope and a fast photodiode. Red: using a neutral density filter placed in front of the photodiode, with an attenuation factor of* 10^4*. Blue: without the neutral density filter. The peaks are spaced by* $\approx$ *12.5ns, corresponding to the oscillator's repetition rate, and are observed on a* $\approx$*100ns time window, which is comparable to the pump pulse duration.*

4.1.4 Spatio-Temporal couplings

The spatio-temporal couplings (STC) in the beam going in and coming out of the hollow-core fiber were measured in the frame of a collaboration with Antoine Jeandet and Spencer Jolly, working at *CEA Saclay* at that time, with the TERMITES device. At that time, the compressor was still the GRISM, and we were interested in knowing how slight misalignments of the compressor could affect the output beam.

Introduction

All the above-mentioned methods that we used for characterizing the pulses do not allow to observe correlations between the spatial and temporal properties of the beam, *ie* spatio-

temporal couplings. However, laser systems based on the CPA technique intrinsically make use of massive STC, which are induced when broadband beams are diffracted by gratings or refracted by prisms as in most stretchers/compressors, thus it is certainly reasonable to assume that the output pulses of such lasers exhibit some STC.

Aberrations, including STC, always lead to a decrease in peak intensity, therefore it is interesting to understand where they come from and how to eliminate them. This motivated research work on STC metrology [132], which began about 20 years ago, and we are now reaching the point where commercial devices capable of fully characterizing the complex 3D spatio-temporal field (or equivalently spatio-spectral field) of the laser pulses are becoming available [32].

Overview of previous HCF post-compressed lasers measurements

Previous STC measurements of few-cycle pulses obtained via post-compression in hollow-core fibers showed that spectral broadening via SPM (and plasma blue-shift) is not perfectly homogeneous over the full spatial extent of the beam. Typically, there is a slight difference between the center and the periphery of the beam. In [9], the authors used a STARFISH device [8] and measured a broader spectrum, with a 4.5fs duration in the center, whereas the pulse duration in the wings of the beam was found to be 5fs. In *Salle Noire 2*, only the spatio-spectral distribution of the beam had been measured, right after the installation of the post-compression stage ([25], p.78 and p.91) and it was also found that the spectrum is broader in the center, with more blue there than in the periphery. This is simply due to the wavelength-dependent divergence of the beam (eq. 1.40) at the output of the hollow-core fiber.

Except for this expectable feature, other spatio-temporal characterizations of lasers that are post-compressed in gas-filled HCFs were made (e.g in [274] and [275], using a SEA-SPIDER device) and did not show any strong aberration.

TERMITES device

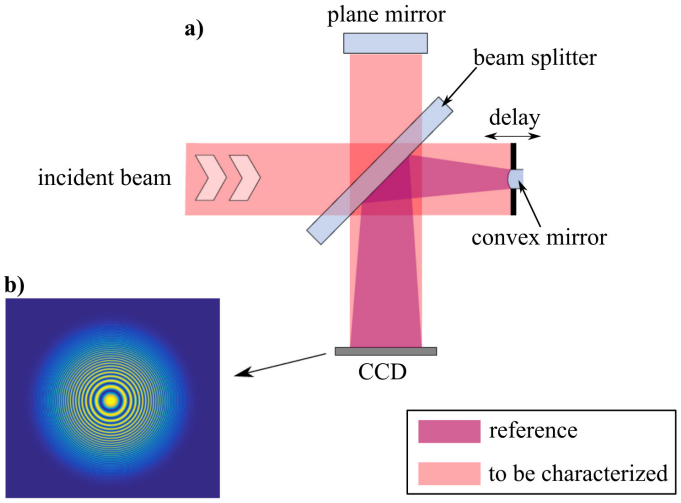

Figure 4.12: *a) Schematic representation of the TERMITES principle. The central part of the beam is reflected by a small convex mirror. Thus thus created convex wavefront serves as a reference for measuring the spatial phase of the incident beam at all other points. The interference pattern (b) is recorded with a CCD camera for different delays between the reference pulse and the one to be measured by moving the convex mirror. Adapted from [200].*

TERMITES is a self-referenced interferometric technique, where the spectral phase in the center of the beam is used as a reference to measure the spectral phase at all other points in the beam (fig. 4.12). A detailed description can be found in [201]. It can give access to $\tilde{E}(x,y,\omega)$ in any arbitrary plane along the propagation axis and works for both temporally compressed and

uncompressed pulses. It has been used on various high-power laser systems worldwide, including BELLA at Berkeley [129], proving its capabilities.

Measurements before and after the HCF in Salle Noire 2

Panel a of Figure 4.13 shows the spatio-spectral amplitude of the beam in the near field, before and after the hollow-core fiber, for different values of gas pressure. Overall, although the spectral phase is not perfect, no clear STC can be identified. Only a small transverse spatial chirp is visible, especially at the highest gas pressure. In panel b, the 2D spatial phase is extracted from the 800mbar case for three different wavelengths, highlighting the high quality of the wavefront.

As a conclusion, pulses delivered by the *Salle Noire 2* laser system do not exhibit any particular aberration and using hollow-core fibers for post-compression in general is very robust and provides high-quality pulses.

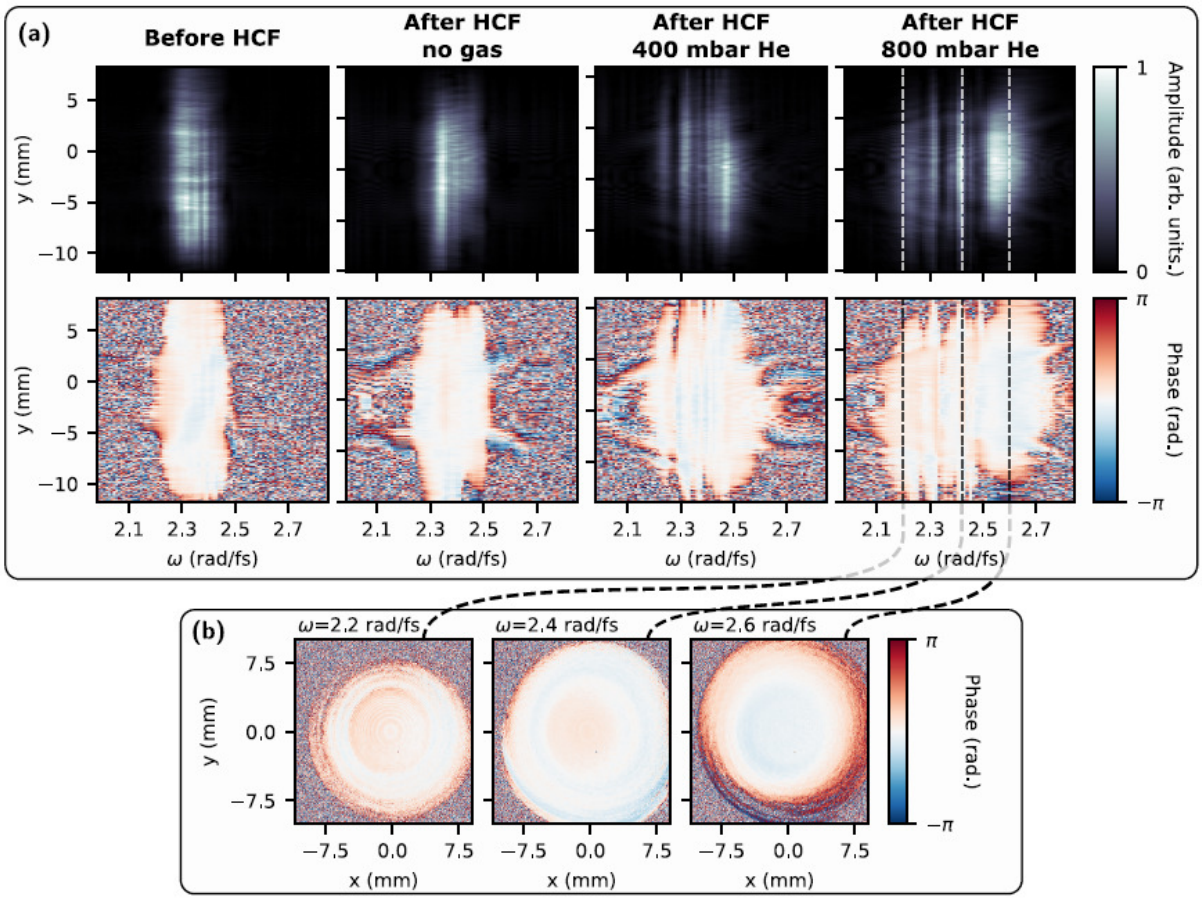

Figure 4.13: *Results of TERMITES measurements before and after the HCF for different gas pressures. a) spatio-spectral slices of the amplitude and phase profiles measured by TERMITES. b) spectrally-resolved wavefronts measured at the HCF output (with 800 mbar) at three different frequencies. Published in [130].*

4.2 Carrier-Envelope Phase stabilisation

The stabilization of the carrier-envelope phase (CEP) of the laser pulses was another important part of my work. In this section, I will first discuss why the CEP can vary from one pulse to the next and then explain how to stabilize it. In *Salle Noire 2*, we currently have two permanent feedback loops (one for the oscillator and one to stabilize the CEP at the end of the chain) which can easily be activated. We also occasionally characterized the CEP stability at various points along the chain with a temporary measurement setup and I will show here some measurements at the output of the first CPA.

4.2.1 Introduction

Where do CEP instabilities come from?

As we have seen in Chapter 1.2.4, the CEP naturally slips upon propagation through dispersive media. This slippage is not a problem as long as it is stable over time. Unfortunately, most of the time, this is not case and here are some of the reasons why:

We have seen that the CEP change upon propagation depends on the propagation length through each material. Therefore, any beam pointing instability will translate into a pulse to pulse CEP change. Thus, mechanical instabilities should be avoided and active beam pointing stabilizers should be carefully implemented. Vibrations from devices like chillers, vacuum pumps, and even floor-vibrations (even in quiet environments without heavy traffic nearby), are known to induce CEP noise. In [88], placing anti-vibration rubber sheets (*Novibra*) under the table legs and the cryocooler in order to isolate the optical tables from floor vibrations greatly enhanced the CEP stability.

To minimize CEP noise, one should also prefer bulk stretchers over gratings, as the dispersion they introduce is much less sensitive to mechanical or beam pointing instabilities [47, 154]. For example, beam-pointing variations leading to a displacement by just a single groove spacing at a grating will translate into a 2π CEP shift, thus imposing beam pointing fluctuations to be much below the μrad level [119, 138].

Similarly, any change of the refractive index in time, for example changes in the refractive index of air due to acoustic waves, temperature drifts or changes in relative humidity [162, 119], will induce CEP instabilities. Shielding the laser chain from air flows by adding covers was particularly helpful in reducing the CEP noise in our laser chain. Similarly, temperature variations of the Ti:Sa crystal can induce CEP noise [119], thus it is better to keep its temperature as low (to minimize the index gradient) and stable as possible.

Any intensity noise will also translate into CEP noise [265] through nonlinearities, because of the intensity-dependent refractive index $n(I) = n_0 + n_2 I$. Therefore, it is important to use pump lasers with stable output power over time, and to avoid temporal jitter of the electronic signals used to trigger the different elements in the chain (Pockels' cells, AOPDFs...).

In conclusion, the CEP is very sensitive and it is generally not possible to keep it stable. Fortunately, some of the CEP noise can be actively compensated for. The idea is to measure the CEP at the end of the chain (we will see how in the next subsection) and act on some element at the beginning of the chain to compensate for the measured CEP drift. Any element that can vary the refractive index can be acted upon. Many techniques have been used, such as varying the insertion of a piece of glass in the beam path [280], changing the dispersion by adjusting gratings or prisms, varying the power of a pump laser, using spatial light modulators [266], etc.

4.2.2 Overview of the different methods for measuring the CEP

Different methods exist to measure the carrier-envelope phase of an optical pulse, from complex setups capable of retrieving the full waveform of the pulse but requiring careful handling

and high vacuum, to the most simple and extensively used f-2f interferometer. Here is a non-exhaustive list of devices:

ARIES: Attosecond Resolved Interferometric Electric-field Sampling

This method [278, 77] requires generating harmonics in gas and detecting the high-energy cutoff of the spectrum. A shift of the cutoff towards higher or lower frequencies is induced by interfering the driving laser with a less intense pulse, which is the one to be characterized. By recording the HHG spectrum for different time delays between the driving laser and the probed pulse, it provides an absolute CEP measurement since the complete waveform of the pulse is retrieved. The setup is quite complex and costly, but provides a lot of information about the precise laser waveform, even for pulses with complex shapes.

Single-shot stereo ATI

The single-shot stereo-ATI phase-meter [276] uses the left/right asymmetry in the yield of high-energy above-threshold ionization (ATI) electrons along the polarization axis to measure the CEP. ATI is in fact multi-photon ionization in the tunneling regime where the electrons are left with excess kinetic energy. Detecting all the electrons is not robust enough as they are deflected multiple times in the laser field again after ionization, therefore in this method they only consider the highest energy electrons, which are electrons that have returned to the ion core and been back-scattered, thus gaining higher energies. The measurement requires focusing the laser beam into a gas jet and placing two MCPs used as Time of Flight detectors on each side of the beam to detect electrons along the polarization direction. The measurement requires 30 μJ pulse energy and ultra-high vacuum conditions ($\sim 10^{-7}$ mbar), which makes this method rather complex to implement experimentally. However, it works very well, has been demonstrated up to 100kHz repetition rate and should theoretically work even at 10 MHz [122]. Moreover, as it is single-shot, it allows robust CEP-tagging (it has been used in [279], for example).

TIPTOE: Tunneling Ionization with a Perturbation for the Time-domain Observation of an Electric field

Not well known yet, but worth mentioning, there is the TIPTOE technique [52] invented at CORELS, IBS (South Korea). It is mostly meant to measure the temporal intensity profile of pulses by focusing a reference pulse in a gaseous medium (e.g. air) with two parallel electrodes on the sides to measure the instantaneous ionization yield. The ionization rate is then modulated by overlapping the reference pulse with a weaker signal pulse (the one to be measured).

Measuring the instantaneous ionization rate for different time delays between the ionizing pulse and the signal pulse allows to reconstruct the signal pulse temporal profile. We tested it in *Salle Noire 2* with its inventors and measured the same duration as our d-scan. It is a quite simple, compact device, which can be used in air. The only limitation is that it requires the pulse duration not to be more than 3 times the FTL duration.

There are different versions and one of them includes a BBO crystal for frequency doubling. The 2ω wave modulates the sampled pulse, thus modulating the sub-cycle ionization yield, which allows to retrieve the CEP [202].

f-2f interferometer

Most of the time, the determination of the absolute CEP value is not necessary or can be deduced by observing the results of the experiments, and it is much more convenient and simple to detect the pulse-to-pulse CEP change, which is directly proportional to the frequency comb offset as we will see. The traditional way to do this is using a f-2f interferometer, which I will describe further. It is very compact and easy to use compared to the other methods previously mentioned. Usually, the spectral fringes given by the f-2f interferometer are mapped into the spatial domain using gratings or prisms and recorded with a CCD array to be analyzed via Fourier transform so as to retrieve the CEP drift. The feedback rate is thus limited by the

acquisition time of the CCD detector and the computation time. Recently, devices capable of measuring the shot-to-shot CEP drift and generate an error signal at high repetition rate have emerged: the Fringeezz (a commercial product by *Fastlite*) can work up to 10kHz ; the combination of a photodiode array with a field-programmable gate-array for real-time FFT calculation was demonstrated up to 100kHz [87] ; the BIRD (acronym for Beat Interferometer for Rapid Detection) technique using the difference signal from two photomultipliers (now used by *Amplitude Laser*) [143, 83] can also measure the CEP at 100kHz [186].

TOUCAN

There is also a slightly different method called the *Temporal dispersion based One-shot Ultrafast Carrier envelope phase Analysis* (TOUCAN) [146]. In this method, the spectral modulations originating from the f-to-2f interferometer are mapped into the temporal domain by propagating through a highly dispersive medium (e.g. in a dispersion compensation fiber) and detected by a photodiode. The temporal waveform is then digitized and recorded with a fast oscilloscope operated in segmented memory mode in order to record every waveform at the full repetition rate. In [146], the authors used it on a 100kHz repetition rate laser system but in principle it should work up to gigahertz repetition rates. However, this method is limited by the internal memory of the oscilloscope (it can only measure in single shot for a few seconds) and the CEP extraction has only been done through post-processing so far, as no real-time measurement is possible yet (this limitation could be overcome using dedicated electronics).

4.2.3 CEP-stable oscillator in SN2

Our commercial oscillator is CEP-stable and I will detail here how it is done. As we have seen in Chapter 1.6, the pulse-to-pulse CEP drift is linked to the frequency comb offset. Measuring this offset is the easiest way to access CEP drifts. We then generate an error signal which is fed back to an element so as to vary the dispersion and therefore stabilize the frequency comb offset.

Measuring the frequency comb offset

In order to detect the frequency f_{ceo}, the beam is focused into a Periodically Poled Lithium Niobate (PPLN) crystal just after the oscillator cavity, in which both spectral broadening and intrapulse DFG occur. The DFG comb has a null offset whereas the broadened comb preserves the offset of the fundamental spectrum.

- DFG spectrum components: $f_m - f_p = (mf_{\text{rep}} + f_{\text{ceo}}) - (pf_{\text{rep}} + f_{\text{ceo}}) = (m-p)f_{\text{rep}}$
- Broadened fundamental spectrum components: $f_n = nf_{\text{rep}} + f_{\text{ceo}}$

Interestingly, in the spectral region where these two combs overlap, a temporal beating at the frequency f_{ceo} occurs (see figure 4.14). This technique is called '0-to-f' interferometry. The beating frequency is detected using a photodiode and a spectrum analyzer, after spectral filtering with a dichroic mirror and an interferometric chromatic filter. After the chromatic filter, if we consider only two frequency components, the resulting wave is

$$\begin{aligned} A_{\text{tot}} &= A_1 \cos[2\pi(j-k)f_{rep}] + A_2 \cos[2\pi((j-k)f_{\text{rep}} + f_{\text{ceo}})] \\ &= A_1 A_2 \cos[-\pi f_{\text{ceo}} t] \cos[\pi(2(j-k)f_{\text{rep}} + f_{\text{ceo}})t] \end{aligned}$$

This corresponds to a beating of the two frequencies at f_{ceo}, which typically falls in the radio-frequency range (*ie* MHz), so it can be detected and treated electronically.

It is interesting at this point to note that pulses resulting from a DFG process are therefore inherently CEP-stable, no matter how the CEP of the fundamental pulse drifts. This is a major

advantage for optical parametric amplifiers seeded by a DFG process [16].

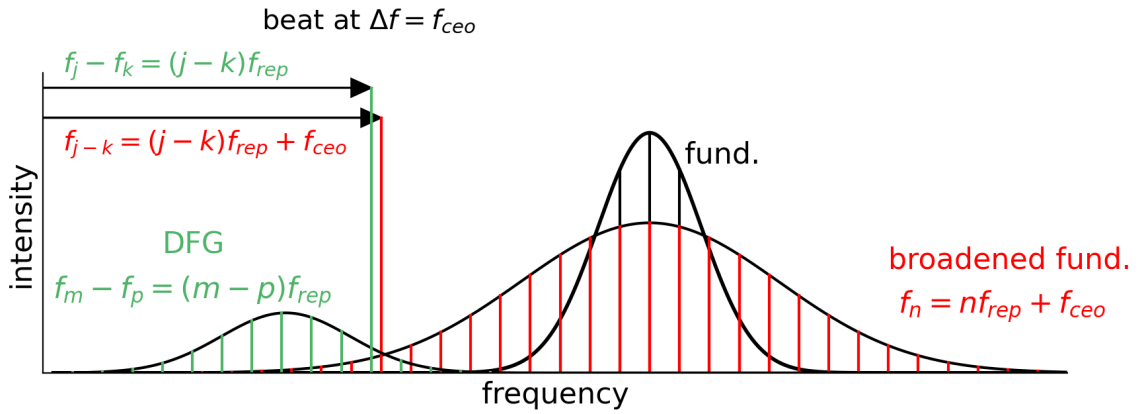

Figure 4.14: *Illustration of the 0-to-f beat signal*

Feedback loop for stabilization

We want every amplified pulse to have the same CEP and there is only one pulse out of 80,000 that will be selected and amplified inside the Femtopower, since the repetition rate is reduced to 1 kHz. Therefore, it is good enough to have every fourth pulse look alike, meaning the CEP drift from one oscillator pulse to the next must be $\pi/2$, which is equivalent to locking the comb frequency offset to 20 MHz:

$$\Delta\phi_{\text{cep}} = \frac{\pi}{2} \Leftrightarrow f_{\text{ceo}} = \frac{f_{\text{rep}}}{4} \approx 20\text{MHz}.$$

There is a pair of intracavity motorized silica wedges for coarse adjustment of the beating signal frequency to 20MHz. The detected signal is then sent to phase-locking electronics (XPS800 from *MenloSystems*) for further adjustment. It compares this signal to the repetition rate of the oscillator divided by four $f_{rep}/4$. A signal proportional to the error is then sent back to an acousto-optic modulator (AOM), which modulates the pump intensity (fig. 4.15). It induces changes in the Ti:Sa crystal nonlinear refractive index, and thus changes in f_{ceo} through nonlinear phase shifts [280, 236]. This technique, relying on the comparison of two frequencies, is called heterodyning and does not allow to have $f_{ceo} = 0$.

The AOM is made of a piezoelectric transducer, a material like quartz and an acoustic absorber (fig. 4.16). The transducer is driven by an oscillating electric signal and generates an acoustic wave in the crystal, similarly to the Dazzler. The pressure variations make the density vary and therefore the refractive index of the medium as well. The incoming laser is diffracted on the density grating thus generated, while the intensity of the diffracted beam depends on the intensity of the sound wave and therefore can be arbitrarily chosen by varying the electric signal amplitude.

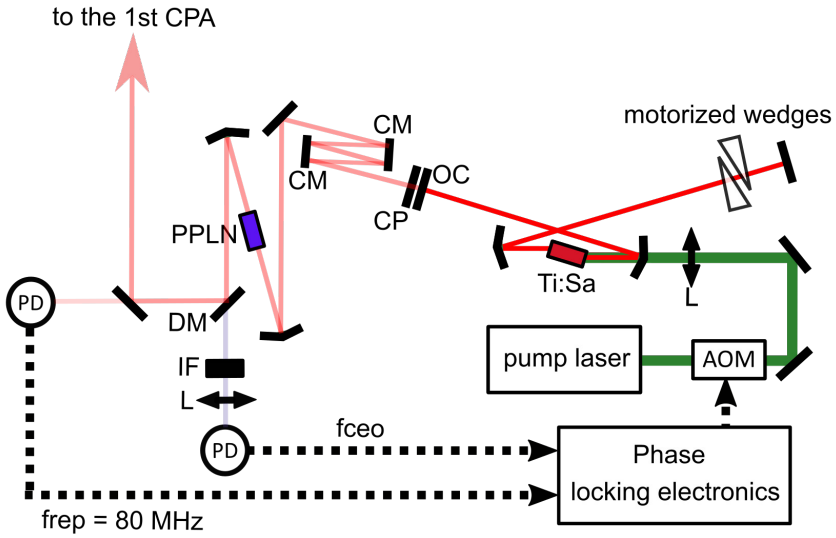

Figure 4.15: *Schematic drawing of the oscillator cavity and CEP detection. CM: chirped mirror ; OC: output coupler ; CP: compensating plate ; L: lens ; AOM: Acousto-Optic Modulator ; PD: photodiode ; IF: inteferometeric filter ; DM: dichroic mirror.*

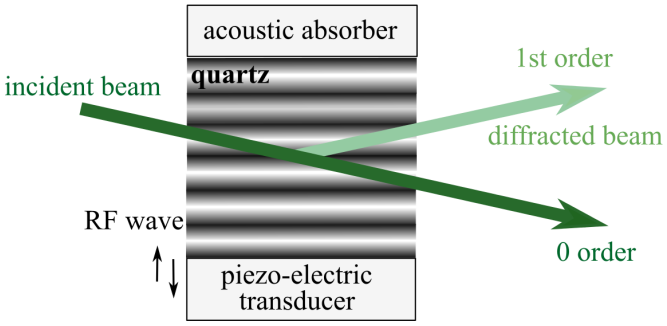

Figure 4.16: *Schematic drawing of the AOM*

4.2.4 Femtopower CEP stability

Stabilizing the oscillator's CEP is necessary, yet insufficient to obtain a CEP-stable pulse train at the end of the laser chain. Indeed, noise is added in the chirped-pulse amplifiers and upon propagation. Since the repetition rate is reduced to 1kHz (which is our final repetition rate) in the first amplifier, and a beatnote at f_{ceo} cannot be locked to a non-zero value, we use a slightly different technique. We are now interested in the beating between a second harmonic comb and a broadened comb (which are both generated in a "f-to-2f" interferometer), still at the frequency f_{ceo} as illustrated in figure 4.17. However, instead of using a photodiode and a spectrum analyzer, we now measure f_{ceo} by looking at the spectral intensity variations using a spectrometer.

Principle of the f-2f interferometer

Let us consider a Gaussian fundamental pulse centered around the frequency ω_0 with a spectral phase $\phi_{\text{fund}}(\omega)$:

$$E_{\text{fund}}(\omega) = \exp\left[-\frac{(\omega-\omega_0)^2}{a_1^2}\right]\exp[-i\phi_{\text{fund}}(\omega)]. \tag{4.1}$$

The fundamental wave is broadened (without changing the comb structure) and then frequency

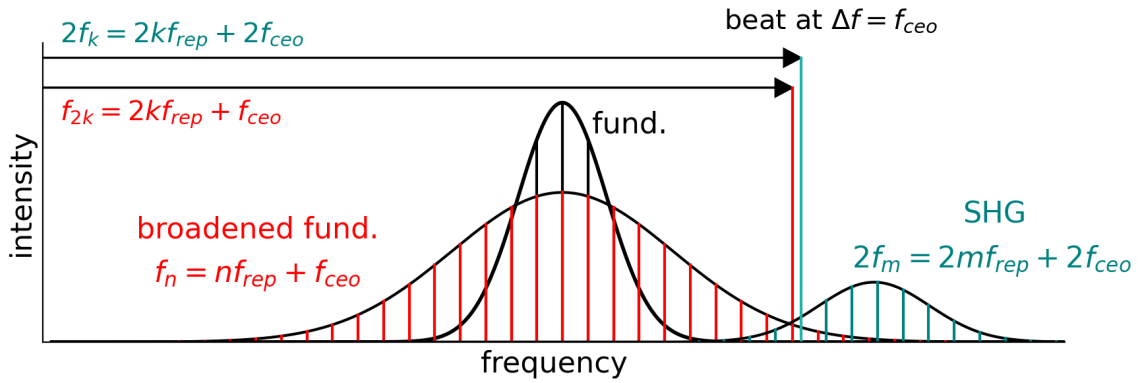

Figure 4.17: *Illustration of the f-to-2f beat signal*

doubled in a BBO crystal to generate an SHG pulse centered around the frequency $2\omega_0$:

$$E_{\mathrm{SHG}}(\omega) = \alpha \exp\left[-\frac{(\omega - 2\omega_0)^2}{a_2^2}\right] \exp[-i\phi_{\mathrm{SHG}}(\omega)]. \tag{4.2}$$

When two photons of the fundamental spectrum combine to make one carrying twice the energy, the new wave carries twice the spectral phase of the fundamental wave (plus a phase shift of $\pi/2$, but it is not important as we only measure relative CEP values). Additionally, the dispersion due to the crystal causes a temporal delay τ resulting in a phase shift $\exp(i\omega\tau)$. Therefore,

$$\phi_{\mathrm{SHG}}(\omega) = 2\phi_{\mathrm{fund}}(\omega/2) + \omega\tau \tag{4.3}$$

$$\tag{4.4}$$

As the fundamental and the SHG waves are focused into the spectrometer, the total detected spectral intensity reads:

$$I_{\mathrm{tot}}(\omega) = |E_{\mathrm{fund}}(\omega) + E_{\mathrm{SHG}}(\omega)|^2 \tag{4.5}$$

$$= I_{\mathrm{fund}} + I_{\mathrm{SHG}} + 2\sqrt{I_{\mathrm{fund}} I_{\mathrm{SHG}}} \cos(\Delta\phi) \tag{4.6}$$

and the spectral modulations are given by the term:

$$\Delta\phi(\omega) = \phi_{\mathrm{SHG}}(\omega) - \phi_{\mathrm{fund}}(\omega) \tag{4.7}$$

$$= 2\phi_{\mathrm{fund}}(\omega/2) + \omega\tau - \phi_{\mathrm{fund}}(\omega) \tag{4.8}$$

Therefore, spectral fringes appear due to the dispersion from the f-to-2f interferometer (the term $\omega\tau$) and dispersion in the fundamental wave. The period of those CEP fringes depends on the amount of dispersion, and, assuming a compressed input pulse *ie* $\phi_{\mathrm{fund}}(\omega) = \phi_0$, then the position of the fringes is simply given by ϕ_0, as illustrated in fig. 4.18.

A reliable measurement?

One may wonder whether this detection scheme preserves the original CEP value or not.

Traditionally, spectral broadening is achieved through white-light generation (e.g. in a sapphire crystal), which is a rather complex process involving several nonlinear wave mixings. The output pulses will generally carry a different CEP value, but in principle, the CEP offset between the input and the output pulses is spatially and spectrally independent, as well as CEP-independent [17]. Therefore, we can rely on it to create a phase-coherent spectrally broadened replica of the input laser pulse.

However, as any nonlinear process, it is rather sensitive to intensity fluctuations, which will translate into a pulse-to-pulse fluctuating CEP offset, therefore there is often a loss of pulse-to-pulse coherence during the propagation through a highly nonlinear medium. For this reason,

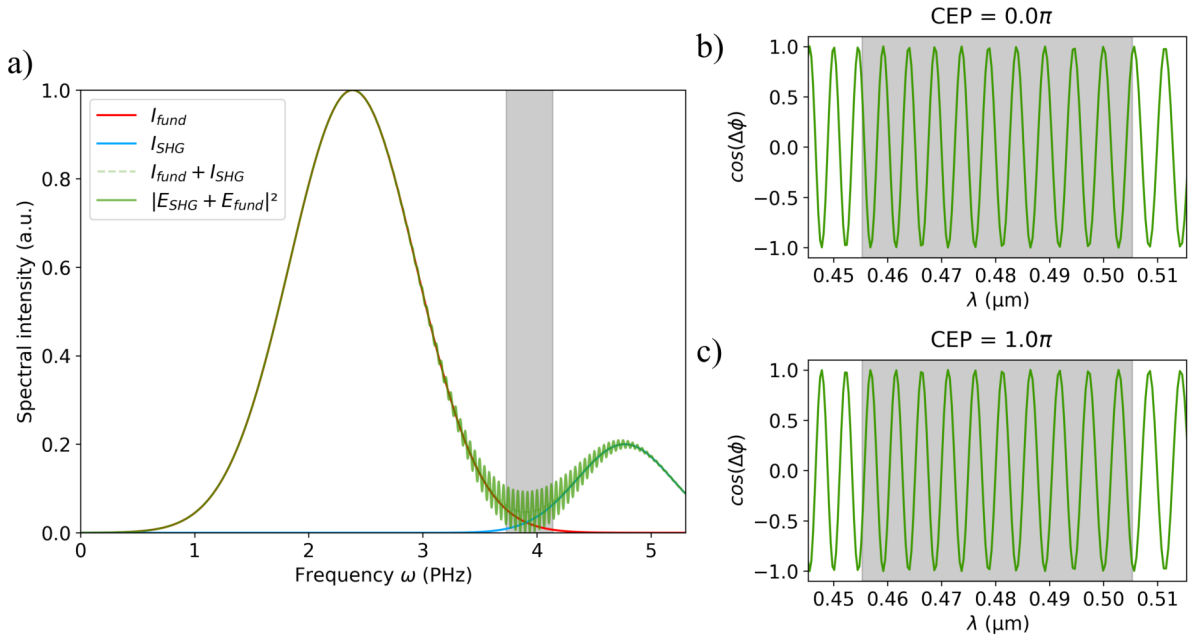

Figure 4.18: *Signal detected with the spectrometer at the output of the f-to-2f interferometer, according to Eq. 4.6. We consider a perfectly compressed Gaussian pulse with an arbitrary SHG efficiency. We set $\tau = 150$fs. The gray shaded areas correspond to the Fringeezz detection range. a) Full spectrum, b) modulation term $\cos(\Delta\phi)$ for a CEP of 0 and c) a CEP of πrad. We see that the fringe maxima are shifted along the wavelength axis as we change ϕ_0.*

it is recommended to broaden the spectrum in bulk sapphire rather than in a photonic crystal fiber (PCF), the latter being very sensitive to beam pointing fluctuations. In [17], the authors found that when a stable single filament is formed in the sapphire plate, which is normally the case for a f-to-2f interferometer, the phase change quasi-linearly depends on the energy (they found that a 1% pulse energy jump translates into a 84 mrad phase shift).

The coherence between different spectral components within one laser pulse was also studied in [216] (termed intra-pulse coherence) and it was found that filamentation-based supercontinuum generation may also lead to intrapulse coherence loss. They also recommend to accumulate self-phase modulation in longer media at lower intensities rather than broadening over short propagation lengths in thin plates.

Similarly, SHG of the red part of the broadened spectrum also causes an intensity-dependent phase shift, increasing the f-2f detection noise level to $\gtrsim$ 100 mrad, typically, and adding a $\pi/2$ phase shift.

Therefore the f-2f interferometer allows measuring the pulse to pulse CEP variations above a certain intrinsic noise level, which is typically around 100mrad, but doesn't give the possibility to access its absolute values.

APS800 f-to-2f interferometer

To characterize the CEP stability at the output of the first CPA, we used a commercial f-to-2f interferometer (*APS800 from MenloSystems*), which was placed on a separate mobile breadboard. The APS800 (see fig 4.19) is made of an iris, a variable ND filter, a HWP, a sapphire plate for spectral broadening, a BBO crystal for Second Harmonic Generation (SGH), a rotable polarizer beam splitter (PBS) and a USB spectrometer (Thorlabs). When we look at the recorded spectrogram, in the region where the SHG and the broadened fundamental spectrum overlap (around 480 nm), a fringe pattern appears due to dispersion within the APS800 itself (similar to fig. 4.18.a). The amplitude and contrast of the fringes are optimized by tuning the

BBO angle, rotating the PBS and the HWF, adjusting the position of the crystals relative to the beam focus, and varying the beam size and intensity.

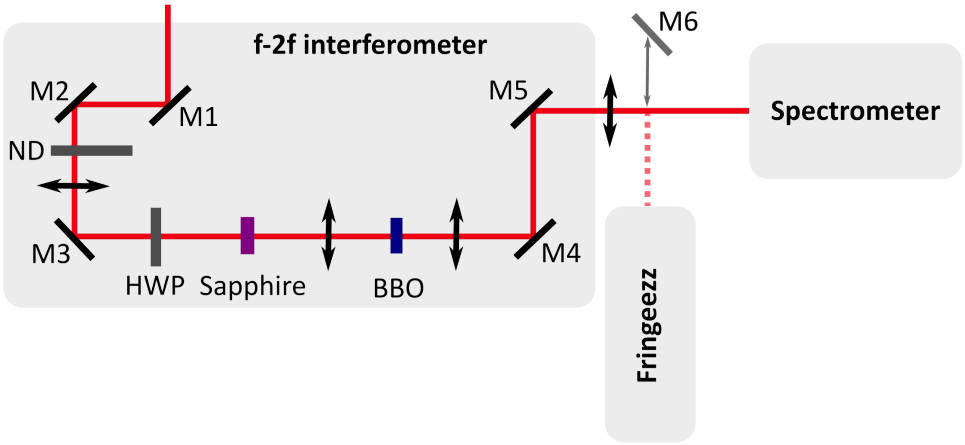

Figure 4.19: *Schematic drawing of the APS800 f-2f interferometer and the spectrometer/Fringeezz detector. ND = Neutral Density ; HWP = Half Wave Plate ; Mn = mirrors.*

If we use the standard spectrometer, the APS800 software analyzes the spectral fringes to retrieve the CEP (relative to an arbitrary offset): we select a spectral window with regularly spaced fringes and the software applies a Fourier transform to the signal. The modulus of the FFT peaks at a position corresponding approximately to the group delay between the f and the $2f$ components, while the phase of the FFT around this peak corresponds to the position of the fringes (*ie* the CEP).

Fringeezz

I added a flip mirror and a $f = +5cm$ (focal length) lens so that the beam could also be directed towards a faster detector (Fringeezz, *Fastlite*) instead of the *Thorlabs* spectrometer. The Fringeezz is a fast spectrometer with onboard calculation capabilities, consisting of a 25μm entrance slit, a transmission grating, a pair of lenses, a line-sensor (or 1D-pixel-array) and an electronic card to process the signal at kHz repetition rate. In our case, it requires approximately 15 fringes with 50% contrast ratio between 465 and 495 nm. If needed, the period of the fringes can be decreased by adding dispersion (e.g. with a thin silica plate) or increased by removing some (when possible). The integration time can be tuned from 1 to 25.5 microseconds and the Fringeezz needs to be triggered so that it is synchronized with the pulses arrival on the detector.

In the case of the Fringeezz, the CEP measurement is performed on a single period (2 fringes): the position of one fringe is divided by the period, which directly gives the CEP in radians (relative to an unknown offset). In order to optimize the signal and choose the fringe on which to perform the measurement, there is an analogue output that allows to read the sensor line and visualize the spectral fringes on an oscilloscope. The signal consists of a flat line lasting the integration time, then a positive bump indicating the start of the measurement, followed by a negative bump 50 microseconds later and fringes in between. We can select the nicest fringe by changing the parameter "measurement start" on the software (time read on the oscilloscope in microseconds).

This method is very easy and allows generating an error signal at a very high repetition rate. However, if the fringes are not perfectly periodic but chirped (due to chromatic dispersion in f-to-2f interferometer or oscillations in the spectral phase of the input pulse), then the Fringeezz can never exactly measure a CEP offset of π from the starting point but always a bit less.

Feedback loop for stabilization

We first implemented a feedback loop with the AOM used to modulate the oscillator's pump power, but it would destabilize the oscillator (mode-locking disappears when the pump power is changed too much), and induce some spikes in the CEP measurement, probably due to interferences between the fast feedback loop and this additional slow one, which both act on the same element (the AOM).

The alternative is to feedback to the Dazzler located inside the Femtopower, which worked much better in general. For fast CEP stabilization, there is a module that allows to arbitrarily control the relative timing between the acoustic carrier and the acoustic temporal envelope, without modifying the dispersion [89]. This CEP module can add a constant phase ϕ_{cor} to the RF signal (eq. 1.71) in order to compensate for the CEP drifts.

Low-jitter option calibration of the Dazzler

For our Dazzler model (HR45), a delay of the acoustic wave τ_{ac} will translate into a delay of the optical pulse $\tau_{opt} = \tau_{ac} 15.2\text{ps}/55.9\mu\text{s}$ and induce a phase jitter:

$$\Delta\phi_{\text{jitter}} = \frac{2\pi}{T}\frac{15.2\text{ps}}{55.9\mu\text{s}}\tau_{ac} \tag{4.9}$$

where T is the period of the laser, *ie* T = 2.7 fs at 800 nm. For example, a 1ns timing jitter of the acoustic wave will induce a CEP jitter of $\approx$ 630 mrad. This jitter originates from the internal sampling clock (sampling frequency $f_{\text{samp}} \approx 70MHz$) of the AOPDF itself. Whenever a pulse from the external kHz trigger signal arrives, if it is not synchronized with this sampling clock, then it is treated with a delay up to $1/70 \approx 14$ ns.

Fortunately, the AOPDF has a low-jitter option, where the acoustic wave launching time is precisely synchronized with the laser pulses: it synchronizes the Dazzler's internal sampling clock with the MHz pulse train coming out of the oscillator (we measured $f_{osc} = 79.7400$ MHz), as well as the kHz trigger from the master clock ($f_{\text{trig}} = 0.996$ kHz). This translates into the following equation: $f_{\text{trig}} = f_{\text{osc}}/m = f_{\text{samp}}/n$, with m and n integers, which means that a trigger event happens every time at the same time as an oscillator pulse and a sampling pulse. The quantity m corresponds to the number of oscillator pulses between two consecutive triggers ($m = f_{\text{osc}}/f_{\text{trig}}$ =80 060), whereas n is the number of sampling pulses between consecutive triggers. We chose n=84063. Doing this calibration helped reducing the temporal jitter between the acoustic wave and the kHz trigger by a factor of 100, from 3.4ns to 21ps RMS (measured with our *Keysight* oscilloscope, see section 4.1.3).

CEP stability measurement

The results of shot-to-shot CEP measurements (relative to an unknown offset) with the Fringeezz after the first CPA on a one minute time scale are shown in figure 4.20 and the corresponding noise frequency analysis is shown in 4.21, where the power spectral density (PSD, expressed in rad^2.Hz^{-1}) is calculated using Welch's method [267] and the integrated phase noise (IPN, in rad) corresponds to the square root of the integrated PSD:

$$\text{IPN}(f) = \sqrt{\int_f^{f_{\text{Ny}}} [\text{PSD}(\nu)]d\nu}, \tag{4.10}$$

with f_{Ny} the Nyquist frequency (500 Hz).

Figure 4.20.a corresponds to the case where the oscillator's CEP is actively stabilized, but there is no correction for the additional noise introduced by the first CPA. In this case, we obtain a standard deviation, defined as

$$\sigma_{\text{rms}} = \sqrt{\text{mean}(\phi_{\text{cep}}^2) - (\text{mean}[\phi_{\text{cep}}])^2}, \tag{4.11}$$

of approximately 300mrad. When we now activate the feedback loop on the Dazzler (fig. 4.20.b), we see that the slow variations are well compensated for, as indicated by the clear decrease of the PSD in Fig.4.21 in the low-frequency noise region (below 20Hz). Most of the fast noise is also reduced, but a peak appears around 173Hz, resulting in the same rms value. When the Dazzler low-jitter option is enabled (fig. 4.20.c), a lot of noise above 20Hz is now also reduced. Only a few peaks, notably one at around 300Hz, remain. The standard deviation is now $\approx$ 150mrad.

Finally, not represented here, the case where we do not stabilize the oscillator's CEP corresponds to a completely randomly fluctuating measured phase.

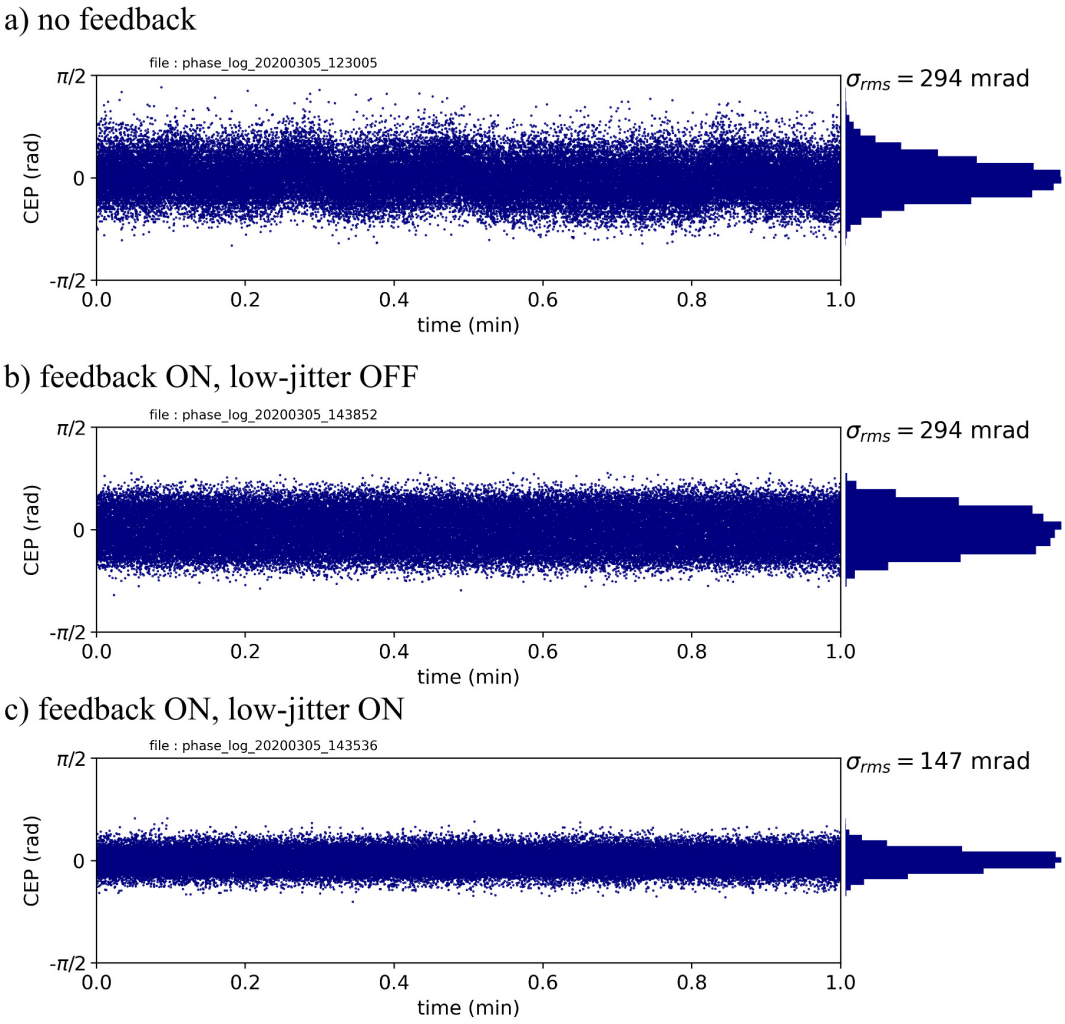

Figure 4.20: *Shot-to-shot CEP measurement after the first CPA, relative to an unknown offset value. The measurement was done using the f-2f interferometer APS800 from MenloSystems and the Fringeezz detector from Fastlite. a) only the oscillator's CEP is locked. b) the feedback loop to the Dazzler is ON but the low-jitter option of the Dazzler is disabled. c) the feedback loop to the Dazzler is ON and the low-jitter option is enabled.*

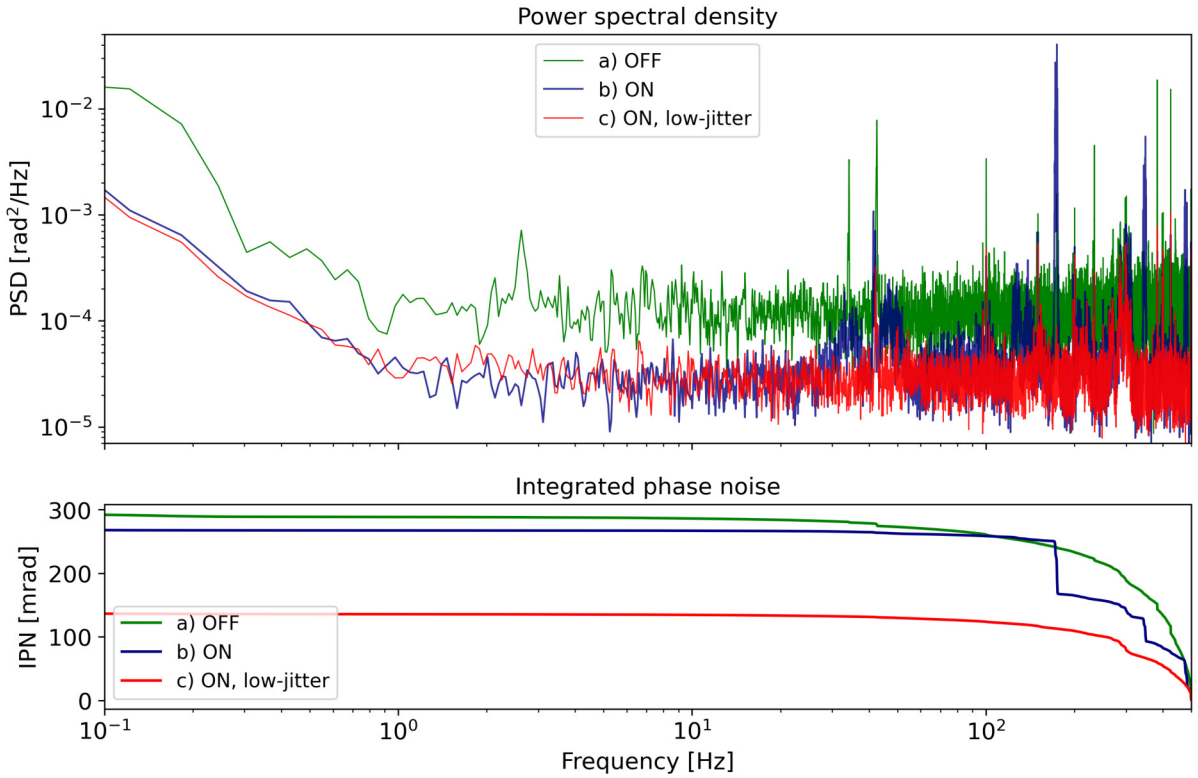

Figure 4.21: *Noise analysis of the shot-to-shot CEP measurements after the first CPA shown in fig. 4.20.*

Perspectives

A higher degree of stability can be achieved using a different scheme for the CEP stabilization of the oscillator, relying on an AOFS-based feed-forward loop (the principle is detailed in Appendix A). For example, in [163], the CEP was characterized at the output of a ten pass Ti:Sa CPA delivering 0.8mJ at 10kHz. The oscillator was CEP-stabilized through the AOFS and the CPA was CEP-stabilized using a f-2f interferometer, which also sent an error signal to the same AOFS. For this second feedback loop, the phase of the AOFS driving signal was controlled, in contrast with the MHz loop which acted on its frequency. The authors achieved a record CEP stability of 98mrad following this scheme.

In our most recent measurements at the output of the first CPA, we measured a 130 mrad RMS phase noise over extended periods of time, which is already very good, considering that we use a less modern technique.

4.2.5 Characterization of the CEP stability at the end of the chain

.

In general, we do not measure or stabilize the CEP at the output of the first CPA, but only at the end of the chain. After post-compression, the CEP of the short pulses, whose spectrum already spans about one octave, is measured with a home-made f-2f interferometer, where no sapphire crystal is needed. To perform the measurement, a wedge reflexion of the prepulse (see fig. 3.12) is sent out through a transparent window for the measurement.

Status of the CEP stability before I arrived

During Frederik's PhD thesis, the CEP was characterized as well. At that time, there was only a slow (100ms cycle time) feedback loop to the AOM in the oscillator. At the beginning of

his PhD, he measured a 360mrad rms CEP noise ([25], p.80), but the measurement was made with a 4 ms integration time (*ie* each measured CEP value is an average over 4 consecutive shots), and the laser chain did not include the vacuum-integrated post-compression stage yet. Moreover, by the end of his thesis, the pump laser in the first CPA had become unstable (which is why we replaced it, see section 3.2.2) and the CEP noise had even increased to 500mrad, measured with the same kind of average. In fact, in his own words, it had become difficult to talk at all about a stable CEP.

Current status of the laser's CEP stability

With the new Fringeezz/Dazzler kHz feedback loop implemented and after all the improvements of the laser described in chapter 3, the CEP stability became much better. The results of shot-to-shot measurements are shown in fig. 4.22 and fig. 4.23, corresponding to a ≈ 370mrad rms residual noise, measured without any averaging over 1 hour.

Below ≈80 Hz, vibrations are absorbed and dissipated by our optical tables (*Newport RS4000*) and most of the remaining CEP noise is above 100 Hz, which is hard to stabilize for a kHz laser. The main frequency components of the PSD are marked in fig. 4.23.b. 50Hz corresponds to the grid frequency in Europe, which can also induce noise at twice the frequency, *ie* 100Hz, if full wave rectifiers are used, as well as harmonics of these frequencies. Perhaps a more careful shielding of the electronic components and cables could help reducing those peaks. The component at 300Hz is quite significant and it might be worth investigating further on its origin. We tried turning off the air conditioning and some chillers but could not find its source so far. Nonetheless, adding vibration damping materials under chillers, vacuum pumps and computers in the room, but also under the table legs might help. The mechanical stability of key components such as the gratings of the second CPA compressor could also probably be improved, e.g. using better mounts.

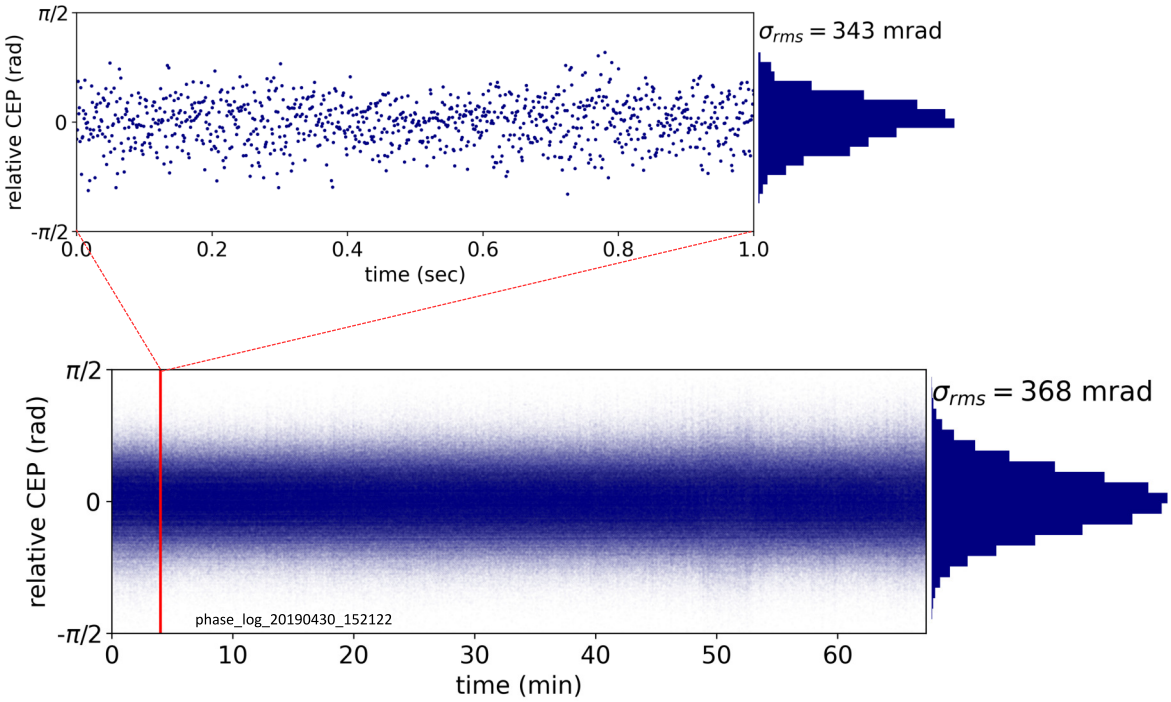

Figure 4.22: *Shot-to-shot CEP measurement (relative to an arbitrary offset) at the end of the laser chain over one hour (bottom) with a zoom on a 1 second time window (top).*

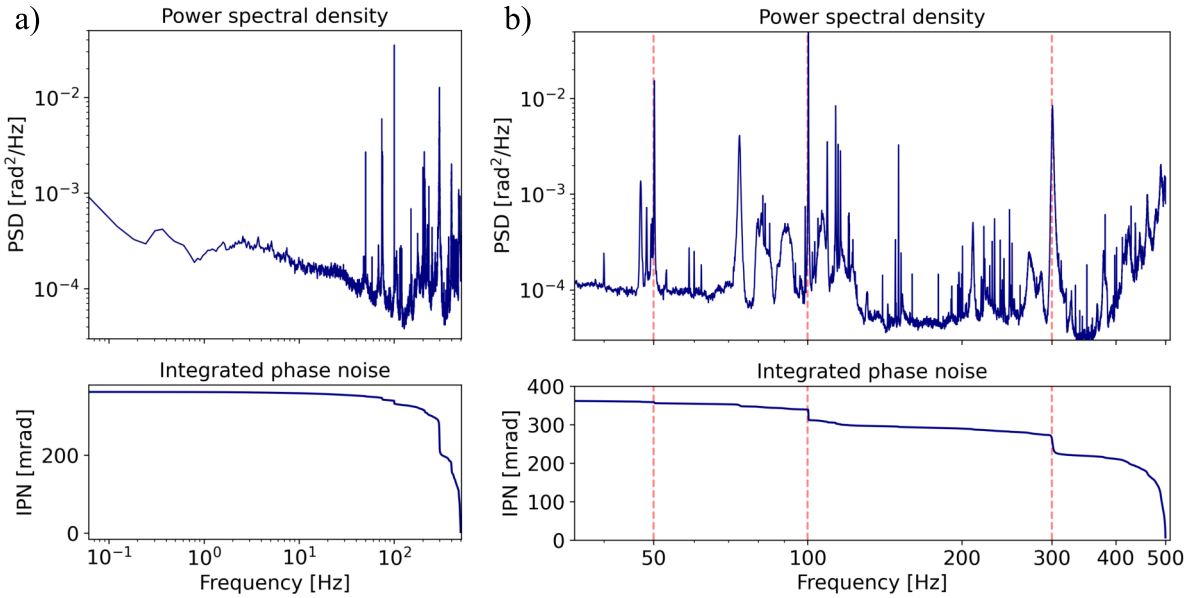

Figure 4.23: *Noise analysis of the shot-to-shot CEP measurement (relative to an arbitrary offset) at the end of the laser chain shown in fig. 4.22. a) from ≈0.06Hz to 500Hz b) from 35 to 500Hz. The main noise contributions are marked by vertical dashed red lines.*

Effect of averaging on the rms value

To compare the two measurements (before and after), I averaged another shot-to-shot measurement shown in 4.24.a over 4 points. It results in a 152 mrad rms CEP noise value, as shown in 4.24.b, that is, half what we truly have! CEP stability measurements are often presented with such kind of averages, thus one must take it into account when comparing performances.

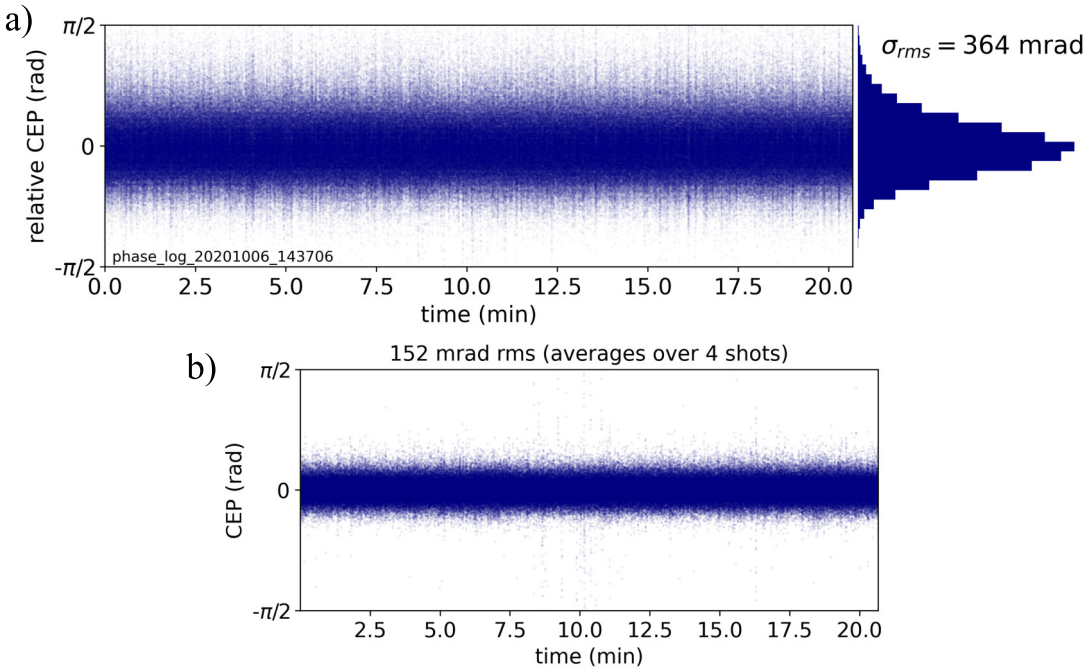

Figure 4.24: *a) Single-shot CEP measurement at the end of the laser chain over 20min. b) Representation of CEP data with a 4-point average.*

4.3 Qualification of laser performance through laser-plasma electron acceleration

Under the direction of Jérôme Faure, laser-plasma electron acceleration experiments were performed by Dominykas Gustas, who was a PhD student at that time. We were able to observe CEP effects on the electron energy spectra for the first time and published the results in [198] together with a description of the laser system, of which I am the first author. The strong CEP dependence of laser-plasma electron acceleration driven by few-cycle pulses was then confirmed in a second, more recent experiment conducted by Julius Huijts, Lucas Rovige and Joséphine Monzac. In the frame of my thesis, these experiments essentially consist of a validation of the laser developments, therefore I will not go into too much details about laser-plasma electron acceleration.

4.3.1 Introduction to LWFA

When an intense laser pulse is focused in a gas jet, it turns it into an underdense plasma, sets the electrons into motion (and the ions, indirectly), and generates plasma waves in its wake. Under the right conditions, some electrons can surf the wakefield and be accelerated over very short distances up to the GeV energy-range [140]. This mechanism is called laser-wakefield acceleration (LWFA).

If most laser-plasma accelerators rely on 100 TW or PW peak power lasers at low repetition rate, it is also possible to use sub-10 TW laser systems which can in turn work at higher repetition rates, thus ensuring a higher stability level. Although this is done at the cost of reduced electron energy, we can still reach the few-MeV energy range, which is well suited for ultrafast electron-diffraction or pulsed radiolysis. A particularly interesting regime, called the "bubble" regime or "blowout" regime [212], is capable of producing low divergence, quasi-mono-energetic electron beams [80].

Bubble regime

In this regime, the laser pulse drives a plasma wakefield which has the shape of a quasi-spherical cavity (see fig. 4.25). The key to scaling the experiment is to find a configuration where the laser pulse is resonant with this cavity *ie* where the transverse dimension of the beam (its waist w_0) and the laser pulse longitudinal extent ($c\tau$, with τ the pulse duration) are comparable to half the plasma wavelength $\lambda_p/2$. Here, $\lambda_p = 2\pi c/\omega_p$, with ω_p the plasma frequency (see eq. 2.4), which only depends on the plasma electron density. This can be summarized as [160]:

$$c\tau \approx \frac{w_0}{\sqrt{2}} \approx \frac{\lambda_p}{2}. \tag{4.12}$$

For few-mJ, kHz repetition rate laser systems such as the *Salle Noire 2* laser, one can show that this resonant condition implies working with near-single-cycle duration. For example, τ =4 fs results in $\lambda_p \approx 2.4$ μm, corresponding to a ∼micrometer laser spot size. This also implies that the plasma electron density should be very high, of the order of $\sim 10^{20}\text{cm}^{-3}$ or more, and the gas jet dimensions should be comparable to the Rayleigh length *ie* of micrometric size. Eventually, all this translates into a challenging gas nozzle design and efficient gas extraction.

Injection Schemes

There are different mechanisms which lead to the trapping of electrons inside the plasma cavities. An overview can be found in [79]. The most common mechanism is self-injection and consists of trapping background plasma electrons in the plasma wave. The mechanism is rather complex and results from a succession of nonlinear effects, such as self-focusing, spectral broadening and self-steepening. Typically, self-injection occurs when the plasma wave amplitude reaches very high levels [39], close to the "wave-breaking" threshold. Wave-breaking occurs

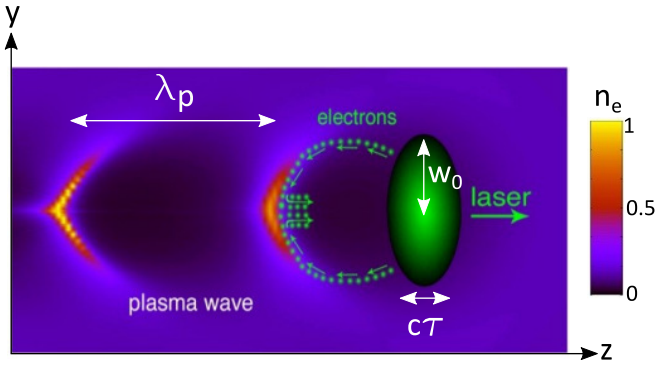

Figure 4.25: *Illustration of the resonant bubble regime. The color scale represents the electron density. Adapted from [167].*

when a large amount of wave energy is transformed into turbulent kinetic energy. It is similar to the breaking of water surface waves on a coastline, and corresponds to the point where the crest of the wave overturns. The quality and stability of the accelerated electron beams can be improved by triggering the injection, e.g. using colliding laser pulses or using negative plasma density gradients to decrease the plasma group velocity.

Another mechanism is ionization injection [49]. The idea is to use a gas with a high atomic number Z. In this case, the first levels of ionization can occur at low intensity, as soon as the laser pulse's leading edge arrives in the gas jet. The gas jet is thus ionized quite early and a large amount of electrons become available to form the accelerating structures. Then, at the peak of the laser, the intensity is high enough to ionize electrons from inner shells. Electrons that are born on a trapped orbit will be injected into and accelerated by the plasma wave.

We use nitrogen as interaction medium because it releases immediately 10 electrons when the laser pulse arrives, thus allowing to reach high electron densities while keeping a reasonably low background pressure (which is of course better for preserving the laser pulse spatio-temporal quality). The atomic number of nitrogen is $Z = 7$ and the ionization energies and corresponding laser intensities are shown in table 2.3.

For our laser intensity ($\sim 10^{18}$W.cm^{-2}), nitrogen atoms are rapidly ionized up to N^{5+} through barrier-suppression ionization. Then, when the peak of the laser arrives, N^{5+} ions can be further ionized via tunnel ionization and inject electrons into the plasma bubble (see fig. 4.26).

In general, ionization injection results in higher quality electron beams than self-injection, with a lower energy-spread.

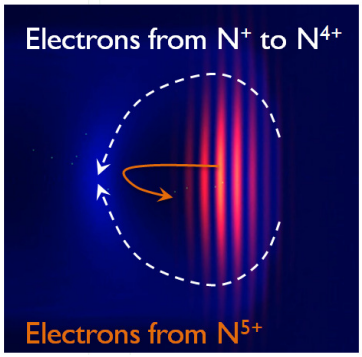

Figure 4.26: *Illustration of the ionization injection mechanism in the case of nitrogen. Courtesy of Jérôme Faure.*

4.3.2 Influence of the CEP

First, it is important to understand that the CEP does not always induce any visible effect. Indeed, effects can only be observed if the CEP remains constant over the electron injection length. As we have seen, the CEP slips as it propagates through the plasma due to the difference between the phase and the group velocity, with the phase slippage length (eq. 1.29) $L_{\mathrm{CEP}} = \lambda_0/(n_g - n_\phi)$. The refractive index of a plasma (see eq. 2.7) reads

$$n(\omega) = \sqrt{1 - \frac{\omega_p^2}{\omega^2}} = \sqrt{1 - \frac{n_e}{n_c(\omega)}}. \tag{4.13}$$

Therefore the difference between the phase and the group index is (see eq. 1.32):

$$n_g - n_\phi = \omega \frac{dn(\omega)}{d\omega} = -\frac{n_e \omega}{2} \times \frac{d}{d\omega}\left(\frac{1}{n_c}\right) \times \left(1 - \frac{n_e}{n_c}\right)^{-1/2}. \tag{4.14}$$

Using $d(n_c)/d\omega = 2n_c/\omega$ and assuming that $n_e << n_c$, this can be simplified:

$$n_g - n_\phi \approx \frac{n_e}{n_c} \tag{4.15}$$

and therefore,

$$\boxed{L_{\mathrm{CEP}} \approx \lambda_0 \frac{n_c}{n_e}}. \tag{4.16}$$

The critical density n_c for 800nm is equal to $\approx 1.7 \times 10^{21}\mathrm{cm}^{-3}$ (eq. 2.8). Considering the typical ratio $n_e/n_c \sim 0.1$ in our LWFA experiments, there is a 2π CEP shift over a distance of approximately 8 μm. Thus, for $\sim 100\mu$m wide plasma jets such as the ones used in our experiments, it is very difficult to see any effect of the CEP, unless we precisely localize the electron injection.

Numerical simulations of LWFA in the few-cycle regime predicted a strong influence of the CEP under certain conditions. In [157], a CEP-dependent electron beam pointing and energy spectrum was predicted in the case of 5 fs pulses, where the dominant mechanism was ionization injection, with an injection length $< 10\mu$m [112, 81]. Other early simulations [293, 192] showed that single-cycle laser pulses can cause significant asymmetries of the plasma wakefield, which are CEP dependent. This can in turn cause the off-axis injection of sub-fs electron bunches into the bubble [126, 283]. As a result, after being accelerated, the electrons leave the plasma with a CEP-dependent beam pointing.

However, so far, no clear observations of such CEP effects had been made experimentally.

4.3.3 First experimental observation of CEP effects

Description of the experiment

In the first experiments, 3.9 fs laser pulses were focused into a gas jet with a F/2, 90° off-axis parabola to a near-Gaussian, $2.5 \times 2.8\mu$m FWHM focal spot. With 2.4 mJ on target, this corresponds to a relativistic peak intensity $I \approx 5 \times 10^{18}\mathrm{W.cm}^{-2}$ (see fig. 4.27). A supersonic nitrogen (N_2 molecules) gas jet was used, and the gas density profile was characterized with a quadriwave lateral shearing interferometer (SID4 HR by *PHASICS*) using Abel inversion. At a distance $\approx 140\mu$m from the nozzle exit, the estimated peak density was $n_e \approx 2 \times 10^{19}\mathrm{cm}^{-3}$, while the gas jet radius at $1/\mathrm{e}^2$ was ≈ 80 μm. This electron density n_e is lower than usual and corresponds to only $\approx 1\%$ of the critical density, which relaxes the constraint on the electron injection length, although at the cost of reduced achievable electron energy.

A magnetic electron spectrometer (a pinhole, a pair of permanent magnets and a phosphor screen) was used to measure the electron spectra.

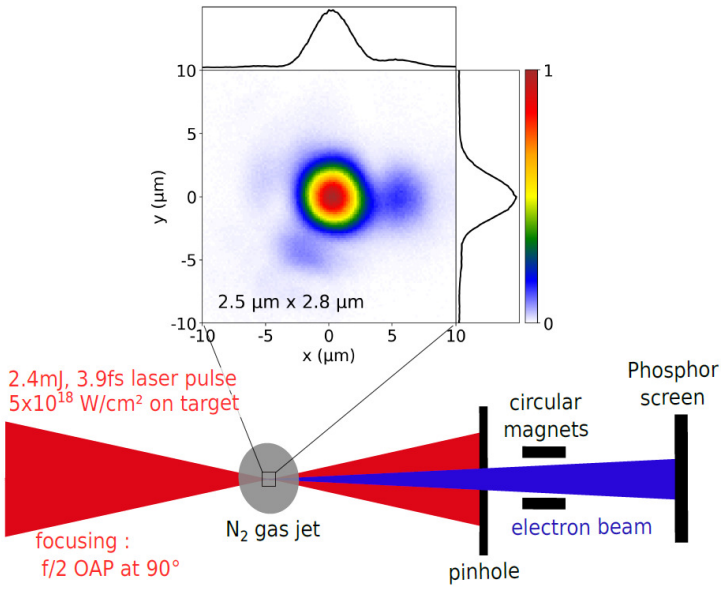

Figure 4.27: *Schematics of the experiment (top view) and picture of the laser focal spot.*

Results: first observation of CEP effects on the electron spectra

The results, which can also be found in [81] and [198], are presented in figures 4.28 and 4.29. The first figure 4.28 shows the electron spectra (top) while the CEP was cycled from 0 to $\pi/2$ (bottom). For this experiment, the fast feedback loop had not been implemented yet, and the CEP was measured with the APS800 software, while the CEP control was achieved by modulating the oscillator's pump power through the AOM. The CEP RMS noise was $\leq$ 200 mrad, measured with a 30-point average.

The effect of the CEP on the electron spectrum, more clearly visible in fig 4.29 showing integrated spectra, is very pronounced at the beginning: for a relative CEP of 0, the spectrum is peaked around 0.5 MeV and displays another smaller feature around 0.65MeV. These features immediately disappear when we change the CEP by $\pi/2$. Thus, although the effect is washed out towards the end of the scan, which is likely due to small fluctuations or drifts of laser properties, or the plasma density profile itself, we were able to see correlations between rapid CEP changes and rapid changes in the electron spectra for the first time.

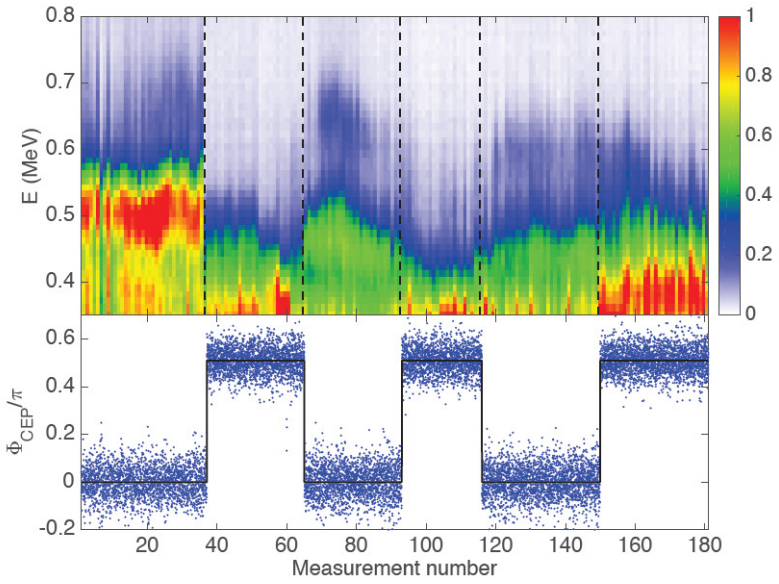

Figure 4.28: *Top: electron spectra. Each spectrum is integrated over 500 consecutive laser shots. Bottom: measured CEP value relative to an unknown offset (blue dots) and command value (solid black line). Each CEP value is averaged over 30 consecutive laser shots.*

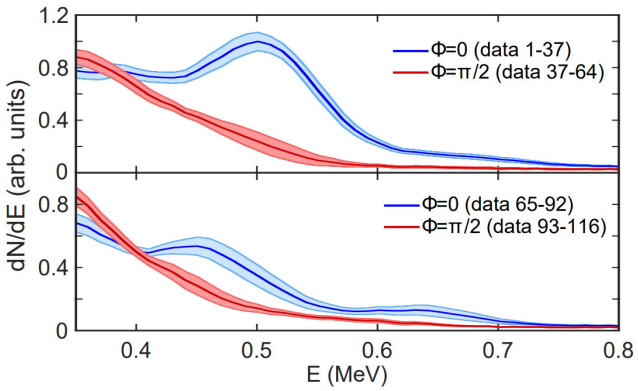

Figure 4.29: *Averaged spectra from the first (top) and second (bottom) CEP cycles shown in fig. 4.28. The solid dark lines represent the average spectra, whereas the light areas indicate the standard deviation.*

4.3.4 Second experiment with CEP dependent electron beam pointing

The strong CEP-dependence of LWFA driven by few-cycle pulses was confirmed in more recent experiments [127] (this time with the kHz Fringeezz/Dazzler feedback loop for CEP control), where the pointing of the electron beam in the polarization plane (s-polarization) was proven to be CEP dependent. In these experiments, the conditions were similar than in the previous one, except the peak plasma electron density was higher: $n_e \approx 1.4 \times 10^{20}\text{cm}^{-3}$, and the dominant injection mechanism was self-injection, according to simulations. As a result of this higher electron density, the electron peak energy was above 1 MeV, which is typical for our LWFA experiments.

Experimental results

Changing the CEP induced some significant beam pointing variations of $\approx$ 15mrad in the plane of polarization (y axis), corresponding to $\approx$ 30% of the beam divergence (50 mrad). The electron beam pointing as a function of the CEP is shown in 4.30, and we see that the two extrema occur for CEP values spaced by π. In contrast, the beam pointing was very stable along the x axis (except for a slow drift), with a pointing jitter below 2 mrad rms.

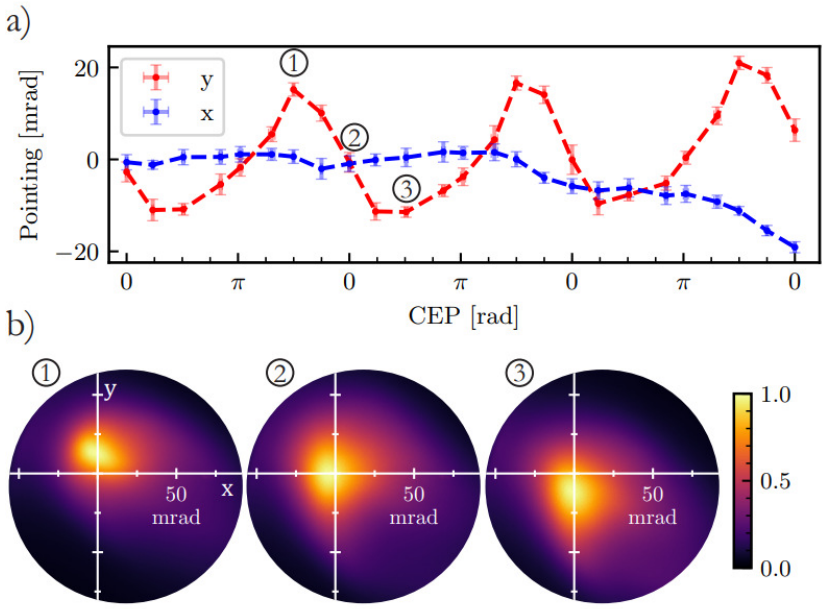

Figure 4.30: *Experimental results showing changes in electron beam parameters as the CEP is varied over three cycles of 2π. a) Pointing of the electron beam in the plane of polarization (y, red) and in the perpendicular plane (x, blue). b) Typical images of the electron beam (acquired in 200 ms, which corresponds to 200 shots) at a high (1), central (2), and low (3) beam pointing. Results published in [127].*

Interpretation

Numerical simulations were made by Lucas Rovige and Julius Huijts to understand the electron dynamics. Here, although the electron injection does not occur over a distance that is short compared to L_{CEP} due to the high electron density n_e, the electron dynamics is governed by a factor which is localized to a fraction of L_{CEP}: the asymmetry of the wakefield. In fact, due to a strong redshift of the laser during propagation in the plasma, the wakefield asymmetry even increases ($\propto \lambda^3$) and thus triggers the very localized injection of electron bunches [126].

In the simulation, four sub-femtosecond electron bunches are injected, two of which containing most of the charge. For example, for an initial CEP $\phi = \pi$ or 0, a first injection event occurs off-axis in the asymmetric wakefield, in the polarization plane. Then, the pulse

propagates and the CEP slips by π, leading to a second injection event on the other side of the wakefield, resulting in the emission of two spatially separated electron beams in the polarization plane. Artificially adding a 15 mrad rms beam pointing fluctuation to simulate the experimental data (which were averaged over 200 laser shots) allowed to reproduce very well the observed behavior (fig. 4.31). The amplitude of the oscillations of the beam with respect to the CEP were ≈ 9 mrad (fig. 4.31.a), which is comparable to what was experimentally obtained.

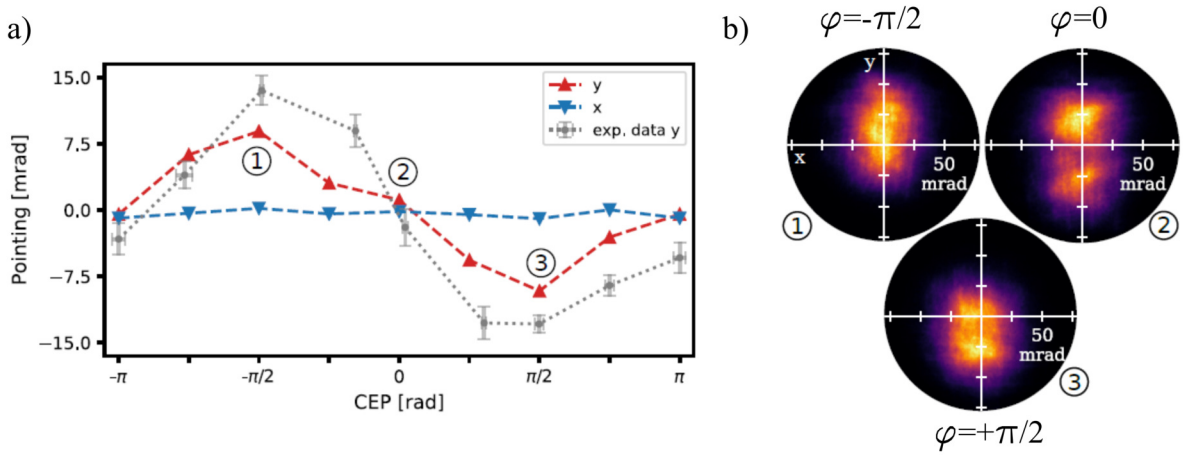

Figure 4.31: *a) Simulated electron beam pointing oscillations (with an added artificial 15mrad beam pointing noise) in blue and red, and experimental data in gray. b) Simulated electron beams for 3 different CEP values with additional 15mrad noise in the beam pointing. Results published in [127].*

4.3.5 Conclusion

My work on the control and stabilization of the CEP has allowed the observation of CEP effects in a laser wakefield accelerator for the first time. The CEP allowed controlling the injection of the electrons into the plasma bubble, thus influencing the energy spectrum and the angle of emission of the electron beam. This is a key step towards the applications of the electron beams, as the precise control of the electron injection permits to improve the quality and shot-to-shot stability of the beam.

Furthermore, the recent laser developments described earlier in this manuscript (Chapter 3) allowed reaching a very high degree of stability and good day-to-day reproducibility of the electron beam. In particular, the energy was measured over 5 hours of hands-off operation (reported in [223]) and, except from a slow drift, the short-term rms variations were only a few percent of the peak energy (2.1MeV).

This is very promising and the electron beam should soon be used in applications, such as ultrafast electron diffraction.

4.4 Conclusion and perspectives

To conclude, we have implemented a new kHz loop to measure and control the CEP at the full repetition rate of the laser. Together with the laser developments described in Chapter 3, this resulted in a shot-to-shot CEP stability of ≈400 mrad rms at the end of the chain over extended periods of time, enabling us to observe CEP effects in relativistic laser-plasma interactions for the first time.

Other laser systems delivering TW peak power, few-cycle pulses with very good CEP stability levels at kHz repetition rate exist. For example, in [38], the authors reported on an OPCPA laser system delivering sub-9fs (corresponding to 3 optical cycles at the central wavelength of 880nm), ≈50mJ pulses at 1 kHz repetition rate with sub-220 mrad CEP stability (a former version of the SYLOS laser installed at the ELI-ALPS facility). Another TW-class laser system was reported in [107], delivering 17.8fs (corresponding to ≈ 7 optical cycles at 800nm), 16mJ pulses at kHz repetition rate with a shot-to-shot CEP stability of 350mrad rms. However, the pulse duration achieved by those systems remains relatively far from the near-single-cycle regime. On the other hand, some multi-TW laser systems with high contrast-ratios do reach the sub-2 [221, 183] or sub-3-cycle [139] duration, and can be focused to relativistic intensities to efficiently drive plasma mirrors, but do not exhibit CEP stability, and only work at a repetition rate of a few Hertz.

Overall, there are currently no other high repetition rate, TW-class laser systems combining all the features of the *Salle Noire 2* laser, *ie* a very high contrast ratio, a 1.5 optical cycle pulse duration together with CEP control, and relativistic intensity achievable. Although better CEP stability levels are achieved by other groups, the CEP stability reached on our laser system is sufficient to clearly influence the dynamics in laser-matter interaction experiments, as we have seen in section 4.3 and as we will see again in the last chapter. This laser system is thus ideal for studying waveform-dependent relativistic laser-plasma phenomena.

Generally speaking, the CEP stabilization of such laser systems involves the systematic elimination of sources of both electronic and mechanical noise and is a lengthy process. Nonetheless, there is still room for improvement: one way to decrease the residual CEP noise would be to replace the oscillator with its newer version including the AOFS, and further improvement (in terms of stability and achievable energy) should arise from the future implementation of a cryo-cooled single-stage amplifier in the second CPA, which is currently under development.

Chapter 5

Relativistic interaction with plasma mirrors: physical mechanisms

"If you can't explain it simply, you don't understand it well enough".
Albert Einstein

Another important part of my work concerns the experimental investigation of the laser interaction with plasma mirrors at high repetition rate in the relativistic regime, which is a promising source of particle beams and attosecond light pulses via HHG.

There are many reasons why studying the interaction of lasers with plasma mirrors is interesting. The main motivation is of course to generate attosecond pulses via HHG in order to enable attosecond pump-probe experiments with a higher flux than that allowed by gas harmonics. Plasma mirrors are also a source of charged particles, and several observations of electron and proton beams were made. Looking at charged particles emitted from the target helps understanding the laser-plasma dynamics and better control the HHG, but the particle beams are also interesting for applications themselves. Another reason is simply that plasma mirrors are a simple testbed for modeling and understanding laser-plasma physics.

In this chapter, I will review the physical mechanisms that have been identified so far. First, I will summarize what the scientific community knows about HHG in the sub-relativistic regime, which has already been studied in detail, in the PCO group and elsewhere. Then, we will see how harmonics can be generated when the laser intensity becomes relativistic. Different mechanisms have been proposed theoretically, and experiments made so far in these extreme regimes of light-matter interaction tend to confirm most of their predictions. In a third section, we will review the different electron acceleration mechanisms that have been identified and finally, I will briefly summarize previous observations of proton emission on the front side of the target, along the normal direction.

5.1 HHG mechanism at sub-relativistic intensity

We first focus on HHG at sub-relativistic intensity (I$\lesssim 10^{18}$W.cm^{-2}, see section 2.4).

Resonant absorption

At moderate laser intensity ($I \sim 10^{16} - 10^{17}$W.cm^{-2}) and relatively smooth density gradients (when the scale length $L_g \approx 0.1 - 0.2\lambda$), the dominant mechanism for HHG is linear mode conversion of plasma waves, excited by the laser through resonant absorption [91, 93], into light. In this case, the electrons do not escape into vacuum ; they remain within the density gradient, where they excite plasma oscillations [246].

Coherent Wake Emission

For higher laser intensities and very steep plasma gradient scale lengths, resonance absorption is no longer relevant and the dominant absorption mechanism is Brunel absorption [36] or vacuum heating [104]. Under the influence of the laser electric field, plasma surface electrons are accelerated toward vacuum beyond the gradient scale length, following different trajectories, while the heavier ions are considered static. This creates a charge separation in space, which tends to pull the electrons back into the plasma. As the laser electric field sign is reversed, its influence helps accelerating electrons further into the plasma, up to the critical density surface and beyond. Once the electrons have passed the critical density surface, they are no longer under the influence of the laser electric field and their kinetic energy, acquired during their excursion into vacuum, is transferred to the plasma.

The timing and the extent of their excursion towards vacuum are linked and directly depend on the instantaneous E field amplitude and sign. Electrons born at a peak of the E-field amplitude will be going further, which takes more time, but will also gain more kinetic energy, while some born at a lower E field amplitude will not go as far but remain slower. In the end, as the electrons come back into the plasma, their different trajectories will cross inside the plasma gradient, resulting in the formation of electron density peaks inside the plasma (fig. 5.1).

This electron density perturbation propagates and excites plasma waves at the local plasma frequency in its wake. The thus generated plasma waves then emit photons at the local plasma

frequency through inverse resonant absorption, which coherently combine to form attosecond pulses. The emission of HHG driven by Brunel electrons is called 'Coherent Wake Emission' or CWE and I will detail its characteristic features in the following.

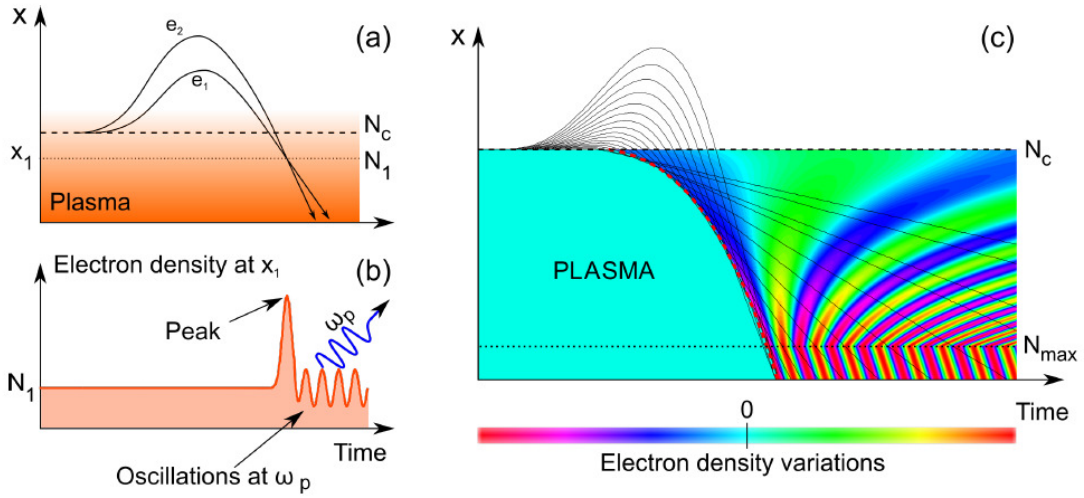

Figure 5.1: *Principle of HHG in the CWE regime. a) Two electron trajectories are represented, which cross into the plasma gradient. b) the electron density peaks propagate and generate oscillations at the local plasma frequency ω_p, leading to the emission of photons at the same frequency. c) Electron density variations in the plasma due to the propagation of the electron surdensity layer (red dashed line). The electron trajectories are displayed in solid black lines. Reprinted from [168].*

Plasma gradient scale length

In order to maximize the HHG efficiency, the plasma gradient scale length must be typically shorter than the excursion length of the electrons towards vacuum. If the gradient is too long, the electronic overdensity does not have the time to propagate up to the highest density part of the plasma before the end of one optical cycle, and no high harmonics are generated. The HHG efficiency decrease with increasing L_g is easily observed experimentally. In fact, at long gradients, some electrons are even able to escape the plasma and are ejected into vacuum, resulting in the emission of an electron beam which is anticorrelated with the XUV emission.

On the other hand, if the gradient is too steep ($L_g < \lambda/300$), the plasma oscillations are dissipated and strongly damped (Landau damping) [246], which is much harder to observe experimentally, as it requires a very high laser contrast (it was nonetheless already observed, e.g in [21] p.70, fig 4.9.b, using low-intensity laser pulses with a_0=0.35 and a prepulse intensity of 1.3×10^{14}W.cm^{-2}).

The typical optimum gradient scale length for CWE harmonics is $L_g \sim 0.01\lambda$. During our experiments at sub-relativistic intensity, we never observed a non-zero optimum: HHG was always most efficient for the steepest density gradient that we can achieve (*ie* for the shortest prepulse delay (see 2.2.2), or equivalently without prepulse), and then the signal dropped with increasing L_g. Therefore, we can conclude that our driver pulses' finite contrast induces a minimal plasma density gradient scale length L_0 which is at least $\sim \lambda/100$, in spite of the XPW filter.

Spectrum cutoff

The created photons are limited in energy by the maximum plasma frequency

$$\boxed{\omega_{\mathrm{p,max}} = \sqrt{\frac{n_{\mathrm{e,max}} e^2}{e_0 m_e}} = \omega_0 \sqrt{\frac{n_{\mathrm{e,max}}}{n_c}}} \tag{5.1}$$

In the case of a fully ionized target, $\omega_{\mathrm{p,max}} \approx 46$ PHz, corresponding to a photon energy of 30 eV, which sets the maximum limit for the emission of harmonics via the CWE mechanism. Any harmonic line observed beyond 30 eV therefore cannot be attributed to this mechanism.

Intensity requirements and efficiency

The required intensity is typically $\sim 10^{17} - 10^{18}\mathrm{W.cm}^{-2}$. The CWE conversion efficiency is constant *ie* it does not vary with the laser intensity, therefore the CWE signal is expected to increase linearly with the driving laser intensity. This was observed both theoretically [246] and experimentally [214].

Periodicity

Unlike gas harmonics where the process is repeated twice per laser cycle, here the situation is non symmetric and the process occurs once per laser cycle. Therefore, the harmonics are spaced by the driving laser frequency, and we observe both odd an even orders. Since there is no CEP shift from one cycle to the next, we expect a null offset of the frequency comb.

Atto and femto chirp

Let us consider a single optical cycle n of the driving laser pulse. Because each photon energy originates from a different plasma wave frequency and therefore comes from a different depth inside the plasma, each photon energy is emitted at a different time within one laser cycle $t_n(\omega) \neq t_n(\omega')$. Consequently, the individual attosecond pulses (emitted once per laser cycle) are chirped.

Now, if all the photons with a frequency ω were emitted in a perfectly periodic way, from one optical cycle n of the driving laser to the next $n+1$ (that is, $t_n(\omega) = t_{n+1}(\omega)$), we would observe very thin harmonics, like the convolution of a Dirac comb with the femtosecond pulse envelope. However, when the driving pulse only contains a few cycles, each optical cycle has a very different maximum field amplitude from its neighboring cycles, thus resulting in a cycle-dependent emission time of a given photon frequency ($t_n(\omega) \neq t_{n+1}(\omega)$). This variation of the XUV emission time delay within the femtosecond pulse envelope is commonly called the "femtosecond chirp" (although this term may be misleading as it is not an actual femtosecond chirp) and results in the broadening of the harmonics lines (detailed studies and explanations can be found in the thesis of A. Malvache [168]). Interestingly, this femtosecond chirp can be precompensated for by positively chirping (literally, this time) the driving pulse [179, 169, 214].

This hand-waving explanation can also be derived from the Brunel model, as done in [169]. The authors found the following analytical expression for the crossing time of the electron trajectories originating from the nth laser optical cycle of period T_L:

$$\frac{t_c(n,\omega)}{T_L} = n + 0.307 + 0.725\left(\frac{x_\omega}{\lambda a_0 \sin\theta}\right) \tag{5.2}$$

where x_ω is the position where the XUV radiation of frequency ω is born, measured with respect to the reflective surface (*ie* the surface where $n = n_c \cos^2\theta$) position. From this equation, we see that t_c depends on the intensity through a_0 and therefore varies from cycle to the next. We also see that the cycle-to-cycle delay of the emission time is reduced for sharper plasma density gradients (because x_ω decreases and the attosecond pulses are emitted earlier).

Divergence

The XUV source on target can be pictured as a coherent [245] superposition of point sources with a well-defined phase relation between them. Since the XUV photon emission time is intensity-dependent, it occurs sooner in the center of the beam than in its periphery, resulting in a convex XUV beam. Studies have shown that when the focus of the laser beam is placed beyond the target surface, this spatial phase can be pre-compensated for, resulting in a lower XUV beam divergence [213]. The plasma surface inhomogeneities, as well as variations in

the driving laser intensity distribution in focus, will translate into additional XUV wavefront aberrations.

Thus, apart from the attosecond chirp described above, which results in the temporal stretching of the individual attosecond pulses, a main drawback limiting the applicability of this CWE mechanism as an XUV light source is its large beam divergence. Indeed, the more divergent, the harder is it to refocus the XUV beam for applications.

Nonetheless, means of reducing the divergence have been identified, e.g in [210], where the authors were able to obtain a nearly diffraction limited XUV beam.

5.2 HHG mechanisms at relativistic and ultra-relativistic intensities

The analytical modeling of harmonic emission from plasma mirrors at relativistic intensities ($I \sim 10^{19}\text{W.cm}^{-2}$) has evolved over time, starting from the Doppler effect, evolving into the ROM model, which describes the harmonics generation qualitatively. Further developments of the model even allowed to predict the shape of the harmonics spectrum. The latest theoretical developments now include energy storage into the plasma, or even propose a mechanism based on synchrotron emission. However, these last models are more relevant for ultra-relativistic intensities ($\sim 10^{20} - 10^{23}\text{W.cm}^{-2}$). Finally, all these models provide some very interesting insights into the physics but their predictions are not as precise as numerical simulations.

5.2.1 Periodic Doppler frequency upshift

Doppler effect

The first models [270, 41] attributed HHG to the Doppler effect produced by the relativistic oscillations of the reflective plasma surface. Let us consider a plasma with a step-like density profile, ions are immobile and the plasma electrons move at the velocity βc along the direction $-\vec{e_x}$ (see. figure 5.2). By introducing the concept of retarded times (the signal received by an observer located at a position x at a time t depends on the position x_e and time $t_{ret} = t + (x - x_e)/c$ where the signal was created), one can show [247] that a normally incident electromagnetic wave with frequency ω propagating along the x-axis will experience a frequency shift

$$\frac{\omega_{ref}}{\omega} = \frac{1+\beta}{1-\beta} \approx 4\gamma^2, \tag{5.3}$$

where the last result corresponds to the ultra-relativistic limit when the mirror moves towards the observer ($\beta \approx 1$), therefore setting an upper limit for the harmonic order:

$$\boxed{n_{max} = 4\gamma_{max}^2}.$$

ROM model

A few years later, Lichters et al [156] developed this idea further and proposed a 1D analytical model which they called the ROM (Relativistic Oscillating Mirror) model. This model describes the harmonic generation at high intensity by Doppler effect using a linearly polarized laser beam with oblique incidence θ on the target, and the plasma electron density is modeled with a step function.

BGP or γ-spikes model

In 2004, Gordienko *et al* [110] proposed that at each moment of time there is an apparent reflection point (ARP) at which the energy flux vanishes (thus assuming there is no energy transferred to the plasma). Two years later, following this idea, the Baeva-Gordienko-Pukhov

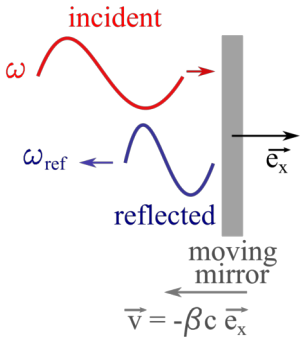

Figure 5.2: *Doppler effect on a laser beam induced by a relativistically moving mirror.*

(BGP) theory [14] provided a full analytical description of the ROM model for ultrarelativistic intensities, in which the sharp spikes in the temporal variation of the Lorentz factor are the key to the production of the highest harmonics, hence the name "γ-spikes". This theory predicts a spectral shape of the HHG emission given by a power law of exponent -8/3:

$$\boxed{I_n \propto n^{-8/3}}, \tag{5.4}$$

where n is the harmonic order, up to a threshold:

$$\boxed{n_{\text{threshold}} = \sqrt{8\alpha}\gamma_{max}^3}, \tag{5.5}$$

beyond which there is an exponential decay. Here, γ_{max} is the largest value of the Lorentz factor of the plasma surface and α the second derivative of the surface velocity at this moment.

Although the assumptions on which this model is based are subject to discussion [246, 11], a few experiments that were performed in the ultrarelativistic regime (10^{20}W.cm^{-2}) on the Vulcan Petawatt laser tend to support these predictions [70].

5.2.2 HHG from synchrotron radiation

In the relativistic models presented above, the harmonics result from a pure phase modulation of the incident laser wave.

Relativistic Electron Spring (RES)

In [109], the authors argued that the above mentioned models neglect the fact that there is energy accumulated in the plasma, which is later re-emitted. For very strong field interactions, the energy storage into the plasma becomes non-negligible and needs to be taken into account: a more detailed treatment of the electron motion is required. Following this idea, A. Gonoskov developed the Relativistic Electron Sping (RES) model for ultrarelativistic ($a_0 \gg 1$) incident waves and predicted a power law:

$$\boxed{I(n) \propto n^{-1.31}} \tag{5.6}$$

for $a_0 = 300$, which was confirmed with numerical simulations [108]. In this model, the incident wave energy is transferred to the plasma and extremely dense, nano-scale electron layers are formed due to the ponderomotive force of the laser. When the eletron nano-layer is accelerated back toward vacuum, it radiates attosecond pulses.

Coherent Synchrotron Emission (CSE)

Roughly at the same time, D. Brugge and A. Pukhov argued that the BGP theory is only valid for step-like density gradients and described the emission of harmonics via Coherent Synchrotron Emission (CSE) [11]. In a few words, the CSE model, which is similar to the RES one, also

says that the surface electrons may form ultrathin (few nanometers), highly compressed layers which coherently emit synchrotron radiation when they move toward vacuum. It predicts a slowly-varying, synchrotron-like harmonic spectrum scaling as

$$\boxed{I(n) \propto n^{-4/3} - n^{-6/5}} \tag{5.7}$$

up to a threshold frequency beyond which, once again, there is an exponential decay. The predicted energy conversion efficiencies are close to 100% (for $a_0 = 50$ and $L_g \approx 0.33\lambda$).

Emission of relativistic harmonics from solids via synchrotron emission was also proposed in [174] a little bit later, while experimental observation of harmonics in transmission mode using ultrathin carbon foils with nanometer thickness [71], on which laser pulses were focused to an intensity I=4×10^{20}W.cm^{-2}, seemed to correspond to the decay law 5.7.

5.2.3 Properties and dependencies of relativistic surface harmonics

Influence of the plasma gradient scale length

For short gradient scale lengths, for which CWE is optimized, the gyromagnetic effect prevents electrons from escaping the plasma and the relativistic HHG mechanisms are not efficient [98]. On the other hand, when $L_g \geq \lambda/5$, the relativistic harmonics disappear due to the onset of chaotic electron dynamics [55]. The optimum for ROM harmonics is around $L_g \approx 0.1\lambda$.

Periodicity

In contrast with CWE, the ROM mechanism is perfectly periodic (except in the ultra-relativistic regime where the plasma mirror surface deformation starts to complicate things). Because its efficiency more strongly depends on the laser intensity, fewer attosecond pulses are emitted, and the emission time of each attosecond pulse does not vary with the laser amplitude from one cycle to the next [213]. A perfectly periodic train of Fourier-transform limited attosecond pulses is expected.

Conversion efficiency

The predicted laser-to-XUV conversion efficiencies from relativistic plasma mirrors range from 10^{-4} to 1 [256, 11, 66], although experimentally measured efficiencies are rather $\sim 10^{-4}$ so far [118, 128, 222, 287]. Nonetheless, since the attosecond pulses should be Fourier transform limited, and because the mechanisms allow working at very high laser intensities, this already constitutes an evidence of the greater attosecond pulse intensity achievable using plasma mirrors compared to gas-phase harmonics. Methods were proposed to further increase the attosecond pulse generation efficiency, such as using Super-Gaussian beams [10] to increase the power law, or focusing the laser slightly ahead of the plasma mirror [292].

Spatio-temporal characterization of the XUV beam

Very few temporal measurements of the attosecond pulses from SHHG have been made. A first temporal measurement [195] was made in 2009, in which the XUV beam generated in the CWE regime was focused in a gas jet to perform a photo-electron time of flight measurement. Through two-photon ionization of helium atoms, the authors measured the nonlinear intensity autocorrelation function of a superimposition of several harmonics and thus provided the first experimental evidence of sub-femtosecond duration.

In [55], a more precise spatio-temporal characterization was made, using a dynamical, all-optical ptychographic method. The authors measured temporal intensity profiles with 560 and 450as durations FWHM, in the CWE and ROM regimes respectively, and measured a GDD value $\approx$0 in the case of ROM harmonics. This work thus confirmed the prediction saying that relativistic surface harmonics should be associated with FTL attosecond pulses in the time domain.

Spatial properties

In contrast with CWE harmonics, the XUV radiation generated though the ROM mechanism is not associated with any intrinsic phase, thus in general ROM harmonics are found to be less divergent than CWE harmonics [213].

For a planar plasma mirror surface, we expect the divergence θ_n of the n^{th} harmonic to be diffraction limited and decrease with the harmonic order n. It would thus only depend on the XUV source size on target w_n according to equation 1.40. For example, for λ_n = 50nm, and considering that the source spot size is the same as the laser waist on target (*ie* $w_n = w_0 = 1.3\mu$m), we theoretically obtain a half angle $\theta_n \approx$ 10mrad only. And for λ_n =120nm, we find $\theta_n \approx$ 30 mrad. Of course, we can expect the source size to be much smaller for the highest harmonic orders, as the intensity is only high enough in the very center of the beam to produce those very short wavelengths. For instance, in [261], numerical simulations revealed that the source size of the 15th harmonic (corresponding to 50nm for a 800nm driving laser) is ≈0.4-0.6 w_0, independently of the laser intensity and plasma gradient scale length, thus doubling the diffraction limited divergence to ≈20mrad for this harmonic.

In the highly relativistic regime, experiments revealed a deformation of the plasma mirror surface induced by the laser, which was called *plasma denting* [124]. Indeed, due to the spatially inhomogeneous laser radiation pressure (or ponderomotive force), the surface of the plasma mirror may become concave and this deformation of the surface can affect the spatial [69, 286] and spectral [10] properties of the harmonics. When this curvature becomes dominant, the generated XUV beam may be focused slightly after the target, thus the decrease in divergence with the harmonic order is no longer observed in the far field [69].

A detailed analytical model of the surface dynamics and its consequences on the XUV beam can be found in [261, 259]. The model was validated by numerical simulations and the predicted XUV wavefront curvature induced by the distortion of the plasma surface was also verified experimentally using a ptychographic method [149, 150]. To summarize, the electron inward excursion increases with the laser amplitude a_0 and the gradient scale length L_g, while the slower subsequent ion inward excursion increases with the pulse duration. For example, in [261] (fig. 1.d), we see that for a ≈1.5 optical-cycle pulse and a_0 = 8 (at λ=800nm), the electrons are pushed inside the plasma by a few hundreds of nanometers, while the ions only have the time to move by a few tens of nanometers. For our $a_0 \approx 1$ or 2, in the case of 1.5 optical cycles, we can thus expect the ion motion to be negligible.

5.3 Electron acceleration mechanisms

At sub-relativistic intensities, a fraction of Brunel electrons can escape into vacuum, leading to the observation of an electron beam. Contrary to CWE harmonic emission (which requires the electrons to return to the high density part of the plasma to excite plasma waves), for electrons to be sufficiently accelerated towards vacuum, it is preferable to have longer L_g, $\approx 0.1\lambda$ [23].

At relativistic intensities, several different electron acceleration mechanisms have been identified. One at short gradients ($L_g \ll \lambda$), which is correlated to the ROM harmonics and can be explained through the ponderomotive force and vacuum laser acceleration, one more chaotic regime at intermediate gradients ($L_g \approx \lambda$) and one at much softer gradients ($L_g \approx 2-3\lambda$), similar to laser-wakefield acceleration.

5.3.1 Electrons at short gradients

Based on 1D and 2D PIC simulations, a push-pull mechanism was described by M. Thévenet [247] during his PhD thesis to model the electron ejection at the plasma surface. It consists of

a periodic push-pull mechanism occurring once per period of the laser field (fig. 5.3). Basically, during the first half-period of the laser, the incident field pushes electrons further inside the plasma, thus creating a space charge separation. During the next half-period, the sign is reversed and the combined effect of the laser field and the space charge pulls electrons towards vacuum. As the electron peak is accelerated towards vacuum, it radiates an attosecond electromagnetic pulse through the mechanisms previously described, whereas a small fraction of the electrons escapes the plasma and travels along the reflected pulse.

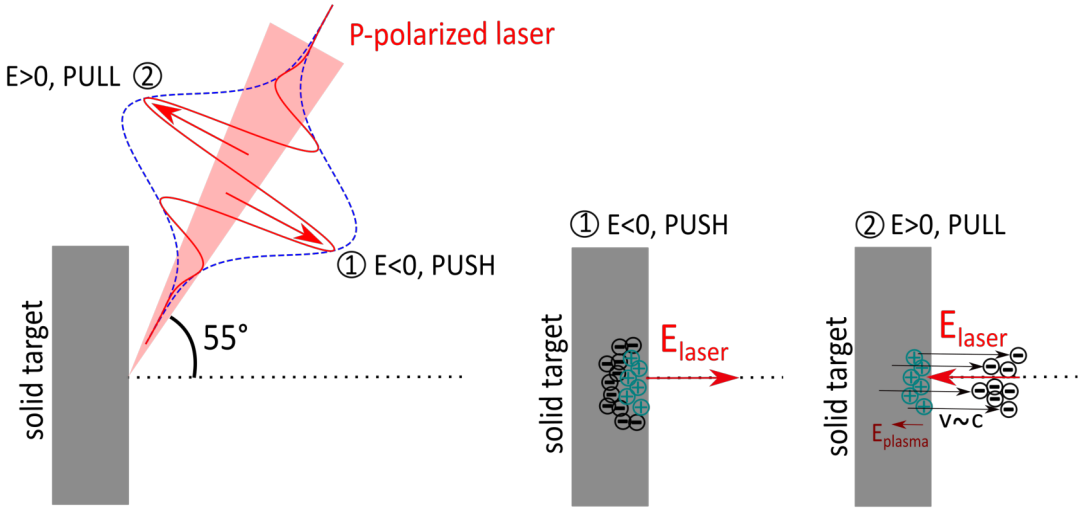

Figure 5.3: *Illustration of the push-pull mechanism*

According to PIC simulations, the reflection of the ultraintense laser pulse off the plasma mirror surface leads to the injection of attosecond electron bunches in the reflected field. For multi-cycle drivers (e.g. a 25fs pulse centered at λ=800nm), a train of attosecond electron bunches is expected, whereas 5.2fs pulses generate only 2 electron jets. It was also found that the charge contained in each attosecond electron bunch can strongly vary from one laser period to the next [249].

The gradient length dependence was also investigated and the emission of electrons was found to be asymmetric with respect to the specular direction (55°): for short gradients ($L_g \ll \lambda$), there are more electrons ejected at angles slightly offset from the specular towards the normal direction ($\theta_e \leq 55°$), whereas for slightly longer gradients (L $\approx \lambda$), simulations suggest that electrons are emitted closer to the target surface ($\theta_e > 55°$), indicating a different mechanism.

According to previous works, the electrons ejected from the plasma at short gradients may be divided into four categories: first, a population of electrons which interact with the reflected laser field and are isotropically pushed away from the laser pulse by the ponderomotive force. Then, some electrons are further accelerated in the reflected field afterwards (vacuum laser acceleration) and gain more kinetic energy. Additionally, some electron bunches born at the tail of the pulse can be exempted from the repulsive ponderomotive force and streaked by the reflected laser field. The last mechanism occurs at slightly longer gradients, and is still under investigations but would be due to stochastic heating.

- **Ponderomotive electrons**

As explained in Chapter 2 (section 2.5), an electron oscillating in an electromagnetic wave suffers a deflection force that pushes it out of the high field region: the ponderomotive force. We thus define the first category of electrons, which we call ponderomotive electrons. These are typically low energy electrons, born around the rising edge of the driving pulse, which do not have enough kinetic energy to remain in phase with the reflected electromagnetic field. These electrons oscillate several times in the reflected field and see different periods of oscillation of

the laser before being expelled from the high field area isotropically. Thus, they form a kind of ring structure (see fig. 5.5.c and 5.4.c, case "$N_{oc} \geq 3$"). The center, where no electrons are detected, is usually called the 'ponderomotive hole'.

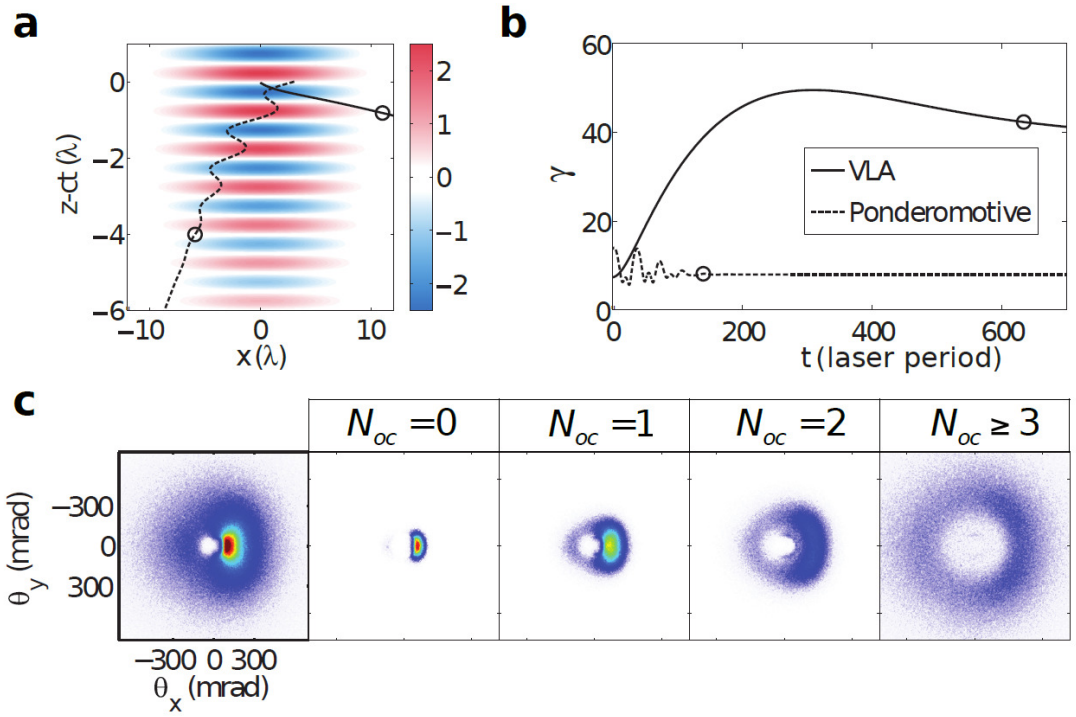

Figure 5.4: *Results of 3D "test-particle" simulations. a) trajectories of ponderomotive (dashed line) and VLA (solid line) electrons, and electric field amplitude (colors). b) evolution of the Lorentz factor along the two trajectories. c) electron angular profiles depending on the number of laser oscillations seen by the electron (N_{oc}). Reprinted from [247].*

- **Vacuum Laser Acceleration**

In vacuum laser acceleration (VLA), the electrons are accelerated directly by the laser without the need of a material structure such as a cavity or a plasma [290]. This mechanism is particularly interesting because of the very high accelerating field, even higher than that in a LPA. Recent work suggests the use of radial polarization to reduce the electron beam divergence and a normal laser incidence on target [291], but we did not explore those options during my PhD, therefore I will focus on our experimental conditions.

Contrary to ponderomotive electrons, VLA is the dominant mechanism for relativistic, high energy electrons, since only those are fast enough to remain in phase with the reflected EM field. For example, electrons with a kinetic energy E_{kin} = 1MeV will travel almost as fast as the light wave, at $v \approx 0.94c$ (see section 2.4). At the relativistic limit (E_{kin} =0.5MeV), we get $v \approx 0.86c$, which is still quite fast, but these electrons will keep up with the light wave for much shorter distances. Electrons that are fast enough can surf the laser wavefront without seeing different optical cycles of the reflected laser and without oscillating, thus these electrons gain energy and are ejected towards vacuum after propagating over a distance comparable to the Rayleigh length. They form a rather collimated electron beam along the polarization direction.

The direction of ejection (towards the normal or on the other side of the specular direction) depends on the injection phase (*ie* whether the electrons are injected in the reflected beam at a point where E=0, E=+E_0 or E=-E_0, and so on...). The real injection phase corresponds to 0 (a node of the electric field), and leads to an emission of VLA electrons towards the normal [149].

The first clear experimental evidence of VLA electrons was made at CEA Saclay [248]. The

electron distribution consisted of a bright spot emitted with a $\approx 10^{\circ}$ offset with respect to the specular direction toward the target normal, and a weak isotropic halo centered about the specular direction. The authors measured the electron spectra on both sides of the beam and concluded that VLA electrons were twice more energetic than the ponderomotive electrons emitted on the other side. More recently, the CEP-dependence of attosecond MeV electron pulses accelerated from nanoplasmas and experiencing vacuum laser acceleration was also experimentally demonstrated [46].

• **Streaked attosecond electron bunches**

A third category was described in [294], where Zhou *et al* reported on similar experiments with sub-relativistic intensity ($a_0 = 0.3$), ≈30fs pulses. They compared the experimentally obtained electron spatial distribution with a 3D test particle model (the same that was used in fig. 5.4) and divided the electrons into three different categories (see fig. 5.5.c). First, the ponderomotive electrons born on the rising edge of the laser pulse which form the characteristic doughnut shape, then the VLA electrons born at the peak which form the bright dot on the edge of the ponderomotive hole along the polarization direction, and finally a train of attosecond electron bunches born at the tail of the pulse.

This last category of sub-relativistic electrons, injected at zero crossings of the electric field (fig. 5.5.b) close to the tail of the pulse, is exempt from the most intense repulse of the ponderomotive force. These electrons are only deflected by the weak laser field and suffer a momentum change $\Delta p(t) = eA(t)$ which only depends on the vector potential $A(t)$ of the associated laser optical cycle, therefore their angle of emission slightly varies from one cycle to the next. Because of their very narrow energy spread, these electrons resulted in the observation of thin, periodic electron density fringes in the far field along the polarization direction. Furthermore, the authors estimated the duration of the attosecond bunches to be ≈200as, according to the angular spread (width) of the fringes in the polarization plane.

For the specific value of a_0 used in their experiments, the streaking pattern was observed into the ponderomotive hole but most of the time, for higher field amplitudes a_0 such as ours, they can overlap with the other categories of electrons and not be seen at all.

• **Electrons at intermediate gradients**

Predicted by M. Thévenet through numerical simulations, the plasma gradient dependent variation in the angle of emission was experimentally observed at CEA Saclay [55] recently (see fig. 5.6.a and b.). They first observed a strong electron emission with the typical ponderomotive/VLA distribution at shorts gradients, which seemed to correlate with the generation of high-order harmonics. Then, at softer gradients $L_g \approx 0.3$ to 0.5λ, only electrons emitted at angles larger than the specular direction (corresponding to negative angles in fig. 5.6.a) remained. We are now interested in the latter.

So far, the interpretation is that electrons in the underdense part of the density gradient gain energy in the interference pattern formed by the overlap of the incident and reflected laser fields [56]. Theoretical work previously established that the dynamics of electrons trapped in the overlap of noncollinear fields gets chaotic and can lead to high energy transfer from the laser to the electrons, a process known as stochastic heating [232, 173].

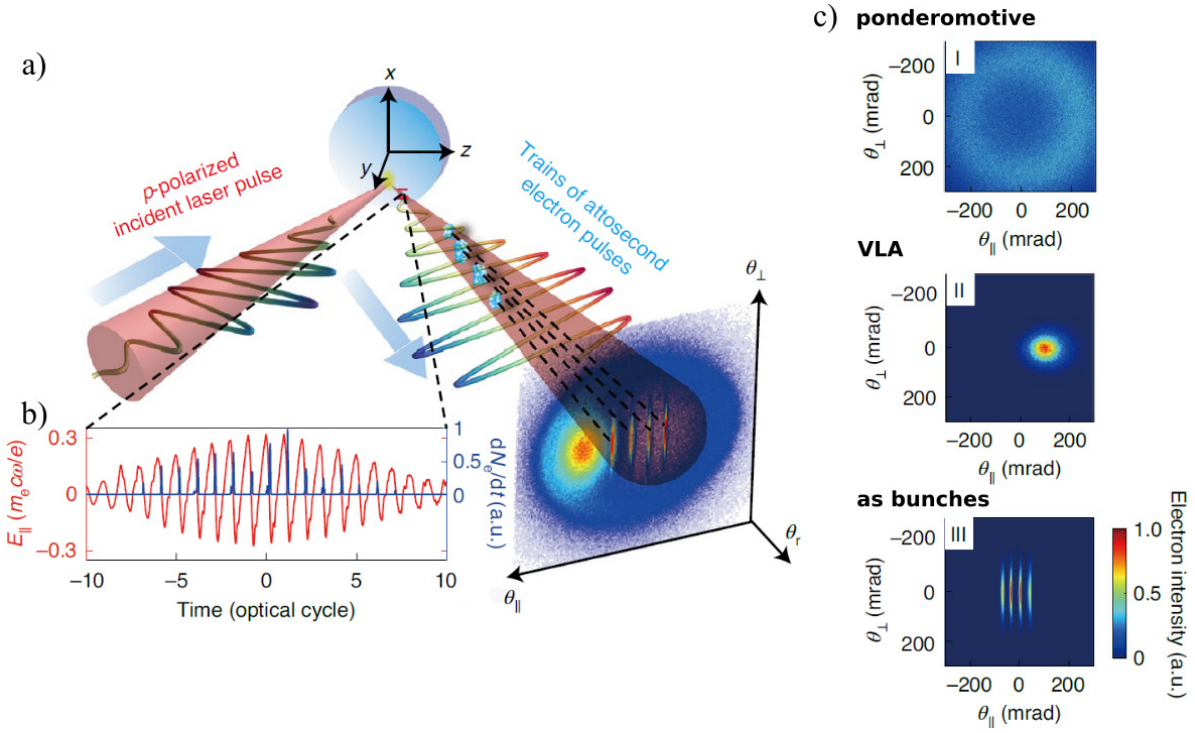

Figure 5.5: *a) experimental setup b) reflected laser field in red and injected electrons in blue c) different categories of electrons observed in the far field. Reprinted from [294].*

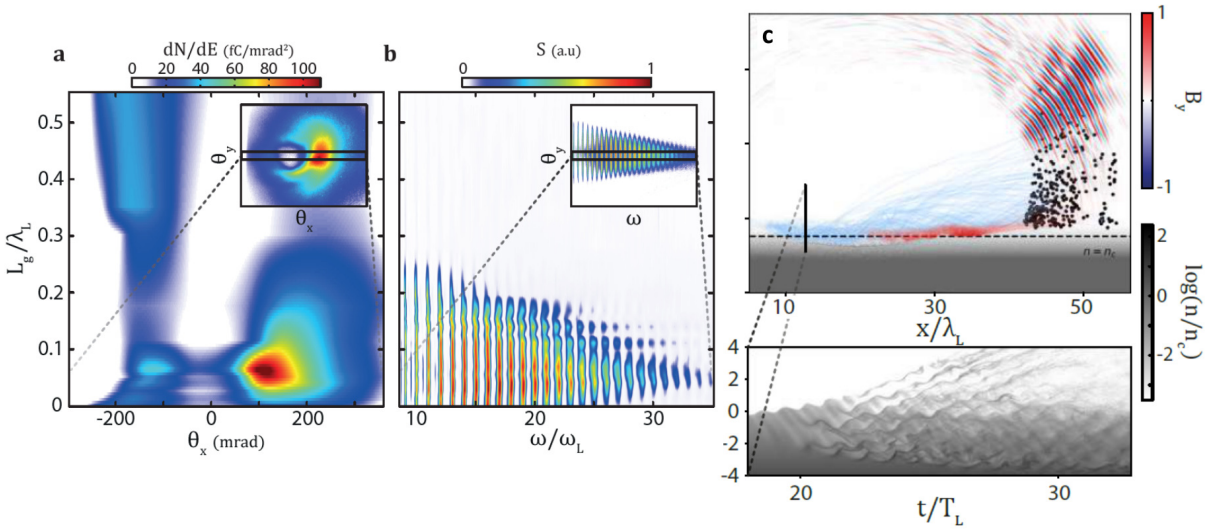

Figure 5.6: *a) Electron distribution in the azimuthal plane for different gradient scale lengths (here, θ_x=0 corresponds to the specular direction) b) HHG spectra for different gradient scale lengths. c) 2D PIC simulation for $L_g = \lambda/1.5$. The light blue lines represent the electron trajectories. Taken from [53].*

5.3.2 Electrons at very long gradients

We now move to a totally different regime of electron acceleration from plasma mirrors, which occurs at much longer plasma gradient scale lengths ($L_g > \lambda$) and was discovered experimentally during the PhD thesis of Frederik Böhle, in *Salle Noire 2* [25]. It was then theoretically studied through PIC simulations within the frame of Neïl Zaïm's PhD thesis [288], which led to

the only publication (to my knowledge) on this phenomenon: [289].

• **Laser Wakefield Acceleration**

Simulations at long gradients revealed that high amplitude plasma waves are formed in the wake of the laser pulse and that their wavefront is bent by the density gradient.

A first population of electrons coming from the 2s and 2p atomic orbitals of silicon atoms, which are ionized around the peak of the laser field, is injected in the wakefield (ionization injection scheme), whereas a second, smaller population of electrons originates from self-injection.

Those electrons are trapped and accelerated by the strong electric fields (up to 1TV/m) of the plasma waves, and then emitted with a $\approx 50°$ angle with respect to the normal, as was found experimentally. The electron acceleration mechanism was therefore identified as LWFA, just like in gases, except that the wavefront is bent in our case (see figure 5.7).

Similar to experiments, the highest wakefields were found to occur for few-cycles pulses, and were almost absent in the case of 24 fs driving pulses. This is explained by the resonance condition mentioned in section 4.3 (the pulse duration must be on the order of half the plasma wavelength): for 5 fs pulses, the resonant density is $\sim n_c/23.5$, versus $n_c/300$ in the case of 24 fs pulses.

According to the simulations, 55° is the optimum angle of incidence for this mechanism: it yields the highest electron charge (7pC/μm) and the lowest divergence. Electron energies up to 2.5 MeV were predicted, but were never measured experimentally, and the spectrum should be angle-dependent, with the most energetic electrons emitted closer to the specular direction.

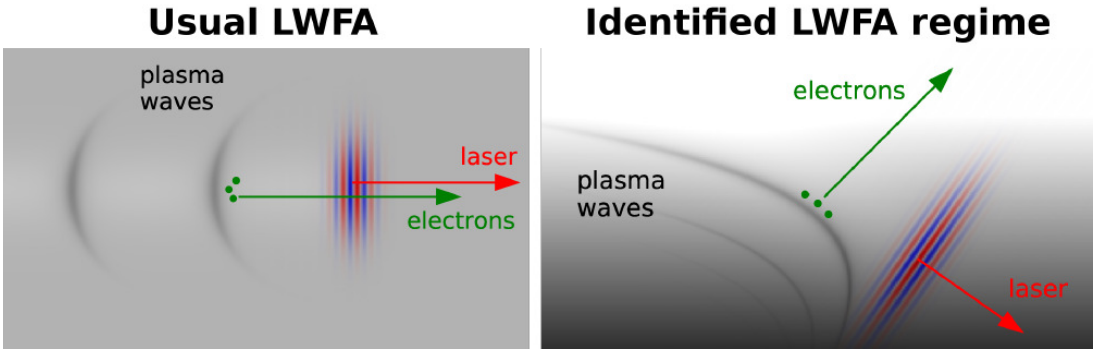

Figure 5.7: *Schematic illustration of standard LWFA regime (left) and LFWA regime occuring in the solid-target experiments (right). Reprinted from [288].*

5.4 Proton acceleration

Under the same experimental conditions (oblique incidence on a solid target, high contrast), the backward emission of a proton beam along the target normal direction was experimentally observed in [125] and [258].

Just like in TNSA experiments, the protons most likely originated from contamination at the target surface. Those contaminants essentially consist of carbon, hydrogen and oxygen atoms (water vapors and hydrocarbons of human origin, out-gassing plastics, grease of translation stages/mirror mount screws, etc). Ionization intensities required to ionize carbon and hydrogen atoms are displayed in Tab. 2.2, and we see that our typical prepulse intensity is only sufficient to generate protons from hydrogen atoms, which tends to confirm the presence of such contaminants.

In [125], 55fs, 3mJ pulses were focused on a BK7 target with a 51° angle of incidence, to intensities of 2×10^{18}W.cm^{-2} at 0.5kHz repetition rate. Hou *et al* measured a laser contrast

ratio $\sim 10^8$ and thus estimated the plasma scale length at the target surface to be $\leq \lambda/10$. The interaction resulted in the emission of protons along the target normal direction with energies exceeding 0.5 MeV and an opening angle of 16° FWHM (for protons with E>265 keV). The authors also performed 2D PIC simulations and concluded that the acceleration of ions is due to the formation of a sheath field on the front surface, created by electrons under the influence of the incident and reflected laser fields.

In [258], the experiments were performed in *Salle Noire 2*. Veltcheva *et al* varied the driving pulse energy, polarization (from p to s) and duration (from 5 to 500fs). Compared to the laser system now, the maximum energy that they could obtain at the time was lower (1mJ), the minimum pulse duration was 5fs, and there was no control over the plasma gradient scale length either.

The maximum proton energy was obtained for p-polarized laser beams and was found to increase with the laser intensity.

Then, varying the pulse duration while keeping the energy constant, they found that the proton energy quickly increased with the laser pulse duration up to 40fs, and then they observed a plateau up to 200fs, followed by a slower decrease in proton energy.

From analytical calculations and 2D numerical simulations, the authors concluded that the proton acceleration is directly driven by Brunel electrons dragged in and out of the plasma by the laser field and only takes place during the laser duration.

In the experiments, no auxiliary pulse was used to control the plasma gradient, therefore the density gradient was as steep as possible. For very steep density gradients, Brunel electrons returning into the plasma go beyond the critical surface. Thus, most of the electron energy flows into the target and no significant heating of the plasma occurs. Unlike in classical TNSA, electron thermal pressure therefore hardly contributes to the acceleration of ions.

Chapter 6

Relativistic interaction with plasma mirrors: experimental setup

"The game of science is, in principle, without end. He who decides one day that scientific statements do not call for any further test, and that they can be regarded as finally verified, retires from the game".
Karl Popper

In this chapter, I will describe the existing experimental setup in *Salle Noire 2* for studying the interaction of relativistic laser pulses with plasma mirrors at kHz repetition rate. Fortunately, the experimental chamber, including most of the diagnostics, were already there when I arrived. Stefan Haessler and I took over the experiment after the last PhD student left and had to make it work again. The following additions were made:

- In the frame of a *Laserlab* collaboration with Dan Lévy, Victor Malka (Weizmann Institute, Tel Aviv) and Alessandro Flacco (LOA), we added diagnostics for protons and ions so as to pursue the work that had been started in [258].

- Another collaboration between Rodrigo Lopez-Martens, Philippe Zeitoun (LOA) and Li Lu (Shenzen Institute, China) was started for the spatial characterization of the XUV beam. Diagnostics for the XUV beam wavefront were added and used.

- Stefan Haessler and I also built an electron magnetic spectrometer, with some help from Jérôme Faure.

Towards the end of my thesis, I started thinking of a new design for the electron and XUV diagnostics, which will be presented at the end of this manuscript. Along with the diagnostics, I will also briefly describe the principles behind data analysis. *Matlab* scripts written by Frederik Böhle and Maïmouna Bocoum were already existing when I started my thesis. Stefan Haessler, Jaismeen Kaur and myself largely extended them to include the XUV spectrum calibration, the proton data analysis (with the help of Dan Lévy), the electron spectrum analysis and the possibility of sorting the data depending on the laser CEP. I also adapted all the scripts for *Python* as I am more familiar with it.

6.1 Description of the SHHG chamber

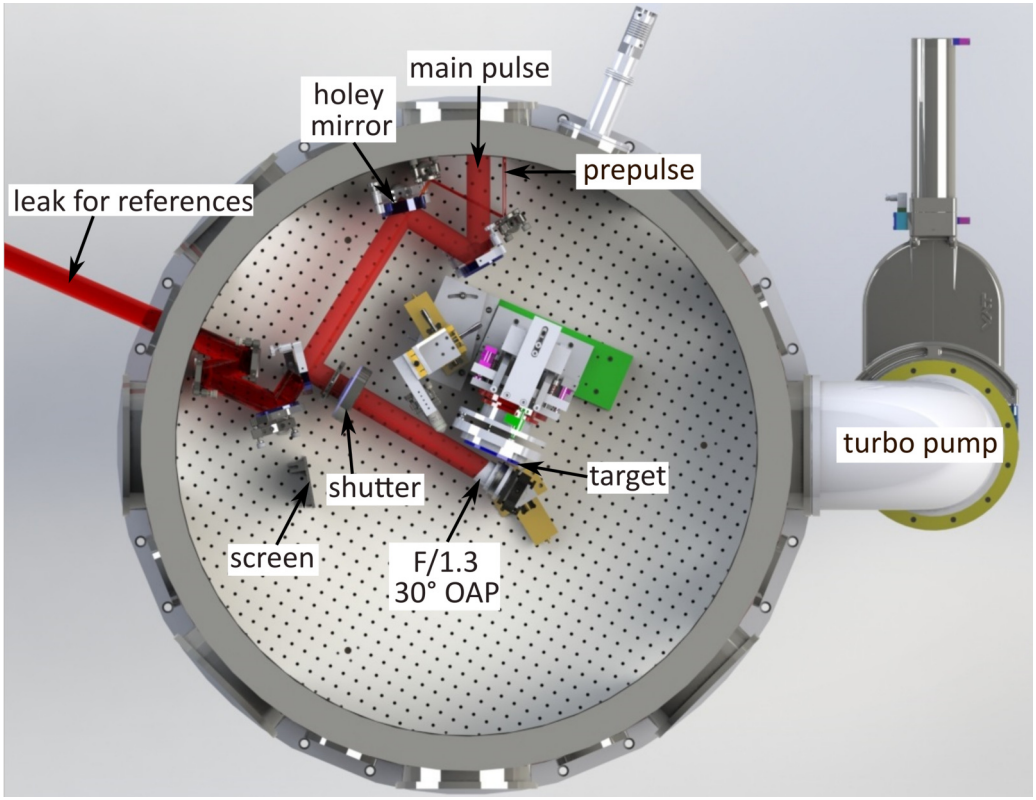

Figure 6.1: *3D drawing of the SHHG experimental chamber with the rotating target device and the IR beam transport to the target.*

As we have seen, the beam is split into two with a holey mirror at the output of the laser

chain (fig. 3.12). The small auxiliary beam (prepulse) is used to form the preplasma. A convex (visible in fig. 3.12) and a concave (not shown) 1 inch lens further reduce its beam diameter so as to obtain a large, 12μm FWHM focal spot on target.

After introducing a delay between the two pulses with a retro-reflector placed on a motorized translation stage (marked as "delay line" in fig. 3.12), the two beams propagate into the SHHG experimental chamber. The chamber diameter is 1m and it is pumped with dedicated primary (down to 10^{-1} mbar) and turbo-molecular vacuum pumps to reach a pressure of 10^{-6} mbar. This low pressure is required for preserving the pulse duration and preventing ionization, but also to meet the requirements of our detectors (MCPs).

The two beams are recombined with a second, identical holey mirror (fig. 6.1) and then co-propagate to a 3inch, 45° plane silver mirror. Then, there is a slow and a high-speed mechanical shutter (45mm diameter, *Uniblitz CS45*, with a 14ms opening time), allowing to respectively block the beam for long times and control the shooting sequence length. Finally, the parabola focuses the beam on an interferometrically aligned rotating solid target device (details regarding this target device and its alignment are given in Appendix B) which provides a clean surface area for each laser shot at kHz repetition rate.

The last plane silver mirror is slightly transmissive so that we can send a leak of the beam outside the chamber in order to have references: the near-field reference is an image of the holey mirror (fig. 6.2), while the far-field reference is taken by focusing the beam with another OAP onto a CCD camera.

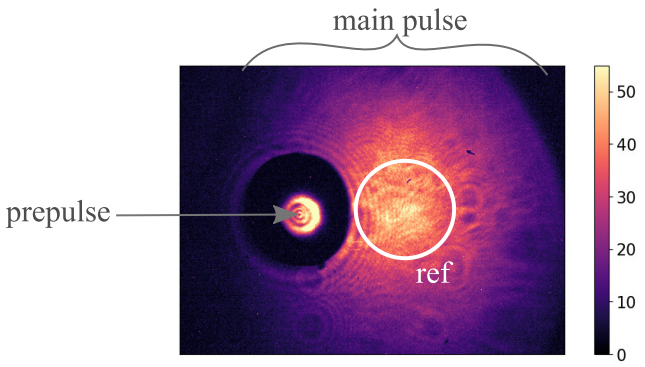

Figure 6.2: *Example of near field reference image, corresponding to the plane of the second holey mirror. The white circle is manually placed and saved so as to be used as a reference for the next day. The hole diameter is ≈ 6mm.*

Angle of incidence

The laser electric field polarization is chosen to be p (*ie* in the horizontal plane), so as to maximize the absorption by the target. For a p-polarized laser field, the angle of incidence θ which maximizes the harmonic spectral extent is 55°. Indeed, the projection of a p-polarized electric field $\vec{E_0}$ along the target normal is given by $E_x = E_0 \sin\theta$ and the intensity on target is reduced due to the oblique incidence, therefore the effective electric field amplitude is given by $E_0 \sin\theta\sqrt{\cos\theta}$, whose value is maximized for $\theta \approx 55°$, as shown in figure 6.3.

Solid targets

As previously stated, we use fused silica as target material. Other materials such as gold, aluminum and plastic were tried in the past [244, 246]. In principle, the higher the electronic density, the higher the frequency cutoff will be in the CWE regime. Indeed, Au (Z=79, $n_{e,max} = 4.7 \times 10^{24}\text{cm}^{-3}$) or Al (Z=13, $n_{e,max} = 7.8 \times 10^{23}\text{cm}^{-3}$) targets result in a higher observed harmonic order, whereas CH (Z=7, $n_{e,max} = 3.8 \times 10^{23}\text{cm}^{-3}$) yields lower harmonic orders. However, in the relativistic regime, it does not really matter. Fused silica was eventually chosen for convenience (cheap and easy to find with a good surface quality) and availability.

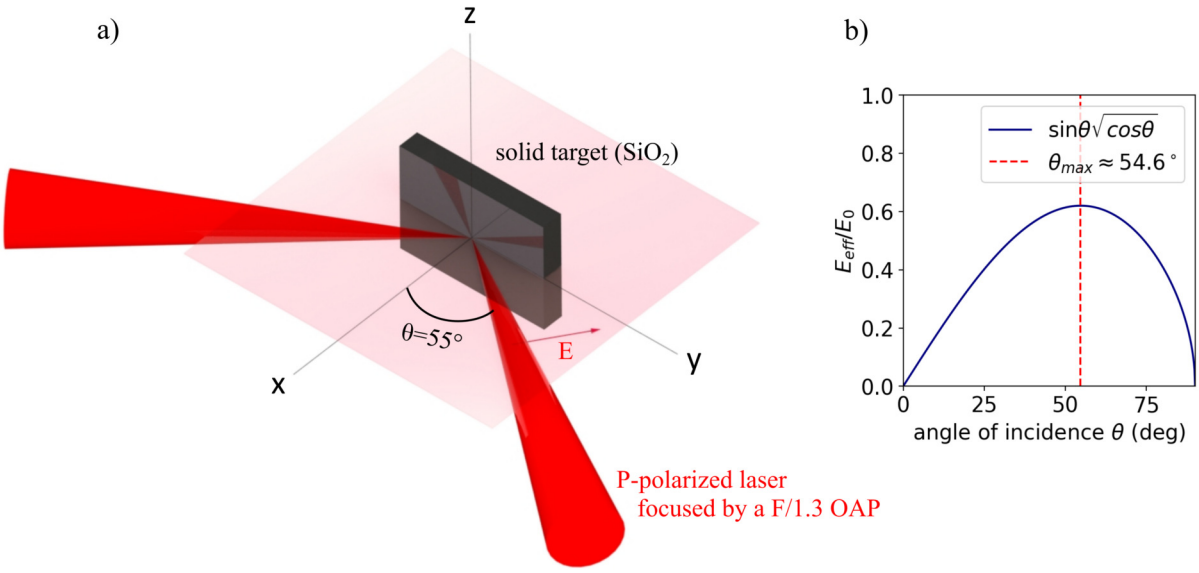

Figure 6.3: *a) Illustration showing the laser/target interaction geometry. b) Effective electric field amplitude depending on the angle of incidence on the target.*

We use 4 or 5 inch diameter (we can switch from one to the other diameter using an adaptor which I had made by our mechanical workshop), 12.5mm thick, UVFS targets that are optically polished to a surface flatness of $\lambda/20$ on both sides. Besides, unlike the plasma mirrors that are used for contrast cleaning [117, 175], no AR coating is needed in our case.

Focusing

The beam diameter is approximately 33 mm at $1/e^2$ and we use 3 inch diameter mirrors for beam transport. We then tightly focus the beam with a 30° off-axis parabola (*Winlight*), so as to minimize aberrations. The OAP has a very short paraxial focal length $f = 51.25$mm and the useful area diameter is 40 mm, corresponding to an F-number $F = f/diameter \approx 1.3$ (we could hardly go for a shorther focal length parabola in this configuration). Examples of typical beamprofiles obtained in focus are shown in fig. 6.4.

The parabola surface is coated with a protected silver layer and the substrate is made of Zerodur, which was chosen because of its low thermal resistivity, meaning there will be less thermal-induced surface distortions. However, this is probably not very important in our case because thermal effects occur on long time scales and we only shoot in burst mode, with sequences of about 100 consecutive shots only.

The OAP is mounted on a motorized translation stage along the focused beam propagation direction, and the mount has two picomotors for precise tip and tilt adjustment.

Finding the right parabola-to-target distance

The OAP is on a motorized translation stage in order to be able to optimize its position under vacuum by looking at the harmonic signal. As shown in fig. 6.5, it gives us a quite precise idea where the focus is, as expected from the strong intensity-dependence of the generation efficiency in the relativistic regime. However, it is useful to pre-optimize it in air with an alignment laser. In order to determine the right position of the off-axis parabola for which the focal spot coincides with the target surface, we use a rather simple trick: we try to find (or deposit on purpose) a small dust particle on the target surface and focus the He-Ne alignment laser onto it. We observe a Speckle pattern in the reflected beam a few tens of centimeters away from the target. This pattern can simply be looked at by eye with a white paper sheet (denoted as 'screen' in fig. 6.1). As we approach the focus, the features of this pattern become bigger and bigger and

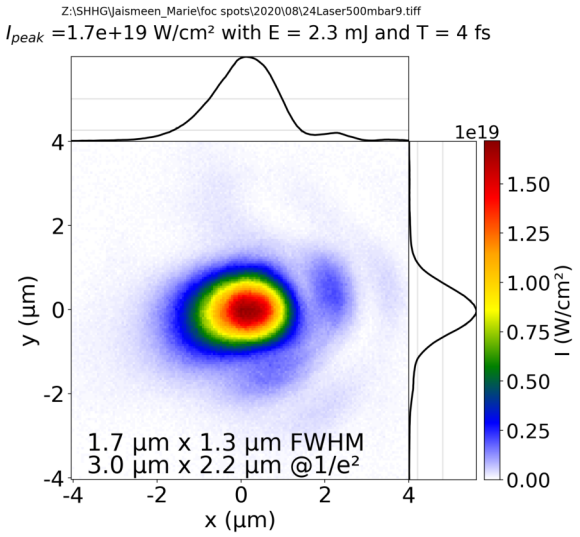

(a) Beamprofile of the driving laser in the focal plane, measured with the × 40 objective (here with 500 mbar of gas at the output of the hollow-core fibre). The diameter is 1.3 × 1.7 µm FWHM and 3 × 2.2 µm at 13.5% of the peak. For 4fs and 2.3mJ on target, it corresponds to a peak intensity of $1.7 \times 10^{19}\mathrm{W.cm}^{-2}$.

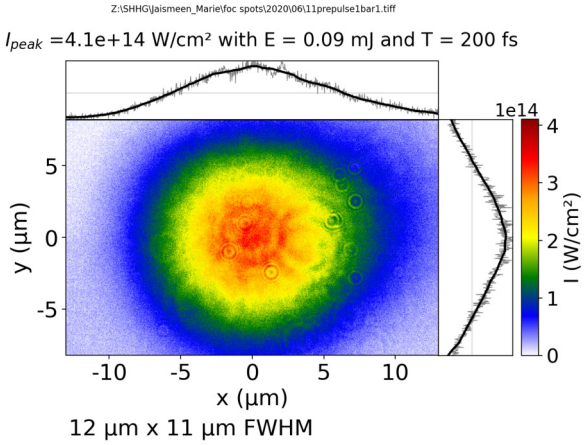

(b) Intensity distribution of the prepulse in the focal plane, measured with the × 40 objective (here with 1.1 bar of gas at the output of the hollow-core fibre). The diameter is ≈ 11 by 12 µm FWHM.

Figure 6.4: *Examples of beamprofiles in the focal plane.*

as we go through the focus, the bright and dark areas of this pattern are reversed.

Another method was described by Frederik Böhle [25]: he proposed to introduce a double-hole mask in the main beam path, with the two holes on either side of the beam profile. Thus, when the target plane is out of focus, there are two distinct beams on the target, each one resulting in an XUV beam generated through the CWE process at certain distance from the optical axis. On the contrary, when the target is in focus, the two beams overlap and we observe a single XUV beam on the optical axis in the far field. However, this method is unnecessary, since optimizing the ROM harmonic signal gives similarly good results, therefore we did not use it.

Zero-delay

Finally, one needs to find the position of the delay line for which the prepulse and the main pulse overlap in time. A first approach is to use the fast photodiode and oscilloscope described in subsection 4.1.3, but the resolution is limited to about 50 ps. A more precise way is to look at the image of both the prepulse focal spot and the irised main pulse focal spot on the camera, while varying the translation stage position in small steps, corresponding to 0.1ps delays. As the two pulses overlap in time, some spatial interference fringes appear. The contrast of the fringes is maximized by adjusting the diameter of the aperture in the main beam path so that the two beams have the same intensity in focus, as well as using a narrow band filter at 800nm before the camera.

Diagnostics

Then, there is a series of diagnostics for the electrons, ions, and the XUV light emitted from the plasma (fig. 6.6). The XUV spectrometer is placed in the specular direction, the LANEX screen for electrons is placed between the specular and the normal direction, whereas a Time of Flight (TOF) detector and a Thomson Parabola Spectrometer (TPS) are positioned along the target normal direction to detect ions.

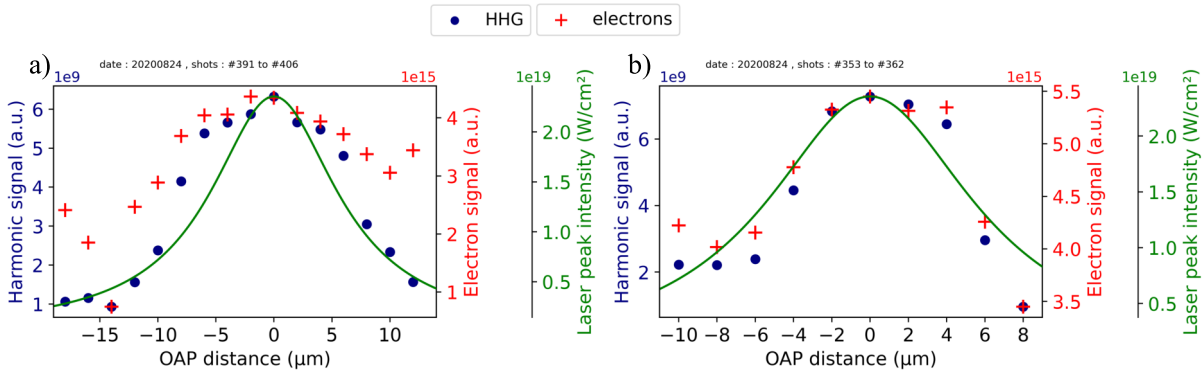

Figure 6.5: *Integrated HHG and electron signal (a.u.) as a function of the OAP distance with respect to the target along the direction of the incident beam. a) for a prepulse lead time of 1ps and b) for a prepulse lead time of 2ps. The CEP was locked to an arbitrary value. An estimation of the laser peak intensity as a function of the OAP position is shown in green (using Eqs. 1.35, 1.34 and 1.37, and assuming the following laser parameters: 2.5mJ on target, a minimum beam waist of 1.3μm, a pulse duration of 4fs and a central wavelength of 0.8μm).*

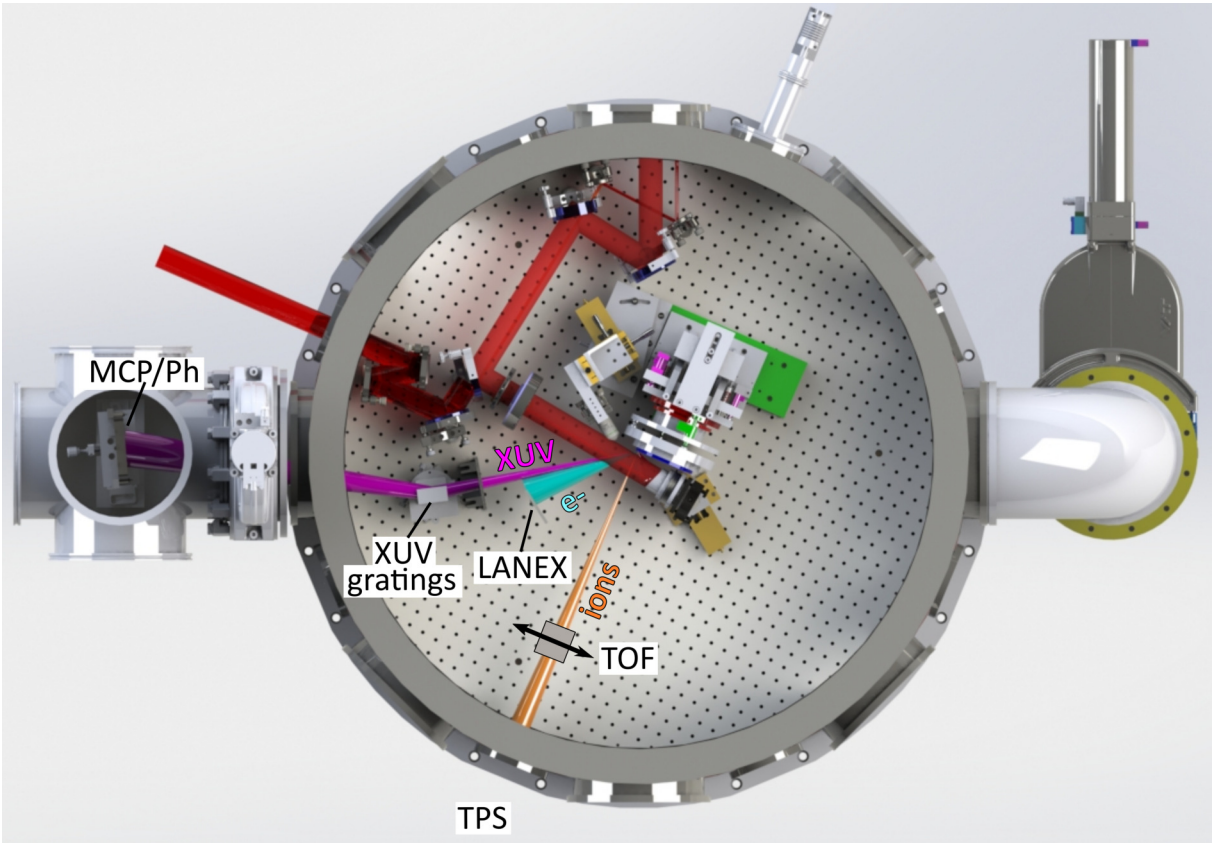

Figure 6.6: *3D drawing of the SHHG experimental chamber with the position of all the diagnostics.*

6.2 XUV detection

6.2.1 XUV spectrometer

In the experiments, I used an XUV spectrometer (fig. 6.7) which had been installed in the experimental chamber before the beginning of my thesis. It allows measuring the spectrum of the reflected light in the specular direction, for wavelengths ranging from 30 to 120 nm, corresponding to photon energies from 10 to 40 eV approximately. More details, as well as explanations regarding the calibration method that I used, can be found in Appendix C.

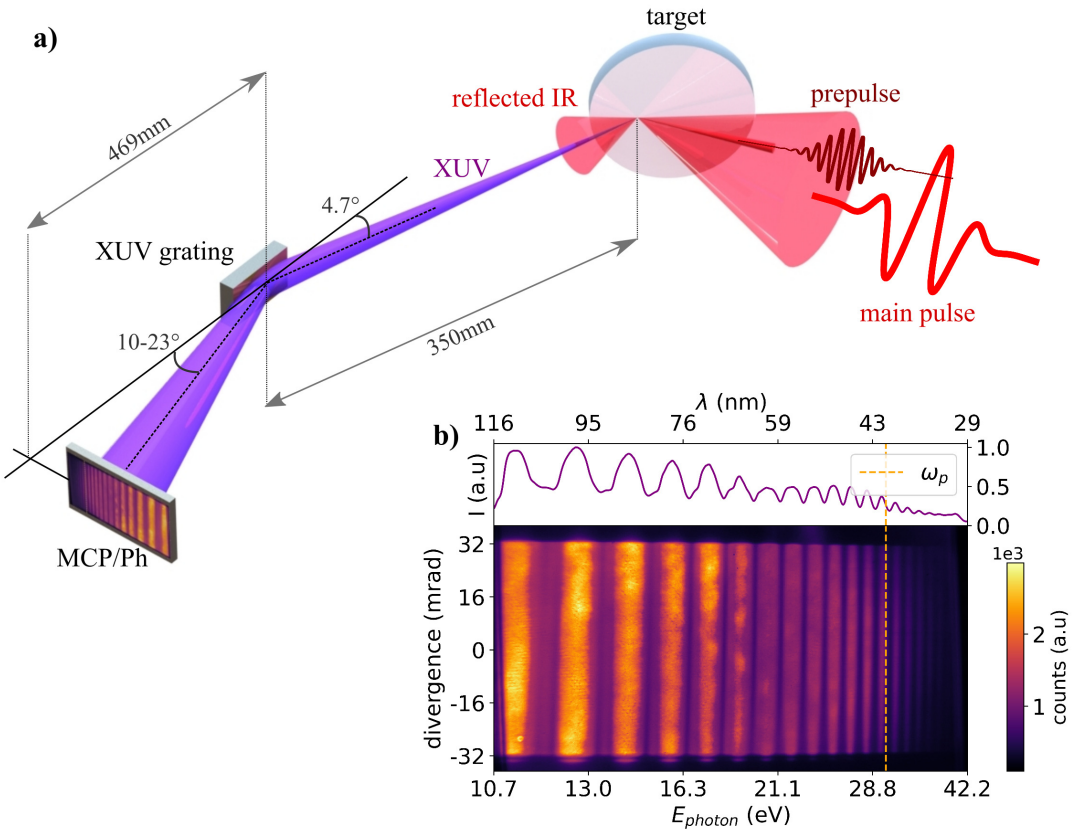

Figure 6.7: *a) Schematic drawing of the experimental setup for XUV spectral measurements. b) Example of raw harmonic spectrum, with calibrated axes. The vertically integrated raw signal is shown on top. The orange dashed line represents the maximum (in the case of a fully ionized target) high frequency cutoff for CWE harmonics, corresponding to the maximum plasma frequency.*

6.2.2 XUV spatial detection

During our experiments, we also used a micro-channel plate(MCP)/phosphor assembly which we placed in front of the XUV grating for measuring the spatial intensity distribution of the XUV light. However, this is quite difficult: the challenge is to detect the full XUV beam (which is quite divergent) while detecting neither the reflected IR-visible beam nor the electrons.

Indeed, although the MCP is not sensitive to IR and visible light (*ie* no primary electrons are created and amplified), laser light can leak through the single-stage MCP channels and hit the phosphor screen, which then scatters and also partially transmits this light. Shielding from IR-visible light can be achieved using very thin (hundreds of nm thickness) Al filters, which are very expensive and fragile, but only transmit photons with an energy higher than $\sim$ 15eV

(see fig. D.1.a.). Additionally, one can have a chromatic interferometric filter in front of the camera which only transmits at the central emission wavelength of the phosphor screen, and add opaque foils around the detector to block ambient light. Finally, we also used a pair of permanent magnets in front of the MCP to deviate electrons upwards, as represented in fig. 6.8.

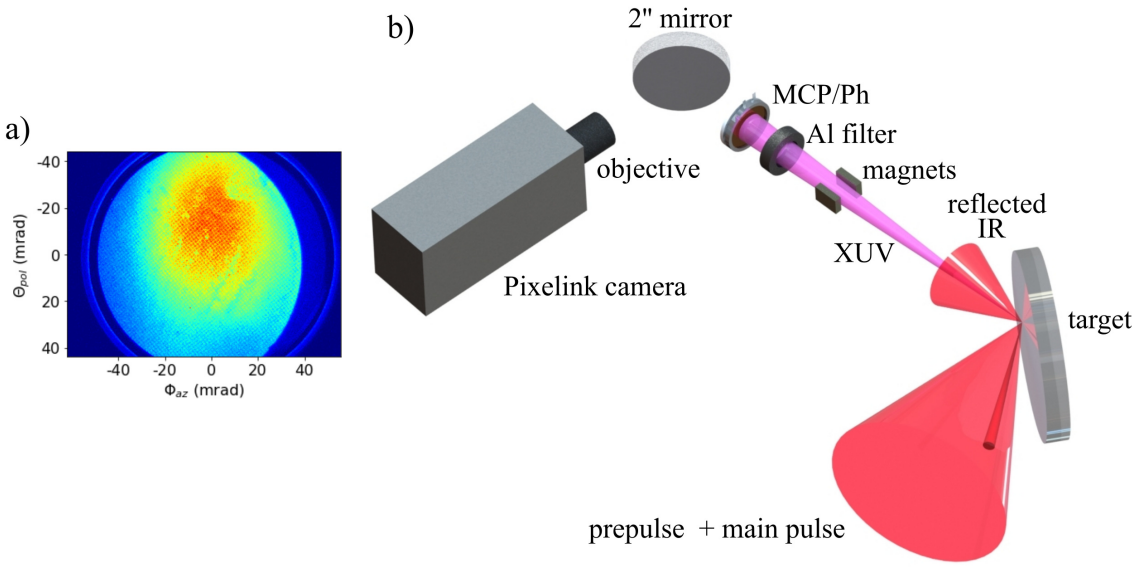

Figure 6.8: *Schematic drawing of the experimental setup for XUV spatial measurement*

6.2.3 XUV wavefront measurements

Measuring the wavefront is of critical importance, as it eventually determines whether or not the harmonic beam will be well focusable for applications. We thus started a *Laserlab* campaign with Li Lu (Shenzen institute, China) and Philippe Zeitoun (LOA), aiming at measuring the wavefront of the XUV beam. They had developed a Hartmann XUV wavefront sensor in collaboration with the company *Imagine Optics*, which we had planned to use for looking at narrow spectral bandwidths and at the full XUV beam footprint.

XUV wavefront sensor

The principle of the Hartmann wavefront sensor is represented in fig. 6.9. The wavefront is sampled with an aperture array (the Hartmann plate) and the transmitted light is recorded with a CCD. For a plane wavefront, the sub-beams after the mask propagate parallel to each other and we observe regularly spaced bright spots on the CCD. In the case of a distorted wavefront, the local wave vectors are no longer orthogonal to the propagation direction and their orientation varies in space. This leads to a small displacement of the bright spots centroids on the CCD, and measuring their offset with respect to the reference position allows retrieving the wavefront.

We used a soft X-ray CCD (*Princenton Instruments, PI-MTE:2048B*), sensitive to photon energies from $\approx$ 10eV to 10keV. The sensor is a square 27.6 by 27.6mm pixel array while the circular nickel Hartmann plate is 36 mm in diameter and installed 45 mm away from the CCD chip. More technical details can be found in [155].

Implementation in the experimental chamber

The main difficulty arises from the limited space available whereas the XUV sensor is very long and large, as can be seen in fig. 6.10.a. The footprint of the soft X-ray CCD alone is $\approx$ 80 by 120mm. Additionally, the WFS needs to be very precisely aligned so as to be perfectly

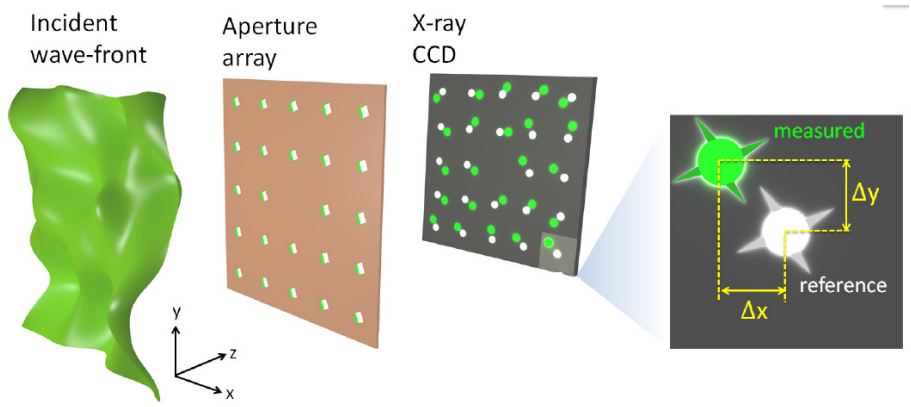

Figure 6.9: *a) Schematic representation of the incoming distorted wavefront (in green), going through the Hartmann plate and reaching the detector. b) The white dots correspond to the diffraction spots when a perfect beam reaches the detector, while the green dots correspond to an unknown beam. Courtesy of Li Lu.*

orthogonal to the beam and centered with respect to it. Therefore, it stands on a plate with four picomotors to finely adjust its orientation, as well as motorized translation stage in the direction orthogonal to the beam propagation. Finally, the sensor needs to be thermo-electrically cooled to minimize the dark current, therefore water circulation is required, which further increases its footprint.

Moreover, the XUV optics used to spectrally filter the harmonics must be used at specific angles of incidence, which results in a quite long propagation length from the target to the sensor.

Additionally, we only had up to 30mm diameter aluminum filters, which further limited the angular acceptance.

Monochromatic measurement

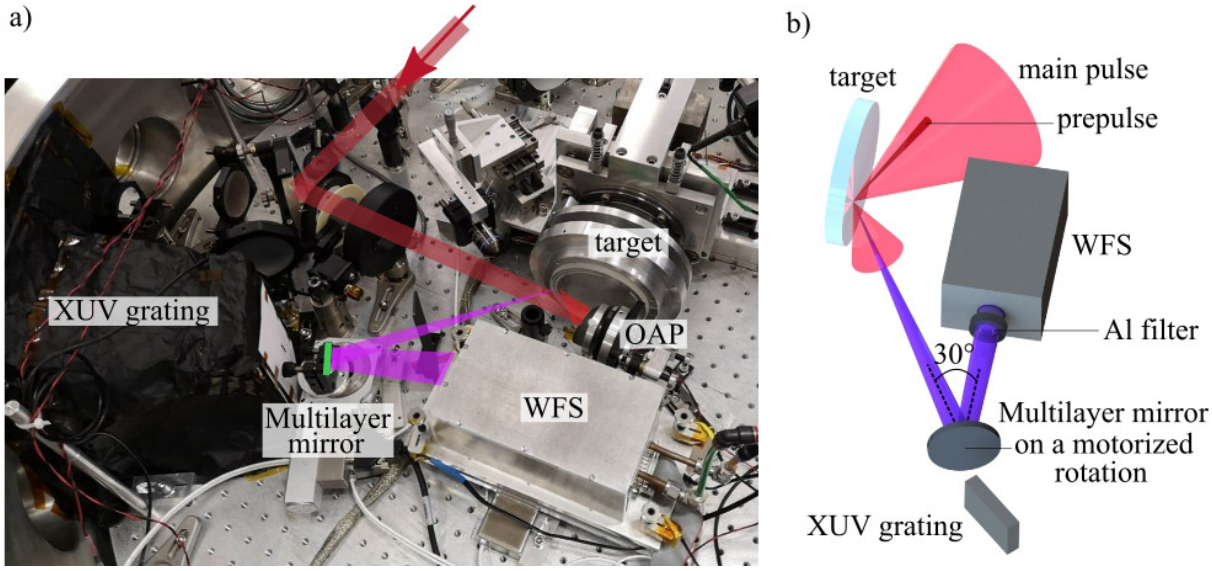

Figure 6.10: *a) picture of the experimental setup for the monochromatic XUV wavefront measurement. b) 3D drawing of the setup.*

Although planned, broadband measurements (see Appendix D) were not performed due to experimental issues which I will detail in the next chapter. Nonetheless, we performed monochromatic measurements using a multilayer mirror (see fig. 6.10). We had three different multilayer

mirrors with an optimum reflectivity (around 10 %) at respectively 44.4, 33.3 and 23.5nm (with a ≈ 3eV bandwidth), all optimized for use at 15° angle of incidence. The wavelength 23.5 nm is actually just below our usual detection range with the XUV spectrometer, whereas 33.3nm is detected but falls below the spectral cutoff wavelength for CWE harmonics, where we do not always have signal. Therefore, we decided to start with the 44.4nm mirror (see fig. 6.11).

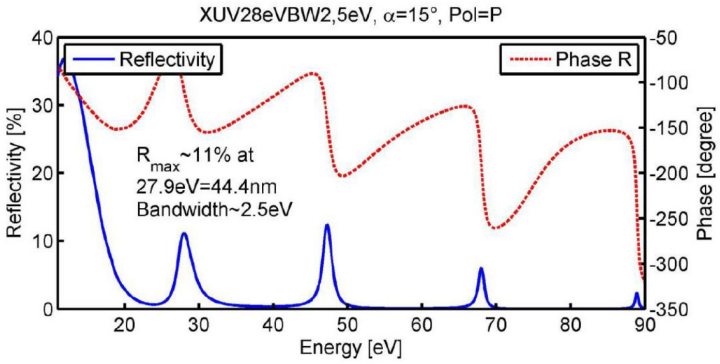

Figure 6.11: *Reflectivity and phase introduced by the multi-layer mirror optimized for 44.4 nm as a function of the photon energy.*

6.3 Electron detection

6.3.1 Spatial detection

For the electron spatial detection, we used a 75mm wide LANEX scintillating phosphor screen (covered with an aluminum foil to block low-energy electrons) placed between the normal and the specular direction so as to be used simultaneously with the XUV spectrometer. The screen was placed ≈ 20cm from the interaction point and imaged on a CCD camera. Details about this diagnostic, which was also implemented by my predecessors, can be found in E.

6.3.2 Magnetic electron spectrometer

Stefan Haessler and I built and implemented a magnetic electron spectrometer to measure the energy spectrum of the electron beam. It was designed with the help of Jérôme Faure's Matlab code, also used for the electron energy measurement in the LWFA experiments presented earlier. The electron beam is spatially filtered with a 0.9mm diameter pinhole and then goes through a pair of neodymium circular permanent magnets with a $R_a = 10$mm radius and 10mm thickness, before reaching the LANEX screen detector (fig. 6.12). The position of the electrons on the screen due to the deviation by the magnetic field gives direct access to their kinetic energy, as demonstrated in Appendix F.

The whole assembly was put on a motorized horizontal translation stage in order to move it to the side of the Lanex screen and be able to switch between spatial and spectral measurements during experiments. The magnets were mounted on a motorized vertical translation stage to allow taking a reference image with the pinhole only.

Calibration of the spectrometer

To calibrate our spectrometer, we measured the magnetic field strength in the center of the two magnets with a Hall probe: B≈84mT, and a 2D map of the magnetic field between the two magnets was then generated with the *Poisson Superfish* software. The accuracy of the theoretical B field map produced by this software has been previously checked by comparing it with measurements of the B field at different positions between the two magnets ([113], p.52).

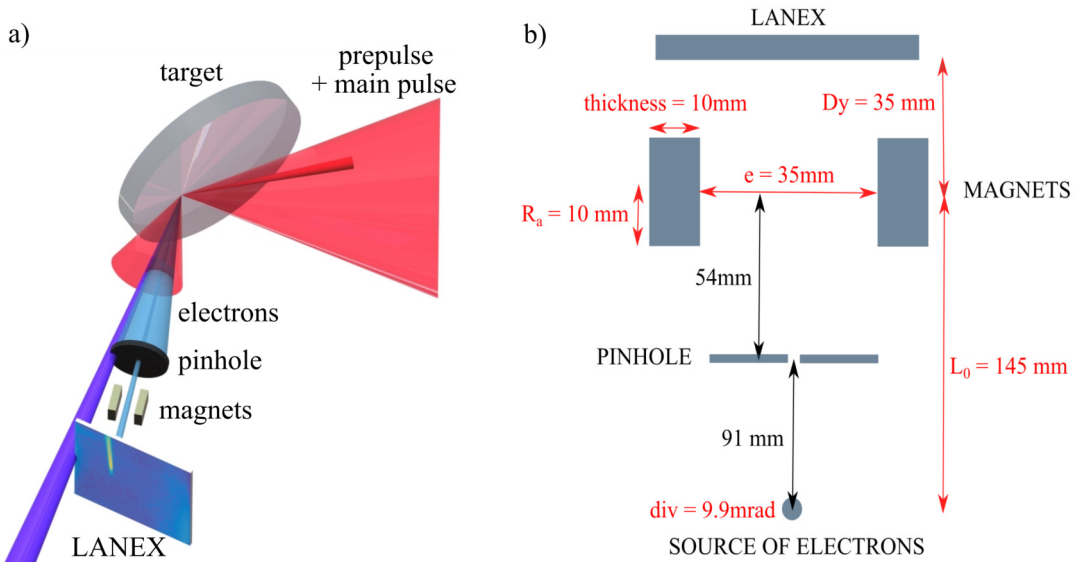

Figure 6.12: *a) 3D schematic drawing of the experimental setup for electron spectra measurement. Not shown here are the shielding aluminum box behind the Lanex, the Al foil covering the Lanex screen, the 45 degree plane mirror and the Pixelink camera with the objective used to image the Lanex screen. b) Schematic drawing with the lengths and distances indicated (top view).*

The Matlab script that we used then calculates numerically the propagation of relativistic electrons through the magnetic field given by the field map, and gives us the impact points of the electron trajectories for different initial velocities on the detection plane.

6.4 Proton detection

We used two different diagnostics for ion detection: a Thomson Parabola Spectrometer (TPS) and a small MCP used as a Time Of Flight (TOF) detector. The TPS was lent to us by Alessandro Flacco (LOA): all its constituents were already mounted in a separate small chamber that we simply had to connect to a spare flange of our experimental chamber. Dan Lévy (Weizmann Institute, Tel Aviv) helped us make it work and analyze the data.

6.4.1 Thomson parabola spectrometer: description

The Thomson parabola spectrometer (TPS) allows measuring the proton spectra in the normal direction. It consists of a 300μm pinhole that spatially filters the beam, two parallel copper electrodes (to which a 2kV DC voltage is applied, resulting in an electric field strength of 2kV/cm) and a pair of permanent magnets (an average magnetic field strength of 0.32 T was measured between the two magnets), which deflect the ions and protons depending on their charge to mass ratio, along with a circular MCP-Phosphor assembly placed 210mm away from the far edge of the magnets that converts the signal into visible light (see fig. 6.13). A negative 1.1 kV DC high-voltage is applied to the front of the MCP (the side on which the protons impact the MCP) so as to attract positively charged particles, while the back side of the MCP is grounded. The Phosphor screen is biased with a positive 3.5kV DC HV to attract the electrons. Finally, the detector is imaged on a CCD camera (*Pixelink*). An example of recorded image is shown in figure 6.14.

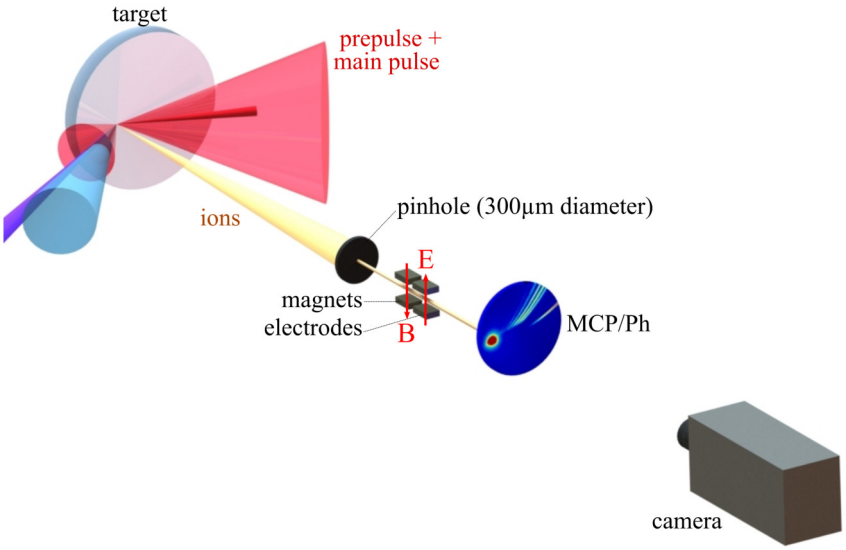

Figure 6.13: *Experimental setup with the Thomson Parabola Spectrometer (TPS) for measuring the protons spectra.*

TPS Data analysis

One can derive the following expression for the position of the charged particles on the detector [28]:

$$\begin{cases} x = Ze\dfrac{E}{E_i}\dfrac{lD}{2} \\ y = Ze\dfrac{B}{\sqrt{ME_i}}\dfrac{lD}{\sqrt{2}}, \end{cases}$$

where $M = Am_p$ is the ion mass, E_i its kinetic energy, D is the distance from the magnets to the detector, l is the length of the electric and magnetic plates, and E and B are the electric and magnetic field strengths, respectively.

In these equations, the dependencies $x \propto Z$ and $y \propto Z/\sqrt{M}$ indicate that a given parabolic trajectory corresponds to a given Z/M ratio, whereas the dependencies $x \propto 1/E_i$ and $y \propto 1/\sqrt{E_i}$ tell us that the most energetic ions will fall on the detector close to the center. Thus, the distance from the center along a given parabolic trajectory corresponds to the energy, which allows to retrieve the energy spectrum.

Among all parabolic trajectories, the protons are easy to distinguish as they are further from all the other trajectories (see fig. 6.14).

The proton trace clearly appeared immediately during the first laser shots after we installed the detector. Protons cannot come from the target material directly, therefore we assume that they originate from pollution (water vapors and hydrocarbon contaminants) on the target surface. Thus, we consider the existence of carbon and hydrogen atoms in addition to silicon and oxygen in order to interpret the data. The charge to mass ratios (with the masses expressed as multiples of the proton mass m_p) of all the different potential ions are shown in Table 6.1.

For focused laser intensities around 3.10^{17}W.cm^{-2}, corresponding to the example shown in fig. 6.14, the highest Z/M ratio (after protons) that we can hope to see is 0.38 and corresponds to O^{6+}, according to barrier-suppression ionization values. Nonetheless, the analysis of the TPS data indicates the presence of ions with a higher ratio, such as C^{5+}, probably due to tunnel ionization or electron-impact ionization.

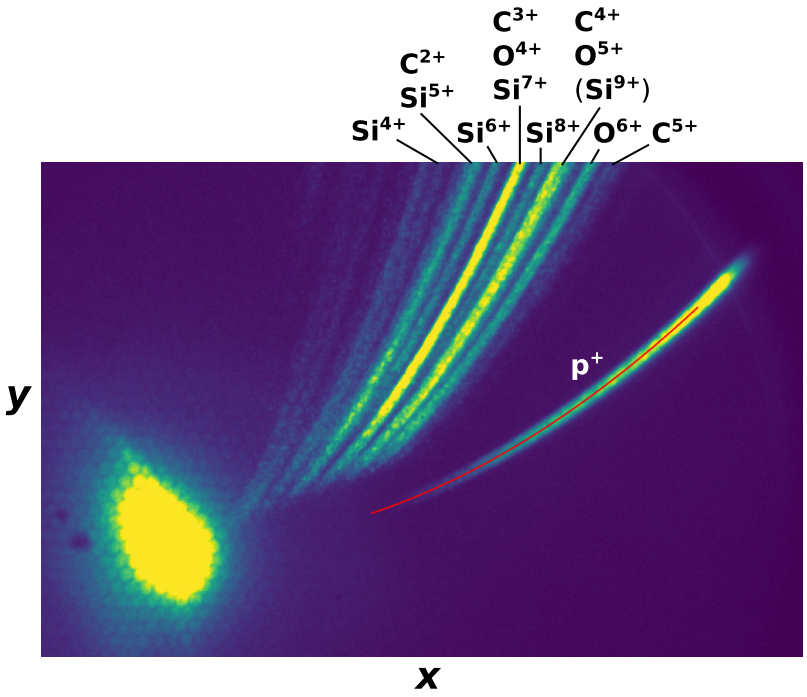

Figure 6.14: *Example of image recorded with the TPS for 200 fs (chirped) pulses at the steepest density gradient. Possible ion species are identified according to their charge to mass ratios. The red curve corresponds to the theoretical proton parabola.*

mass	I	II	III	IV	V	VI	VII	VIII	IX	X	XI	XII	XIII	XIV
1 (H)	1													
12 (C)	0.08	0.17	0.25	0.33	0.42	0.5								
16 (O)	0.06	0.13	0.19	0.25	0.31	0.38	0.44	0.5						
28 (Si)	0.04	0.07	0.11	0.14	0.18	0.21	0.25	0.29	0.32	0.36	0.39	0.43	0.46	0.5

Table 6.1: *Charge to mass ratios of carbon, hydrogen, oxygen and silicon ions, in m_p units*

6.4.2 Time Of Flight detector

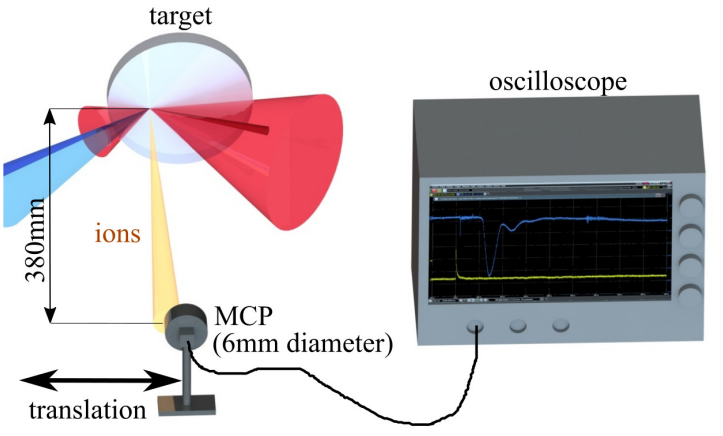

Figure 6.15: *Schematic drawing of the exeperimental setup for the angular profile measurement of the proton beam.*

Alternatively, we also measured the proton beam angular distribution around the normal

direction with a small, 6mm diameter, 0.5mm thick MCP (grounded on the front side, which is facing the particles, and biased by a positive 600V voltage at the back), mounted on a motorized translation stage located at a distance d =380 mm away from the interaction point. Combined with our fast oscilloscope (described in subsection 4.1.3), it was used as a time of flight detector (see fig. 6.15). The oscilloscope was operated in *Segmented Memory Acquisition* mode, which allowed us to record the 100 consecutive acquisitions spaced by 1ms (single-shot measurements), and triggered by a fast photodiode looking at a leak of the laser beam coming out of the chamber (e.g. the leak going to the f-2f interferometer for the CEP measurement). The MCP was calibrated after the experimental campaign so as to determine the proton charge (see Appendix G).

Using TOF detectors in TNSA experiments is not something new, however researchers never seem to use them for measuring angular profiles, which is actually quite simple. This might be due to their larger particle beam divergence, which would require a curved translational trajectory to accurately scan the angular distribution. In our case, the setup provides an acceptance angle of 0.9° and the broadening of the measured angular profile due to the convolution with the detector size is negligible.

Example of measurement

A typical signal obtained during this campaign is shown in 6.16.a. There is first a *photopeak*: t=1.27ns (=380mm/c, with c the speed of light) corresponds to electromagnetic radiation from the interaction, which gives a precise temporal reference for the measurement. The reference signal from the photodiode also confirms that this is the arrival time of the laser, as the temporal separation of the peaks in the two signals corresponds to the propagation distance of the beam between the considered leak and the interaction point. The very short tail (typically up to a few ns) of this photopeak corresponds to the detection of fast electrons, UV and X-ray emission from the plasma.

Then, protons being faster than all the other ions, the peak is easily identified, followed by the ion contribution. We only considered the proton peak, averaged the signal over the 100 shots and converted the arrival time into kinetic energy. The signal amplitude corresponds to the proton charge, which was calibrated. The energy range that we found with this measurement was in quite good agreement with the data from the TPS (see fig. 6.16.b for a comparison).

The noisy signal observed between 0 and 50 ns is very typical of undesirable electromagnetic pulses (EMPs) created in the light-matter interaction. Those EMPs scale with the laser energy and intensity in focus, and can originate from neutralization currents caused by electron emission. Figure 6.17 shows a typical EMP signal obtained in a TNSA proton acceleration experiment with similar intensities and pulse durations on target, from [226]. Those EMPs are coupled to most electronic devices (oscilloscopes, detectors) and are often the main limit on the detectors' resolution. Because of that, determining the precise proton cutoff energy was actually not so trivial.

First interpretation

For energies up to several tens of MeVs, we can use non-relativistic formulas (see section 2.4). The kinetic energy E_i acquired by an ion with a charge state z_i (degree of ionization) in a potential Φ is given by $E_i = z_i q_e \Phi$, with q_e the elementary charge ($\approx 1.6 \times 10^{-19}$ C). On the other hand, we have

$$E_i = \frac{M_i v^2}{2} = \frac{M_i d^2}{2t_i^2}, \tag{6.1}$$

with M_i the nucleon mass. Thus the time of flight of an ion from the target to the detector will be:

$$t_i = d\sqrt{\frac{A_i m_p}{2 z_i q_e \Phi}} = t_p \sqrt{\frac{A_i}{z_i}}, \tag{6.2}$$

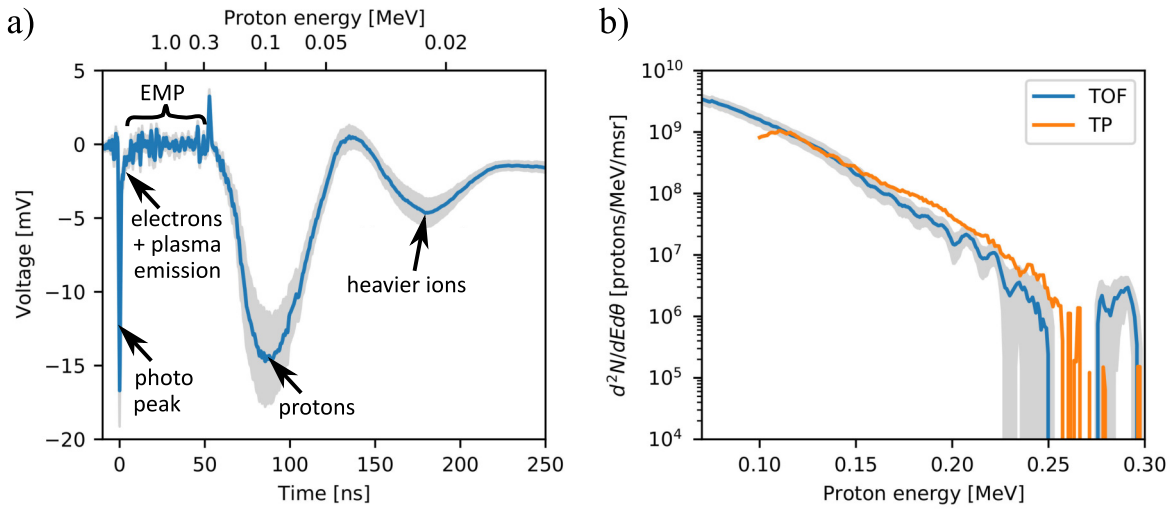

Figure 6.16: *a) Example of ions detection with the small MCP and the oscilloscope used as a TOF detector. For this trace, the pulse duration was 27 fs and the detector was placed along the normal direction ($\theta = 0$). The solid blue line is the average over the 100 consecutives shots, while the shaded gray area is the standard deviation of the data set at each time. b) Comparison of the spectrum retrieved from the TOF measurement in fig. 6.16 and from the TPS.*

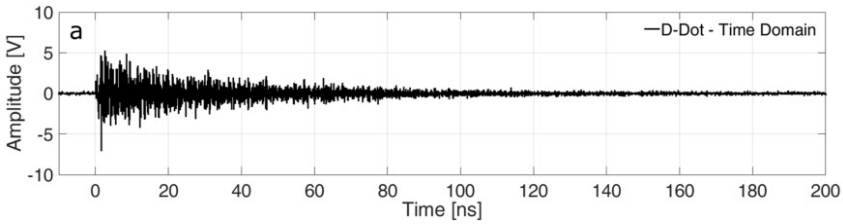

Figure 6.17: *Typical EMP signal, here obtained in a TNSA experiment with $I \sim 10^{19}$W.cm^{-2} and 30fs pulse duration. The signal was detected with a differential electric field sensor placed 31cm from an Al foil target. Reprinted from [226].*

where A_i is the mass number (total number of protons and neutrons in the ion), m_p the proton mass and t_p the time of flight of a proton accelerated by the same potential. For any ion, except protons, $A_i > z_i$, and the protons will reach the detector much earlier than other ions accelerated.

For the maximum accelerating potential, the lightest, fully-stripped (*ie* $z_i = A_i/2$) ions will be separated in time from the fastest protons (reaching the detector at t_{pM}) by an amount

$$\Delta t_M = t_{pM}\left(\sqrt{\frac{A_i}{z_i}} - 1\right) = t_{pM}(\sqrt{2} - 1) \approx 0.4 t_{pM}. \tag{6.3}$$

In fig. 6.18, raw data are shown for four different pulse durations. We can already see that for short pulses, the protons arrive later, and their peak is well separated from the ion peak. On the contrary, for chirped pulses, the protons and ions are both faster, and the two peaks begin to overlap. Thus, although the laser intensity decreases, the acceleration mechanism becomes more efficient as the pulse duration increases and the intensity decreases. Defining the maximum proton and ion energies from these data is non-trivial, but it seems that the time interval between the fastest protons and the fastest ions Δt_M is always much more than 0.4 t_{pM}, indicating that we do not have fully stripped ions (except of course H^+). For example, in fig. 6.18.d, the fastest protons arrive at around 50ns, thus fully stripped ions would reach the detector at approximately 70ns, which does not seem to be the case. Instead the fastest ions arrive

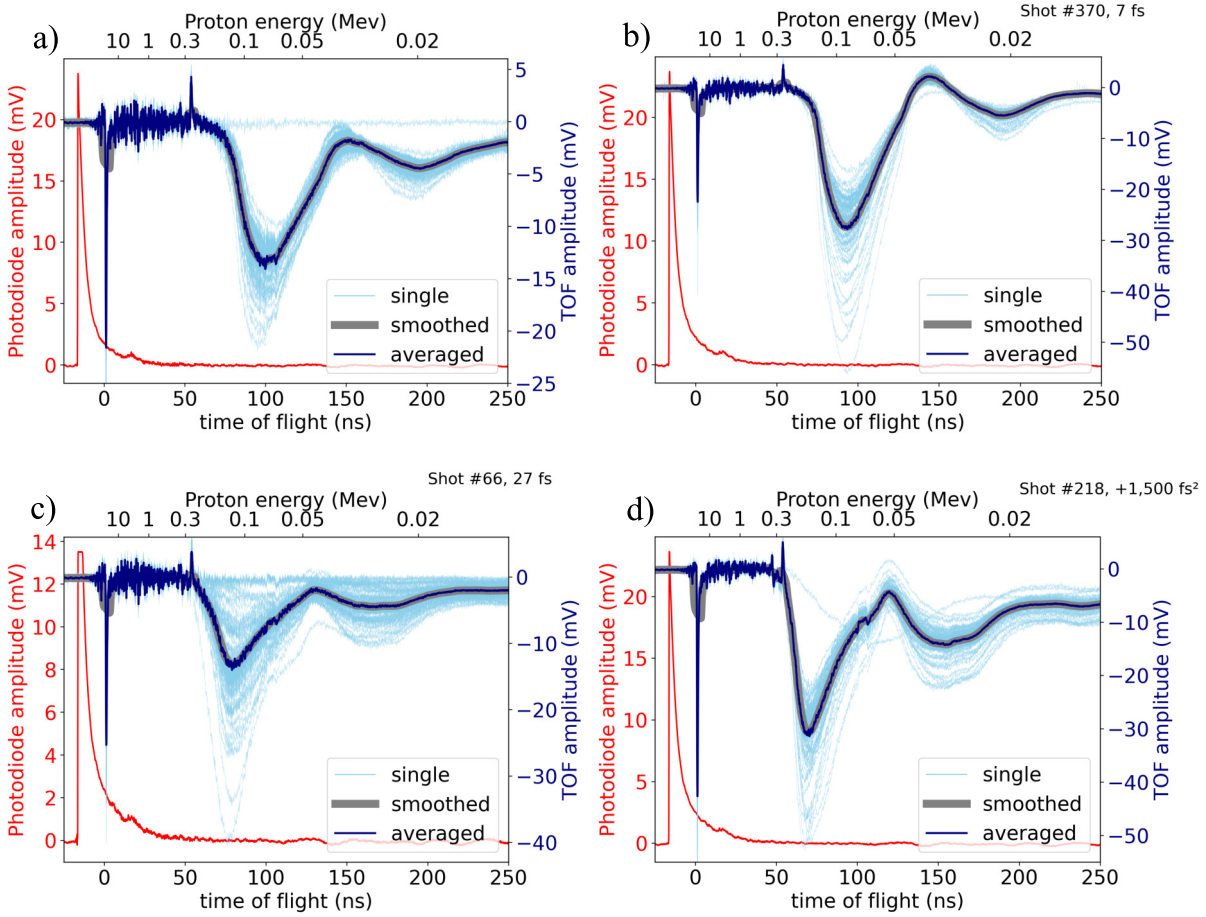

Figure 6.18: *Raw data for four different pulse durations, with the detector at 0° (along the target-normal direction). a) 4fs b) 7fs, c) 27fs and d) 27fs with a 1500* fs^2 *positive chirp. The light blue lines are the 100 consecutive, single-shot acquisitions, while the dark blue line is the average signal and the thick gray line is the smoothed average signal. The red signal corresponds to the laser light leak detected with the fast photodiode, used as a reference and for triggering the acquisitions.*

at ≈110ns, corresponding to $\Delta t_M \approx 1.33 t_{pM}$ *ie* a maximum z_i/A_i ratio of $1/(1+1.33)^2 \approx 0.18$. This ratio is that of Si^{5+}, for example, which can definitely be obtained at laser peak intensities $\approx 4.7 \times 10^{17} W.cm^{-2}$, for which the considered curve (fig. 6.18.d) was measured. Nonetheless, this method is not very precise for determining the ion species that we may have accelerated, and cutoff energies are more reliably determined from the Thomson parabola spectrometer.

6.5 Reflected laser near-field

Another diagnostic is the camera that we use to look at the diffusion of the laser beam from the entrance mask (or slit) of the XUV spectrometer (see fig 6.19.a), which is covered with a basic white sheet of paper. It helps us optimize the parabola-to-target distance at the beginning, but also check that the reflected beam is centered on the XUV grating. If not, we can try to adjust the position of the incident beam near field, or the relative prepulse position. We added a 800nm bandpass filter mounted on a motorized flip in order to be able to insert it or not in front of the camera objective (for plasma expansion speed measurements, see section 6.6). It would have been interesting to detect light at ≈50-100 nm instead, so as to see the XUV beam and not the reflected vis-IR light, but unfortunately we did not have the appropriate filters and

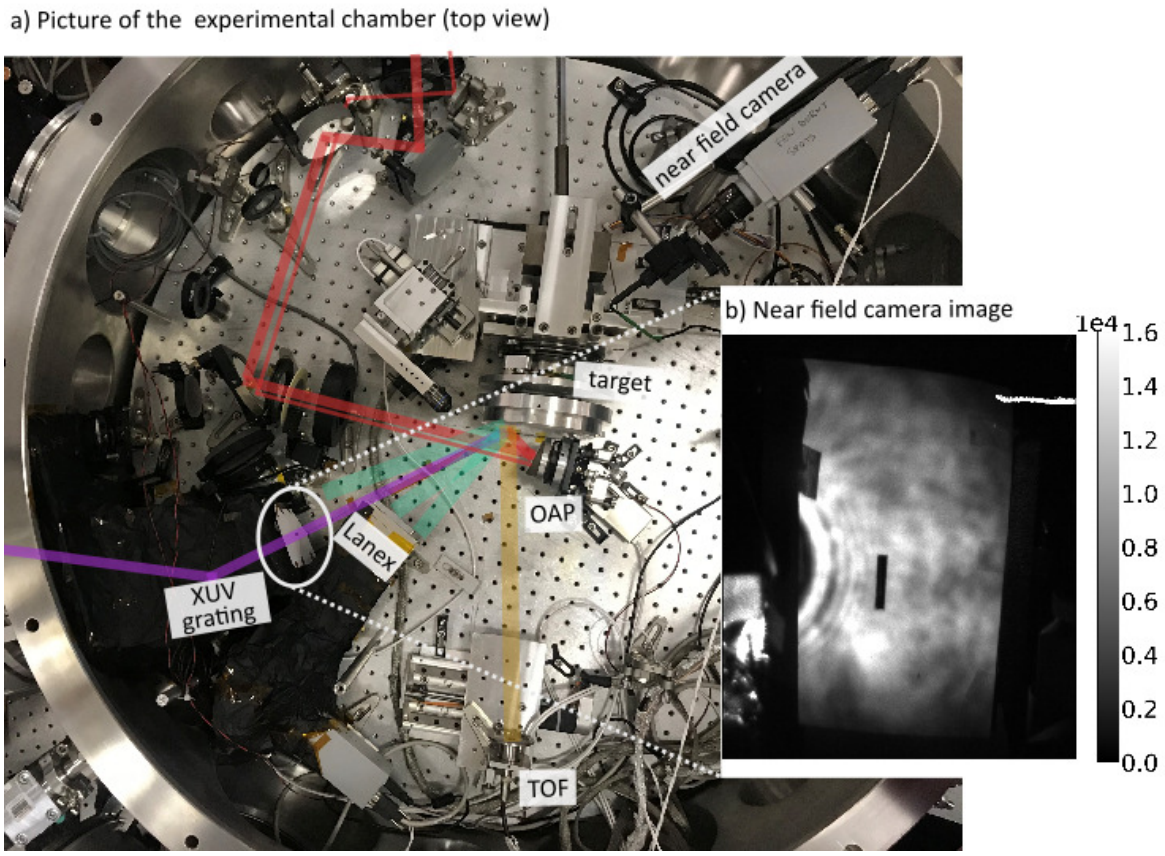

Figure 6.19: *a) picture of the experimental chamber showing the position of the near field camera and some other diagnostics. b) example of image recorded with the near field camera, here without preplasma, when the target is not in the focal plane so that we can nicely see the reflected beam, which is not too distorted. The slit height is ≈ 20mm.*

camera.

6.6 Plasma density gradient measurement

In order to experimentally determine the plasma density gradient scale length L_g at the precise moment when the laser/plasma interaction occurs, we use a technique called Spatial Domain Interferometry (SDI), which was developed a few years ago in the PCO group [22]. By performing this spatial interferometric pump-probe measurement, one can experimentally determine the plasma expansion speed c_s.

This very simple method was inspired from the well established Frequency Domain Interferometry (FDI) or spectral interferometry technique [99, 137]. In FDI, a perturbed laser pulse (perturbed by the preplasma) to be characterized is set up to interfere with a reference pulse in a spectrometer, yielding spectral fringes, whose period and amplitude give access to the preplasma electron density. Obtaining the temporal evolution of the preplasma normally requires multiple shots to probe it at different times, but in [99], the authors proposed a single-shot method which relies on using a very long, chirped pulse to probe the preplasma, so that the temporal evolution is encoded in the spectrum. This single-shot method is particularly interesting for low repetition-rate lasers but unnecessary in our case.

Alternatively, in [128], the authors used a frequency doubled probe beam propagating along the target surface to perform shearing interferometry [3]. The interferogram is a spatial map of

the phase shift induced by the preplasma, from which the plasma electron density can be estimated (assuming radial symmetry of the preplasma with respect to the target normal direction, which allows using Abel inversion for the retrieval).

It would be interesting for us to use this kind of method, although it is rather complex compared to SDI, in order to get additional information about the shape of the preplasma (something that we are quite concerned by, working in the $\sim \lambda^3$ regime).

Other groups simply use hydrodynamic codes, such as MEDUSA [144, 178] or HYADES [148, 158], to estimate their density gradients.

6.6.1 Principle of the SDI measurement

In SDI, the principle is the following: the prepulse (or "pump pulse") ionizes the target and initiates the plasma expansion, just like in experiments (fig. 6.20.a). The main pulse, which is modified by adding a periodic transmission mask T_M of period a in the beam path prior to the focusing parabola, is then used to probe the plasma at a controlled time τ after the prepulse (fig. 6.20.b). Due to the transmission mask, the beam focuses into diffraction spots spaced by

$$\boxed{d = \lambda f / a},$$

where f is the parabola focal length (fig 6.21). Ideally, only the central (0th order) diffraction spot overlaps with the prepulse in focus, therefore experiencing a phase shift $\Delta\phi$ relative to the other higher order diffraction spots upon reflection near the plasma critical density surface.

The reflected probe beams spatially interfere, constructively or destructively depending on $\Delta\phi$. As we increase the delay τ, the critical density surface expands towards vacuum and the phase shift $\Delta\phi$ increases. Every time $\Delta\phi$ is increased by π rad, there is an inversion in the pattern observed far from the target (fig. 6.20.c).

From the delay-dependence of the phase shift, one can estimate the plasma expansion velocity c_s, and therefore the gradient scale length for a given prepulse delay: $L_g = c_s\tau$.

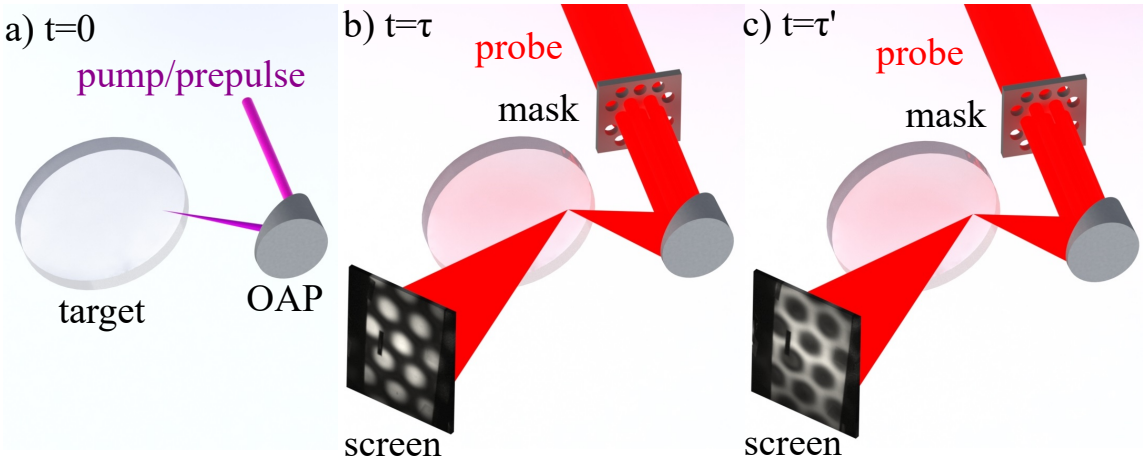

Figure 6.20: *Schematic representation of the experimental setup for the SDI measurement. a) the prepulse/pump pulse initiates the preplasma expansion. b) after a delay τ, the probe beam is reflected by this preplasma and generates a pattern with bright disks far from the target. c) if the probe beam is now delayed by τ' instead of τ (by moving the motorized delay line), the pattern is inverted when the phase shift is increased by π. Note that the images displayed on the 'screen' are actual recorded data from a typical SDI measurement.*

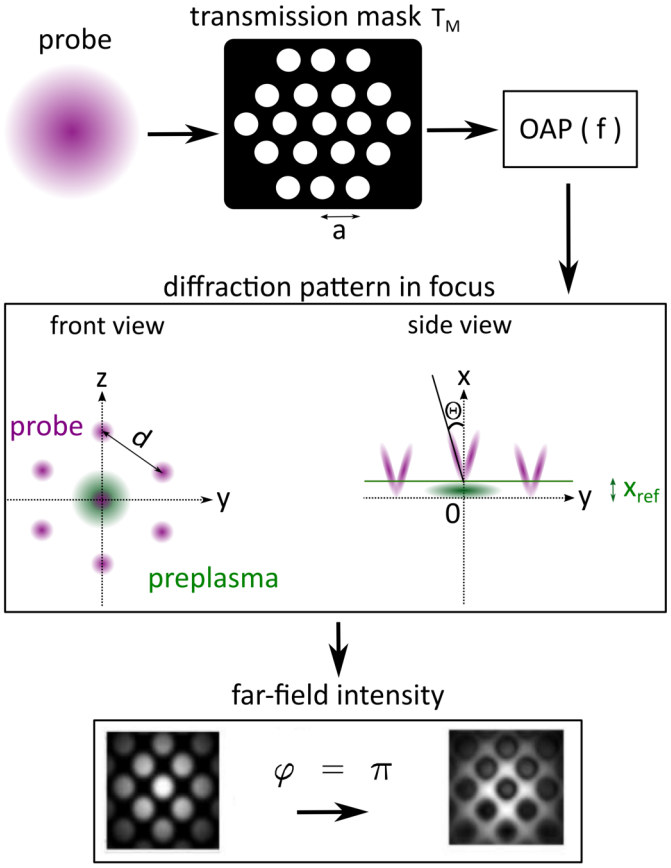

Figure 6.21: *Principle of the SDI measurement. The probe beam goes through a periodic transmission mask (of period a). As it is focused by the OAP (of focal length f), a diffraction pattern is generated on target (with diffraction spots spaced by $d = \lambda f/a$). The central spot experiences a phase shift due to the reflection at $x = x_{ref}$ instead of at x=0. This induces a phase shift Φ between the central and the satellite spots. The pattern observed far from the target is reversed every time the phase shift is increased by π. Inspired from [22].*

6.6.2 SDI measurement in practice

In practice, this measurement is extremely simple: it only requires inserting a periodic mask (which can be on a motorized flip) in the main beam path, and image the reflected beam diffused on a screen placed a few tens of centimeters away from the target, with the near field camera described in the previous section. We do this for different delays τ and save the images. There is one detail which helped a lot improving the contrast of the images: placing a 800nm narrow-band chromatic filter in front of the camera.

6.6.3 Data analysis procedure

We first select a small bright area and a small dark area on the image corresponding to a non-delayed prepulse and integrate the signal over each area, which gives the quantities S_{bright} and S_{dark}. The SDI contrast for a given prepulse delay τ is then defined as:

$$SDI_{contrast}(\tau) = \frac{S_{bright}(\tau) - S_{dark}(\tau)}{S_{bright}(\tau) + S_{dark}(\tau)} \tag{6.4}$$

The curve $SDI_{contrast}(\tau)$ oscillates between extrema, occurring at prepulse delays τ_n (fig.

6.23). Each extremum corresponds to a phase shift $\Delta\phi = n\pi$ of the central spot with respect to the satellite spots. The scattered plot $(n\pi, \tau_n)$ can be fitted with a linear function $\Delta\phi = f(\tau)$, whose slope is related to the plasma expansion speed c_s (fig. 6.24).

Let us now see how the coefficient of the slope is connected to c_s using the isothermal model described in section 2.2. Due to the preplasma expansion, the main/probe beam is not reflected at $x = 0$ (initial target surface position) but at the position x_{ref} at which the plasma density is $n_c \cos^2\theta_i$, with θ_i the angle of incidence, instead. Using equation 2.15,

$$n_e(x_{ref}) = n_c \cos^2\theta_i \Leftrightarrow x_{ref} = c_s \tau \ln\left(\frac{n_{e0}}{\exp(1) n_c \cos^2\theta_i}\right) \tag{6.5}$$

The total optical path difference is $\Delta x = 2x_{ref}\cos\theta_i$ (see figure 6.22) and the dephasing is given by $\Delta\phi = -k\Delta x = -2\pi/\lambda \Delta x$. Finally,

$$\Delta\phi = -\frac{4\pi c_s \cos\theta_i}{\lambda} \ln\left(\frac{n_{e0}}{\exp(1) n_c \cos^2\theta_i}\right) \times \tau \tag{6.6}$$

where the only unknown parameter is c_s.

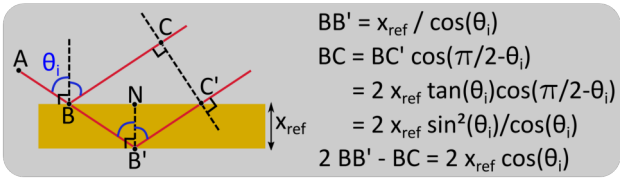

Figure 6.22: *The total optical path difference induced by a difference in reflection depth x_{ref} corresponds to the difference between the path ABC and the path AB'C'. As shown here (in agreement with [22] and contrary to what was written in [288]), it is equal to $2x_{ref}\cos\theta_i$.*

However, in practice, the 1st order diffracted spots also experience a phase shift and what we measure is actually the phase difference between the first order spots and the 0 order spot:

$$\Delta\phi_{exp} = \frac{4\pi\cos\theta_i}{\lambda}\left[\tau(c_{s0} - c_{s1}) \ln\left(\frac{n_{e0}}{\exp(1) n_c \cos^2\theta_i}\right)\right], \tag{6.7}$$

with c_{sn} the plasma velocity seen by the nth order spot. Assuming that the ion speed velocity at a given position is proportional to the square root of the local prepulse fluence, this becomes:

$$\boxed{\Delta\phi_{exp} = c_{s0} \times \frac{4\pi\cos\theta_i}{\lambda}\left[\tau\left(1 - \sqrt{\frac{F_1}{F_0}}\right) \ln\left(\frac{n_{e0}}{\exp(1) n_c \cos^2\theta_i}\right)\right]}, \tag{6.8}$$

where F_n is the prepulse fluence at the location of the n^{th} order diffracted spot. The expansion speed c_{s0} is then deduced from the slope of the experimental $\Delta\phi = f(\tau)$ plot.

6.6.4 Discussion

The above derivation is based on the assumption that the expansion speed is proportional to the prepulse fluence ($c_s \propto \sqrt{F}$), commonly expressed in J.cm^{-2}. This is motivated by the isothermal model, in which $c_s \propto \sqrt{T_e}$ and the assumption that the prepulse absorption coefficient is the same everywhere at the target surface.

Therefore the plasma expansion speed c_s does not depend on the pulse duration, which we verified experimentally. However, it depends on the pulse energy, the laser beamprofile in

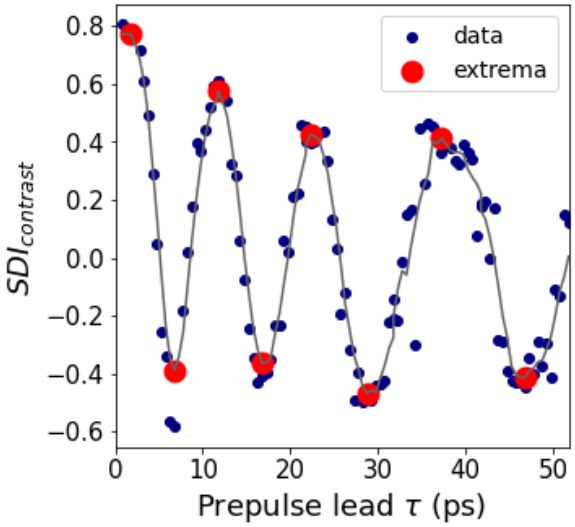

Figure 6.23: *Experimentally measured SDI contrast for different prepulse delays τ (blue dots), smoothed curved (solid gray line) and identified extrema (red dots). Pulse duration: 4fs.*

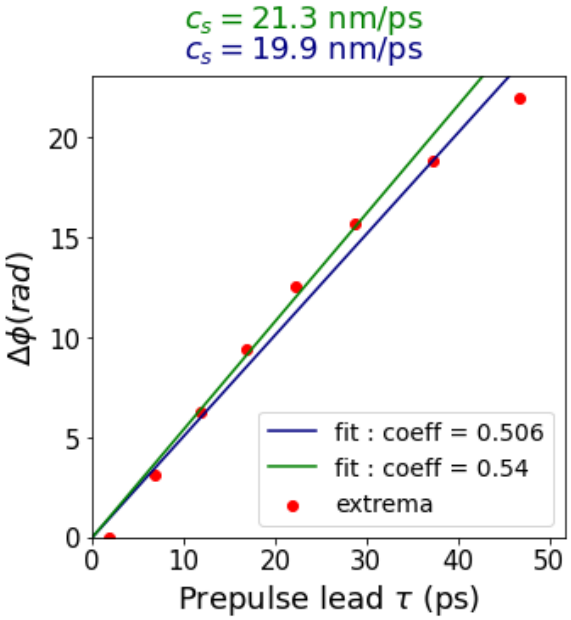

Figure 6.24: *Experimentally measured central spot dephasing as a function of the prepulse delay τ (red dots), and the corresponding linear fit when taking all the points into account (dark blue line) or when only considering the first four points (green line).*

the plane of the holey mirror, the position of the beam with respect to the holey mirror, and the prepulse spatial intensity distribution in focus. Unfortunately, we did not carefully check everyday what the prepulse energy was, and we did not make SDI measurements everyday either, therefore slight differences in alignment from one day to the next result in some uncertainty on our estimation of c_s.

There are other sources of uncertainties. First, it is quite difficult to estimate n_{e0}. In the original publication on the SDI method [22], a density of $300n_c$ was used, and the authors measured a plasma expansion velocity $c_s = 10.8$ nm/ps. However, in this paper, the authors assumed that the laser reflects at n_c and that the density at $x = 0$ is n_{e0} rather than $n_{e0}\exp(-1)$. Moreover, using barrier suppression ionization thresholds, for our prepulse intensity of 3.5×10^{14}W.cm^{-2}, we only set free 4 electrons per molecule. Therefore, a more accurate assumption would be to use $n_{e0} = 50n_c$ instead, as suggested in [288].

Additional errors may come from:

· the assumption of an exponential density profile

· the assumption that the prepulse energy is spatially homogeneously absorbed

· the assumption that n_{e0} is spatially homogeneous at the target surface

· the estimation of the prepulse intensity...

Overall, this method is very convenient and easy to implement, but the uncertainty on the expansion velocity measurement probably exceeds 50% [288].

Final parameters for the SDI analysis

Eventually, for the SDI analysis, we chose to use $n_{e0} = 50n_c$, $\lambda = 800$nm, $\theta = 55°$ and the ratio F_1/F_0 was determined experimentally from a recorded image of the prepulse intensity distribution in focus (such as the one shown in fig 6.4b), after verifying the locations of the

diffracted spots.

Finally, to account for the finite temporal contrast of the main pulse, we consider the plasma gradient scale length to be

$$\boxed{L_g = L_0 + c_s \tau}, \tag{6.9}$$

where L_0 is an unknown offset, which we estimate to be $\sim \lambda/100$, as discussed in section 5.1.

Chapter 7

Light and particle beams from plasma mirrors: experimental results

"The Universe is under no obligation to make sense to you".
Neil deGrasse Tyson

This last chapter is dedicated to the experimental results obtained using the experimental setup described in the previous chapter for studying the laser interaction with plasma mirrors. I divided this chapter into three different parts: in the first section, we will focus on our observations at low intensities (proton acceleration and CWE harmonics). In a second part, we will explore the high intensity interaction with plasma mirrors and talk about ROM harmonics, XUV beam measurements, as well as LWFA of electrons in long gradients. The third and last part will be dedicated to CEP-dependent measurements.

7.1 Interaction at low intensity

We are first interested in what happens at sub-relativistic intensities. The main phenomena occurring at low intensities are 1) the emission of CWE harmonics, which is anti-correlated to the electron emission, and 2) the acceleration of protons.

7.1.1 Anticorrelation of electrons and CWE harmonics

The gradient dependencies of electrons and harmonics in the case of a Brunel dominated interaction have already been detailed in the frame of Maïmouna Bocoum's thesis for $\approx$ 30 fs pulses. Their behavior is now well understood. In order to verify the reproducibility of our experimental results regarding CWE harmonics and to check that we are now in a higher intensity regime, we reduced the intensity on target by placing a circular aperture in the beam path or by chirping the laser pulse to increase its duration.

Reduced intensity using a 15mm diameter aperture

First, we irised the beam with a 15mm diameter aperture placed in the collimated beam path before the OAP, so as to reduce the intensity on target. The pulse energy was 2.4 mJ before the iris and 0.9mJ after the iris, measured with a *Gentec* energy meter inside the SHHG chamber. We obtained a $3.2 \times 2.8\mu$m FWHM beam in focus (see fig. 7.1.a.) with the 15mm aperture, corresponding to 3×10^{17}W.cm^{-2} on target *ie* $a_0 \approx 0.4$ in the case of 27fs pulses and $a_0 = 1.1$ for 3.7fs pulses.

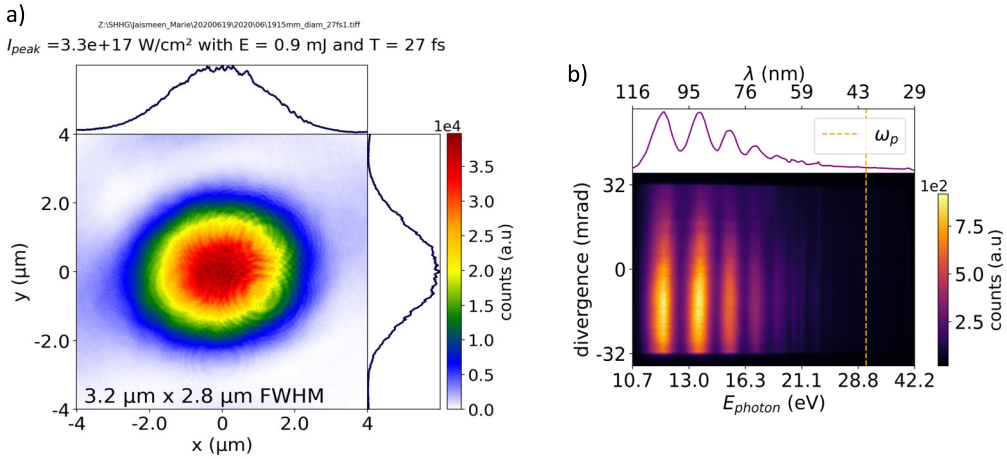

Figure 7.1: *a) Laser beamprofile in the focal plane for the 27fs driving pulses b) Raw image of the harmonic spectrum with calibrated x and y axis, obtained with 3.7fs pulses at 1.3ps prepulse lead time (from the same data set as shown in 7.2.b).*

The CWE harmonics divergence was $\lesssim$ 60 mrad FWHM, based on the raw spectrum for a

3.7fs driving pulse at 1.3ps prepulse lead time, shown in fig. 7.1.b. Theoretically, at 90nm, for a 2.5μm (based on 7.1.a.) source spot radius at $1/e^2$, we should have $\theta \approx 11$ mrad via Eq. 1.40 *ie* a 22 mrad full angle. The experimental value is three times more, which is consistent with the prediction of an initially convex wavefront, as discussed in section 5.1.

The harmonic and electron signals were acquired for different prepulse delays and the resulting gradient scans for 27fs and 3.7fs driving pulse durations, are shown in figure 7.2. The harmonics' spectral extension is optimized for the shortest gradient scale length, and then quickly drops in intensity with increasing gradient scale lengths, which is a well-known behavior of HHG in the sub-relativistic regime, via the CWE mechanism.

We also observed that the emission of harmonics and electrons is anti-correlated, as had been observed previously [23]. For very sharp gradients, the electrons all return into the plasma and trigger plasma waves up to far in the gradient, thus generating broadband harmonics. On the contrary, for softer density gradients, the electrons are able to gain more kinetic energy in the space-charge field created at the target surface and thus escape Brunel's confined orbitals.

At the shortest pulse duration, we were also able to see some LWFA electrons (fig. 7.2.c.), although their charge was much lower than that of Brunel electrons. This had already been observed by Frederik Böhle for the first time ([25], p. 144).

Finally, we note that for the long pulses, the position of the harmonics is very stable as we vary the gradient scale length. On the contrary, for the near-single-cycle pulses, we see a gradual, linear shift of the harmonic peaks along the wavelength axis as we increase the prepulse delay. We may want to attribute these features to variations in the temporal structure of the very short attosecond pulse train emitted (essentially one or two pulse long), but we cannot because the results shown in figure 7.2 were obtained while the CEP was not stabilized at all (even the oscillator's CEP was unlocked, therefore we can consider the CEP as randomly fluctuating from one pulse to the next). This observation is the pure result of the gradient scale length-dependence of Brunel electron dynamics, which is very strong since its effect survives averaging over the CEP.

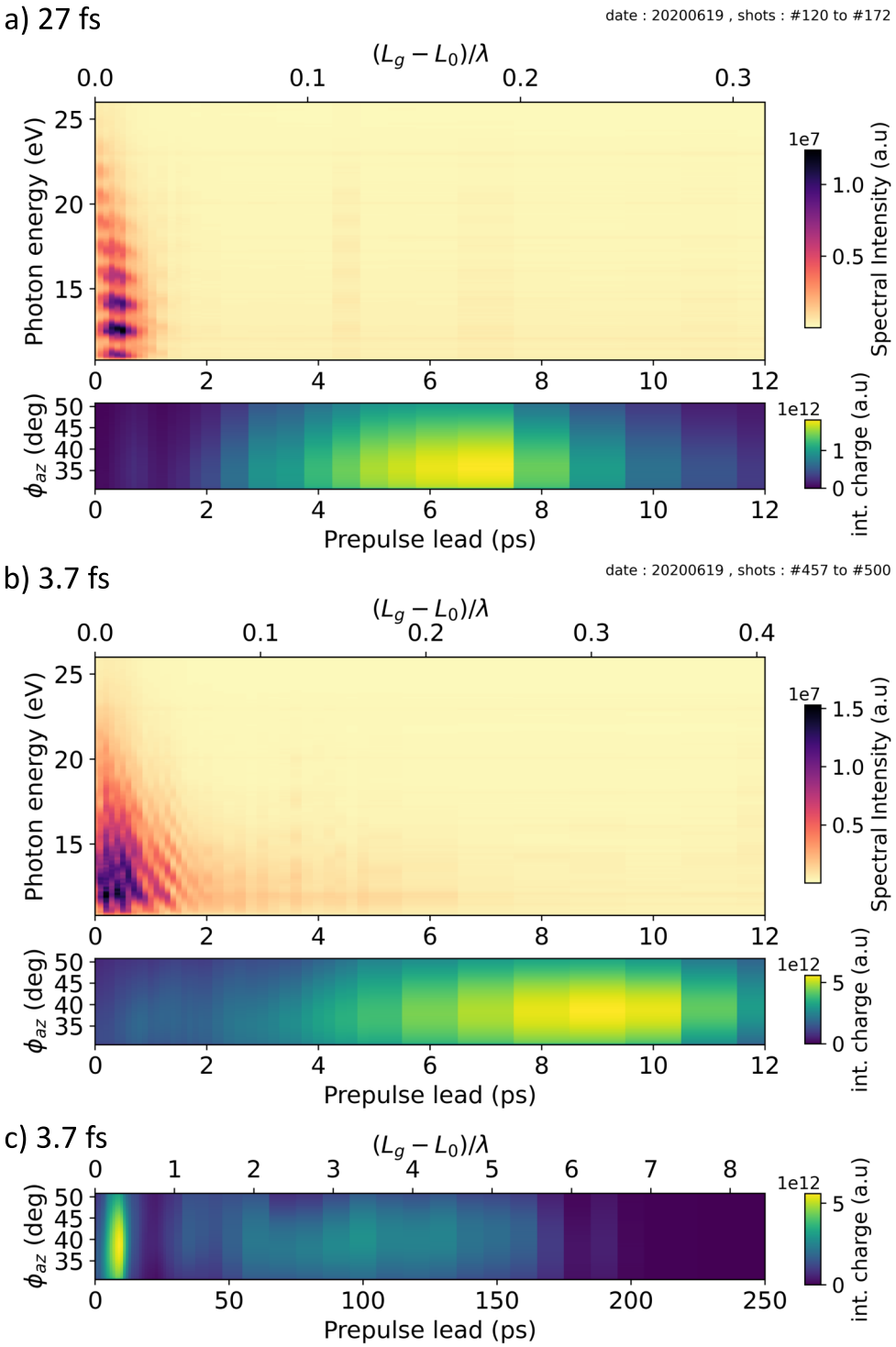

Figure 7.2: *Panels (a) and (b): vertically integrated HHG spectra (top) and electron angular distribution in the horizontal plane (bottom) obtained with a low intensity driving laser (the intensity was reduced by inserting a 15 mm diameter aperture in the beam path). For each prepulse delay, the data is integrated over 100 consecutive shots. The pulse duration was a) 27 fs and b) 3.7 fs. The bottom graph (c) shows the electron angular distribution for 3.7 fs pulses (same data set as in b) up to longer plasma gradient scale lengths. No protons were detected for all these scans on the TPS. All the measurements were done on the same day. Based on SDI measurements made 7 days before, I used a plasma expansion speed $c_s \approx 21$ nm/ps for the long pulses and $c_s \approx 27$ nm/ps for the shortest pulses to calibrate the x axes.*

Reduced intensity by adding GDD with the AOPDF

The intensity can also be reduced by chirping the pulses with the AOPDF located in the second CPA. In figure 7.3.a, we can see a gradient scan for near-Fourier-limited, 24fs driving pulses, whereas in fig 7.3.b, we use the same pulses, but chirped to 85 fs by adding positive GDD (+500fs^2) with the AOPDF. The laser spot size on target was ≈1.6 × 1.2 μm FWHM, with a peak intensity of 2.7×10^{18}W.cm^{-2}. Thus, $a_0 = 1.1$ for the compressed pulses and $a_0 = 0.6$ for the chirped pulses.

In both cases, for prepulse lead times $\lesssim$3ps, the harmonics intensity quickly drops with increasing gradient scale length, indicating that we are still in the CWE regime. At the shortest gradients, the harmonics are broad for the FTL pulses and much thinner in the case of positively chirped pulses (fig. 7.4), which is consistent with the fact that CWE harmonics are intrinsically negatively chirped, due to the aperiodicity of the attosecond pulse train. Compared to the previous measurements with the 15mm beamsize, we also notice in fig. 7.4 that the divergence of the CWE harmonics is larger (>70mrad), probably owing to the smaller source size.

For $a_0 = 1.1$, *ie* barely relativistic intensities, the harmonic signal increases again around 5ps prepulse delay (*ie* $L_g - L_0 \approx 0.2\lambda$, which is within the optimum theoretical range for ROM harmonics), and we also observe a correlated, stronger electron emission. These harmonics are remarkably spectrally narrower than those observed at short prepulse delay in the scan (see fig. 7.5), corresponding to the prediction of a periodic train of FTL attosecond pulses produced in the ROM mechanism.

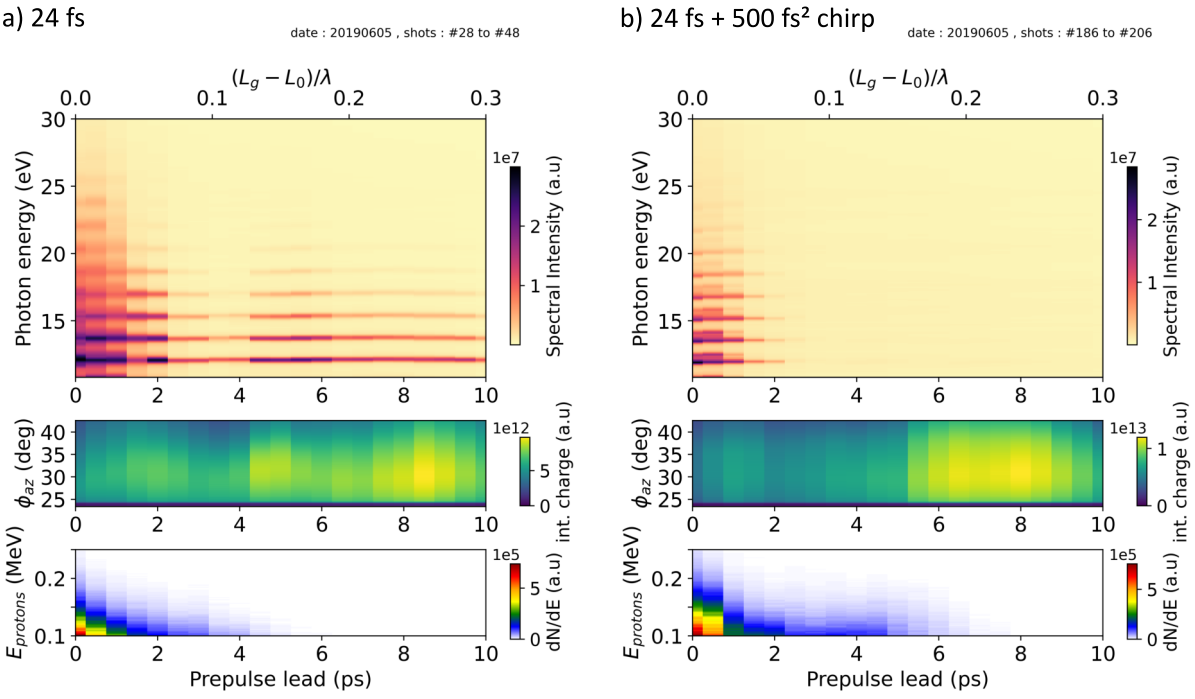

Figure 7.3: *Vertically integrated HHG spectra (top), electron angular distribution in the azimuthal plane (center) and proton spectra from the TPS (bottom) obtained with a) 24fs driving pulses b) 24fs driving pulses chirped to 85fs by adding 500*fs^2 *GDD with the second Dazzler. A value $c_s \approx 24$nm/ps was found from the SDI measurement performed on the same day.*

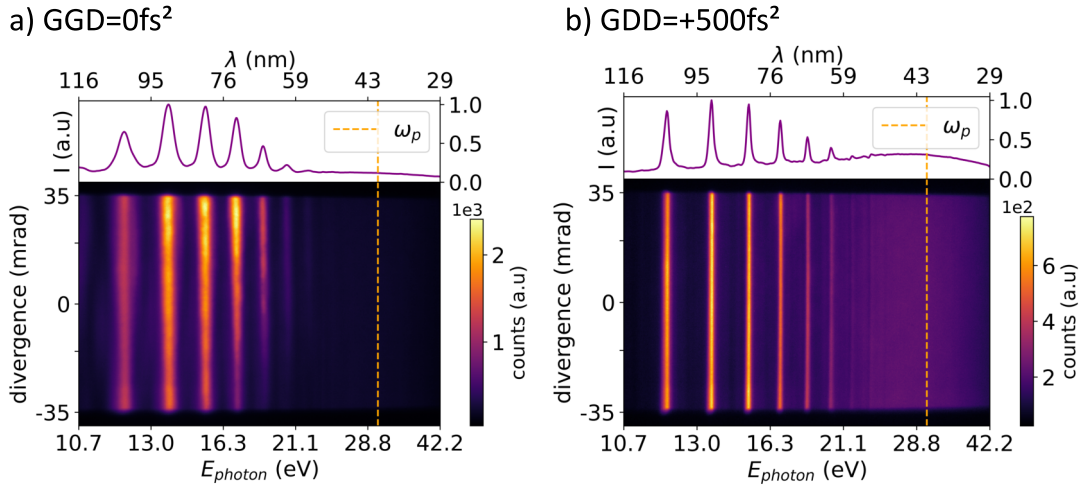

Figure 7.4: *Raw images showing the harmonic spectra with calibrated axes, for a 1.5ps prepulse lead time a) for near Fourier-transform limited 24fs pulses b) for 24fs pulses positively chirped by adding 500* fs^2*. Data corresponding to the scans shown in fig. 7.3.*

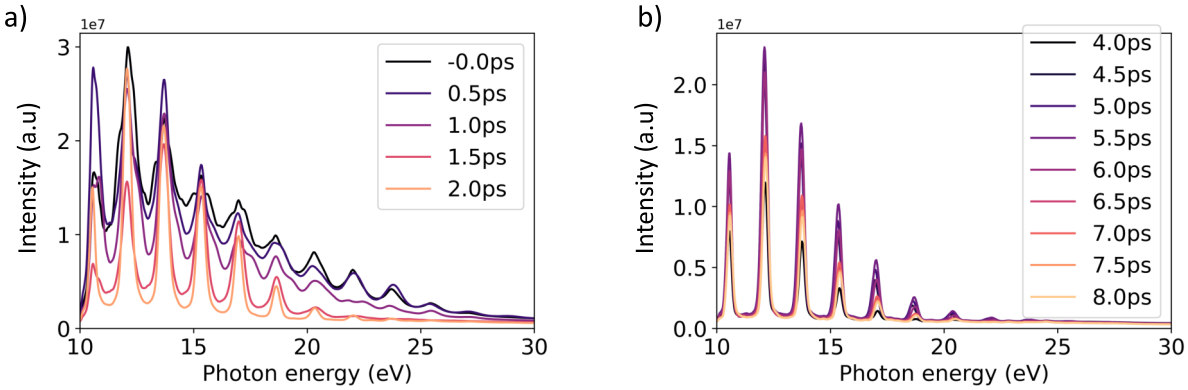

Figure 7.5: *Integrated harmonic spectra obtained with near Fourier-transform limited 24fs pulses a) at short gradients, for which the CWE mechanism dominates b) for slightly longer gradients, corresponding to the optimum scale length for ROM harmonics. Data corresponding to the scan shown in fig. 7.3.a.*

7.1.2 Proton acceleration regime

Let us now look into more details of the proton acceleration. Following up on the work done in 2012 [258], I performed the experiments in *Salle Noire 2* together with J. Kaur, S. Haessler and D. Lévy to further investigate the front side acceleration of ions from thick silica targets, using the TPS and the TOF MCP described in the previous chapter. In our experiments, we were able to simultaneously observe harmonics, electrons and protons, as well as measure the proton beam divergence for the first time. Jaismeen Kaur did most of the proton data analysis, with help from all of us, whereas Igor Andriyash performed numerical simulations and helped us understand the underlying physical mechanisms through analytical models.

Experimental results

We performed a detailed parametric study: we varied the pulse duration from sub-4fs to ≈1.5ps (by varying the gas pressure in the HCF and chirping the pulses with the second Dazzler) and the plasma gradient scale length, which had never been done before. We kept the beamsize and pulse energy constant for all the measurements, which was estimated to be 2.5 mJ on target (we measured the energy at the output of the HCF and divided it by two, to account for previously measured energy losses in the compression chamber and SHHG chamber).

The first thing that we noticed is that the proton signal is in all cases significantly enhanced for the sharpest plasma density gradient (see 7.6.a) *ie* a 0 ps prepulse delay, and if there is a non-zero optimum gradient scale length, it lies beyond our resolution. This is already visible in the scans presented in the previous subsection (fig. 7.3).

Secondly, keeping the gradient scale length constant and as steep as possible, we varied the pulse duration and observed a similar behavior as had been observed before [258] regarding the evolution of the ions' peak energy and charge (see 7.6.b). The peak energy increases as we make the pulse duration longer, up to an optimum pulse duration of ≈250 fs, for which a maximum proton energy of 0.48 MeV was obtained, and then it slowly decreases. Even for the longest pulses that we used, obtained by adding $10.5\times10^3 \text{fs}^2$ with the AOPDF, there was still a strong proton signal. The cutoff energy was determined by comparing the signal on the TPS to a background signal, obtained by defining a parallel thick curve below the proton curve. The maximuum energy is given by the position along the proton curve where the average signal over the proton curve width (to which the standard deviation of the signal within the curve width was substracted) is lower than the background average level.

Finally, a very interesting feature is the low divergence of the proton beam, measured from the scanning time-of-flight device in the absence of prepulse (0ps delay). We obtained for all pulse durations (4, 7, 27 and 200 fs) a divergence of only ≈ 3° FWHM (see fig. 7.7), which is well below the typical divergence of proton beams from TNSA experiments, ranging from 10 to 30°. A maximum proton charge of ≈100 pC per shot was measured with the calibrated TOF detector.

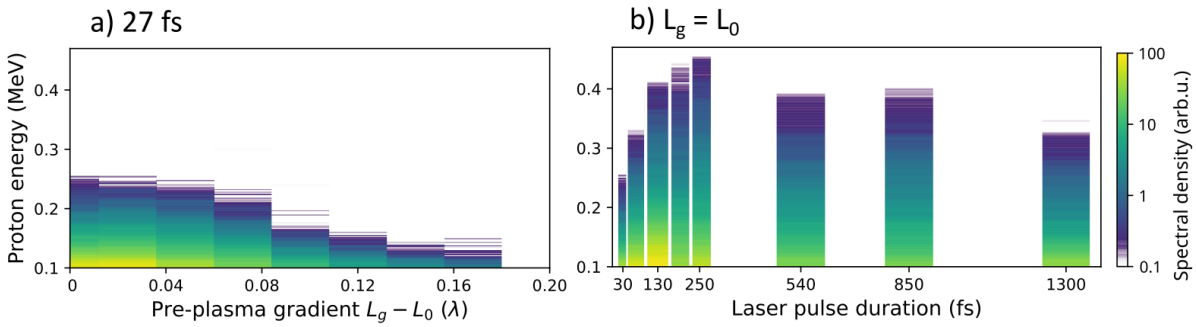

Figure 7.6: *Data obtained with TOF detector along the target normal direction. a) Proton spectra obtained with 27fs driving laser pulses, for different plasma gradient scale lengths. b) Proton spectra for different pulse durations, with a prepulse delay of 0ps.*

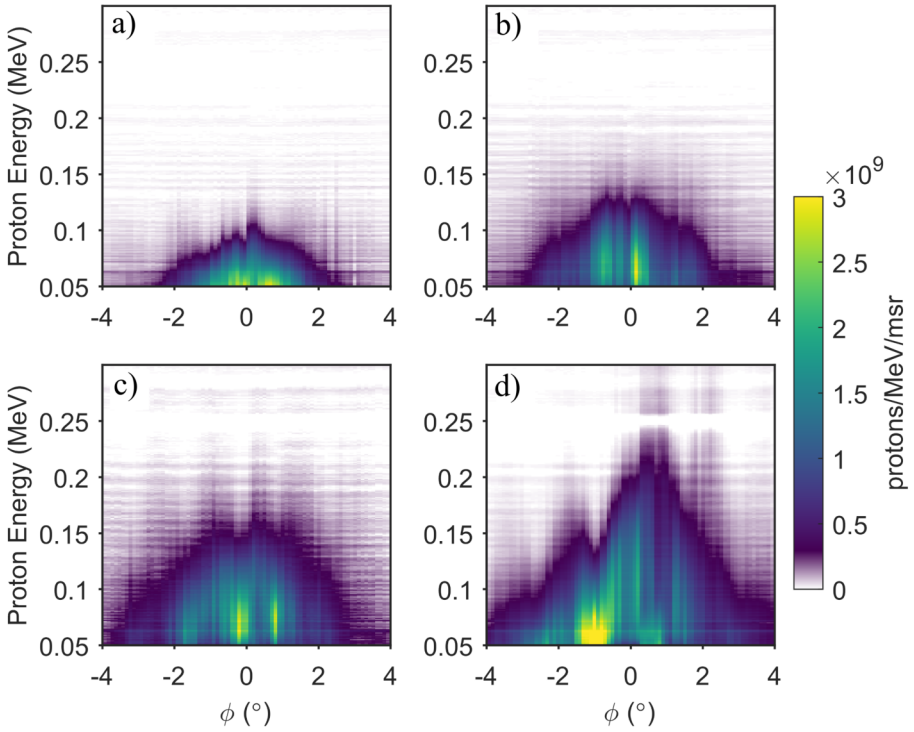

Figure 7.7: *Angularly resolved proton spectra (measured with the TOF detector) for a pulse duration of a) 4 fs b) 7 fs c) 27 fs d) 200 fs (chirped pulses). Figure courtesy of Jaismeen Kaur.*

Simulations

In order to understand the underlying physical mechanisms, 2D particle-in-cell (PIC) numerical simulations were made using the code WarpX (v21.04.86).

In the simulation, for $z < 0$, the initial plasma consisted only of Si^{8+} ions (for simplicity) and was modeled by a uniform electron density $n_{pe0} = 250n_c$, with $n_c = 1.74 \times 10^{21}\text{cm}^{-3}$ the critical density at 800nm. For $z > 0$ (towards vacuum), an exponentially decreasing density profile was used: $n_{pe} = n_{pe0}\exp(-|z|/L_g)$ with L_g estimated to be $\sim \lambda/100$ (8nm) for a 0ps prepulse delay. The choice of the ion species was motivated from the analysis of the TPS data and corresponds to the average charge-to-mass ratio of the heavy ion species observed. A second very small population of protons and electrons was added in the simulation, with $n_{pH} = 0.005n_c$ at $z = 0$. To account for the ion sound velocity difference, the gradient scale length was set to $L_{gH} = L_g\sqrt{M_{Si}/(Z_{Si}m_p)} = 15\text{nm}$. This population was there as test-particles to look at the protons behavior, and simulated the presence of contaminants at the target surface.

The considered laser parameters on target were: $\theta = 55°$, E=1.5mJ (this value is lower than in our measurements, but better reproduced the experimentally observed harmonic spectra), $R_{las} = 1.8\mu\text{m}$ FWHM diameter, and $\tau_{las} = 9\text{fs}$, 27fs, 100fs and 200fs. A snapshot of the plasma electron density distribution at $t = -240\text{fs}$ before the laser peak field arrival on target is shown in fig. 7.8 in the case of 200fs pulses, corresponding to the optimum duration for proton acceleration. We can see the plasma denting and the slight curvature of the plasma mirror surface, as well as the presence of a positively charged disk of ions close to the surface (in red). The temporal evolution of the accelerating electrostatic field E_z strength generated by this positively charged disk is shown in fig. 7.9, and the final angularly resolved proton spectra obtained for three different pulse durations are shown in fig. 7.10.

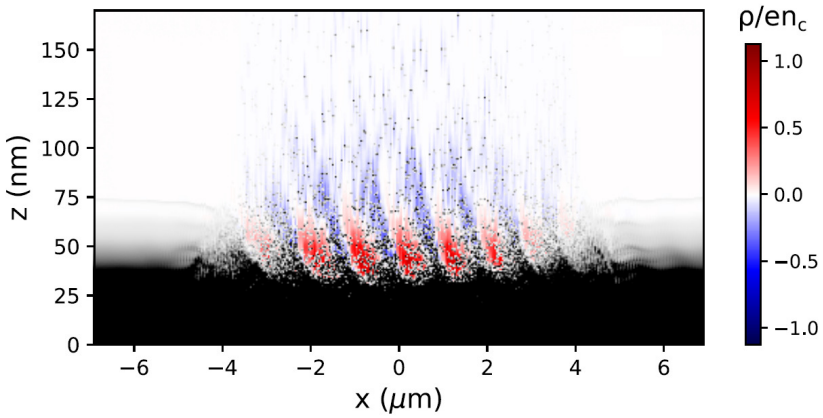

Figure 7.8: *Charge density (red-blue, n_c units) and electron density (grey, normalized for visibility) for a 200 fs pulse duration, represented at t = -240 fs before peak field arrival. Figure courtesy of Igor Andriyash.*

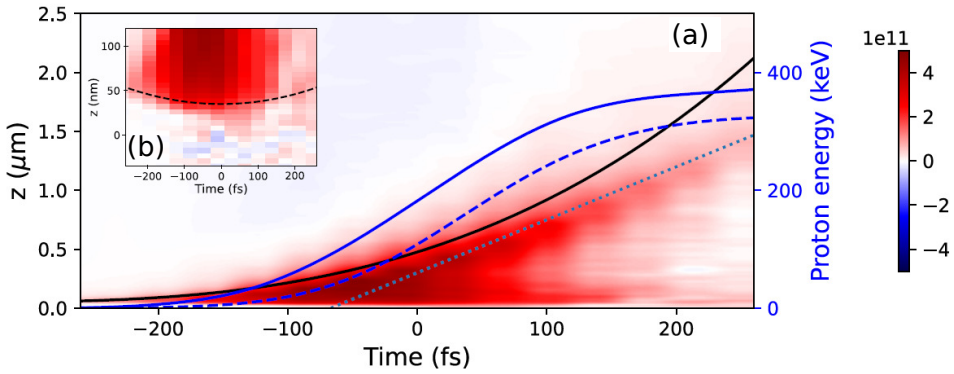

Figure 7.9: *a) Temporal evolution of the x-averaged electrostatic field E_z (red-blue colormap), maximum proton energy (blue curve) and corresponding z-coordinate (black curve) from the simulation. Maximum proton energy from Eqs. 7.4 and 7.5 (blue dashed curve); b) Zoomed in E_z map (red-blue colormap) and depth estimate (black dashed curve) predicted by Eq. 7.4. Figure courtesy of Igor Andriyash.*

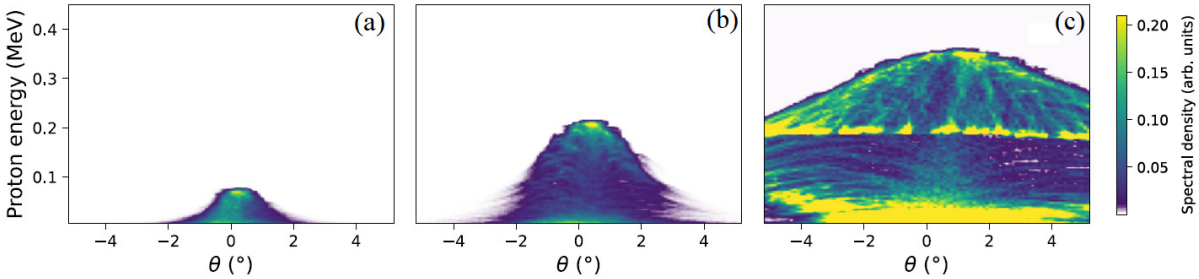

Figure 7.10: *Final angular spectral distributions for a) 9 b) 27 and c) 100 fs driving pulses. Figure courtesy of Igor Andriyash.*

Proton acceleration: physical interpretation

The main laser field penetrates the preplasma gradient until it reaches the reflective layer, thus introducing a radiation pressure

$$P_{rad} = \frac{2\cos^2\theta I_{las}}{c}, \tag{7.1}$$

which pushes the electrons inside the plasma up to a depth z_0, where P_{rad} is balanced by the electrostatic pressure P_{es} generated by the charge separation. This pressure can be estimated from the capacitor model:

$$P_{es} \approx \sigma_i^2/\epsilon_0, \tag{7.2}$$

where $\sigma_i = e\int_{z_0}^{\infty} n_{pe}dz$ is the charge density of un-neutralized ions per unit area.

For short gradient scale lengths ($L_g \ll \lambda$), the laser and electrostatic fields are screened by the dense plasma. Electrons returning to the target can escape deep inside the plasma (*Brunel absorption* or *heating*), leaving a positively charged layer of ions behind. These ions then generate a large accelerating field. The field pointing inwards the target is screened for the same reason, and only a positive field pointing outwards the target remains (as shown in fig. 7.9). Thus, the protons can be quickly accelerated before this positively charged layer explodes due to Coulomb repulsion.

The thickness of the accelerating ion layer can be estimated from the balance condition for an exponential plasma density profile:

$$P_{es} \approx P_{rad} \Leftrightarrow \sigma_i = \cos\theta\sqrt{\frac{2\epsilon_0 I_{las}}{c}}. \tag{7.3}$$

For the considered exponential plasma density profile, the electrons are thus pushed down to a depth:

$$z_0 \approx L_g \ln\left(\frac{e n_{p0} L_g}{2\cos\theta}\sqrt{\frac{c}{\epsilon_0 I_{las}}}\right). \tag{7.4}$$

Using the interaction parameters corresponding to the simulation shown in fig. 7.8, *ie* $I_{las} = 2.2 \times 10^{15}\mathrm{W.cm}^{-2}$, we find analytically $z_0 \approx 50$ nm, whereas from the simulation itself (fig. 7.8), we find a maximum electron penetration depth $z_0 \approx 34$nm. The difference between these two values can be explained by the presence of remaining electrons within the penetrated plasma layer, which are trapped by the transverse standing wave (formed by the overlap of the incident and the reflected laser waves), resulting in a reduced effect of the electrostatic pressure.

The accelerating field of the ion layer may then be theoretically estimated using the model of a thin charged disk. If we consider a charged ion disk, whose size corresponds to the projected laser spot size $R_i = R_{las}/\cos\theta$, the electrostatic field reads:

$$E_z(t,z) = \frac{E_{0,las}(t)\cos\theta}{2} \times \left[1 - \exp\left(-\frac{z-z_0}{L_g}\right)\right] \times \left(1 - \frac{z}{\sqrt{z^2+R_i^2}}\right) \tag{7.5}$$

with $E_{0,las} = \sqrt{2I_{las}/(\epsilon_0 c)}$ the amplitude of the laser field. The second factor in eq. 7.5 accounts for the field distribution within the preplasma and the third factor accounts for the 3D field geometry. The maximum energy evolution of a test-proton in the accelerating field defined by this equation (eq. 7.5) is represented in fig.7.9 (blue dashed curve), and it is in good agreement with the proton energy evolution based on numerical simulation (same figure, blue solid curve).

Proton energy VS laser duration and energy

For long pulse durations, the ion layer has more time to expand towards vacuum. Protons which are in phase with the field thus further gain energy. However, due to the surface curvature, some transverse fields are generated during the expansion, which result in an increase in divergence. This is visible in the simulation shown in fig. 7.10 for 100fs pulses, but we did not observe it experimentally for 100fs pulses. The difference could be due to the 2D geometry of the simulations, resulting in a faster plasma expansion speed.

The optimum laser pulse duration τ_{las} (100-300fs) corresponds to the transition from a regime where the maximum proton energy E_{pM} scales with τ_{las} to a regime where E_{pM} scales with the driving laser intensity $I_{las} \propto 1/\tau_{las}$, as had been found in [258]. At the optimum duration of 200fs, we are in a situation where the acceleration length is short compared to the positively charged disk size (R_i) but long compared to the gradient scale length L_g. In particular, the optimum occurs when the laser duration τ_{las} matches the protons propagation time to $R_i/2$. This behavior was observed both experimentally and from simulations, and is also predicted by Eq. 7.5. The results from these three methods are summarized together in fig. 7.11.a.

The linear dependence for short durations can be retrieved by discarding geometric factors in Eq. 7.5:

$$E_z(t) = \frac{E_{0,las}(t)\cos\theta}{2}. \tag{7.6}$$

We can then estimate the maximum proton energy as $E_{pM} = p_{max}^2/(2m_p)$, where p_{max} is the maximum proton momentum. From the equation of motion $d_t p = eE_{acc}$, we obtain $p_{max} = e\int_{-\infty}^{+\infty} E_z(t)dt$ and therefore:

$$E_{pM} = \sqrt{\frac{\ln 2}{\pi}}\frac{e^2}{m_p c\epsilon_0}\frac{E_{las}\tau_{las}}{R_i^2}, \tag{7.7}$$

with E_{las} the laser energy. This equation corresponds to the black dashed line in fig. 7.11.a.

Moreover, the field defined by Eq. 7.5 becomes evanescent where $z \geq R_i/2$. And if we assume that the interaction stops at $2\tau_{las}$, we find that this equation (eq. 7.7) is only valid when

$$2\tau_{las} \leq \frac{R_i}{2}\frac{1}{v_{moy}}, \tag{7.8}$$

with $v_{moy} = \sqrt{E_{pM}/(2m_p)}$ the proton velocity averaged over the acceleration (the average velocity corresponds to half the velocity reached at the end of the acceleration). Using Eqs. 7.8 and 7.7, the maximum proton energy obtained for the optimum pulse duration depends on the laser energy as follows:

$$E_{pM,opt} = \left(\sqrt{\frac{2\ln 2}{\pi m_p}}\frac{e^2}{4c\epsilon_0}\frac{E_{las}}{R_i}\right)^{2/3} \tag{7.9}$$

and the results are plotted in fig. 7.11.b. (dashed line), together with the results from the PIC simulation (blue diamonds) and those obtained using eq. 7.5 (black solid line). These results predict that the final proton energy is only determined by the driving laser energy. Thus, this work might pave the way to the production of low-divergence, MeV-class protons.

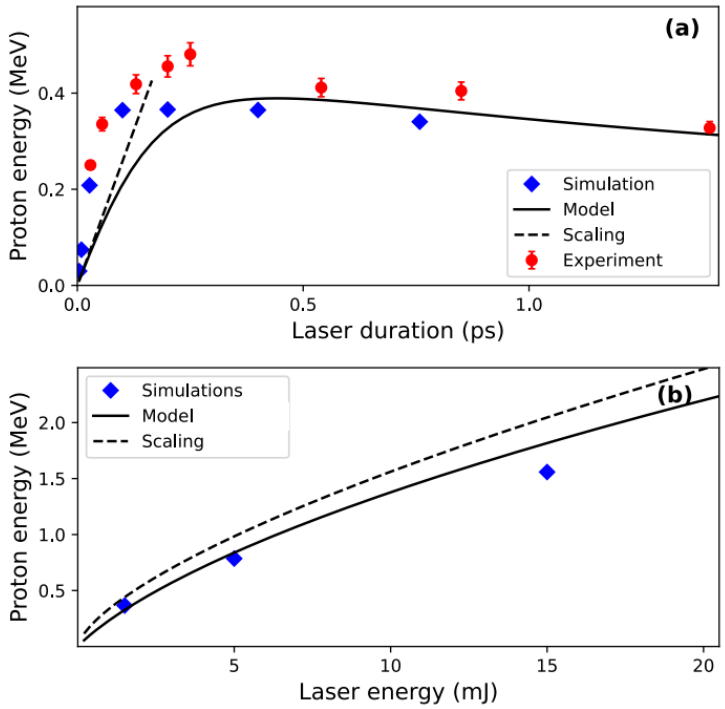

Figure 7.11: *a) Maximum proton energy as a function of laser pulse duration obtained experimentally (red dots), from numerical simulations (blue diamonds), from numerical integration of proton motion with Eqs. 7.4 and 7.5 (black solid line), and from the Eq. 7.7 (dashed line). b) Maximum proton energy as a function laser energy for a 200 fs pulse, obtained from numerical simulations (blue diamonds), from numerical integration of proton motion with Eqs. 7.4 and 7.5 (black solid line) and from Eq. 7.9 (dashed black line).*

Conclusion

To summarize, we have measured low-divergence proton beams at kHz repetition rate over a wide range of laser and plasma parameters. Proton energies up to 0.5MeV were found for the optimum pulse duration ≈ 200fs at the steepest plasma gradient density profile. The total charge (above a 0.1MeV threshold) reached a maximum of ≈ 100pC. At kHz repetition rate, this corresponds to an average current ≈ 0.1μA.

Numerical simulations and a simple theoretical model allowed identifying the mechanism and predicting the proton energies.

The properties of these proton beams, and the predicted proton energy increase with the laser energy are interesting for numerous applications, such as ion implantation [250] and the production of radioisotopes for positron-emission tomography, which requires a few MeV [94].

7.2 Interaction at relativistic intensities

Let us now move to the results obtained for higher, relativistic intensities on target.

7.2.1 Electrons and ROM harmonics

Gradient scans for different pulse durations

For $a_0 \geq 1$, the mechanism is different, as we have seen. XUV photons no longer originate from the overdense part of the plasma, but from the modulation of the laser field upon reflection off the relativistically moving critical density layer (and possibly synchrotron emission by the moving thin electron layer). Gradient scans for 27fs, 6.3fs and 4.1fs are shown in figure 7.12. For 27fs (panel a), the intensity was 3.1×10^{18}W.cm^{-2} *ie* $a_0 = 1.2$. For 6.3fs (panel b) and 4.1fs (panel c), the normalized laser amplitudes were respectively $a_0 = 2.1$ and a_0=2.7. Thus, in all cases, the intensity on target was beyond the relativistic limit.

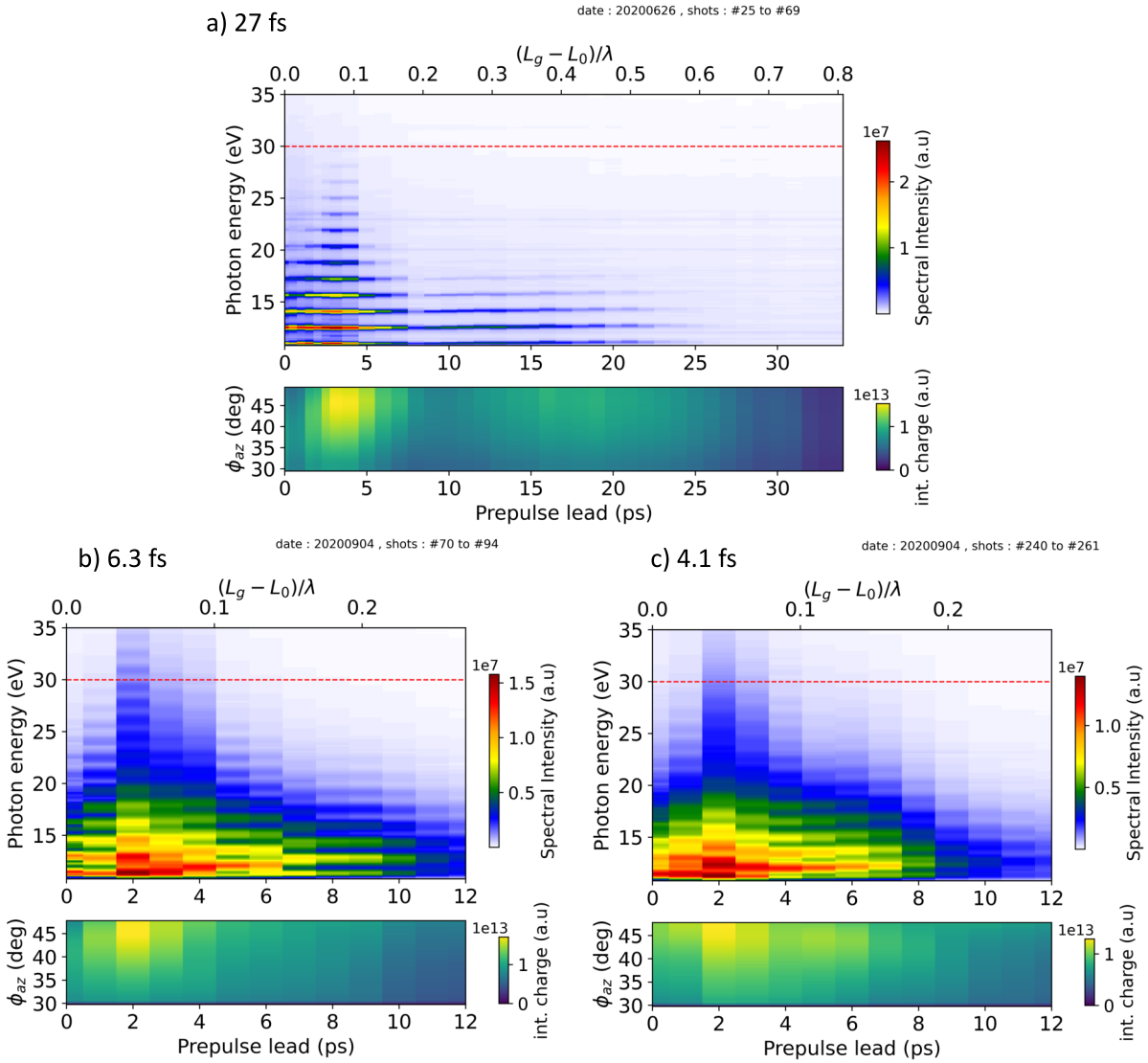

Figure 7.12: *Gradient scans for different pulse durations with the vertically integrated harmonic spectra (top) and the vertically integrated electron distribution in the azimuthal plane (bottom). a) 27 fs, 3.15 mJ on target, with $c_s = 19nm/ps$ b) 6.3 fs, 2.3mJ on target and c) 4.1 fs, 2.3mJ on target, with c_s=18 nm/ps for both (b) and (c).*

Observations

We observe for all three durations an optimum for harmonic generation at a softer gradient scale length than for CWE harmonics, around 2 or 3ps prepulse lead time, corresponding to $L_g \approx L_0 + 0.05\lambda$. Moreover, as we observe signal above the CWE cutoff (at least for 6.3fs), there is no doubt that we are in a relativistic regime. Another clear indication comes from the fact that harmonic generation is much less efficient for the steepest gradient scale lengths (e.g. for a 1ps prepulse lead time) than for this optimum delay, as expected for ROM harmonics and contrary to CWE harmonics.

In the case of 27fs pulses, we obtain well modulated, thin harmonics, with a constant position along the wavelength axis (see fig. 7.13.a). This is in agreement with the theoretical prediction that attosecond pulses generated via the ROM mechanism should be Fourier-transform limited. For 6.3fs pulses, we observe spectrally overlapping, broader harmonics. A similar observation was made in [118], where the authors found that using 3-cycle optical pulses result in a 17 % likelihood to generate isolated attosecond pulses. Reducing the pulse duration further down to 4.1fs results in even broader harmonics (fig. 7.13.b).

We can also observe variations of the harmonic peaks positions (more visible in fig. 7.13.b). However, for this scan, the CEP was randomly fluctuating from one pulse to the next and each acquisition is averaged over 100 consecutive shots, therefore the results shown here are averaged over all possible CEP values, and this spectral shift cannot be attributed to CEP-dependent interaction dynamics.

Finally, the optimum ejection of electrons occurs for the same gradient as the most efficient harmonic generation, similar to what has been reported recently in [56].

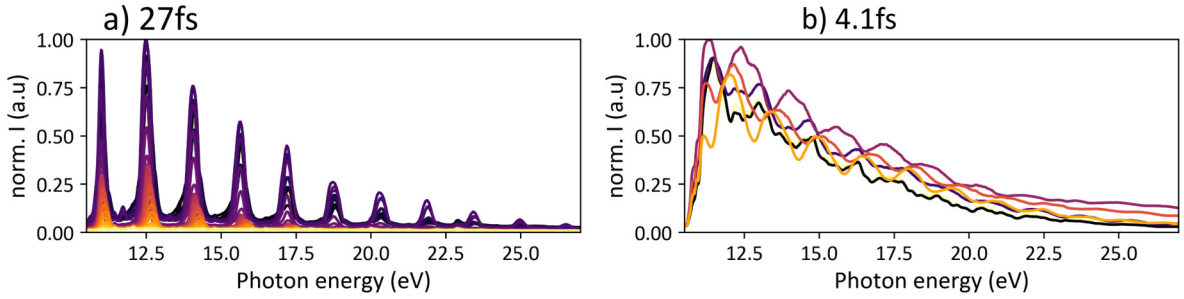

Figure 7.13: *a) all the vertically integrated harmonic spectra from 0 to 25ps for a 27fs driving pulse (same data set as in fig 7.12.a.) plotted together. b) all the integrated harmonic spectra from 0 to 5ps for a 4.1fs driving pulse (same data set as in fig 7.12.c.) plotted together.*

Double optimum?

The scans shown in fig. 7.12 are representative of what we would typically obtain and were rather reproducible from day to day. However, on a few scans (and particularly in the case of 27fs pulses), we could sometimes see what seemed to be a double optimum for ROM harmonics. An example is shown in fig 7.14, where we observe a strong harmonic signal around 2ps and around 9ps as well. Both optima correspond to a high electron charge. The existence of 2 optima was proposed in [95] based on 2D numerical simulations and a 1D analytical model. However, as this was not reproducible, it is more probably due to some unknown varying experimental parameter.

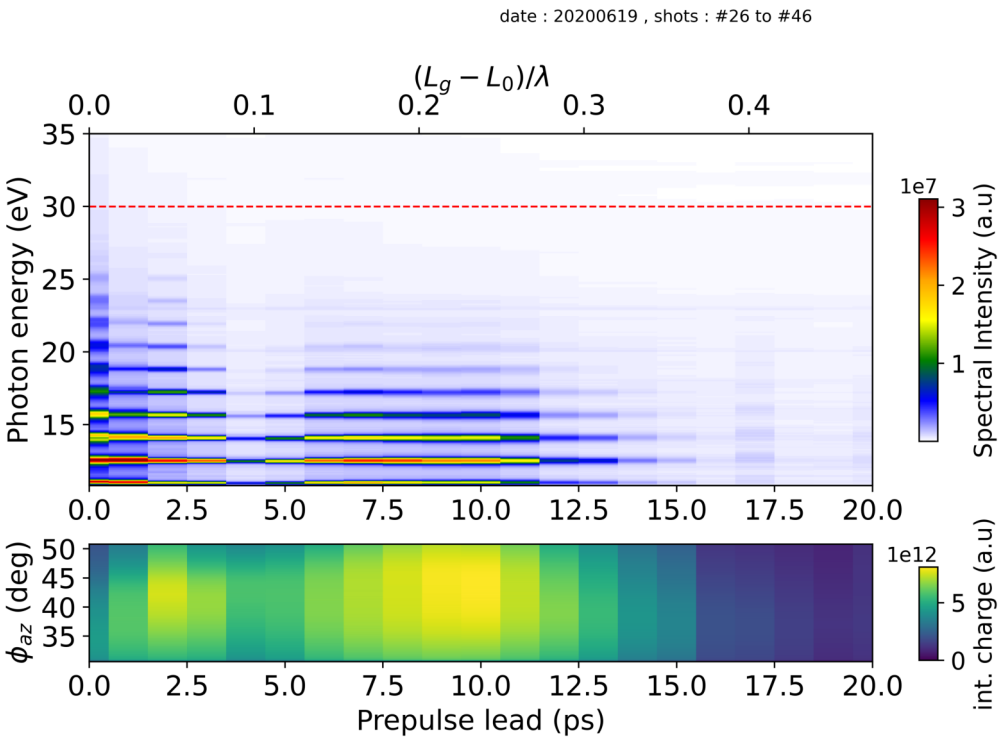

Figure 7.14: *Gradient scan for a 27 fs pulse duration and $a_0 = 1.2$. top: vertically integrated harmonic spectra. bottom: electron distribution in the horizontal plane.*

7.2.2 LWFA of electrons at very long gradients

The spectra of LWFA electrons from plasma mirrors, which are ejected at long gradients, have never been measured before. Thanks to our newly implemented electron spectrometer, Jaismeen Kaur, Stefan Haessler and I were able to perform those measurements during my thesis.

The results for 2.3mJ, 4fs pulses are shown in figure 7.15. The electron spectrometer could only be centered at an azimuth angle Φ_{az} up to ≈40° without blocking the harmonics, and we kept it at a fixed position $\Phi_{az} \approx 38°$, $\theta_{pol} \approx 0°$ for the entire scan. The spectrometer pinhole position is indicated by the black horizontal dashed line in panels (b) of figs 7.15 and H.4.

The observed optimum electron charge corresponds to a prepulse lead time of 200 to 260 ps. Using $c_s \approx 18$ nm/ps, this corresponds to $L_g \approx 4.5$-6 λ. The maximum electron cutoff energy around this optimum is E_{cutoff} ≈2.1 MeV, reached for 260 ps. The corresponding electron spectrum is shown in fig. 7.15.d, where the red dashed line indicates the threshold used to define the energy cutoff. This line corresponds to 2% of the maximum electron spectral density (maximum taken over the entire scan). This value is quite close to the maximum of 2.5 MeV predicted by numerical simulations (section 5.3). Moreover, simulations predict a higher energy closer to the specular direction, which should be verified in the future.

The results for 6fs pulses are shown in Appendix H, figure H.4. The electron spectrometer was also kept centered at an azimuth angle $\Phi_{az} \approx 39°$. Here, we observe slightly lower energies (1.6 MeV maximum at a 190 ps prepulse lead time, see fig. H.4.d.), but the electron beam center was also closer to the specular direction (55°) on that day, *ie* further from the pinhole used to filter the electron beam in the spectrometer. Thus, it is hard to conclude about the difference between this scan and the previous one with 4 fs pulses.

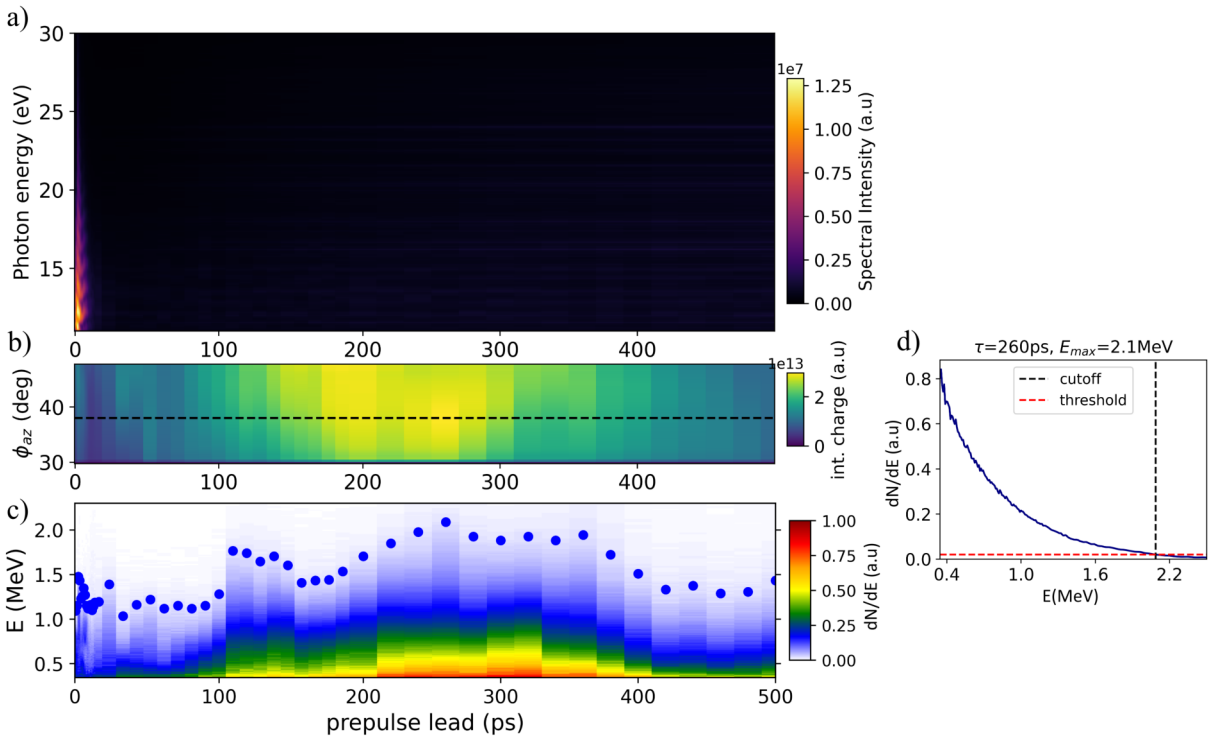

Figure 7.15: *Gradient scan for a 4 fs pulse duration. a) vertically integrated harmonic spectra. b) electron spatial distribution along the azimuthal direction. c) electron spectra measured at $\phi_{az} = 38°$ in color-scale, and electron cutoff energy represented with blue dots. d) electron spectrum at a 260 ps prepulse lead time, showing how the cutoff energy is defined. Scans a) and b) were acquired simultaneously whereas scan c) is a different data set from the same day (04.09.2020).*

7.2.3 Spatial XUV beam and wavefront measurements

I will present here the spatial XUV beam measurements. We always used an Al filter, blocking low-energy photons below ≈ 20eV (60nm), to shield the MCP and the camera from the reflected laser radiation around 800nm. As a result, the only possible XUV beam detection was in the case of the highest intensities *ie* the shortest driving pulse durations. In fact, for ≈ 30fs pulse durations, we could not even distinguish any beam shape, probably owing to the greater divergence of CWE harmonics.

XUV beam: dispersion scan

We recorded the spatial intensity distribution of the XUV beam using a 31mm diameter circular MCP/Ph detector placed 294mm away from the target interaction point, with a 200nm thick aluminum filter in front of it (see subsection 6.2.2). The angular acceptance was reduced in the horizontal plane due to a slight position offset between the detector and the filter, which was made on purpose because the Al filter was damaged on the edge.

In fig 7.16, we varied the GDD by changing the insertion of one of our motorized fused silica wedges (see fig. 3.12) and recorded the spatial XUV beamprofile in the specular direction. For this measurement, the prepulse lead time was 3ps, the energy was 2.3mJ on target and the pulse duration ≈ 4fs.

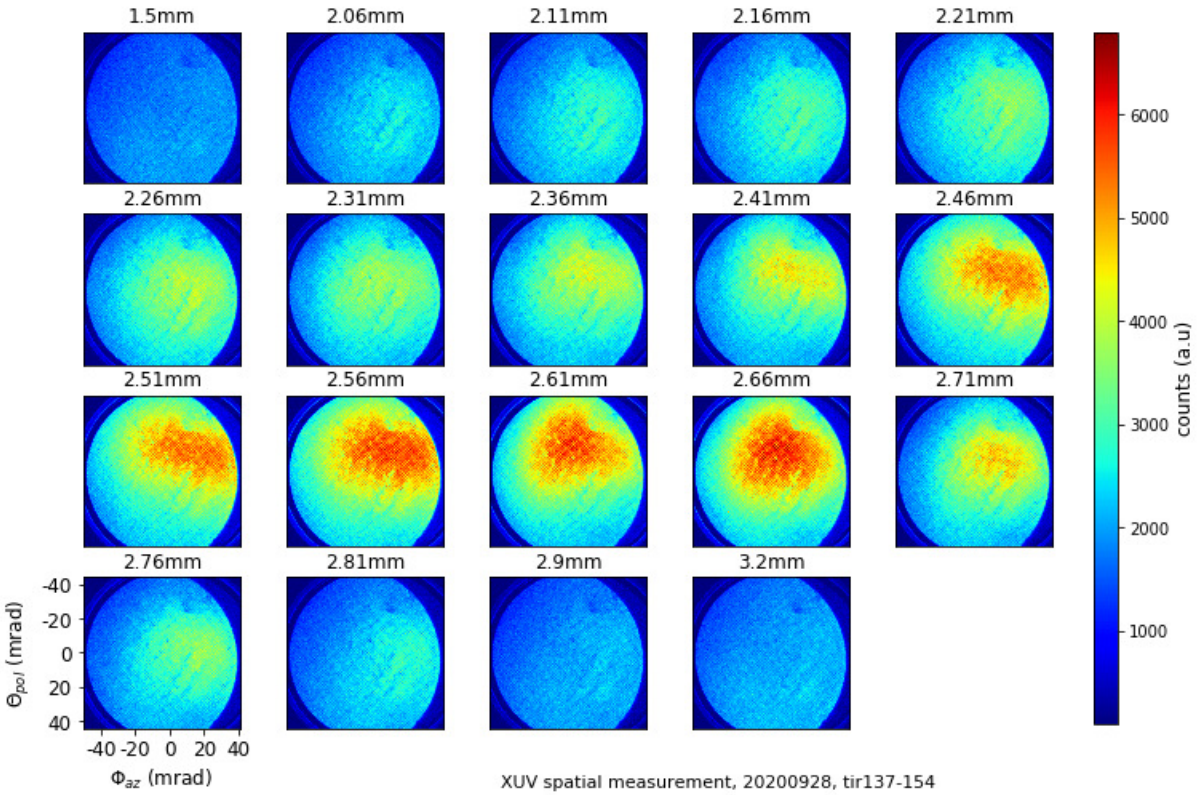

Figure 7.16: *Spatial XUV beam measured for different wedge insertions (equivalent to GDD), for a 3ps prepulse delay (found to be the optimum for ROM harmonics in a gradient scan on the same day).*

There is a maximum signal around 2.56mm wedge insertion (fig 7.17.b), which corresponds quite well to the optimum found by the dscan measurement made on that day (2.51mm, see fig 7.18). We clearly see from this scan that for pulse durations of 14fs or more, there is no signal at all to detect, which is consistent with the absence of beam shape for longer pulses. We can also note that the signal drops faster when we add positive dispersion than when we add negative

GDD. Since propagation through the underdense plasma introduces negative GVD, this cannot be the reason for this observation. A similar dependence is observed in the SHG d-scan trace (fig. 7.18.b) and might be due to higher order dispersion terms.

The XUV beam divergence for the optimum wedge insertion is ≈44 by 77 mrad FWHM (see fig 7.17.a). This low divergence is consistent with the diffraction limited value for a 60nm wavelength and a source size that would be approximately half the laser spot size on target, as discussed previously (section 5.2).

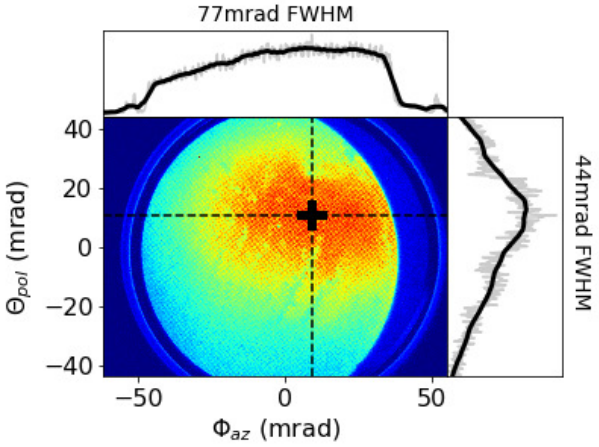

(a) Beamprofile for a 2.56mm wedge insertion.

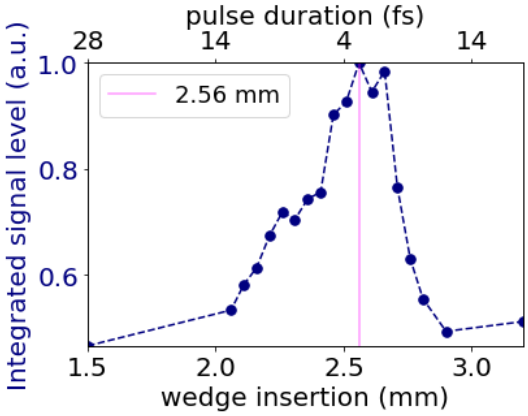

(b) Integrated signal VS wedge insertion or pulse duration.

Figure 7.17: *Analyzed data from scan presented in figure 7.16*

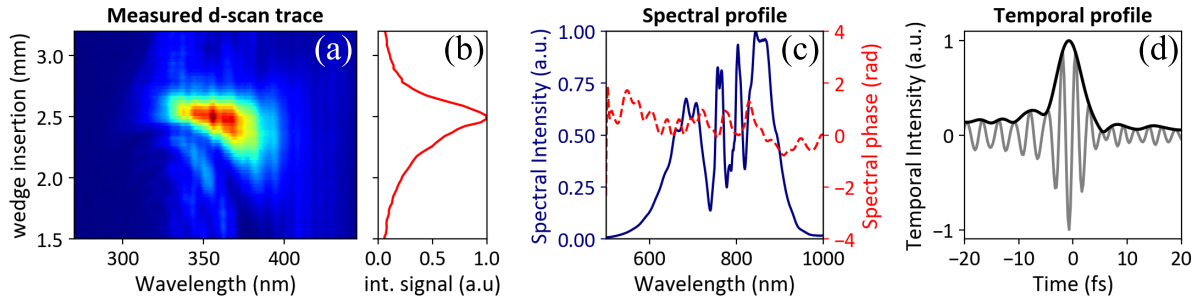

Figure 7.18: *Dscan measurement from the same day as the XUV spatial measurements, with a pressure P=1.1 bar at the output of the hollow-core fiber. a) Measured SHG d-scan trace. b) Integrated SHG signal on the spectrometer as a function of the wedge insertion. c) Spectrum of the fundamental pulse (solid blue) and retrieved spectral phase (dashed red). d) Retrieved temporal intensity profile, with a pulse duration of 4fs FWHM.*

XUV beam: gradient scale length scan

We also recorded the XUV beam profile for different gradient scale lengths on the same day (see fig. 7.19 and H.1, there is no difference in the experimental conditions between these two scans) and we found that in the absence of prepulse (zero or negative prepulse lead time), the XUV emission more or less homogeneously fills the MCP area. We know from our spectral measurement that CWE harmonics are generated in the absence of prepulse, thus we probably detect both CWE harmonics, which are expected to be more divergent than ROM harmonics, as well as plasma emission in that case.

In the presence of a prepulse, we start seeing a more defined beam shape, whose divergence is smaller, as expected in the relativistic regime. At around 0.5ps or 1ps, the XUV emission is rather weak, then it peaks around 2ps and continuously decreases until it disappears around 6ps. This behavior, with an optimum at a few ps prepulse lead time, is similar to the one observed with the spectral measurements.

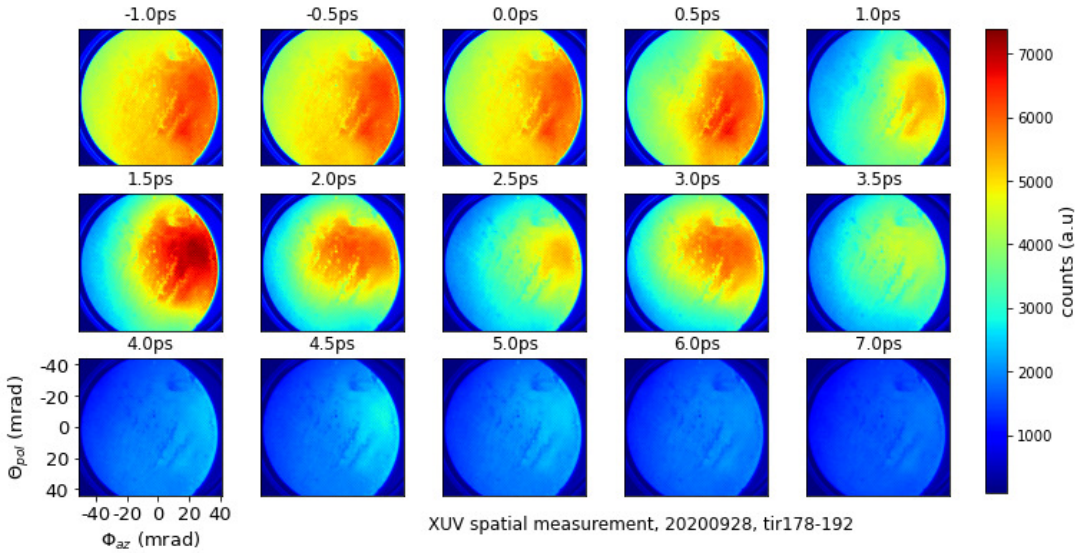

Figure 7.19: *Spatial XUV beam measured for different prepulse delays. Data set number 1.*

Preliminary results of XUV wavefront measurement

We are now interested in measuring the wavefront of the XUV beam. First attempts were made during my thesis, with the help of Li Lu. However, as we will see, these measurements are far from trivial.

We began by replacing the MCP used for spectral measurements with the X-ray CCD to look at the harmonic spectrum and make sure that it was possible to detect them. We were not certain about this because, unlike the MCP used for spectral measurements, the CCD acquisition cannot be temporally gated on a ∼100 ns time window. Moreover, this way, we were confident that the CCD would be safe (the grating eliminates the 0 order beam and has a limited diffraction efficiency) and we could evaluate how much attenuation we needed. We detected stronger plasma emission (recognizable by its characteristic thin lines, see [25]) with the CCD but we could clearly see harmonics, which progressively disappeared as we increased the delay between the prepulse and the main pulse (fig. 7.20).

We thus started measurements using the CCD as part of the wavefront sensor and tried monochromatic measurements at 44.4nm with the multilayer mirror, but we faced a major issue: there were so many hotspots in the detected signal that the data was too noisy to be properly analyzed. Only when the 28fs laser pulses were strongly chirped (+1000fs^2 with the Dazzler, corresponding to a ≈100 fs duration) could we obtain a decent signal, as shown in fig. 7.21. These hotspots probably originate from hard X-rays, which can be generated when heavy nuclei are bombarded by energetic electrons through *Bremsstrahlung radiation*, which scales with the atomic number Z (or proton number). We also certainly get characteristic X-rays or *K-lines*, emitted when outer-shell electrons fill vacancies in atoms' inner shells.

Thus we tried different things aiming at preventing electrons emitted during the interaction from colliding with heavy nuclei, and blocking X-rays. We tried adding teflon plates (Z=2 and 4) and/or lead (to shield from X-rays) around the metallic parts (the multilayer mirror mount,

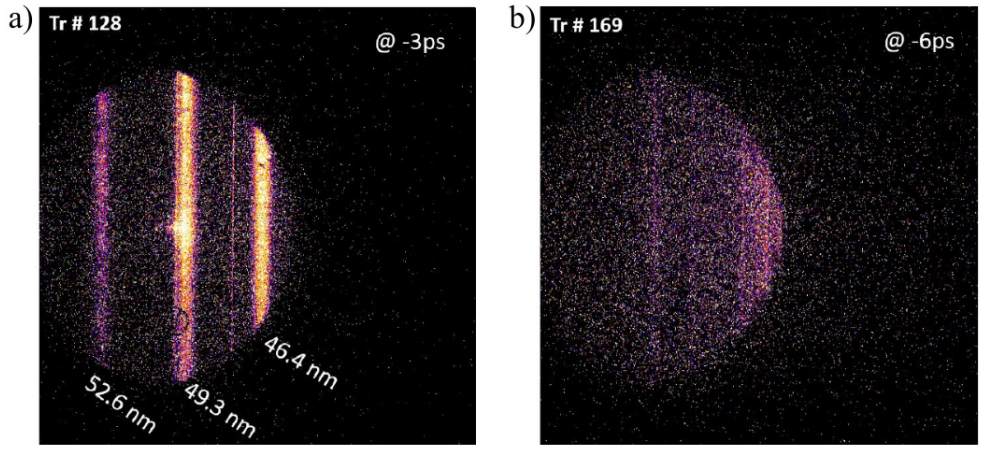

Figure 7.20: *Images recorded with the X-ray CCD in the spectral plane of the XUV grating. a) for a 3ps prepulse lead time and b) for 6ps prepulse lead time. The pulse duration was ≈10fs, the energy 2.1mJ and the acquisition time 300ms.*

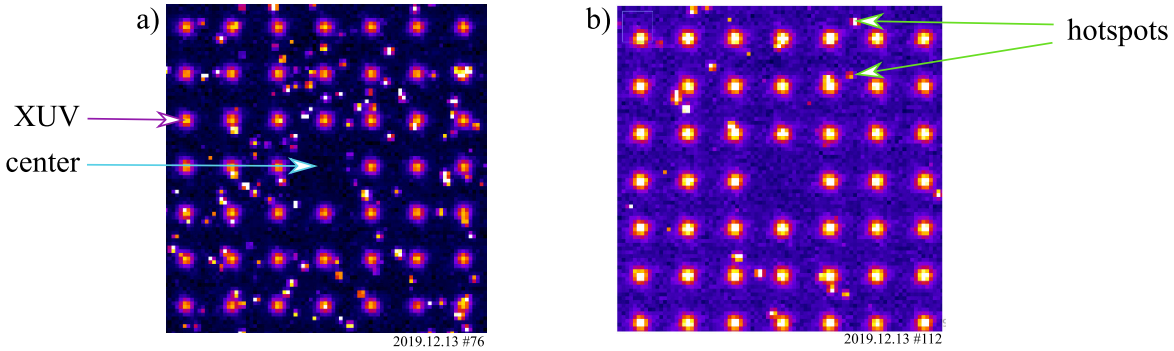

Figure 7.21: *Zoomed in, raw images acquired with the XUV wavefront sensor, using a multilayer mirror to select the 44.4nm wavelength. The CCD acquisition time and shooting sequence length was 800ms. The prepulse lead time was 1.5ps. a) 28fs pulse duration and b) 28fs pulses chirped by adding 1000fs^2 with the AOPDF. The smallest bright dots correspond to hotspots, which pollute the signal. The absence of hole in the center is used for aligning the sensor.*

the XUV CCD aluminum casing...) and the sensor. We also tried adding strong magnets before the multilayer mirror to deviate the electrons upwards. This reduced a little bit the number of hotspots and allowed treating data obtained for strongly chirped pulses only.

With a lot of efforts put into the analysis, most of the hotspots were removed in post-processing using a Fourier Transform technique and Li Lu was finally able to extract the wavefront data from the raw images, even for short pulse durations. The analysis of the retrieved wavefronts is summarized in fig. 7.22. The RMS wavefront value, which expresses the statistical deviation from a perfect spherical wavefront (averaged over the entire wavefront), is ≈4.6λ, with $\lambda = 44$nm. This value seems to slightly decrease as we add more positive dispersion to the laser pulse, and remains constant for all gradient scale lengths. However, we do not observe an optimum in signal counts for intermediate plasma gradients as we usually do when looking at the XUV spectrum, which is strange. This RMS error would be mostly due to astigmatism at 0 and 45 °, contributing by ≈ 1.5λ each to the final value. Measurements of the incident laser wavefront before the parabola (in the compression chamber) with a Shack Hartmann sensor (which we unfortunately did not save) usually gave lower RMS values ∼ λ/10 ≈ 80nm, thus the XUV spatial phase aberrations might come from the OAP alignment, target surface imperfections or

inhomogeneous plasma expansion, but at this point we cannot conclude about their origin. This needs to be further investigated on.

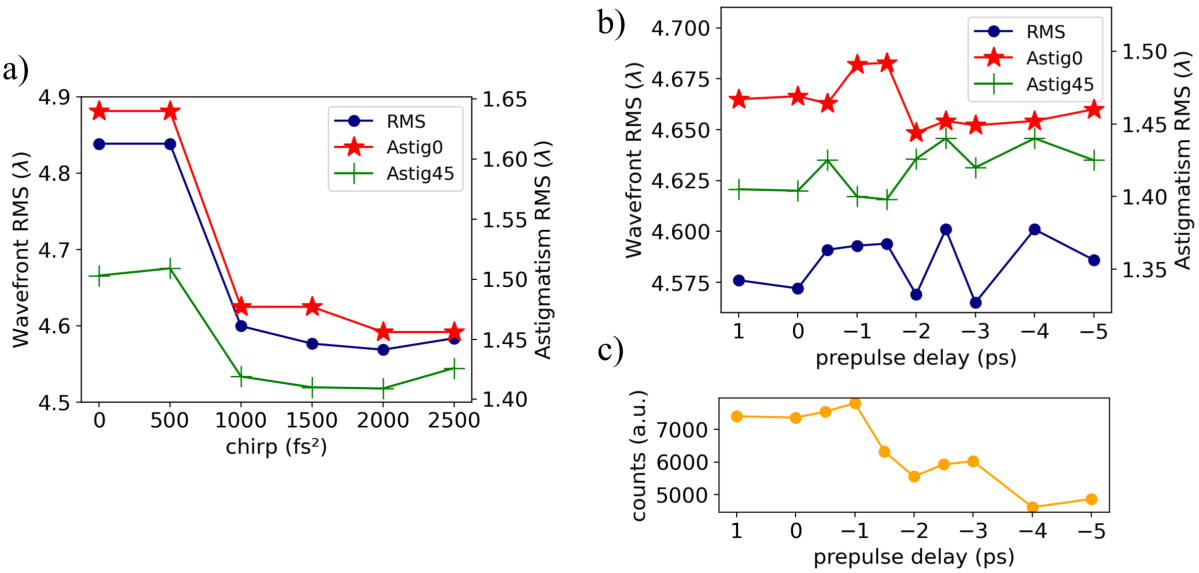

Figure 7.22: *Results of the wavefront analysis, with λ=44nm. a) for different chirp values at fixed gradient scale length (prepulse lead time of 1.5ps) b) for different prepulse delays with 28fs pulses chirped by adding +2000 fs^2 and c) integrated counts per pitch as a function of the prepulse delay for the data set shown in (b).*

However, the hotspots removal makes the results less reliable, as it is difficult to do it without losing or artificially modifying useful signal, and the small angular acceptance ($\approx$ 37 mrad) did not give access to the full XUV beam. Therefore, those results are not very convincing and new experiments should be made. One should try to reduce the divergence of the XUV beam, use larger size optics and filters, and improve the shielding from hard X-rays.

7.3 CEP effects

7.3.1 Introduction and state-of-the-art

Generating an isolated attosecond pulse (IAP) rather than a train of attosecond pulses is particularly interesting for applications. In order to do so, different techniques have been proposed and experimentally demonstrated.

One of them is called the attosecond lighthouse: wavefront rotation is introduced in the driving pulse, so that each attosecond pulse of the train is emitted at a different angle [262]. In practice, it can be done in *Salle Noire 2* by changing the polarization (so that the wavefront rotation does not influence the angle of incidence on target), rotating one of the two motorized silica wedges about the vertical axis (see fig. 3.12), and changing the polarization back to p (e.g. with a crossed periscope). This technique was experimentally demonstrated in *Salle Noire 2* about 10 years ago at sub-relativistic intensity [268]. The authors even showed that the emission angle of each sub-attosecond pulse is directly linked to the CEP, therefore it could be used to directly lock the laser CEP on target, compared to a few mirrors before as we currently do.

Another way is to create a polarization gate [13, 285], so that only a very short fraction of the driving pulse (at the peak of the envelope) is p-polarized and efficiently generates an XUV burst, while the leading and trailing edges of the pulse are circularly polarized.

Another method for producing IAP, already demonstrated with gas harmonics, is to use multi-colour drivers (e.g. superimpose a beam at ω_0 and one at $2\omega_0$) to break the symmetry and decrease the number of attosecond pulses produced per laser cycle, thus relaxing the constraint on the driving pulse duration and making it easier to generate an IAP [206]. This technique has already been used to enhance the efficiency of HHG from plasma mirrors using $\approx$ 10-cycle long pulses [287, 54]. In [235], the authors even proposed to combine this technique with polarization-gating.

However, these methods have the drawback of being costly in terms of driving intensity. Instead, isolated attosecond pulses (or rather single attosecond pulses) can be created straightforwardly by forming an intensity gate at the surface of the plasma mirror with CEP controlled near-single-cycle driving pulses. It is technologically very challenging. Nonetheless, there have been three reports on experimental observations of the CEP dependence of relativistic harmonics from plasma mirrors very recently, in which the authors looked at the XUV spectrum while measuring the CEP in parallel.

First, in [144], 5.1fs, 40mJ pulses at a central wavelength of 765nm from the LWS-20 laser system [221], at the output of which a plasma mirror was installed for contrast enhancement, were used. The beam was focused with a f/1.2 OAP to $I \approx 1.2 \times 10^{20}\mathrm{W.cm}^{-2}$ on a silica target with a 55° angle of incidence, at 1 Hz repetition rate. The CEP was measured for each shot with a stereo-ATI phase-meter and the CEP-sorted data revealed a linear shift of the harmonic spectra along the wavelength axis. A Fourier transform of the spectral intensity between 33 and 57 eV, corresponding to the auto-correlation in the time-domain, lead the authors to the conclusion that for a given CEP, a train of three attosecond pulses was emitted, where the central one was 30 times more intense than the satellite pulses.

Secondly, in [128], the authors used a 10 Hz repetition rate OPCPA laser [139] delivering 7fs, 25mJ pulses at 900nm, that were focused to $I \approx 4 \times 10^{19}\mathrm{W.cm}^{-2}$ on a BK7 target. They used a F/1.6, 90° OAP and the angle of incidence on target was 45°. The relative CEP was measured with a f-to-2f interferometer for each shot and after re-organizing the data, they also observed a CEP dependent harmonic position shift and integrated harmonic yield. Here as well, a Fourier transform of the least modulated spectrum showed that, after selection of the 40 to 50eV spectral region, an IAP could be obtained.

The third reference [27] is actually one from our group, reporting on experiments done in *Salle Noire 2* before I started my PhD. At that time, the CEP stability was not good enough to control it so my predecessors simply CEP-locked the oscillator and measured the phase at the end of the chain with an f-2f interferometer and a standard spectrometer. The XUV spectra were

integrated over 30 consecutive shots and were attributed a CEP value by comparing time stamps. A CEP-dependent modulation depth of the harmonics was also observed. The improvement compared to the previous two reports was 1) a higher repetition rate laser was used (1kHz, vs. 10 Hz), 2) the driving pulses in the two previous references contained $\gtrsim$2 optical cycles, thus mostly double or triple attosecond pulses were generated, whereas here only one or two attosecond pules were generated regardless of the CEP value and 3) IAPs were obtained for the majority of CEP values, and simulations predicted that a good isolation degree (defined as the intensity ratio of the main attosecond pulse to the satellite pulses) of ≈ 10 could be obtained even without any spectral filtering, whereas Fourier transform of the harmonic spectra (E>10eV) resulted in an IAP isolation degree between 10 and 50 depending on the CEP.

However, all the experiments done so far following this approach relied on data binning, as there was no actual control over the CEP. Thus, no clear XUV continuum has ever been experimentally produced and measured in a reproducible, controlled way. Thanks to recent progress on the *Salle Noire 2* laser, we could do this for the first time as will be shown next, thus paving the way for attosecond pump/probe experiments with very bright isolated attosecond pulses at kHz repetition rate. Moreover, we also observed the electron distribution and energy spectrum at the same time as the harmonics while varying the CEP, which to the best of my knowledge has never been done before. The experimental results, which still need to be interpreted, may open up the path to the production of single attosecond electron bunches with MeV energy via phase-locked injection of a sub-fs electron bunch into the laser field and vacuum-laser acceleration, similar to what has been predicted in [188] and [158] through numerical simulations at grazing incidence. The experiments that will be presented in this Chapter thus provide us a with new insights into the dynamics of the interaction.

7.3.2 CEP scans for different plasma gradient scale lengths

Experimental results

We first simultaneously observed the XUV spectrum and the spatial electron distribution (for Φ_{az} between 30 and 49° with respect to the target normal direction) while varying the CEP. We made a series of CEP scans for different prepulse delays: -1ps (*ie* a post-pulse, see fig. 7.23.a), +1ps (fig. 7.23.b), +2ps (fig. 7.23.c) and +3ps (fig. 7.23.d). The energy on that day was 2.5mJ, the pulse duration 3.6fs and the intensity 1.8×10^{19}W.cm^{-2} ($a_0 = 2.9$). The plasma expansion speed measured on the same day was $c_s \approx 20$ nm/ps.

Spectral shift

We observe a clear CEP-dependent shift of the harmonics along the wavelength axis for all gradient scale lengths. It is particularly visible in subfigures (a) and (b), where we see that a 2π CEP shift corresponds to a ω_0 offset of the harmonic comb, and the slope of the linear drift is $\approx -\omega_0/(2\pi)$. In fig 7.23.e, I plotted harmonic spectra for two different CEP values separated by $\approx \pi$, where it is clear that the harmonic peaks are in phase opposition. This behavior is very similar to what had been previously observed in the sub-relativistic regime [31] with 5fs pulses, and more recently in the relativistic regime [128, 144]. For our pulse duration, we can reasonably consider that we generate two attosecond pulses per laser shot, and this spectral shift is probably due to a varying time delay from one attosecond pulse to the next within the driving pulse envelope, which itself would originate from a difference in optical path length due to the evolution of the plasma denting from one optical cycle to the next, as suggested in [128, 144].

XUV continua

For an optimum prepulse delay of 2ps, which gives the highest harmonic spectral extent, we observe the CEP-dependent transition from a very modulated spectrum (around 0 rad) to a much smoother, quasi-continuous XUV spectrum (around -3 rad). Let me remind the reader

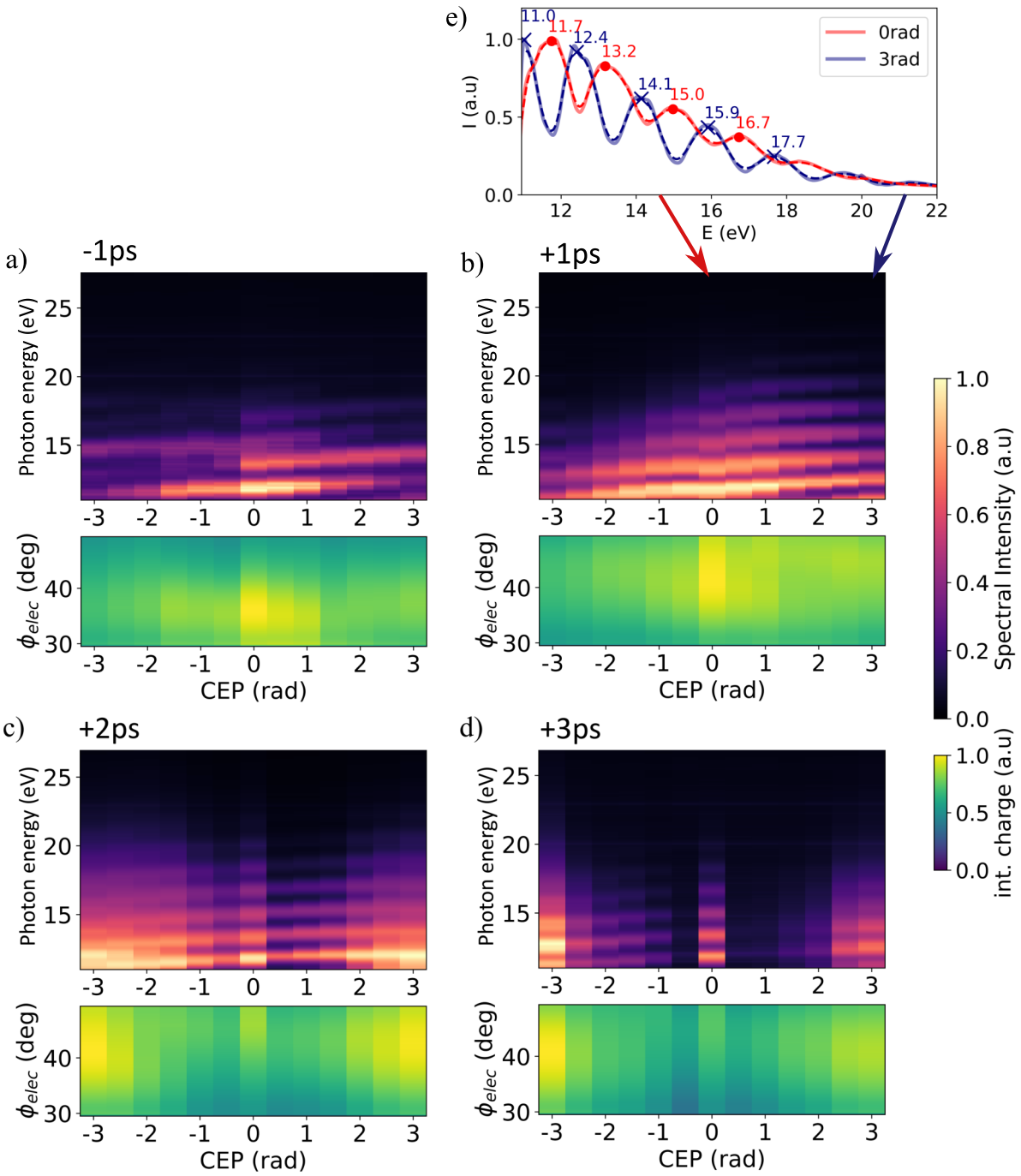

Figure 7.23: *Simultaneous detection of the XUV spectrum (top, vertically integrated) and the electron spatial distribution (bottom, vertically integrated) for different CEP values (from left to right), relative to an arbitrary CEP value offset. Prepulse delay of a) -1ps and b)+1ps: for these scans, the CEP was linearly increased in steps of 0.5rad from 0 to +3rad and then linearly decreased in steps of 0.5rad from -0.5rad to -3rad. Prepulse delay of c) +2ps and d)+3ps: for these scans, the CEP acquisition followed this sequence: (-3,+3,0,-2.5,+2.5,-2,+2,-1.5,+1.5,-1,+1,-0.5,+0.5) rad. For all the scans, each data is averaged over 5 consecutive sequences of 100 shots each ie 500 shots. e) Linear plot of the harmonic specra at a relative CEP of 0 rad (red) and +3 rad (blue) in the case of a +1ps prepulse lead time.*

again that all CEP values are relative to an unknown offset, therefore no conclusion can be made regarding the absolute values without comparing the results to numerical simulations.

Discussion

On that day, as we noticed and corrected later, there was a progressive decrease in signal intensity as we shot. The target rotation axis was not perfectly orthogonal to the target motorized translation axis, so that even though the target had been aligned with the interferometric method, the target plane still moved away from the focal plane every time it was translated (*ie* every $\approx$ 10 sequences of 100shots). This drift was quite small, $\approx$ 8 μm every 100 acquisitions of 100 shots, but the CEP was not varied completely randomly for these scans (the acquisition sequence is detailed in the caption of the figure), and we acquired 5 sequences of 100 consecutive shots for each CEP value. Therefore, we can see a decrease in the harmonic yield if we sort the data by acquisition order. Nonetheless, we clearly see that the influence of the CEP dominates. These scans are the only ones that were affected by this misalignment issue, which was corrected for all the other data sets presented in the following.

7.3.3 Gradient scans with the CEP locked

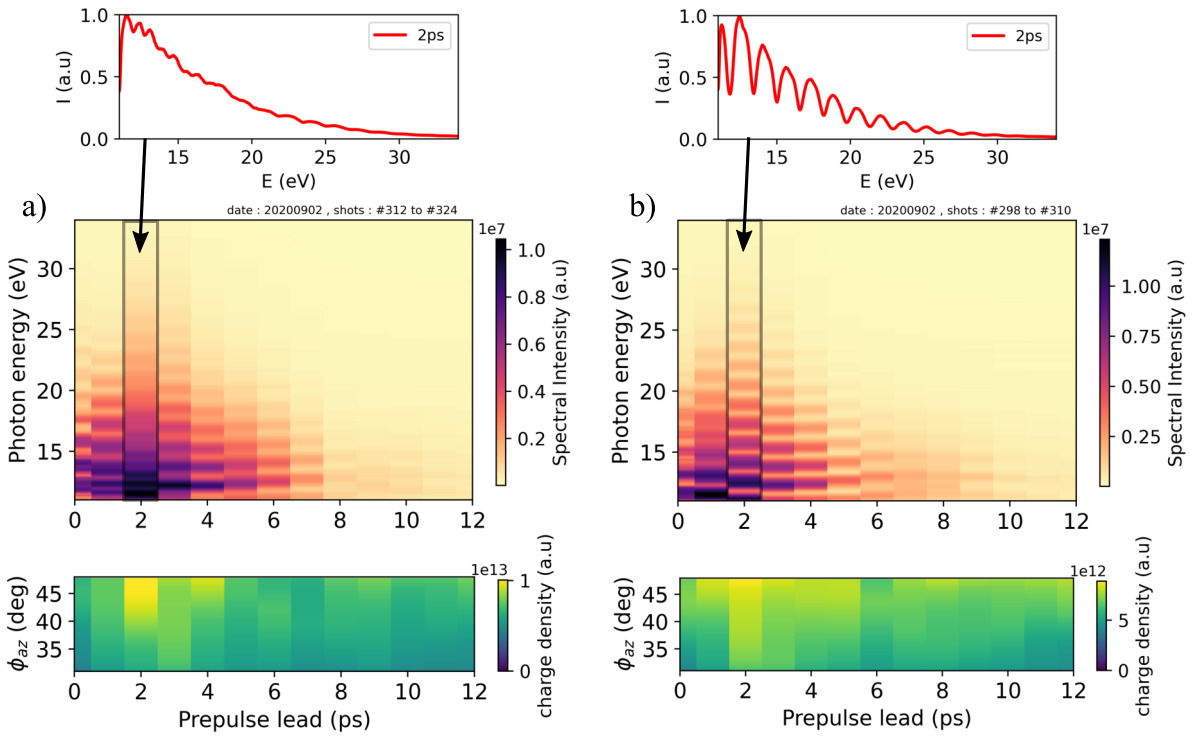

Figure 7.24: *Simultaneous detection of the XUV spectrum and the electron spatial distribution for increasing prepulse lead times. a) the CEP is locked to the value which gives the most continuous spectrum for a 2 ps prepulse lead time (CEP$\approx 3\pi/2$) and b) the CEP is locked to the value which gives the most modulated spectrum for a 2 ps prepulse lead time (CEP$\approx \pi/2$).*

We can also do the opposite, *ie* lock the CEP at a given value, and then vary the plasma gradient scale length (fig. 7.24). In panel (a), we locked the CEP to the value ϕ_0 which gave the most continuous XUV spectrum at a 2ps prepulse lead time, whereas in panel (b) we locked the CEP to ϕ_0+3 rad. We see here again that the continuous spectrum only appears at a certain optimum L_g value, and that the modulation depth depends on the plasma gradient as well as

on the CEP.

7.3.4 CEP-controlled transition from a continuous to a deeply modulated XUV spectrum, and simultaneous observation of the electron beam distribution

The optimum gradient scale length to generate an IAP has now been identified ($L_g \approx L_0 + 0.02\lambda$, equivalent to a 2 to 3 ps prepulse lead time) and we can keep it fixed. Instead, let us vary the carrier-envelope phase only.

Isolated Attosecond Pulses

First, let us focus on the scan at +2ps from figure 7.23 and extract four different CEP values spaced by $\approx \pi/2$ (see fig. 7.25.c). We clearly see that the two extreme cases are separated by π and that the modulation depth progressively varies in between these two values.

These measurements were very well reproduced by 2D numerical simulations from Maxence Thévenet, in which the laser parameters were chosen to mimic our experiments: $a_0 = 2$, θ_i=55°, τ = 3.5fs, $w_0 = 1.5\mu$m, $\lambda = 0.8\mu$m. Fig. 7.25.a shows the incident laser magnetic field and fig. 7.25.b shows the reflected field obtained in the simulation. The pulse intensity may then be obtained using a Hilbert transform (so as to reconstruct the complex laser field from the real signal). In the optimum case, a quasi-isolated (with an isolation degree of 10), 300 attosecond pulse containing approximately 35 % of the incident pulse energy (assuming symmetry around the beam propagation direction) is obtained without any spectral filtering.

According to the simulations, the CEP value on target corresponding to the continuous spectrum is $3\pi/2$, because there are two equally intense half-cycles of the electric field at the peak of the envelope, coming in the right order on target so as to first push the electrons inside the plasma and then pull them towards vacuum. This generates one big plasma oscillation, therefore the Doppler frequency upshift (and/or synchrotron emission) happens efficiently once. When the CEP is changed by π to reach the value $\pi/2$, there is now below the peak of the envelope: the end of a push-pull cycle and the beginning of a new one, which would explain that the temporal compression (therefore high frequency generation) mechanism happens twice in that case.

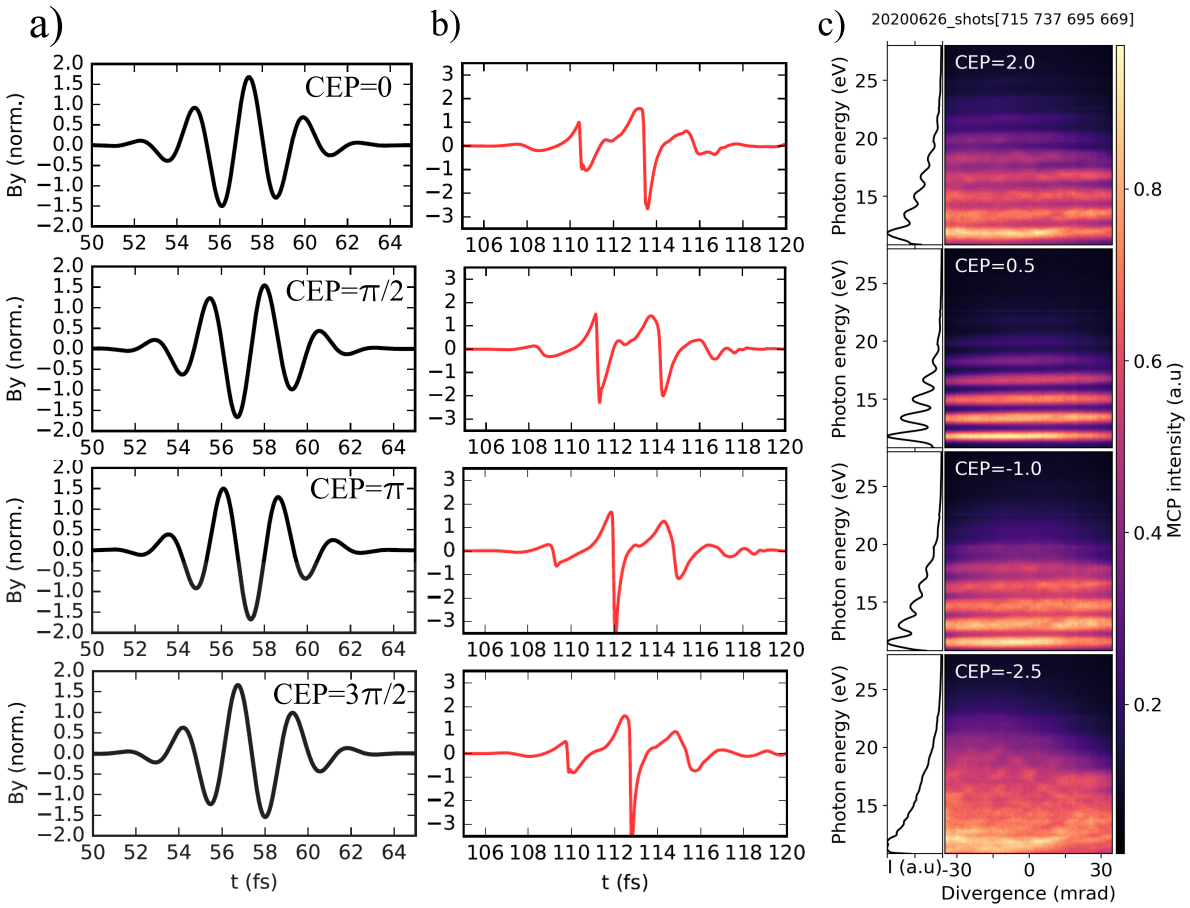

Figure 7.25: *a) Incident laser magnetic field (normalized to a_0) and b) Reflected laser magnetic field for four different CEP values on target: 0, $\pi/2$, π and $3\pi/2$ from top to bottom. c) Experimental XUV spectra for four different CEP values, spaced by $\pi/2$ (with an arbitrary offset) for a 2ps prepulse lead time. Each image is averaged over 100 consecutive laser shots. Subfigures (a) and (b) are from numerical simulations by Maxence Thévenet, whereas subfigure (c) is from our experiments.*

Transition from a continuous to a deeply modulated XUV spectrum, and associated electron beam

To verify the reproducibility and eliminate any experimental bias, we made some truly random scans as well. One of them is shown in fig. 7.26, and the two extreme cases are shown in fig. 7.27.a again. For a relative CEP of 0.5 rad, the XUV spectrum is very smooth in most of the beam, and weak modulations only appear on the very edge (around -30mrad), whereas for a CEP of -2.5 rad we obtain well modulated harmonics. On some other days, we only observed a continuum in the high energy part of the harmonic spectrum (e.g fig. 7.27.b), while the low-energy part of the spectrum was still slightly modulated. However, similar trends were always observed. To show the reproducibility, in fig. 7.27 I extracted the two extreme cases, separated by a CEP $\approx \pi$, from four different data sets and dates. It is clear that a greater peak and integrated electron charge was obtained for the same CEP value as the least modulated XUV spectrum in all cases, compared to the electron charge obtained after changing the CEP by $\approx \pi$ rad.

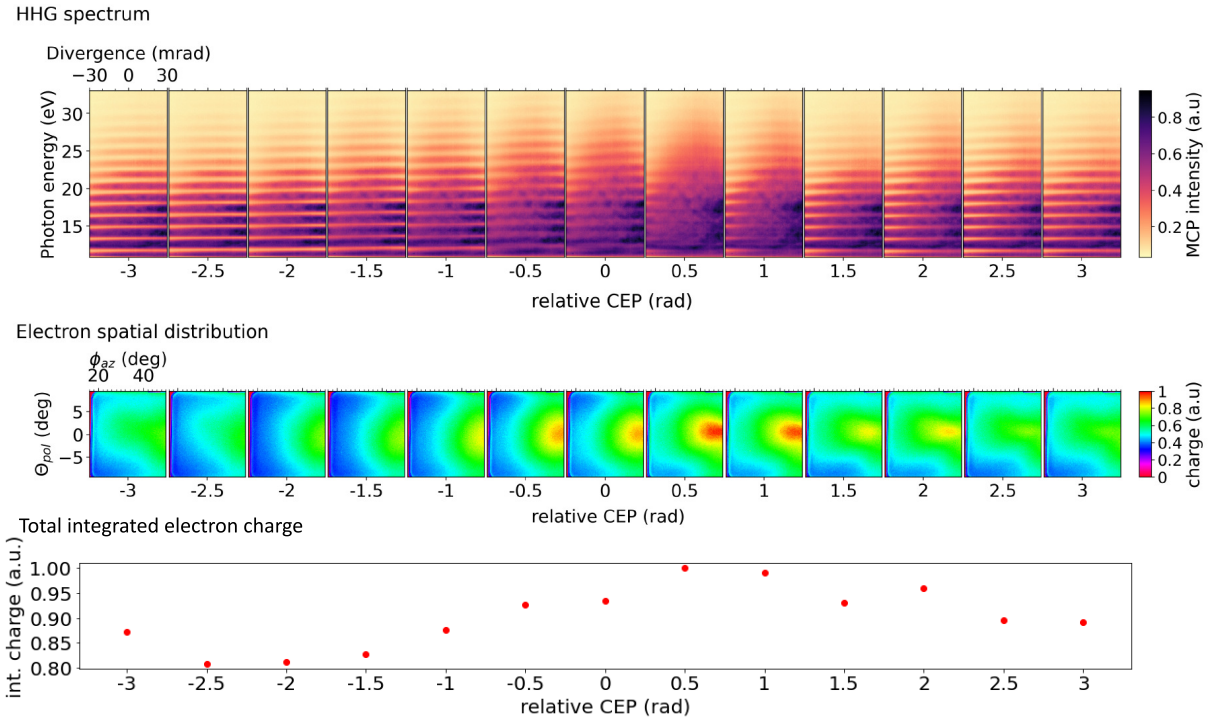

Figure 7.26: *Simultaneous detection of the angularly resolved XUV spectrum (top) and the electron spatial distribution (center) for different CEP values (with an arbitrary offset). The bottom graph shows the total integrated electron charge as a function of the CEP (normalized to unity). The CEP was varied completely randomly for this scan, the prepulse delay was 2 ps and the pulse duration 3.9 fs (date: 2020.09.02, shots 325-350).*

Regardless of CEP effects, one may also note the large differences in the high energy cutoff from one day to another: for example in fig. 7.27.b the signal clearly extends up to 40 eV whereas in 7.27.c it stops at 20 eV. The laser parameters were very similar and there were no noticeable differences in the experimental conditions for all these data. We nonetheless suspected the OAP reflectivity to decrease over time due to pollution of its surface by debris emitted from the target during the interaction, thus we had its surface re-polished, which immediately resulted in a clear increase in harmonic energy. We also suspect the XUV beam to be deflected and thus miss the XUV grating but we could not observe any evidence of that during my thesis. This should be investigated further.

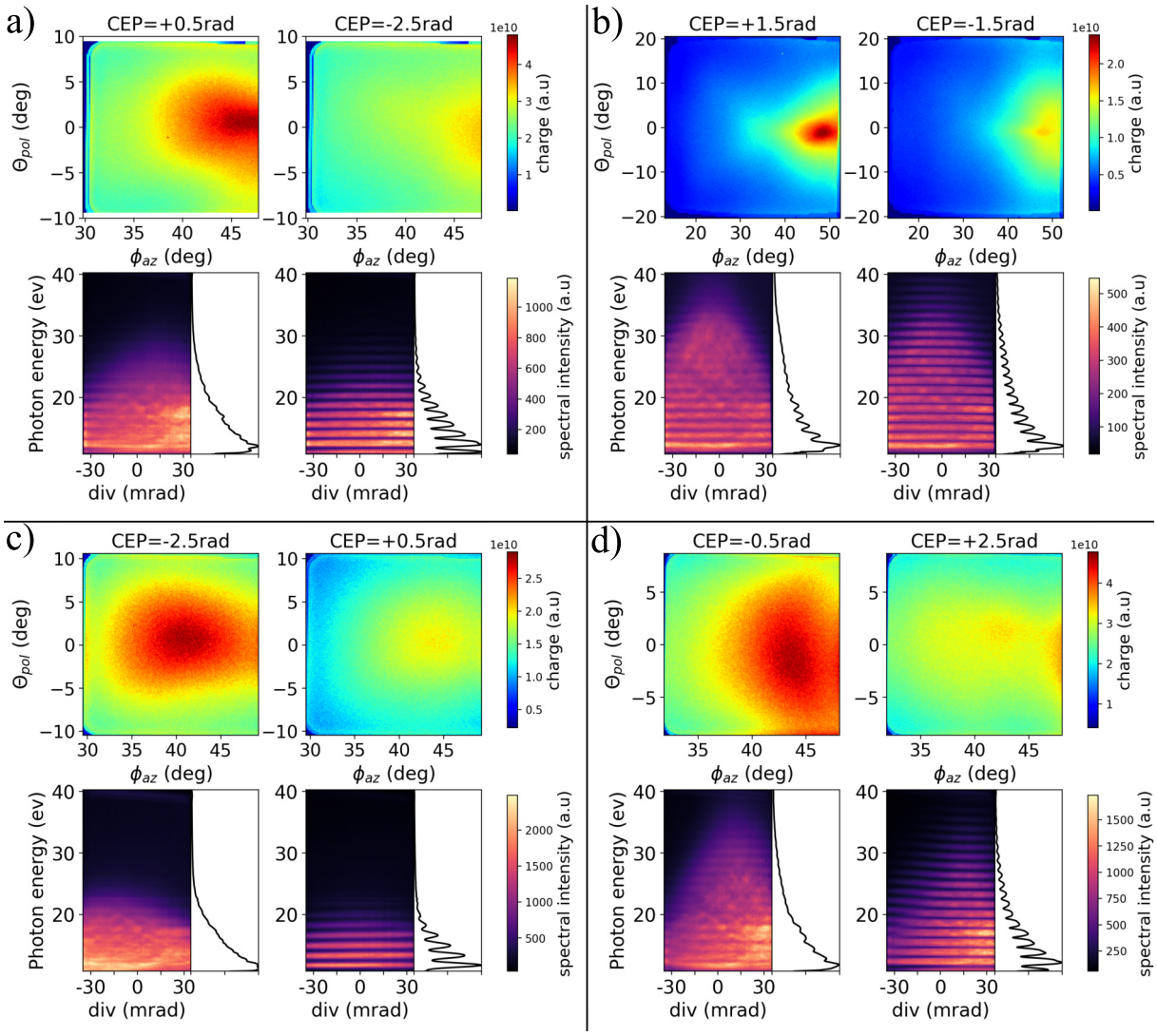

Figure 7.27: *Simultaneously acquired electron spatial distribution and vertically resolved harmonic spectra for two different CEP values spaced by $\sim \pi$, corresponding to the two extreme gating scenarios. a) extracted from the scan in figure 7.26 (date: 2020.09.02) b) on a different day, with the Lanex screen placed closer to the target (date: 2020.09.23). c) From 2020.06.26 d) From 2020.08.24. In all cases, the pulse duration was $\approx$ 4 fs and the energy on target $\approx$ 2.4mJ.*

7.3.5 CEP-dependent electron beam

Spatial distribution with a bigger Lanex screen

We were curious to see the full electron beam and whether or not there were electrons emitted at larger angles ($\phi_{az} \geq 55°$). We thus dedicated two days of the experimental campaign to the detection of the full electron beamprofile. We used a 177mm wide and 60 mm high Lanex screen to look at electrons from 20 to 70° emission angle (fig. 7.28) in the azimuthal plane. With this setup, it was impossible to simultaneously look at the XUV spectrum, therefore we cannot be absolutely certain about how it relates to the harmonics and whether we were in the exact same interaction conditions or not. However, we know that electron emission and harmonic generation are both optimized when the target is in the laser focal plane (see fig. 6.5), which is already a good indication.

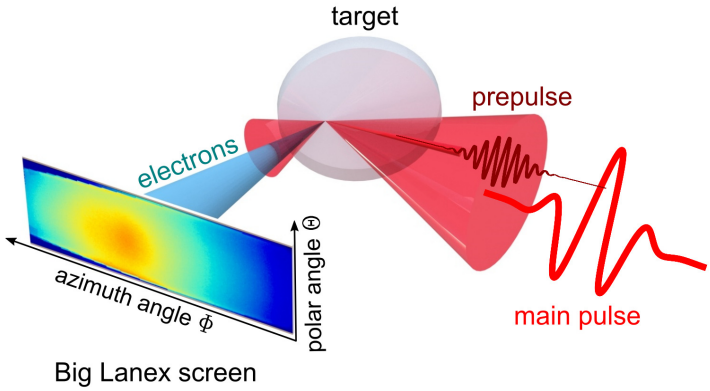

Figure 7.28: *Experimental setup for the spatial electron detection with the big Lanex screen.*

Randomized CEP scans for different prepulse delays are shown in fig. 7.29 and H.2, obtained with ≈ 3.6fs and 4fs pulses respectively. Whenever there is no prepulse (the gradient is too steep) or the gradient is too soft, there is no visible effect of the CEP on the electron beam spatial distribution. However, there is a clear effect of the CEP at the optimum gradient scale length (corresponding to a 2 to 3ps prepulse lead time) for ROM harmonics. If we compare it to the scans in fig. 7.26 and 7.27, we can assume that when the electron charge towards the normal ($\phi_{az} \approx 50°$) is the highest, then we are in the gating scenario which only gives one attosecond pulse. For a CEP change of π, we see instead a centro-symmetric electron distribution, with a hole in the center.

Here is a first hypothesis: in the optimum gating scenario (absolute CEP=$3\pi/2$ according to simulations), corresponding to the optimum push/pull in focus, the electrons have the highest kinetic energy. They remain in phase with the reflected laser field and undergo VLA. Then they are expelled towards the normal, as explained previously (subsection. 5.3), in the polarization plane. In contrast, for a CEP shift of $\pi/2$, there are two, less intense push/pull cycles. Thus, the electrons start with a lower kinetic energy, and they are under the influence of more than one optical cycle, therefore they oscillate in the laser field. The ponderomotive force dominates, electrons are pushed away isotropically from the high field region, and we observe this ring structure. This hand-waving explanation could be verified with the same test-particle code as the one used to produce the plots shown in fig. 5.4 as a first approach, ideally after verifying the initial injection phase of the electrons through PIC simulations.

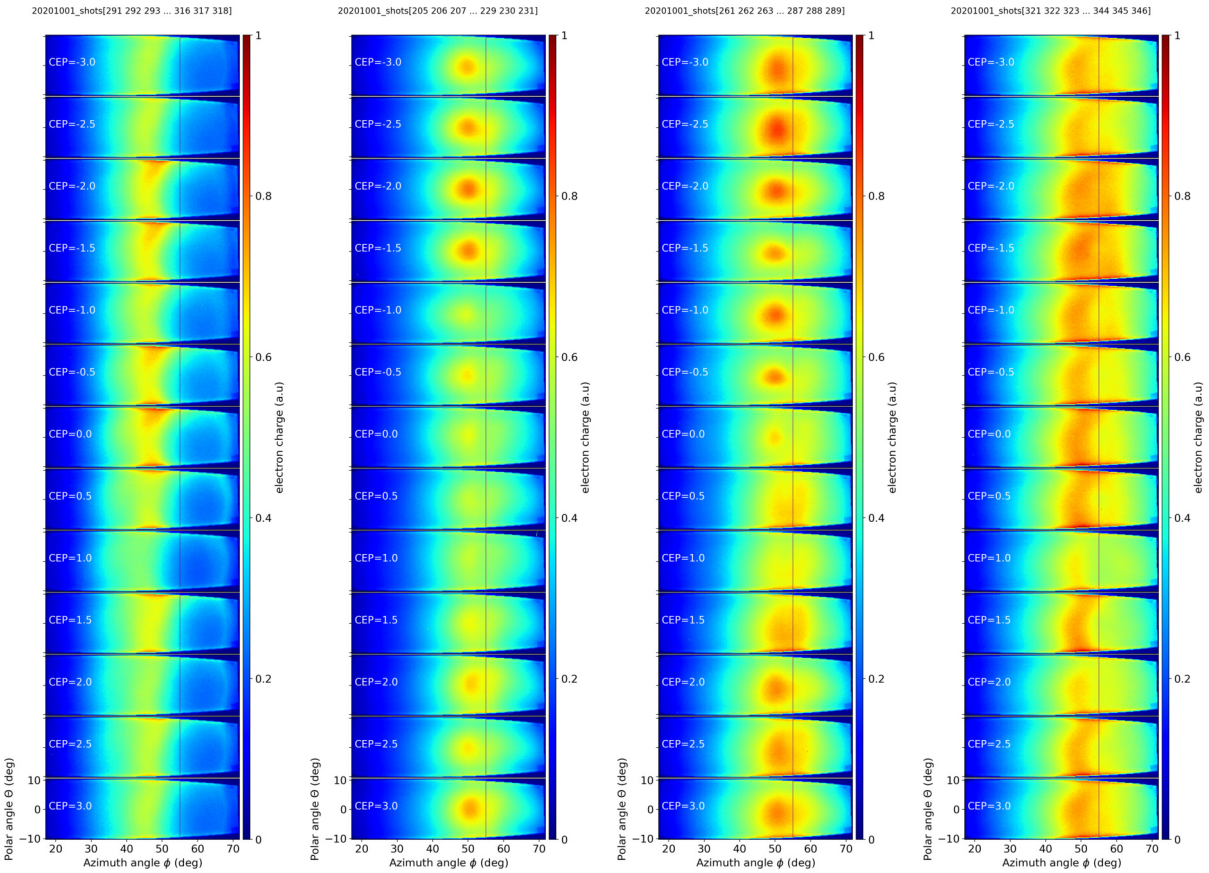

(a) *-1ps pre-pulse delay*

(b) *2ps pre-pulse delay*

(c) *3ps pre-pulse delay*

(d) *4ps pre-pulse delay*

Figure 7.29: *Consecutive randomized CEP scans of the electron beamprofile for different plasma gradient scale lengths, shown from -3 rad (top) to +3 rad (bottom) in steps of 0.5 rad. The thin vertical purple line indicates the laser specular direction* $\phi_{az} = 55°$.

CEP-dependent electron spectra

We also looked at the electron spectra and the harmonics simultaneously, for different CEP values (still relative to an unknown offset), as shown in Figs. 7.30 and 7.31. Here again, the CEP values were changed randomly to eliminate any experimental bias, and the shot-to-shot CEP deviation was $\lesssim 400$ mrad rms, measured with the Fringeezz. In both Figures, the pinhole was centered at $\Phi_{az} = 39°$ and $\theta_{pol} \approx 1.7°$ in order to be able to see harmonics simultaneously. The scan in fig. 7.30 was made on the same day as the one in fig. 7.26 and, unfortunately, as we can see in fig. 7.26, the pinhole was quite far from the electron beam center. Ideally, this measurement should be done again with a different spectrometer design (with an (X,Y) motorization or a horizontal slit instead of a pinhole).

Nonetheless, we see reproducible features which clearly depend on the carrier-envelope phase of the laser. These are more visible in the linear plots (subfigures 7.30.f and 7.31.f). The experimental setup was exactly the same as for the scans at long gradients (see subsection 7.2.2) corresponding to the wakefield acceleration regime of electrons, which had been made only two days before the one in fig. 7.30, and the data sets were analyzed exactly the same way, therefore the spectra are directly comparable. Whereas for LWFA electrons, the spectrum was exponentially decaying, here we clearly see a dominant peak at around 1MeV for most CEP values, and sometimes a second sharp peak at lower energy (at 0.6MeV in fig 7.30 and at 0.8MeV in fig.7.30). This lower-energy feature only appears for some values of the CEP, which correspond

to the production of the most modulated harmonic spectra, whereas the peak at 1 MeV becomes broader and more intense for CEP values which produce smooth XUV spectra, compared to the CEP values yielding modulated spectra.

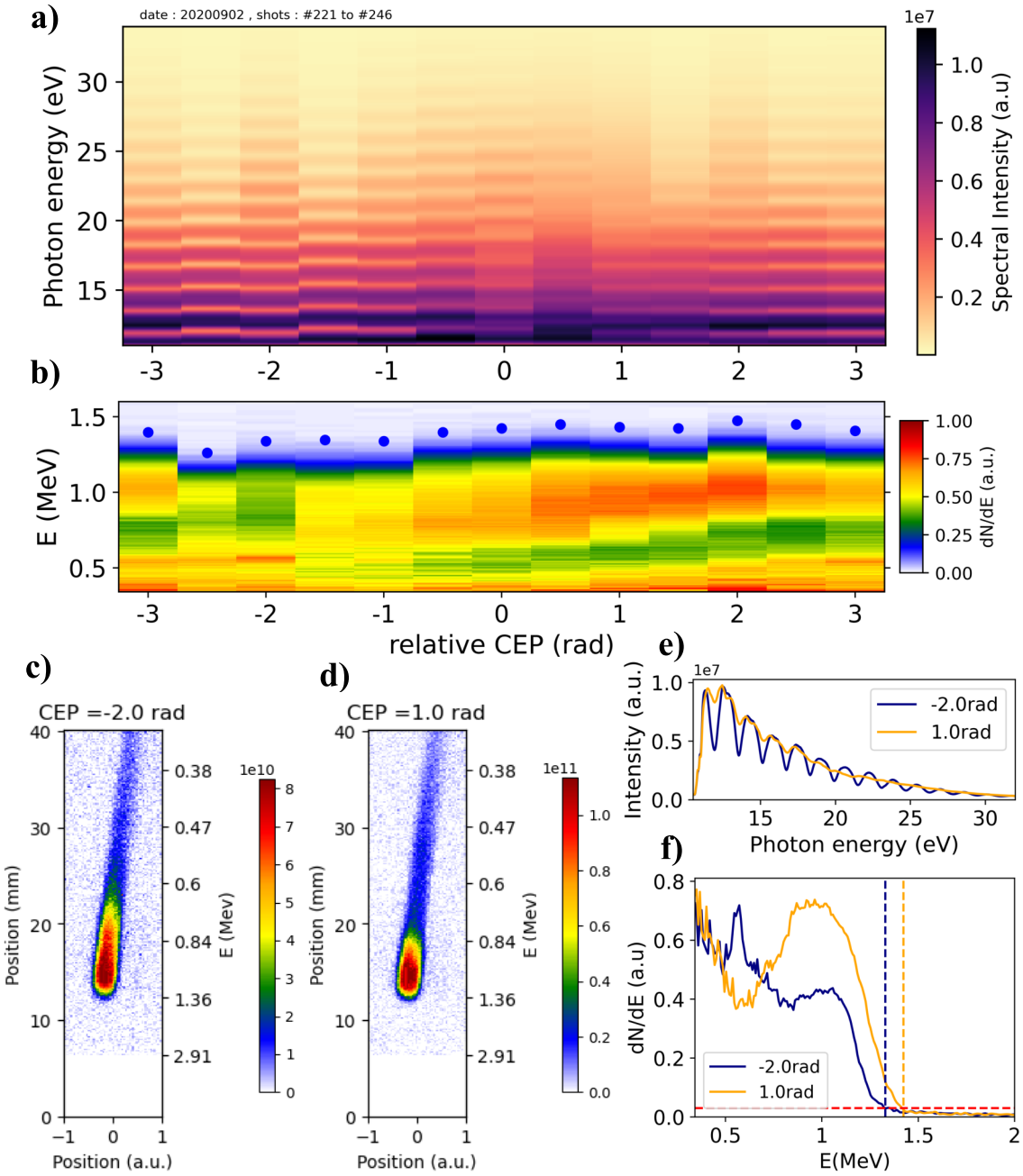

Figure 7.30: *Randomized CEP scan from 02.09.2020. a) Harmonic spectra and b) Electron spectra for increasing relative CEP values (rad). c) and d) raw images of the Lanex screen with calibrated y-axis for a CEP value of -2rad and +1rad, respectively. The 0mm position corresponds to the undeviated electron beam going through the pinhole when the magnets are not inserted. e) the two harmonic spectra and f) the two electron spectra for -2 and +1rad plotted together. The prepulse lead time was 2ps and the pulse duration was 3.6fs, with ≈ 2.2mJ on target.*

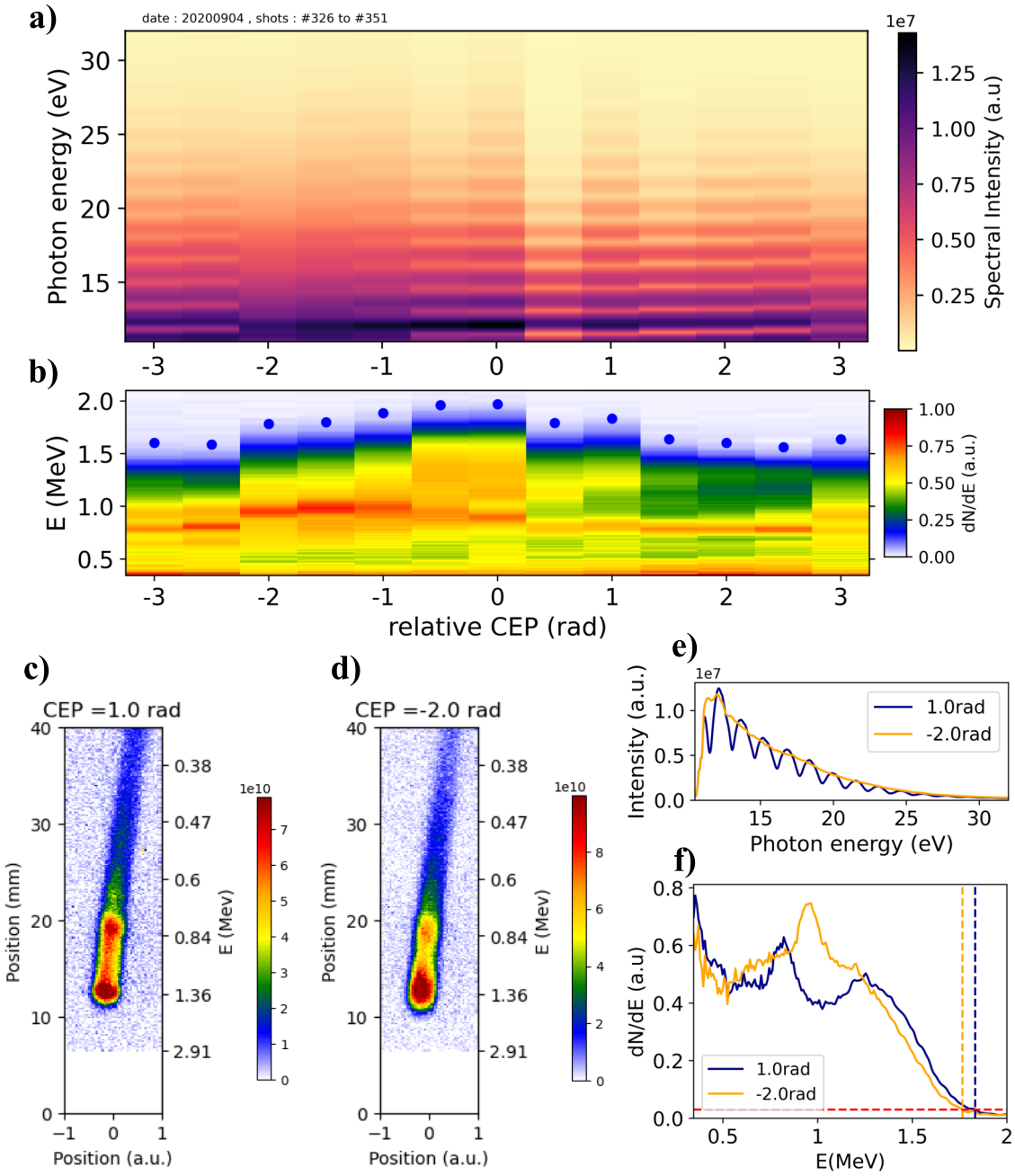

Figure 7.31: *Randomized CEP scan from 04.09.2020. a) Harmonic spectra and b) Electron spectra for increasing relative CEP values (rad). c) and d) raw images of the Lanex screen with calibrated y-axis for a CEP value of +1rad and -2rad, respectively. The 0mm position corresponds to the undeviated electron beam going through the pinhole when the magnets are not inserted. e) the two harmonic spectra and f) the two electron spectra for +1 and -2rad plotted together. The prepulse lead time was 3ps and the pulse duration was 4fs, with ≈ 2.2mJ on target.*

7.3.6 Gouy phase shift around the focus at fixed CEP

The CEP is now locked to a fixed value. The gradient scale length is also kept constant around the value which maximizes the ROM HHG efficiency. Instead, we vary the distance between the off-axis parabola and the target. This can be easily done under vacuum since the OAP is mounted on a motorized translation stage, moving along the beam propagation direction from the OAP to the target.

The results for a prepulse lead time of 3 ps are shown in Appendix H, figure H.3, while the results for a 4 ps prepulse lead time are shown in figure 7.32. In both cases, the modulation depth of the harmonics is clearly larger on one side of the focus compared to the other side. This becomes even more obvious if we normalize the harmonic spectra individually, as done in fig 7.32.c. In this case, for example, we find that the distance required to go from the most modulated spectrum to the least modulated one is approximately 14μm (fig 7.32.d.).

As explained in the theoretical introduction, the pulses experience a phase shift, called Gouy phase (Eq. 1.42), around the focus. The evolution of this phase depends on the spatio-spectral distribution of the beam via the dimensionless "Porras" factor g_0. The phase shift corresponding to our experimental parameters was shown in fig. 1.5 for three different Porras factors. The plot corresponding to a factor of -2 indicates a π phase shift from -5μm to +5μm from the focus, whereas for g_0=+2 or 0, the phase shift is smoother. Therefore, the experimental values that we observe are not aberrant and the variations in the modulation depth around the focus are consistent with the effect of the Gouy phase.

Of course, during the scan, the modulation depth is also influenced by the simultaneously induced laser intensity variations on target, which also cause the plasma gradient scale length to slightly change (the prepulse's Rayleigh length is of the order of 100μm so the preplasma scale length should not change, but the contribution of the main pulse's finite contrast to the final scale length -the L_0 term- does vary). Another possible explanation would be that the CWE harmonics' divergence decreases when the target plane is before the focal plane (see section 5.1 and fig 2b in [213]). Since the CWE mechanism is efficient for lower intensities than ROM harmonics, the attosecond pulse would be less isolated when CWE dominates therefore the spectrum would appear more modulated when the CWE harmonics are generated with a plane wavefront (*ie* when the target plane is out of focus). On the contrary, due to plasma denting, ROM harmonics could be better detected on the spectrometer when the target plane is after the focus, but as discussed in section 5.2, the plasma denting is probably negligible for our pulse duration and laser intensity (which is by the way corroborated by the observation of the decrease in divergence with the harmonic order, visible in fig. 6.7.b for example).

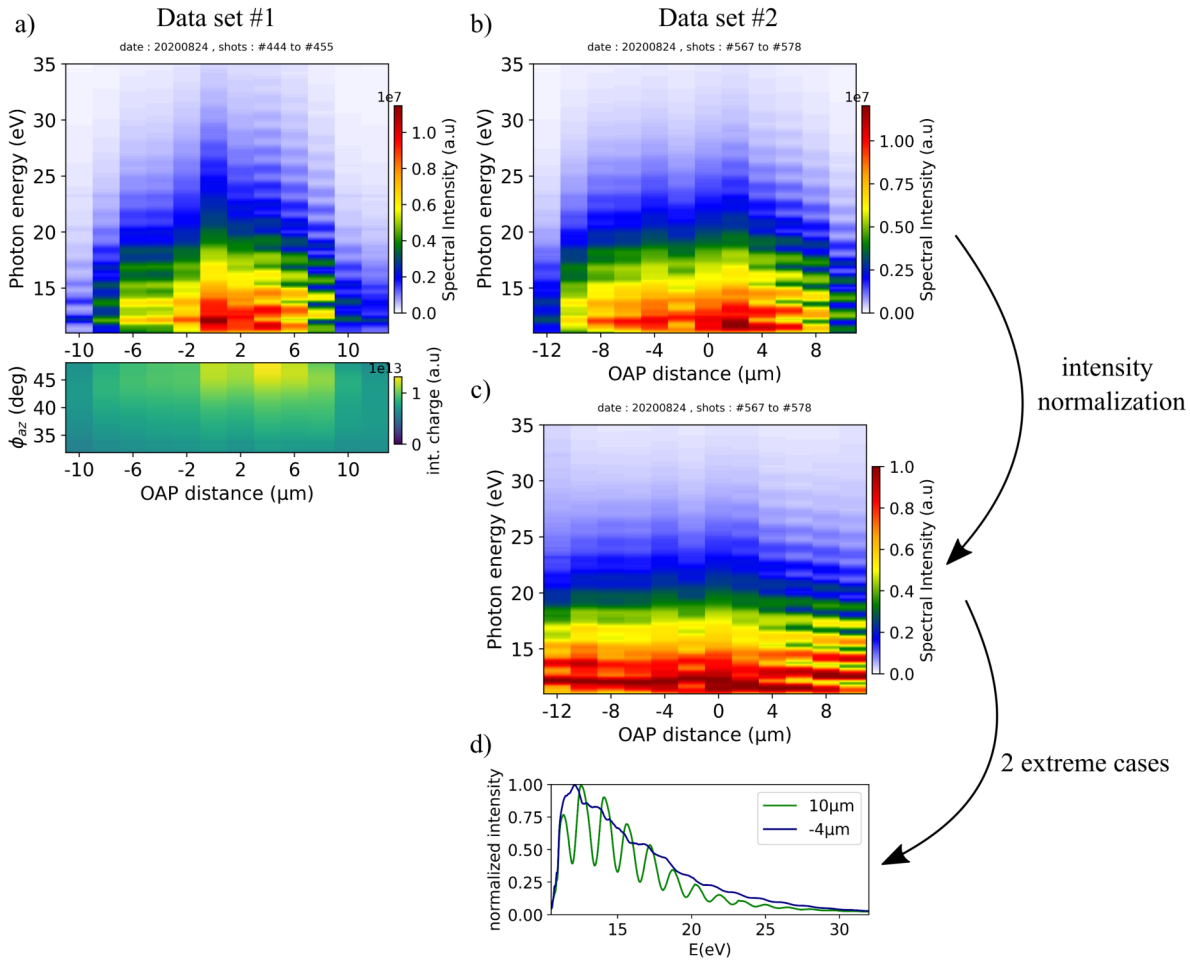

Figure 7.32: *a) Integrated harmonic signal (top) and electron distribution (bottom) as we vary the OAP distance with respect to the target. b) Second data set with the integrated harmonic signal from the same day. c) same as (b) but after normalisation of the individual harmonic spectra. d) Linear plot of the most modulated and the least modulated harmonic spectra from (c). The prepulse delay was set to -4ps. Positive OAP position values mean that the distance between the OAP and the target was decreased. The CEP was actively stabilized to a constant arbitrary value.*

7.4 Conclusion and perspectives

7.4.1 Conclusion on the experimental results

In summary, the plasma mirror experiments performed in *Salle Noire 2* during my thesis allowed to:

· better understand the proton acceleration regime and demonstrate extremely promising low proton beam divergence

· measure the energy spectra of electrons accelerated in the ROM regime and in the LWFA regime

· provide experimental evidence of the controlled generation of continuous XUV spectra via CEP gating at kHz repetition rate

· experimentally explore CEP effects on the electron beam (spatial distribution, energy) emitted from the target at short plasma density gradients for the first time

· make first steps towards the full XUV beam characterization through preliminary XUV wavefront measurements.

7.4.2 Future experiments and challenges in *Salle Noire 2*

In the future, changes should be made to the existing set-up to improve the measurements, in particular for the electron energy spectra.

A major issue that we faced was the regular pollution of the off-axis parabola surface by debris from the target, as it is very close to its surface, resulting in a strong decrease in the detected HHG signal every few months. The solution of placing a thin (a few 100 μm) silica plate in front of the OAP should be tried to determine whether it degrades the laser properties in focus or not.

Experimental challenges remain, such as properly measuring the XUV beam footprint and wavefront in CWE and ROM regimes. Attempts could be made to try to reduce the XUV beam divergence [153], bigger MCPs could be used and an improved shielding should be tried for the wavefront sensor.

A major piece of work would be to refocus the XUV beam and fully characterize it, including the temporal intensity profile and the energy.

Now that CEP control is possible, the lighthouse effect could be tried again, and one could possibly use the CEP-dependent position of the XUV sub-beams to stabilize the CEP directly on target.

7.4.3 Upgraded diagnostics

During the experimental campaigns, we always regretted not being able to look at the full electron beamprofile at the same time as looking at the XUV spectrum. Similarly, when measuring the electrons' spectra, we could not center the pinhole at an angle larger than 40 degrees without blocking the XUV beam, and there was no possibility of moving the pinhole vertically at all either.

We thus started thinking of a new setup, which is under construction. A 3D drawing of the setup is shown in fig. 7.33. The idea is to use a big Lanex screen (200x120mm) and cut a rectangular aperture so as to let a portion of the XUV beam pass through it. Then, there is a custom-made rectangular mirror at 45 degree behind the screen with a rectangular aperture (35 by 4 mm) as well. Even though it is a custom product, it can be made for a very low cost because the quality should not matter. On top of this LANEX/mirror assembly, there is a breadboard for the *Pixelink* camera (with a camera objective) and a 2 inch mirror placed right in front of it. Finally, there is a home-made motorized horizontal translation stage (≈20 cm long) placed

in front of the Lanex, with two additional small vertical translation stages (not represented in 7.33): one for the pinhole and one for the pair of permanent magnets.

Another possibility for the electron spectrometer would be to have a horizontal slit instead of a pinhole, so as to have a "single shot" angularly resolved electron energy spectrum. This makes the data analysis more complex, but it is certainly feasible, as some groups already use such spectrometers (e.g. at CEA Saclay, see Supplementary Material of [56]). The slit could even cover angles extending above the specular direction 55° without completely blocking the harmonics.

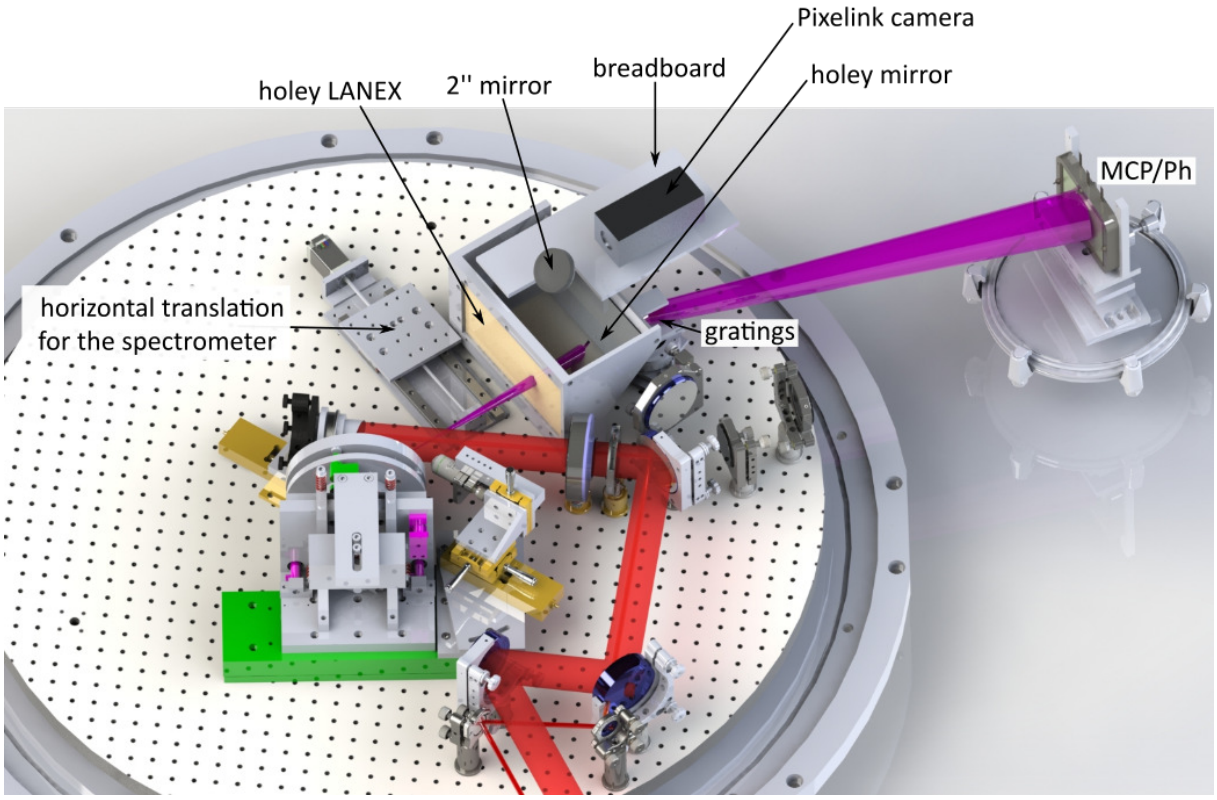

Figure 7.33: *3D drawing of my proposition for new diagnostics.*

Final conclusion and perspectives

Summary of the work achieved during this thesis

The objective of this experimental thesis work was i) to improve the reliability, stability and control of a near-single-cycle laser source delivering TW peak power pulses at kHz repetition rate, and ii) use this light source to finely control the properties of particle and radiation beams generated in relativistic laser-plasma interactions.

In Chapter 3, I described the latest improvements that have been made to the laser source. The first CPA pump laser was replaced with a new one to enhance the energy and CEP stability ; the pulses' stretching ratio in the first CPA was increased to ensure its damage proof long term operation ; the XPW filter was rebuilt in a more modern way ; the second CPA compressor was modified into a transmission grating compressor to increase the energy and the spatial quality of the beam ; and an extension was added to the post-compression stage to ensure long-term operation without damaging optics. On top of that, a kHz feedback loop for the CEP control and stabilization was implemented, resulting in a ≈400 mrad rms residual noise, and a detailed characterization of the output pulses was performed, in particular to verify the absence of spatio-temporal couplings for the first time. This was presented in Chapter 4.

In the future, this laser source could be further improved in terms of stability by replacing the two amplification stages in the second CPA with a single cryo-cooled amplifier. Another interesting option would be to replace the oscillator with its newer version including an AOFS for more robust CEP stabilization. Although not demonstrated yet, the PCO group (and Louis Daniault in particular) is also envisaging the possibility of combining both contrast cleaning and post-compression in a single stage, e.g. through the nonlinear ellipse rotation effect, which is very promising as it would allow considerably simplifying the laser chain. Finally, ideally the laser characterization should be directly made on target, e.g. by looking at the d-scan trace of the third harmonic in the specular beam (similarly to the work reported in [152]), which the PCO group started working on, together with *Sphere Photonics*.

As shown at the end of Chapter 4, the *Salle Noire 2* laser was used to accelerate electrons though laser-wakefield acceleration in the near-single-cycle regime (although it was not my primary focus, but that of the APPLI team). The prevailing influence of the carrier-envelope phase on the shape of the plasma wakefield and the precise injection of electrons into it was demonstrated in two experiments, in which clear differences in energy and beam pointing were observed depending on the CEP. Controlling these features is a very important step for applications which require a high degree of stability of the electron beam. With the electron beam properties currently achieved, applications are now clearly envisaged in the near future in the APPLI group.

In Chapters 5 to 7, we then dived into the experimental study of plasma mirrors, my second main focus during this thesis. Previous works were completed by looking at different observables: the spatial and spectral distribution of electrons, ions and XUV radiation, under various experimental conditions (plasma gradient scale lengths, pulse duration and peak intensity). Through international collaborations, we were able to demonstrate the production of very low divergence, 0.5 MeV protons along the target normal direction and understand the underlying physical mechanism, as well as make first steps toward the XUV wavefront characterization. In-

ternal PCO experimental campaigns (made by myself, Stefan Haessler, Rodrigo Lopez-Martens and my successor Jaismeen Kaur) allowed to gain knowledge on and further control the emission of electrons and harmonics. We measured electron energy spectra in the laser wakefield acceleration regime (at long gradients), thus confirming theoretical predictions by Neïl Zaïm for the first time. Last but not least, we clearly demonstrated sub-cycle control of the harmonic and electron emission properties in the relativistic regime at kHz repetition rate. We are now able to produce, on demand via CEP control, XUV continua and relativistic electrons peaked at 1 MeV. Numerical simulations (by Maxence Thévenet) show that these XUV continua should be associated with extremely bright isolated attosecond pulses, which should be verified in the future. The work presented in Chapter 7 is thus a major technological step towards the realization of a plasma-based attosecond light source, as we are the only group in the world capable of producing such XUV continua from the plasma phase on demand (to the best of my knowledge). Moreover, thanks to our unique laser system aiming at the lambda cubed regime, we are able to do this at kHz repetition rate, while most groups work at a few Hertz, which is of course an additional advantageous feature for applications.

Future perspectives for the field of SHHG

As I have shown in this PhD work, plasma-mirror-based SHHG sources are very challenging to implement and there are only a few groups in the world actually working on the subject. Although the interest of the scientific community for plasma mirrors is currently lower than that for gas-phase harmonics and electrons accelerated from gas jets, I believe it is a complementary growing field with many things left to discover which should have a bright future. Examples of exciting perspectives for the future are listed below.

Relativistic lambda-cubed regime

Theoretical work predicts that in the lambda-cube regime, the few generated attosecond pulses are spatially isolated simply due to the plasma surface dynamics, leading to the production of an IAP even with a ≈2 cycle pulse (5 fs at λ=800nm) [189]. However, this varying beam pointing from one optical cycle to the next has never been observed in experiments, which is an additional reason for us to persevere with the spatial XUV measurements.

In simulations, increasing the laser focused intensity is found to improve the attosecond pulse brevity and focusability while the conversion efficiency remains high [191], which might be verified in the future, e.g. with the new SHHG-SYLOS beamline at the ELI-ALPS facility.

Besides, the spatio-temporal characterization of attosecond pulses produced on plasma mirrors in the relativistic regime has only been performed once [55], with relatively long driving pulses (25 fs), and the very high laser-to-XUV conversion efficiencies predicted in this regime [256] (and from relativistic SHHG in general) have never been demonstrated experimentally either. Thus, it would be interesting for the scientific community to persevere in this field and see what might come out of future experimental works.

Characterizing the attosecond pulses produced in the near-single-cycle regime is now seriously envisaged in the PCO group.

SHHG beamlines at ELI-ALPS

A beamline dedicated to surface high-order harmonic generation (SHHG) will be installed at the ELI-ALPS facility in Szeged, Hungary. This beamline will be implemented at the output of the current SYLOS 2 laser system, which takes advantage of the OPCPA technology and has demonstrated the following performances: 5TW peak power, 30mJ, 7fs pulses (<2.3 optical

cycles), also at kHz repetition rate, and with an impressive shot-to-shot CEP stability of 210 mrad rms over hours, as well as a contrast ratio better than 10^{10} up to 10ps before the main pulse [252]. Furthermore, an upgrade of the SYLOS 2 laser system into "SYLOS 3" in the near future will increase the output pulse energy to 120mJ. Thus, the SYLOS 2 and 3 laser systems can be seen as the new generation of lasers for relativistic laser-plasma interaction at high repetition rate.

The SHHG beamline final design and implementation has been attributed to the company *ARDOP Industrie* and should be commissioned in 2023. Through my PhD thesis, which was organized in collaboration with the company, the PCO group further transferred its expertise with plasma mirrors and helped *ARDOP* finalizing the technical design report for the beamline, which has been accepted by ELI. The design includes a set of diagnostics for SDI measurements, electrons and XUV harmonic detection, similar to the ones used in *Salle Noire 2*, as well as a refocusing of the XUV and IR beams for characterization and eventually applications to pump-probe experiments.

This beamline should thus be the perfect opportunity to characterize the attosecond pulses generated from plasma mirrors in the few-cycle regime, and even fully demonstrate their potential by using them in applications for the first time.

It should also be noted that a second SHHG beamline will be installed at the output of a PW laser (SHHG-HF [145]). Post-compression of this laser [105] would allow combining the advantage of temporal gating with a large number of photons produced.

Plasma mirrors as a tool for reaching the Schwinger limit?

Plasma mirrors could also help exploring new regimes of light-matter interaction. A growing field of research is the experimental investigation of strong-field quantum electrodynamics. According to quantum field theory, vacuum is not just an empty space but is filled with short-lived virtual pairs of particles and antiparticles. If one applies a strong electric field, capable of separating the particle from the antiparticle within the pair lifetime, then they will exist for as long as they do not encounter their matter/antimatter counterpart again. The laser intensity required for that is called the Schwinger limit and corresponds to $4.7 \times 10^{29}\mathrm{W.cm}^{-2}$ [231]. A few pioneering experiments have been made, for instance the E-144 experiment at SLAC [18] where researchers generated electron/positron pairs in two steps, by first colliding 46GeV electrons with a TW laser focused down to sub-relativistic intensity ($a_0 \sim 0.4$), thus producing Gamma-rays through nonlinear Compton scattering, and then colliding those gamma-rays with several laser photons to generate the electron/positron pairs (a process known as multiphoton Breit-Wheeler pair production). More experiments are planned. However, this interaction was in a perturbative regime, well below the Schwinger limit, and pure Breit-Wheeler pair production has never been observed so far.

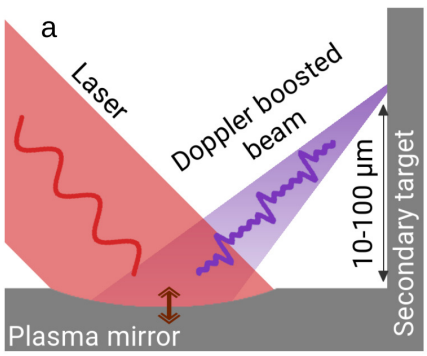

Figure 7.34: *Schematic illustration of the newly proposed schemes for electron/positron pairs generation using Doppler-booster laser beams. Reprinted from [82]*

The relativistic lambda-cubed path would be one way to reach such high intensities [191]. Another approach is to combine existing [165, 131] and forthcoming [251] multi-PW lasers capable of reaching focused laser intensities $\sim 10^{23}$W.cm^{-2} with curved plasma mirrors (fig 7.34). The idea is to focus the PW laser on a plasma mirror so that, under the right conditions (plasma gradient scale length), the reflected beam contains higher frequencies/temporally compressed optical cycles (it is "Doppler boosted"). Additionally, the reflected beam is focused slightly after the plasma mirror due to plasma denting, thus the intensity is spatio-temporally boosted via SHHG and due to the plasma surface curvature. First suggested in 2003 [40], researchers now seem to have converged towards a feasible experiment [260, 82, 111] thanks to the development of more precise numerical simulation tools.

Liquid plasma mirrors?

Another promising approach is to use thin liquid sheets instead of solid targets as plasma mirrors to generate high-order harmonics in the relativistic regime. This is the focus of Antoine Cavagna, a new PhD student in the PCO group, who works in collaboration with Enam Chowdhury from the Ohio State University (USA). There are many advantages: first the target surface is intrinsically more stable than that of rotating solids, then it would allow working in continuous mode at kHz repetition rate (since it is self-refreshing) which would greatly facilitate the characterization and the application of SHHG and particle beams, and finally the achievable sub-micrometer thickness may be suitable for generating harmonics in transmission mode via coherent synchrotron emission (such as was already observed with ultra-thin carbon foils [71]).

However, to date, liquid sheets have been used to generate electrons and ions [100], as plasma mirrors for contrast enhancement [12], or to generate harmonics in the sub-relativistic regime [118] but were never tested for relativistic surface harmonics or CSE.

Appendix A

Sate-of-the-art CEP stable oscillator based on an AOFS

Although this does not directly concern the work done in *Salle Noire 2*, it is important to note the existence of a more recent technique relying on an Acousto-Optic Frequency Shifter (AOFS), which has been implemented in the upgraded version of the oscillator (*Rainbow CEP 4, Femtolasers*), used in our second laser room dedicated to new laser developments, the *Salle Noire 3*. Instead of detecting the beatnote and feeding it back to modulate the pump intensity, we feed the error signal forward to an acousto-optic device [142], which adds an offset frequency to the input comb so as to lock the frequency comb offset to zero (fig. A.1). The -1st diffracted beam after the AOFS corresponds to a frequency comb

$$f'_n = f_n - f_{\text{ac}}, \tag{A.1}$$

with f_{ac} the frequency of the acoustic wave. Through the feed-forward loop, f_{ac} is locked to:

$$f_{\text{ac}} = f_{\text{ceo}} + f_{\text{RF}}, \tag{A.2}$$

where f_{RF} is a constant radiofrequency added to meet the requirements of the AOFS. By making this radiofrequency a multiple of the oscillator repetition rate

$$f_{\text{RF}} = k f_{\text{rep}}, \tag{A.3}$$

we end up with

$$f'_n = (n-k) f_{\text{rep}}. \tag{A.4}$$

This method has many advantages. First, there is no delay between the detection and the correction as we feed-forward and the correction is done passively, with no computation whatsoever needed. Moreover, in contrast with 0-to-f beating and feedback loops, here it is possible to lock the comb to $f_{\text{ceo}} = 0$ because the detection does not rely on the comparison of two frequencies, which in turn allows stabilizing the CEP of the whole MHz train.

It was used to stabilize the output MHz train of an oscillator that is similar to ours (90MHz repetition rate, 5nJ pulse energy, <10fs pulse duration) in [142]. The authors measured the CEP stability using a photodiode and a fast oscilloscope, and found a residual noise of $\approx$ 50mrad only.

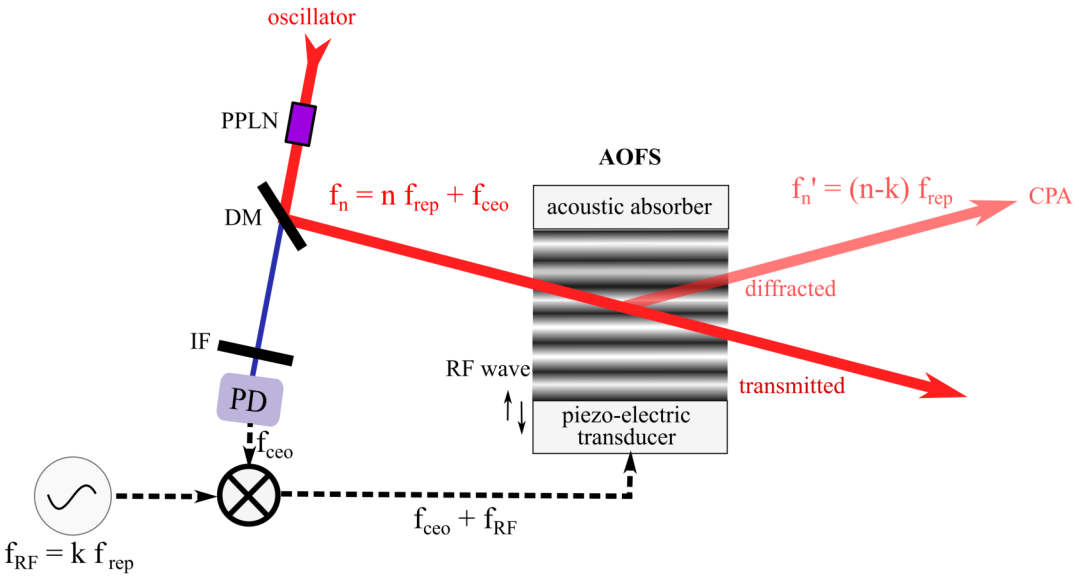

Figure A.1: *Schematic drawing of the CEP stabilization scheme using the AOFS.*

Appendix B

Rotating solid target device and alignment

B.1 Rotating target device

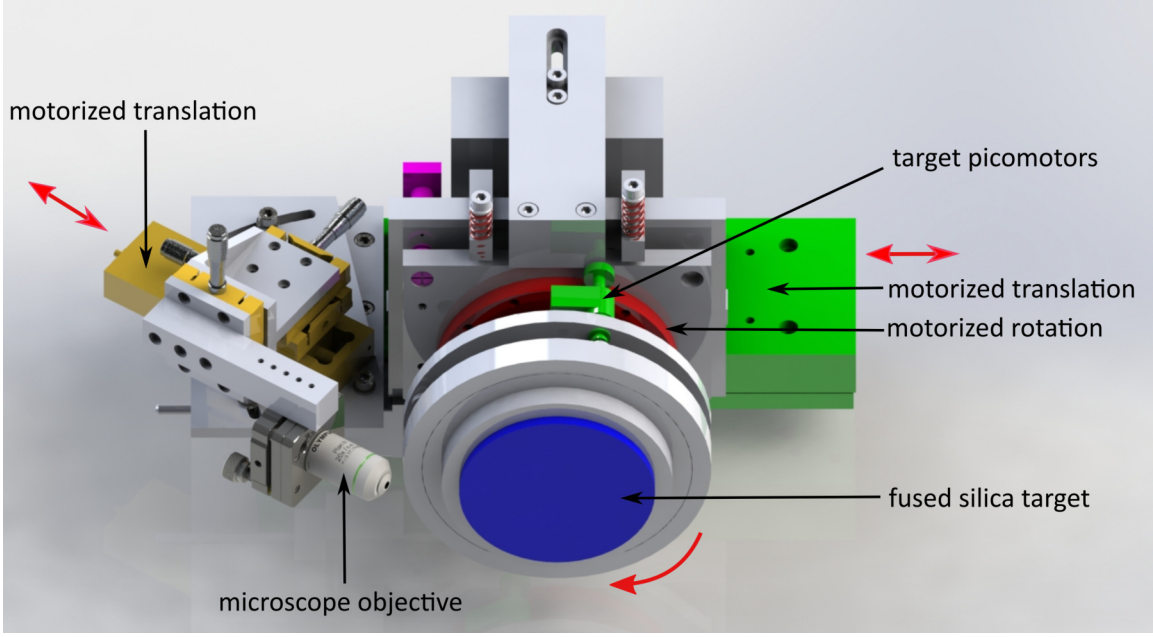

Figure B.1: *3D drawing of the rotating solid target device.*

A rotating target device was developed by Antonin Borot and Rodrigo Lopez-Martens a few years ago in order to provide a clean target surface area for each laser shot while maintaining the same orientation with respect to the laser beam and same position with respect to the beam focus [30]. With a reasonable shot spacing of 100μm, and a 14 cm diameter target, it is possible to make 1.5 million consecutive shots per face, which corresponds to 25 min of continuous operation at 1 kHz. In practice, we would only shoot up to 1,000 sequences of 100 shots per day of experiment and a target could last approximately one month.

The assembly (fig. B.1) sits on a long motorized translation stage moving along the target plane. The target is on a rotating axis and the high torque motor (*Mitsubishi Electric*) sits outside the chamber in order to dissipate heat and reduce vibrations. Its rotation is coupled to the target axis through a mechanical feed-through and double-universal joint connector. There is also a microscope objective on a motorized translational stage moving along the beam propagation direction. One can thus look at the beam profile before, after and in focus, even under vacuum.

B.2 Focal spot imaging

.

We use a ×40 microscope objective (*Olympus UPLFLN40X*) with a 0.51mm working distance to look at the beamprofile in the focal plane. Alternatively, there is a ×20 objective (*Edmund*) to look at the prepulse beamprofile before and after the focal plane and optimize the alignment of the downsizing telescopic lenses to minimize the aberrations.

The objective images the laser intensity distribution in the focal plane onto a CCD camera (*Pixelink PL-B953U*) outside the chamber. The calibration can be done by inserting a grid with a known spacing a in the collimated beam path and looking at the diffraction pattern on the camera. The distance between the central spot and the satellite spots is given by $d = \lambda f/a$, with f the focal length of the OAP.

B.3 Target alignment

In order to align the target surface so as to be perfectly perpendicular to the rotation axis, which is achieved by two tip/tilt picmotors that orient the target plane on the rotating kinematic mount (see fig. B.1), one can first use a pencil-type gauge head placed against the target and a digital electronic amplifier (e.g. a *Millitron* from *Mahr*).

For more precise alignment, we then use a Mach-Zehnder interferometer. A dedicated frequency-stabilized (to increase the coherence length and facilitate obtaining fringes) He-Ne laser is used. The beam is split into two: one is reflected by the target and the other one by a plane metallic mirror. When the two beams recombine on a beamsplitter, spatial interference fringes appear, providing that they are made quasi-collinear. The spacing, drift and tilt of those fringes give us information on the target tip/tilt and depth (fig. B.2). The fringe pattern is recorded on a camera and analyzed in real time with a Labview program, so we can correct the alignment live by adjusting the two tip/tilt picomotors.

The typical residual motion of the target corresponds to horizontal (α_x) and vertical tilts (α_y) ≈ 70 μrad, and the maximum amplitude of depth fluctuations is $\approx$1.5μm (this can only be accurately measured when the chamber is evacuated, though, so we do not systematically check it).

With our typical intensity distribution in focus (see fig. 6.4a), the radius of the beam at $1/e^2$ is 1.3 μm, corresponding to a Rayleigh length $z_R \approx 6.6\mu$m (using eq. 1.38, with a central wavelength of 800nm). Thus, our target is stable enough to make sure that its surface is always in the focal plane of the laser as it rotates.

In practice, replacing the target with a new one and aligning it takes less than an hour, including its stabilization.

B.4 Shutters and shooting sequences

A Labview interface is used to control the target rotation and trigger the shutters' opening, depending on the chosen shot spacing, the sequence length (number of shots per acquisition) and the radial position of the beam on the target. We typically set the shot spacing to 100 μm and the sequence length to 100 ms so that each acquisition is averaged over 100 consecutive laser shots.

Here is what happens during a typical shooting sequence: as we click on "Shoot" on the Labview program, an Arduino micro-controller triggers the slow shutter opening and the target

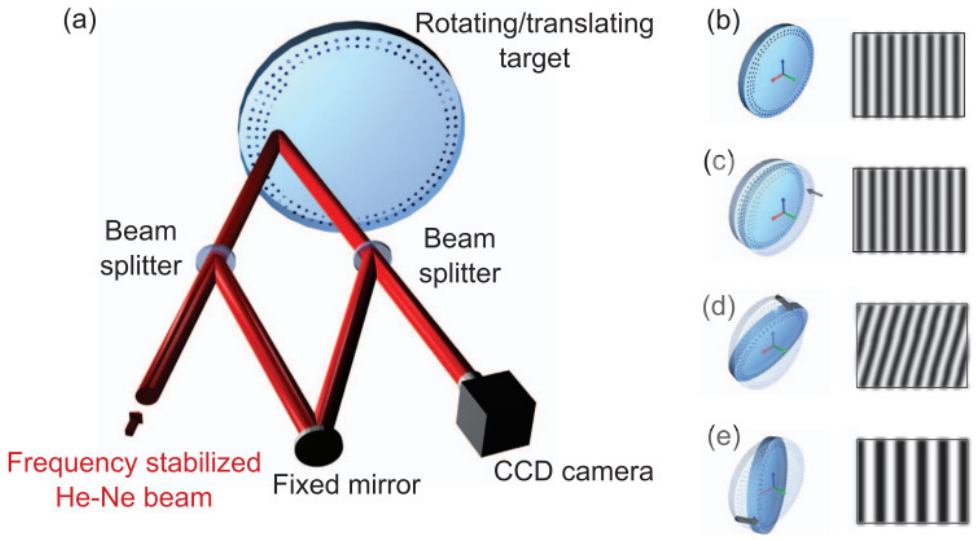

Figure B.2: *Illustration of the alignment procedure with the Mach-Zehnder interferometer. a) 3D representation of the experimental setup, b) reference fringe pattern, c) depth (z) drifts result in a shift of the fringes along the horizontal axis, d) vertical tilts (α_y) of the target induce a tilt of the fringes and e) horizontal tilts (α_x) of the target result in a change in fringe spacing. Image taken from [30]*

motor starts accelerating. Once the rotation motor has reached the right position and speed, it triggers the fast shutter opening and the camera acquisitions (for the diagnostics) a few ms later. After 100ms, the fast shutter closes, the target motor slows down and the slow shutter closes.

Once a full circle at a given radius is completed, we translate the target laterally by $\approx 100\mu$m and repeat the process with a different target rotation speed, which is calculated according to the refreshed, indicated radial position.

Appendix C

Description of the XUV spectrometer

In order to detect the XUV spectrum, we use a concave diffraction grating, allowing to both focus and disperse the light, therefore reducing losses. For gratings with equidistant lines, the spectral images of the entrance slit (in our case, the interaction point on the target) are focused on the Rowland circle [224], which is not convenient as most detectors have a plane surface. A way to circumvent this is to use gratings with non-equally spaced lines (called "flat-field" grating) so as to minimize the defocus in the detector plane. The groove spacing at a distance w from the center of the grating can be expressed as [141]:

$$\sigma(w) = \frac{\sigma_0}{1 + \frac{2b_2}{R}w + \frac{3b_3}{R^2}w^2 + \frac{4b_4}{R^3}w^3}$$

with σ_0 the nominal groove spacing, R the radius of curvature of the grating surface and (b_2, b_3, b_4) the ruling parameters where b_2 is determined to obtain a flat field whereas b_3 and b_4 are chosen to minimize the high-order aberrations in a predetermined wavelength range. Another important feature is that it is a blazed (or echelle) grating *ie* a grating whose lines have a sawtooth-shaped cross section, which helps concentrating most of the energy in the lowest diffraction order [277, 114]. Finally, a gold coating allows reaching an excellent reflectivity of about 90% in the spectral region ranging from 20 to 200 nm for our grazing incidence angle.

Because of the very large angle of incidence on the spherical grating, the imaging is done with a very strong astigmatism: the detector is placed in the tangential focal plane, whereas the saggital focal plane is much further away. As a consequence, the grating only focuses the beam along the diffraction direction and lets it (almost) freely diverge in the vertical dimension, which gives us an idea of the beam divergence.

Our model HITACHI 001-0639 is optimized to detect harmonics between 22 and 124nm in the focal plane. Its active surface is 30 (height) by 50 (width) mm, the radius of curvature is $R = 5649$ mm, the groove spacing at the center is $\sigma_0 = 1/600$mm and the blaze angle of 3.7 ° is optimized for a wavelength of 31 nm. The recommended geometry for its use is shown in figure C.1: the angle of incidence α is 85.3°, the distance from the target is 350 mm, the distance to the spectral plane is 469 mm and the diffraction angles range from $\beta_1 = -67.26°$ for $\lambda = 124$ nm to $\beta_2 = -79.56°$ for $\lambda = 22$ nm. More generally, the diffraction angle is related to the wavelength as follows:

$$m\lambda = \sigma_0(\sin\alpha + \sin\beta) \tag{C.1}$$

$$\Leftrightarrow \quad \beta = \arcsin\left[\frac{m\lambda}{\sigma_0} - \sin\alpha\right] \tag{C.2}$$

with m the diffraction order, and the position along the spectral plane is:

$$L + L_0 = -\frac{469\text{mm}}{\tan\beta} \tag{C.3}$$

A 93 by 75 mm single-stack micro-channel plate (MCP) from *Photonis* then amplifies the signal by creating electrons in avalanche. A pulsed high voltage (1kV) is applied (for 150 ns) every ms at the output of this MCP to selectively amplify the harmonic signal rather than plasma emission. A P46 phosphor screen attached to the back of the plate is biased with a continuous 3 kV voltage (to attract electrons) and converts the electrons into a visible yellow/green light with a maximum emission at 530 nm. The decay of light intensity from 90% to 10% is 300ns, allowing to work at a kilohertz repetition rate while avoiding saturation effects. The phosphor screen is then imaged on a camera (*Pixelfly qe*) placed outside the chamber. This camera has a high-dynamic range (12 bit, 69.5dB), which is important for detecting high harmonics near the cutoff, where the signal quickly drops with the harmonic order. The whole setup is shielded from ambient light using aluminum plates and foils, and an interferometric narrow-band filter at the phosphor emission wavelength is placed in front of the camera.

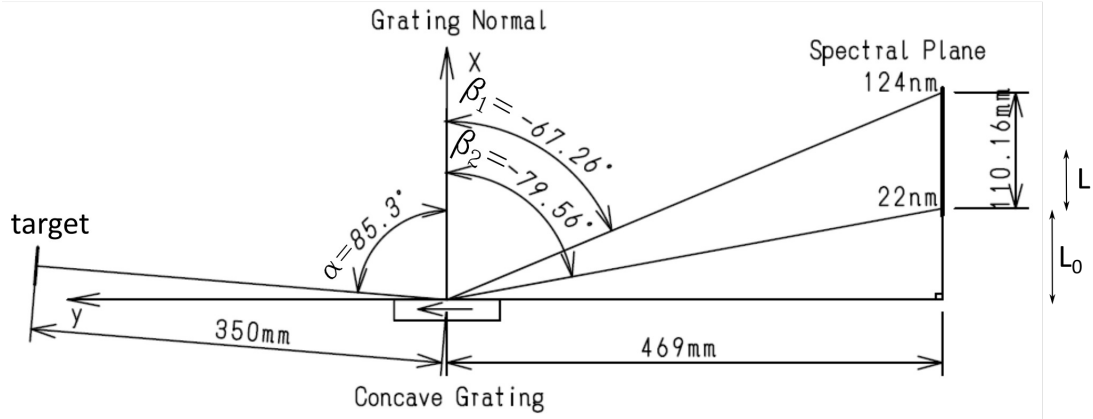

Figure C.1: *Schematic drawing and design specifications of the HITACHI 001-0639 XUV diffraction grating currently used in our setup. Image adapted from the company website (https://www.hitachi-hightech.com).*

XUV spectrum data analysis

Let us only consider the first diffraction order ($m = 1$) and find the expression of the photon energy E (eV) as a function of the position on the detector L using equations C.1 and C.3:

$$E = \frac{hc}{\lambda e} \tag{C.4}$$

$$= \frac{hc}{\sigma_0 e} \times \frac{1}{\sin\alpha - \sin\left(\arctan\left[\frac{469}{L+L_0}\right]\right)} = f(L) \tag{C.5}$$

where h is Planck's constant. Now, let $n + n_0$ be the harmonic order, with n_0 the lowest detected order. The position L_n of the $n + n_0$ order harmonic on the detector is:

$$L_n(n + n_0) = L_n(n) + L_0 = -\frac{469}{\tan\left[\arcsin\left(\frac{\lambda_0}{(n+n_0)\sigma_0} - \sin\alpha\right)\right]}. \tag{C.6}$$

The data analysis consists in first taking a recorded raw image containing as many thin harmonics as possible, integrating it vertically, and finding the positions x_n of the signal maxima along the diffraction direction (fig C.2.a). Then, knowing the camera pixel size, we fit the (x_n, n) curve with $L_n(n)$ (Eq. C.6), which imposes a constant spacing of the harmonics: $\lambda = \lambda_0/(n+n_0)$.

We thus obtain an estimation for the two unknowns n_0 and L_0 (fig C.2.b) and the energy calibration of the whole detector is then easily done using equation C.5. Finally, an additional re-scaling of the signal amplitude is needed (fig C.2.c):

$$\frac{dA}{dE} = \frac{dA}{d\text{px}} \times \frac{d\text{px}}{dE} \tag{C.7}$$

This calibration method is in very good agreement with the one used in [25] where plasma emission lines were used to calibrate the energy axis.

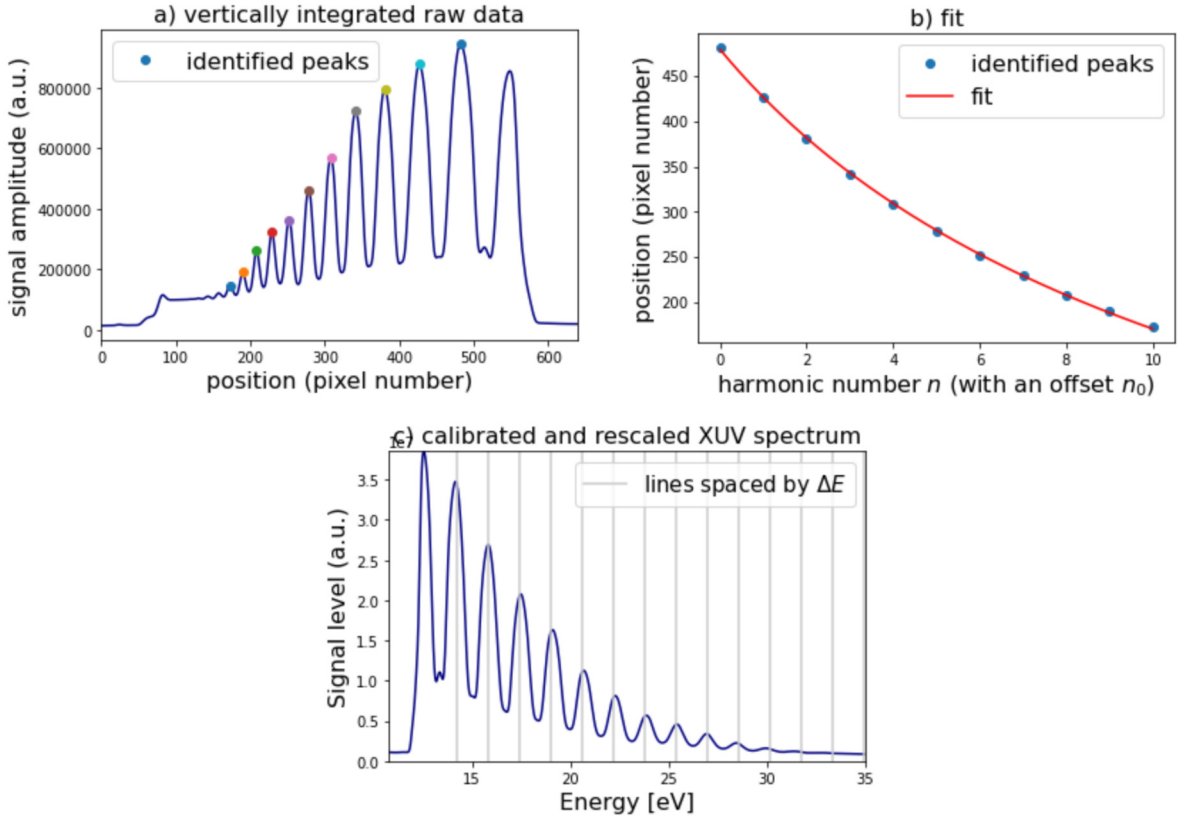

Figure C.2: *Example of XUV spectrometer wavelength calibration procedure. a) vertically integrated raw data, and identification of the harmonic peaks. b) position of the peaks on the camera with respect to their relative harmonic number n (blue dots), and fitting with $L_n(n)$ in Eq. C.6 (red line) to obtain n_0 and L_0. c) Calibrated spectrum.*

Appendix D

Additional information regarding XUV wavefront measurements

D.1 Transmission of Al filters and reflectivity of Si plates

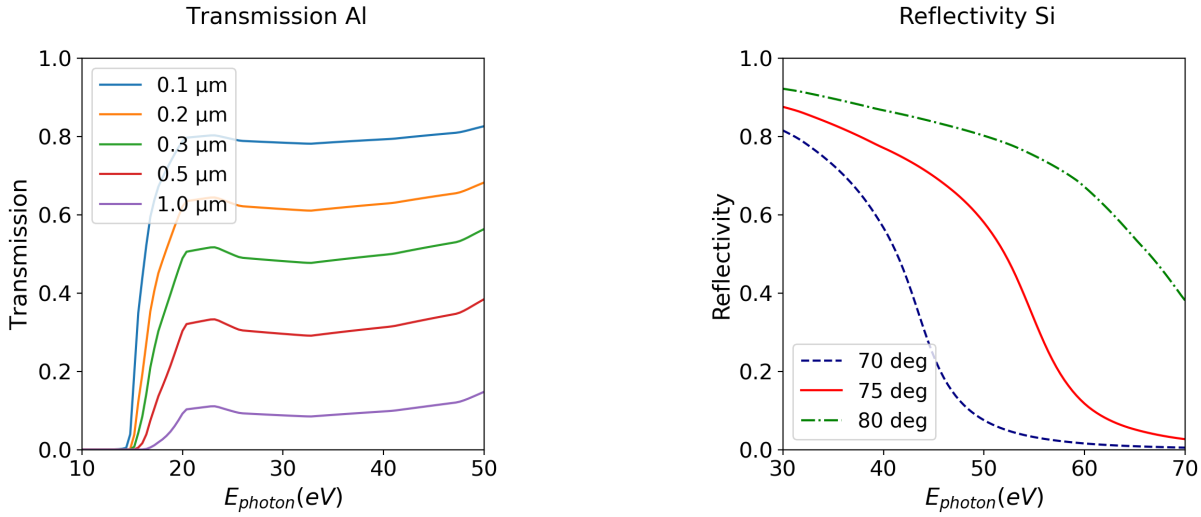

(a) Al filter transmission

(b) Si mirror reflectivity

Figure D.1: *Transmission of thin Al filters and reflectivity of silicon plates (for a p-polarized beam) in the XUV. Data taken from the CXRO website database.*

D.2 Plans for broadband XUV wavefront measurements

A broadband XUV wavefront measurement can be done using silicon plates at 75 degree angle of incidence (fig. D.2.a) to eliminate the p-polarized light at 800nm, as it corresponds to the Brewster angle (fig. D.2.b), while reflecting photons with energies below $\approx$ 50eV (fig. D.1.b.). Combined with Al filters (fig. D.1.a.), this gives a detection range from approximately 20 to 50 eV, which is towards the most energetic harmonics for our experiments.

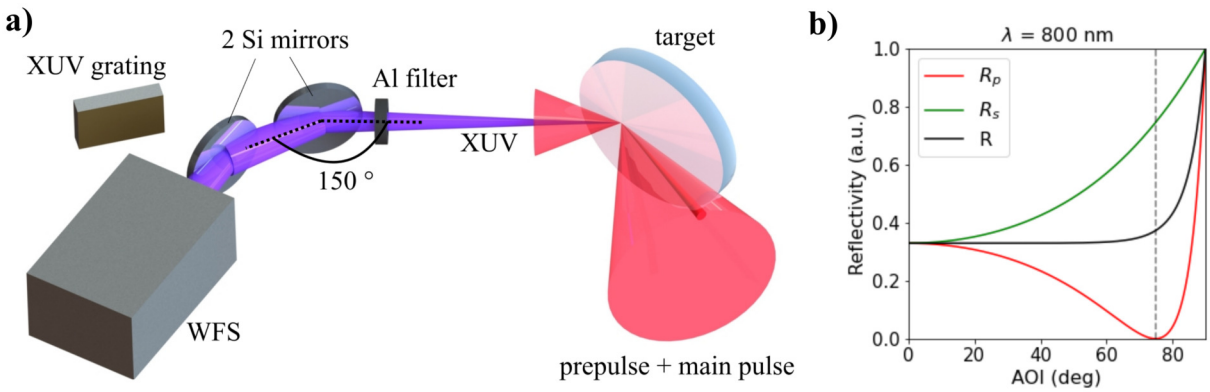

Figure D.2: *a) 3D drawing of the experimental setup for broadband XUV wavefront measurement. Ideally, the Silicon mirrors should be on a motorized translation stage in order to be able to look at the XUV spectrum. b) Reflectivity of silicon at 800nm for S, P and undefined polarization. The minimum (zero) reflectivity for a P-polarized laser is obtained for a 75 degree angle of incidence.*

Appendix E

Electron spatial detection

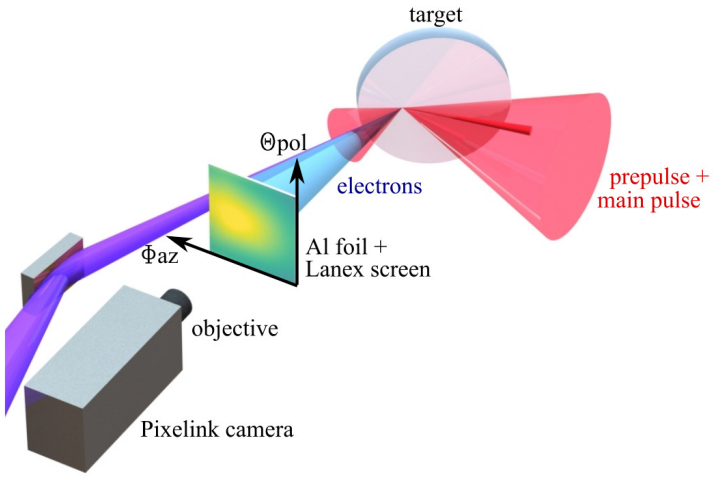

Figure E.1: *Schematic drawing of the experimental setup for spatial electron beam detection. Not shown here are the shielding aluminum box behind the Lanex and the 45 degree plane mirror used between the Lanex screen and the camera.*

For the electron spatial detection, we use a 75mm wide LANEX scintillating phosphor screen (Gd_2O_2S:Tb), which converts electrons into visible light centered at 545nm. The screen is placed between the normal and the specular direction so as to be used simultaneously with the XUV spectrometer. It is located at a distance $\approx$ 20cm from the interaction point and imaged on a camera (*Pixelink PL-B957*) with an objective and an interferometric filter selectively transmitting light around 545nm. In order to place the camera far enough from the screen, as required by the objective, we often had to use a plane metallic mirror at 45° to image it. We also covered the Lanex with a kitchen aluminum foil, so as to block the laser and ambient light, as well as low energy electrons. Low energy electrons are also blocked by the Lanex substrate (a plastic layer) itself, and eventually we only detect electrons with energies above ≈150keV.

To properly calibrate the detector and determine the electron charge as a function of the detected light intensity on the camera, one must take into account the sensor response, the transmission of the objective and the chromatic filter, the reflectivity of the plane mirror, and the overall light collection efficiency. The most precise way to do it is to bring the whole setup as it is, without modifying the distances between the different elements, to a facility where there is a characterized source of electrons, such as a linear electron accelerator (e.g. the ELYSE center or the Photo-injector facility at Laboratoire de l'Accélérateur Linéaire, both part of University Paris-Sud). Alternatively, some researchers use calibration curves found in the literature [37]. Unfortunately, this was not done for the work presented in this manuscript.

Nonetheless, a calibration was done by the previous PhD student ([25], p.110), although for a probably slightly different setup. It is to be noted that this calibration had been done using an electron source with $\approx$ 4MeV (at the Photo-Injector facility) and, whereas the energy deposited in the phosphor layer is independent on the electron energy above $\approx$ 1.5MeV, it varies rapidly below 1.5MeV [106], which is our region of interest. Thus, the calibration is far from trivial and there is still a very large uncertainty on the electron charge measurement. The typical total electron charges per laser shot estimated by F. Böhle were $\approx$30pC for electrons which are correlated with ROM harmonics ($L_g \sim 0.1\lambda$, see [25], p.140) and $\approx$ 90pC for LWFA electrons ($L_g \approx$ a few λ, see [25], p.141), with approximately the same laser parameters ($a_0 \sim 1-3$).

Appendix F

Principle of the electron magnetic spectrometer

The electrons deviation in the vertical plane due to the horizontal magnetic field directly depends on their kinetic energy, therefore each arrival position on the screen corresponds to a given energy and provides the energy spectrum. This can be demonstrated as follows: let us consider an electron of charge $-e$ with a velocity v in a magnetic field $\vec{B}$. It will experience a Lorentz force

$$\vec{F_{Lorentz}} = -e\vec{v} \times \vec{B}.$$

We assume that the electron motion is perfectly perpendicular to the magnetic field and the field is constant, therefore the Lorentz force is equivalent to a centripetal force

$$F_{centripetal} = \frac{\gamma m_e v^2}{R},$$

where R is the radius of curvature and $\gamma^2 = 1/(1 - v^2/c^2)$. We equalize the two forces $F_{Lorentz} = F_{centripetal}$, which gives

$$R = \frac{m_e}{eB}\gamma v = \frac{m_e}{eB}\sqrt{\gamma^2 - 1}c = \frac{m_e c}{eB}\sqrt{(\gamma - 1)(\gamma + 1)}.$$

Then we make the kinetic energy $K = (\gamma - 1)m_e c^2$ appear:

$$R = \frac{m_e c}{eB}\sqrt{\frac{K}{m_e c^2}\left(\frac{K}{m_e c^2} + 2\right)}$$

This can be further simplified using the approximation $m_e c^2 \approx 0.5$ MeV for the electron rest mass energy:

$$R = \frac{2m_e c}{eB}\sqrt{K(K+1)} \approx \frac{\sqrt{K(K+1)}}{0.3B},$$

with K in MeV, R in mm and B in Tesla.

Finally, one can calculate the angle of deflection θ_e (see fig F.1):

$$\tan\theta_e = \left(\frac{R^2 - R_a^2}{2RR_a}\right)$$

Therefore, the point P coordinates are:

$$\begin{cases} x_P = \dfrac{2R}{1 + R^2/R_a^2} \\ y_P = \dfrac{2R_a}{1 + R_a^2/R^2} \end{cases}$$

Assuming that the detector is located at a distance D_y from the center of the magnets, the electron reaches the detector at a point N, whose coordinates are:

$$\begin{cases} x_n = x_P + \dfrac{D_y - y_P}{\tan(\theta_e)} \\ y_n = D_y \end{cases}$$

Finally, the position x_n along the detector vertical direction only depends on the kinetic energy K.

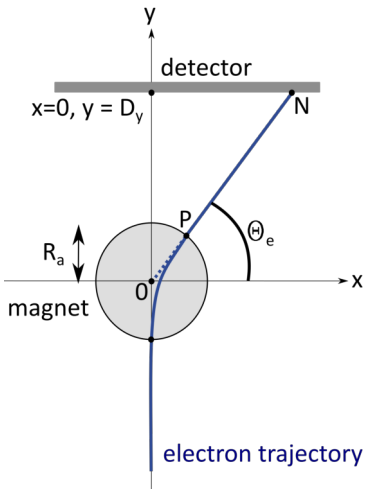

Figure F.1: *schematic drawing of the electron trajectory deviation due to the magnetic field (side view).*

Appendix G

Calibration of the Time Of Flight detector

The calibration of the small MCP used as a TOF detector was done in Tel Aviv by Eyal Kroupp, so as to determine the total emitted proton charge per shot. A calibration system [96] was designed there to reproduce the experimental conditions in *Salle Noire 2*, so that the signals obtained on the MCP were similar to those obtained during the experiments, in terms of voltage and pulse width. The reason behind this is that the amplification factor of the detector may depend on the electron signal level and duration, e.g due to saturation effects. A source of electrons (a carbon brush) is triggered by a pulsed high voltage. The emitted electrons then reach the MCP and two Faraday cups, positioned on each side of the MCP to verify the radial homogeneity. The Faraday cup, which is a metal (conductive) cup, catches the charged particles. The resulting current is measured and used to determine the number of electrons hitting the cup. The signals from the Faraday cups and the MCP are simultaneously recorded and compared. The factor that needs to be applied to the Faraday cup signal for it to fit the MCP signal best determines the amplification factor of the MCP, which was found to be 3 ± 0.3.

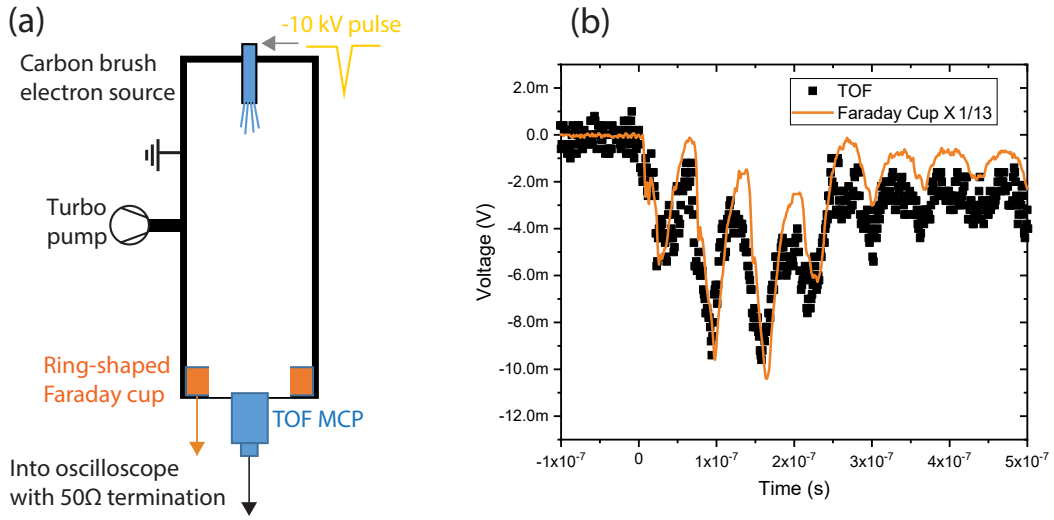

Figure G.1: *Calibration of the TOF detector. a) experimental setup for the calibration. b) measured signals with the faraday cup and the TOF detector. Figure courtesy of Eyal Kroupp.*

Appendix H

Additional experimental results

This Appendix contains additional experimental measurements of secondary emission beams from plasma mirrors.

H.1 XUV beam: gradient scale length scan

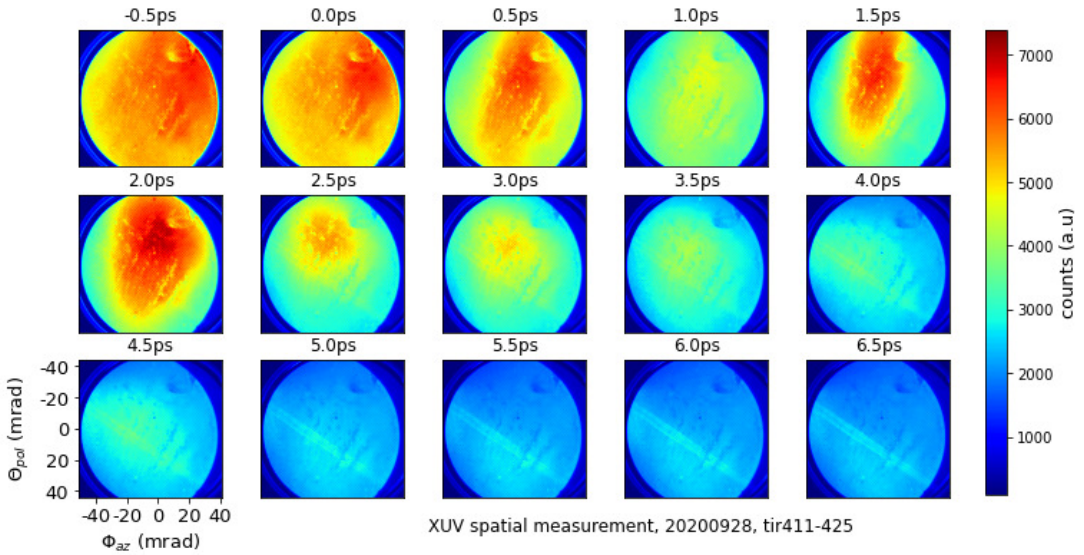

Figure H.1: *Spatial XUV beam measured for different prepulse delays. Data set number 2.*

H.2 CEP-dependent electron beam

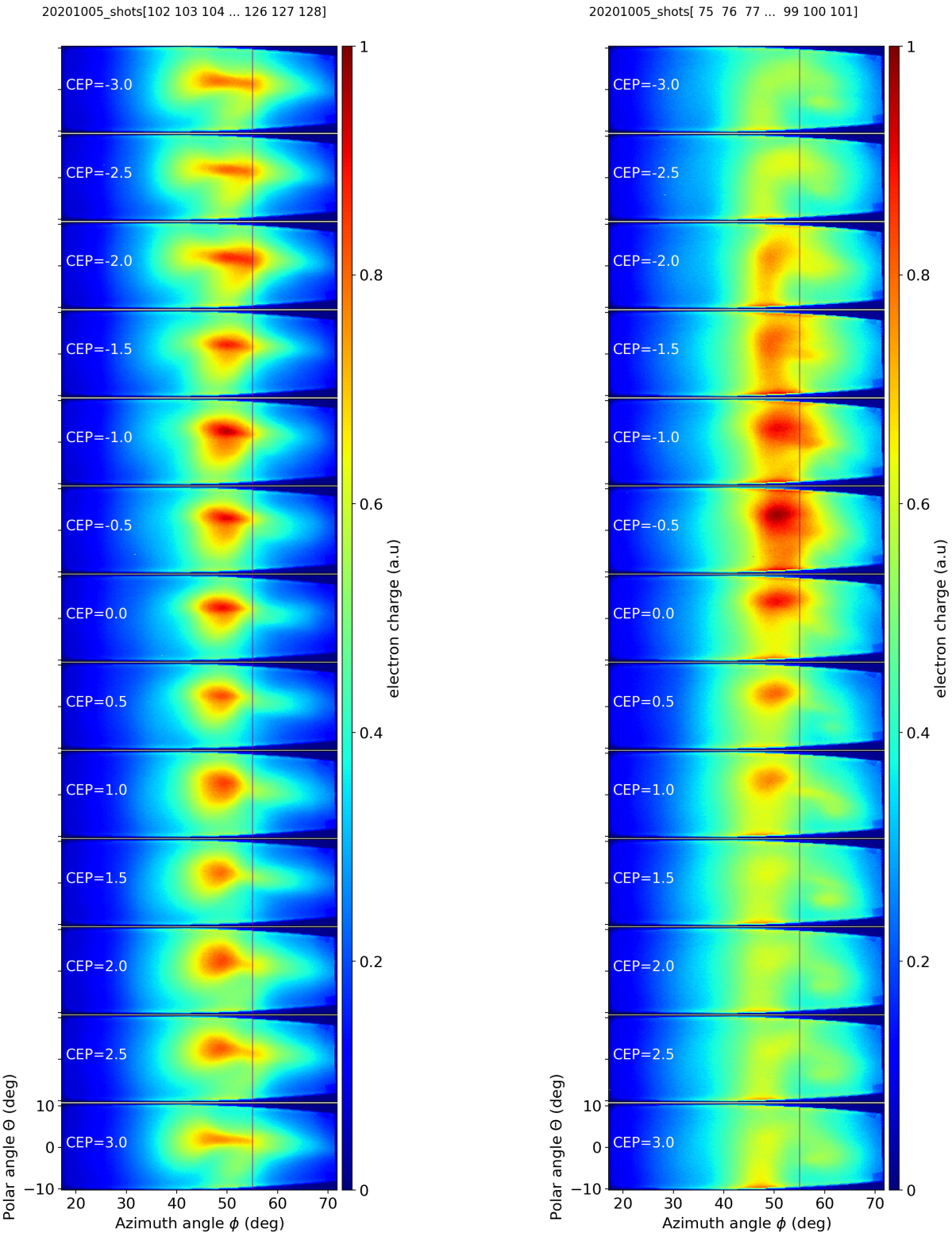

(a) *2ps prepulse delay*

(b) *3ps prepulse delay*

Figure H.2: *Two consecutive randomized CEP scans of the electron beamprofile for a 2 and 3 ps prepulse lead time, respectively. The data are shown for CEPs from -3 rad (top) to +3 rad (bottom) in steps of 0.5 rad. The thin vertical purple line indicates the laser specular direction* $\phi_{az} = 55°$.

H.3 Gouy phase shift around the focus at fixed CEP

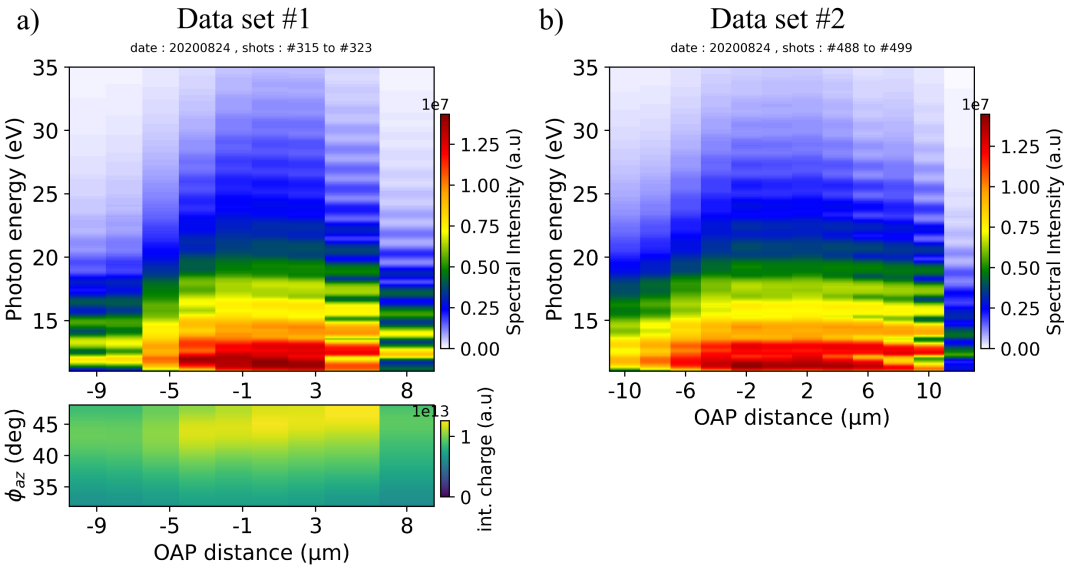

Figure H.3: *a) Integrated harmonic signal (top) and electron distribution (bottom) as we vary the OAP distance with respect to the target. b) Second data set with the integrated harmonic signal from the same day. The prepulse delay was set to -3ps. Positive OAP position values mean that the distance between the OAP and the target was decreased. The CEP was actively stabilized to a constant arbitrary value.*

H.4 LWFA of electrons at very long gradients

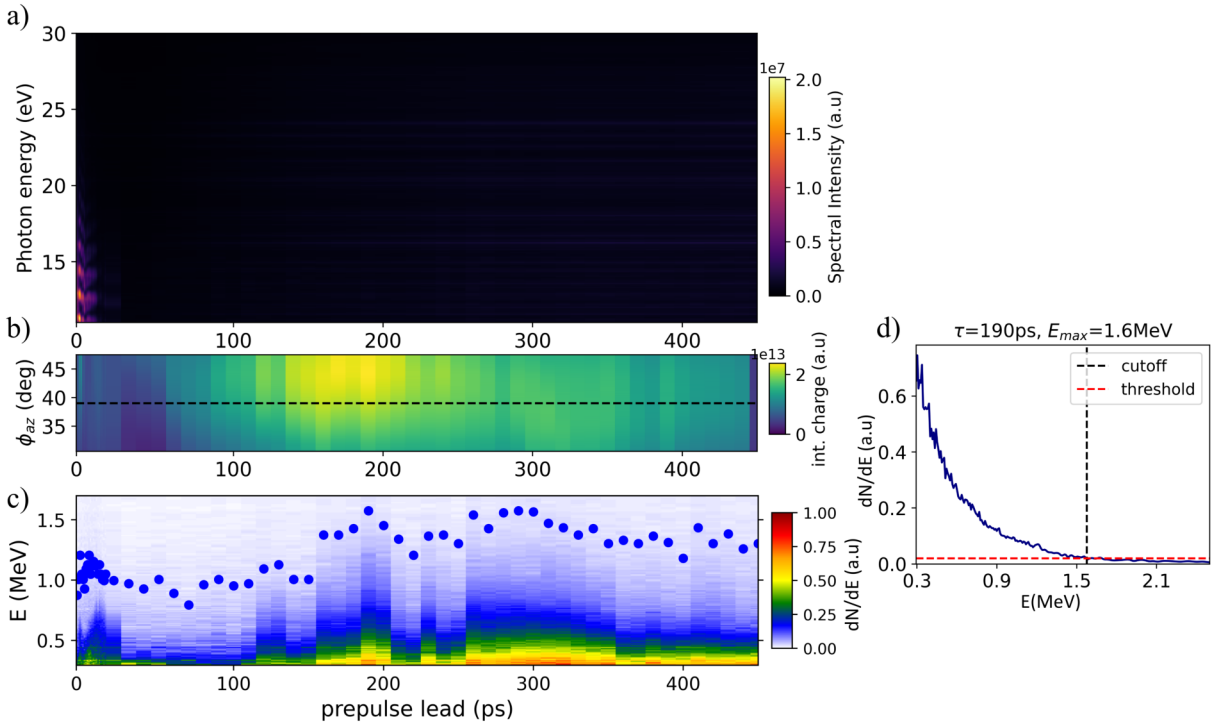

Figure H.4: *Gradient scan for a 6.1 fs duration. a) vertically integrated harmonic spectra. b) electron spatial distribution along the azimuthal direction. c) electron spectra measured at $\phi_{az} = 39°$ in color-scale, and electron cutoff energy represented with blue dots. d) electron spectrum at a 190 ps prepulse lead time, showing how the cutoff energy is defined. Scans a) and b) were acquired simultaneously whereas scan c) is a different data set from the same day (01.07.2020).*

Bibliography

[1] NIST atomic spectra database. URL= "www.physics.nist.gov".

[2] R. Abrams. Coupling losses in hollow waveguide laser resonators. *IEEE Journal of Quantum Electronics*, 8(11):838–843, 1972.

[3] K. Adumi, K. A. Tanaka, T. Matsuoka, T. Kurahashi, T. Yabuuchi, Y. Kitagawa, R. Kodama, K. Sawai, K. Suzuki, K. Okabe, T. Sera, T. Norimatsu, and Y. Izawa. Characterization of preplasma produced by an ultrahigh intensity laser system. *Physics of Plasmas*, 11(8):3721–3725, 2004.

[4] G. P. Agrawal. *Nonlinear fiber optics*. Optics and photonics. Academic Press, San Diego, 1989.

[5] S. Akturk, X. Gu, P. Bowlan, and R. Trebino. Spatio-temporal couplings in ultrashort laser pulses. *Journal of Optics*, 12(9):093001, aug 2010.

[6] F. Albert and A. G. R. Thomas. Applications of laser wakefield accelerator-based light sources. *Plasma Physics and Controlled Fusion*, 58(10):103001, sep 2016.

[7] O. Albert, H. Wang, D. Liu, Z. Chang, and G. Mourou. Generation of relativistic intensity pulses at a kilohertz repetition rate. *Opt. Lett.*, 25(15):1125–1127, Aug 2000.

[8] B. Alonso, M. Miranda, I. nigo J. Sola, and H. Crespo. Spatiotemporal characterization of few-cycle laser pulses. *Opt. Express*, 20(16):17880–17893, Jul 2012.

[9] B. Alonso, M. Miranda, F. Silva, V. Pervak, J. Rauschenberger, J. San Román, Í. J. Sola, and H. Crespo. Characterization of sub-two-cycle pulses from a hollow-core fiber compressor in the spatiotemporal and spatiospectral domains. *Applied Physics B*, 112(1):105–114, Aug 2013.

[10] D. an der Brügge and A. Pukhov. Propagation of relativistic surface harmonics radiation in free space. *Physics of Plasmas*, 14(9):093104, 2007.

[11] D. an der Brügge and A. Pukhov. Enhanced relativistic harmonics by electron nanobunching. *Physics of Plasmas*, 17(3):033110, 2010.

[12] S. Backus, H. C. Kapteyn, M. M. Murnane, D. M. Gold, H. Nathel, and W. White. Prepulse suppression for high-energy ultrashort pulses using self-induced plasma shuttering from a fluid target. *Opt. Lett.*, 18(2):134–136, Jan 1993.

[13] T. Baeva, S. Gordienko, and A. Pukhov. Relativistic plasma control for single attosecond x-ray burst generation. *Phys. Rev. E*, 74:065401, Dec 2006.

[14] T. Baeva, S. Gordienko, and A. Pukhov. Theory of high-order harmonic generation in relativistic laser interaction with overdense plasma. *Phys. Rev. E*, 74:046404, Oct 2006.

[15] V. Bagnoud and F. Salin. Global optimization of pulse compression in chirped pulse amplification. *IEEE Journal of Selected Topics in Quantum Electronics*, 4(2):445–448, 1998.

[16] A. Baltuška, T. Fuji, and T. Kobayashi. Controlling the carrier-envelope phase of ultrashort light pulses with optical parametric amplifiers. *Phys. Rev. Lett.*, 88:133901, Mar 2002.

[17] A. Baltuska, M. Uiberacker, E. Goulielmakis, R. Kienberger, V. Yakovlev, T. Udem, T. Hansch, and F. Krausz. Phase-controlled amplification of few-cycle laser pulses. *IEEE Journal of Selected Topics in Quantum Electronics*, 9(4):972–989, 2003.

[18] C. Bamber, S. J. Boege, T. Koffas, T. Kotseroglou, A. C. Melissinos, D. D. Meyerhofer, D. A. Reis, W. Ragg, C. Bula, K. T. McDonald, E. J. Prebys, D. L. Burke, R. C. Field, G. Horton-Smith, J. E. Spencer, D. Walz, S. C. Berridge, W. M. Bugg, K. Shmakov, and A. W. Weidemann. Studies of nonlinear qed in collisions of 46.6 gev electrons with intense laser pulses. *Phys. Rev. D*, 60:092004, Oct 1999.

[19] D. Bauer and P. Mulser. Exact field ionization rates in the barrier-suppression regime from numerical time-dependent schrödinger-equation calculations. *Phys. Rev. A*, 59:569–577, Jan 1999.

[20] B. Bergues, D. E. Rivas, M. Weidman, A. A. Muschet, W. Helml, A. Guggenmos, V. Pervak, U. Kleineberg, G. Marcus, R. Kienberger, D. Charalambidis, P. Tzallas, H. Schröder, F. Krausz, and L. Veisz. Tabletop nonlinear optics in the 100-ev spectral region. *Optica*, 5(3):237–242, Mar 2018.

[21] M. Bocoum. *Harmonic and electron generation from laser-driven plasma mirrors.* PhD thesis, 2016. Thèse de doctorat dirigée par Lopez-Martens, Rodrigo Physique des plasmas Université Paris-Saclay (ComUE) 2016.

[22] M. Bocoum, F. Böhle, A. Vernier, A. Jullien, J. Faure, and R. Lopez-Martens. Spatial-domain interferometer for measuring plasma mirror expansion. *Opt. Lett.*, 40(13):3009–3012, Jul 2015.

[23] M. Bocoum, M. Thévenet, F. Böhle, B. Beaurepaire, A. Vernier, A. Jullien, J. Faure, and R. Lopez-Martens. Anticorrelated emission of high harmonics and fast electron beams from plasma mirrors. *Phys. Rev. Lett.*, 116:185001, May 2016.

[24] F. Böhle. Building a source of relativistic intensity few-optical-cycle laser pulses. Master's thesis, 2013.

[25] F. Böhle. *Near-single-cycle laser for driving relativistic plasma mirrors at kHz repetition rate - development and application.* PhD thesis, 2017. Thèse de doctorat dirigée par Rousse, Antoine et Lopez-Martens, Rodrigo Physique quantique Université Paris-Saclay (ComUE) 2017.

[26] F. Böhle, M. Kretschmar, A. Jullien, M. Kovacs, M. Miranda, R. Romero, H. Crespo, U. Morgner, P. Simon, R. Lopez-Martens, and T. Nagy. Compression of CEP-stable multi-mJ laser pulses down to 4 fs in long hollow fibers. *Laser Physics Letters*, 11(9):095401, jun 2014.

[27] F. Böhle, M. Thévenet, M. Bocoum, A. Vernier, S. Haessler, and R. Lopez-Martens. Generation of XUV spectral continua from relativistic plasma mirrors driven in the near-single-cycle limit. *Journal of Physics: Photonics*, 2(3):034010, jul 2020.

[28] P. Bolton, M. Borghesi, C. Brenner, D. Carroll, C. De Martinis, F. Fiorini, A. Flacco, V. Floquet, J. Fuchs, P. Gallegos, D. Giove, J. Green, S. Green, B. Jones, D. Kirby, P. McKenna, D. Neely, F. Nuesslin, R. Prasad, S. Reinhardt, M. Roth, U. Schramm, G. Scott, S. Ter-Avetisyan, M. Tolley, G. Turchetti, and W. JJ. Instrumentation for diagnostics and control of laser-accelerated proton (ion) beams. *Physica Medica*, 30(3):255–270, May 2014.

[29] M. Borghesi, A. Schiavi, D. H. Campbell, M. G. Haines, O. Willi, A. J. Mackinnon, P. Patel, M. Galimberti, and L. A. Gizzi. Proton imaging detection of transient electromagnetic fields in laser-plasma interactions (invited). *Review of Scientific Instruments*, 74(3):1688–1693, 2003.

[30] A. Borot, D. Douillet, G. Iaquaniello, T. Lefrou, P. Audebert, J.-P. Geindre, and R. Lopez-Martens. High repetition rate plasma mirror device for attosecond science. *Review of Scientific Instruments*, 85(1):013104, 2014.

[31] A. Borot, A. Malvache, X. Chen, A. Jullien, J.-P. Geindre, P. Audebert, G. Mourou, F. Quéré, and R. Lopez-Martens. Attosecond control of collective electron motion in plasmas. *Nature Physics*, 8(5):416–421, May 2012.

[32] A. Borot and F. Quéré. Spatio-spectral metrology at focus of ultrashort lasers: a phase-retrieval approach. *Opt. Express*, 26(20):26444–26461, Oct 2018.

[33] R. W. Boyd. *Nonlinear Optics, Third edition.* Academic Press, Inc., 2008.

[34] T. Brabec and F. Krausz. Nonlinear optical pulse propagation in the single-cycle regime. *Phys. Rev. Lett.*, 78:3282–3285, Apr 1997.

[35] F.-E. Brack, F. Kroll, L. Gaus, C. Bernert, E. Beyreuther, T. E. Cowan, L. Karsch, S. Kraft, L. A. Kunz-Schughart, E. Lessmann, J. Metzkes-Ng, L. Obst-Huebl, J. Pawelke, M. Rehwald, H.-P. Schlenvoigt, U. Schramm, M. Sobiella, E. R. Szabó, T. Ziegler, and K. Zeil. Spectral and spatial shaping of laser-driven proton beams using a pulsed high-field magnet beamline. *Scientific Reports*, 10(1):9118, Jun 2020.

[36] F. Brunel. Not-so-resonant, resonant absorption. *Phys. Rev. Lett.*, 59:52–55, Jul 1987.

[37] A. Buck, K. Zeil, A. Popp, K. Schmid, A. Jochmann, S. D. Kraft, B. Hidding, T. Kudyakov, C. M. S. Sears, L. Veisz, S. Karsch, J. Pawelke, R. Sauerbrey, T. Cowan, F. Krausz, and U. Schramm. Absolute charge calibration of scintillating screens for relativistic electron detection. *Review of Scientific Instruments*, 81(3):033301, 2010.

[38] R. Budriūnas, T. Stanislauskas, J. Adamonis, A. Aleknavičius, G. Veitas, D. Gadonas, S. Balickas, A. Michailovas, and A. Varanavičius. 53 w average power cep-stabilized opcpa system delivering 5.5 tw few cycle pulses at 1 khz repetition rate. *Opt. Express*, 25(5):5797–5806, Mar 2017.

[39] S. Bulanov, N. Naumova, F. Pegoraro, and J. Sakai. Particle injection into the wave acceleration phase due to nonlinear wake wave breaking. *Phys. Rev. E*, 58:R5257–R5260, Nov 1998.

[40] S. V. Bulanov, T. Esirkepov, and T. Tajima. Light intensification towards the schwinger limit. *Phys. Rev. Lett.*, 91:085001, Aug 2003.

[41] S. V. Bulanov, N. M. Naumova, and F. Pegoraro. Interaction of an ultrashort, relativistically strong laser pulse with an overdense plasma. *Physics of Plasmas*, 1(3):745–757, 1994.

[42] N. H. Burnett, H. A. Baldis, M. C. Richardson, and G. D. Enright. Harmonic generation in co2 laser target interaction. *Applied Physics Letters*, 31(3):172–174, 1977.

[43] F. Calegari, D. Ayuso, A. Trabattoni, L. Belshaw, S. D. Camillis, S. Anumula, F. Frassetto, L. Poletto, A. Palacios, P. Decleva, J. B. Greenwood, F. Martín, and M. Nisoli. Ultrafast electron dynamics in phenylalanine initiated by attosecond pulses. *Science*, 346(6207):336–339, 2014.

[44] L. Canova. *Generation and shaping of ultra-short, ultra-high contrast pulses for high repetition rate relativistic optics*. PhD thesis, 2009. Thèse de doctorat dirigée par Lopez-Martens, Rodrigo Physique Palaiseau, Ecole polytechnique 2009.

[45] L. Canova, S. Kourtev, N. Minkovski, A. Jullien, R. Lopez-Martens, O. Albert, and S. M. Saltiel. Efficient generation of cross-polarized femtosecond pulses in cubic crystals with holographic cut orientation. *Applied Physics Letters*, 92(23):231102, 2008.

[46] D. E. Cardenas, T. M. Ostermayr, L. Di Lucchio, L. Hofmann, M. F. Kling, P. Gibbon, J. Schreiber, and L. Veisz. Sub-cycle dynamics in relativistic nanoplasma acceleration. *Scientific Reports*, 9(1):7321, May 2019.

[47] Z. Chang. Carrier-envelope phase shift caused by grating-based stretchers and compressors. *Appl. Opt.*, 45(32):8350–8353, Nov 2006.

[48] S. Chatziathanasiou, S. Kahaly, E. Skantzakis, G. Sansone, R. Lopez-Martens, S. Haessler, K. Varju, G. D. Tsakiris, D. Charalambidis, and P. Tzallas. Generation of attosecond light pulses from gas and solid state media. *Photonics*, 4(2), 2017.

[49] M. Chen, E. Esarey, C. B. Schroeder, C. G. R. Geddes, and W. P. Leemans. Theory of ionization-induced trapping in laser-plasma accelerators. *Physics of Plasmas*, 19(3):033101, 2012.

[50] X. Chen, A. Jullien, A. Malvache, L. Canova, A. Borot, A. Trisorio, C. G. Durfee, and R. Lopez-Martens. Generation of 4.3 fs, 1 mj laser pulses via compression of circularly polarized pulses in a gas-filled hollow-core fiber. *Opt. Lett.*, 34(10):1588–1590, May 2009.

[51] G. Chériaux. *Influences des distorsions de phase sur le profil d'impulsions femtosecondes dans l'amplification a de rude frequence. Application à la generation d'impulsions de 30 TW a 10 Hz dans le saphir dopé au titane*. PhD thesis, 1997. Thèse de doctorat dirigée par Salin, François Physique Paris 11 1997.

[52] W. Cho, J.-u. Shin, and K. T. Kim. Reconstruction algorithm for tunneling ionization with a perturbation for the time-domain observation of an electric-field. *Scientific Reports*, 11(1):13014, Jun 2021.

[53] L. Chopineau. *Physique attoseconde relativiste sur miroirs plasmas*. PhD thesis, 2019. Thèse de doctorat dirigée par Quéré, Fabien Physique des plasmas Université Paris-Saclay (ComUE) 2019.

[54] L. Chopineau, G. Blaclard, A. Denoeud, H. Vincenti, F. Quéré, and S. Haessler. Sub-laser-cycle control of relativistic plasma mirrors. *Phys. Rev. Research*, 4:L012030, Mar 2022.

[55] L. Chopineau, A. Denoeud, A. Leblanc, E. Porat, P. Martin, H. Vincenti, and F. Quéré. Spatio-temporal characterization of attosecond pulses from plasma mirrors. *Nature Physics*, 17(8):968–973, Aug 2021.

[56] L. Chopineau, A. Leblanc, G. Blaclard, A. Denoeud, M. Thévenet, J.-L. Vay, G. Bonnaud, P. Martin, H. Vincenti, and F. Quéré. Identification of coupling mechanisms between ultraintense laser light and dense plasmas. *Phys. Rev. X*, 9:011050, Mar 2019.

[57] A. Cingöz, D. C. Yost, T. K. Allison, A. Ruehl, M. E. Fermann, I. Hartl, and J. Ye. Direct frequency comb spectroscopy in the extreme ultraviolet. *Nature*, 482(7383):68–71, Feb 2012.

[58] A. Comby, D. Descamps, S. Beauvarlet, A. Gonzalez, F. Guichard, S. Petit, Y. Zaouter, and Y. Mairesse. Cascaded harmonic generation from a fiber laser: a milliwatt xuv source. *Opt. Express*, 27(15):20383–20396, Jul 2019.

[59] P. B. Corkum. Plasma perspective on strong field multiphoton ionization. *Phys. Rev. Lett.*, 71:1994–1997, Sep 1993.

[60] P. B. Corkum and F. Krausz. Attosecond science. *Nature Physics*, 3(6):381–387, Jun 2007.

[61] D. E. Couch, D. D. Hickstein, D. G. Winters, S. J. Backus, M. S. Kirchner, S. R. Domingue, J. J. Ramirez, C. G. Durfee, M. M. Murnane, and H. C. Kapteyn. Ultrafast 1 mhz vacuum-ultraviolet source via highly cascaded harmonic generation in negative-curvature hollow-core fibers. *Optica*, 7(7):832–837, Jul 2020.

[62] S. T. Cundiff. Phase stabilization of ultrashort optical pulses. *Journal of Physics D: Applied Physics*, 35(8):R43–R59, apr 2002.

[63] R. Deiterding, R. Glowinski, H. Oliver, and S. Poole. A reliable split-step fourier method for the propagation equation of ultra-fast pulses in single-mode optical fibers. *Journal of Lightwave Technology*, 31, 06 2013.

[64] N. B. Delone and V. P. Krainov. Tunneling and barrier-suppression ionization of atoms and ions in a laser radiation field. *Physics-Uspekhi*, 41(5):469–485, may 1998.

[65] N. Didenko, A. Konyashchenko, A. Lutsenko, and S. Tenyakov. Contrast degradation in a chirped-pulse amplifier due to generation of prepulses by postpulses. *Opt. Express*, 16(5):3178–3190, Mar 2008.

[66] F. Dollar, P. Cummings, V. Chvykov, L. Willingale, M. Vargas, V. Yanovsky, C. Zulick, A. Maksimchuk, A. G. R. Thomas, and K. Krushelnick. Scaling high-order harmonic generation from laser-solid interactions to ultrahigh intensity. *Phys. Rev. Lett.*, 110:175002, Apr 2013.

[67] L. Drescher and O. Kornilov. Extreme-ultraviolet refractive optics. *Nature*, 564:91–94, 2018.

[68] M. Drescher, M. Hentschel, R. Kienberger, M. Uiberacker, V. Yakovlev, A. Scrinzi, T. Westerwalbesloh, U. Kleineberg, U. Heinzmann, and F. Krausz. Time-resolved atomic inner-shell spectroscopy. *Nature*, 419(6909):803–807, Oct 2002.

[69] B. Dromey, D. Adams, R. Hörlein, Y. Nomura, S. G. Rykovanov, D. C. Carroll, P. S. Foster, S. Kar, K. Markey, P. McKenna, D. Neely, M. Geissler, G. D. Tsakiris, and M. Zepf. Diffraction-limited performance and focusing of high harmonics from relativistic plasmas. *Nature Physics*, 5(2):146–152, Feb 2009.

[70] B. Dromey, S. Kar, C. Bellei, D. C. Carroll, R. J. Clarke, J. S. Green, S. Kneip, K. Markey, S. R. Nagel, P. T. Simpson, L. Willingale, P. McKenna, D. Neely, Z. Najmudin, K. Krushelnick, P. A. Norreys, and M. Zepf. Bright multi-kev harmonic generation from relativistically oscillating plasma surfaces. *Phys. Rev. Lett.*, 99:085001, Aug 2007.

[71] B. Dromey, S. Rykovanov, and S. Yeung. Coherent synchrotron emission from electron nanobunches formed in relativistic laser plasma interactions. *Nature Physics*, 8:804–808, 2012.

[72] F. Druon, M. Hanna, G. Lucas-Leclin, Y. Zaouter, D. Papadopoulos, and P. Georges. Simple and general method to calculate the dispersion properties of complex and aberrated stretchers-compressors. *J. Opt. Soc. Am. B*, 25(5):754–762, May 2008.

[73] J. Duris, S. Li, T. Driver, E. G. Champenois, J. P. MacArthur, A. A. Lutman, Z. Zhang, P. Rosenberger, J. W. Aldrich, R. Coffee, G. Coslovich, F.-J. Decker, J. M. Glownia, G. Hartmann, W. Helml, A. Kamalov, J. Knurr, J. Krzywinski, M.-F. Lin, J. P. Marangos, M. Nantel, A. Natan, J. T. O'Neal, N. Shivaram, P. Walter, A. L. Wang, J. J. Welch, T. J. A. Wolf, J. Z. Xu, M. F. Kling, P. H. Bucksbaum, A. Zholents, Z. Huang, J. P. Cryan, and A. Marinelli. Tunable isolated attosecond x-ray pulses with gigawatt peak power from a free-electron laser. *Nature Photonics*, 14(1):30–36, Jan 2020.

[74] E. Esarey, C. B. Schroeder, and W. P. Leemans. Physics of laser-driven plasma-based electron accelerators. *Rev. Mod. Phys.*, 81:1229–1285, Aug 2009.

[75] E. Escoto, A. Tajalli, T. Nagy, and G. Steinmeyer. Advanced phase retrieval for dispersion scan: a comparative study. *J. Opt. Soc. Am. B*, 35(1):8–19, Jan 2018.

[76] T. Esirkepov, M. Borghesi, S. V. Bulanov, G. Mourou, and T. Tajima. Highly efficient relativistic-ion generation in the laser-piston regime. *Phys. Rev. Lett.*, 92:175003, Apr 2004.

[77] D. Fabris. *Ultrafast light sources and methods for attosecond pump-probe experiments*. PhD thesis, 2015.

[78] G. Farkas and C. Tóth. Proposal for attosecond light pulse generation using laser induced multiple-harmonic conversion processes in rare gases. *Physics Letters A*, 168(5):447–450, 1992.

[79] J. Faure. Plasma injection schemes for laser-plasma accelerators. *Proceedings of the 2014 CAS-CERN Accelerator School: Plasma Wake Acceleration*, 1, February 2016.

[80] J. Faure, Y. Glinec, A. Pukhov, S. Kiselev, S. Gordienko, E. Lefebvre, J.-P. Rousseau, F. Burgy, and V. Malka. A laser–plasma accelerator producing monoenergetic electron beams. *Nature*, 431(7008):541–544, Sep 2004.

[81] J. Faure, D. Gustas, D. Guénot, A. Vernier, F. Böhle, M. Ouillé, S. Haessler, R. Lopez-Martens, and A. Lifschitz. A review of recent progress on laser-plasma acceleration at kHz repetition rate. *Plasma Physics and Controlled Fusion*, 61(1):014012, nov 2018.

[82] L. Fedeli, A. Sainte-Marie, N. Zaïm, M. Thévenet, J. L. Vay, A. Myers, F. Quéré, and H. Vincenti. Probing strong-field qed with doppler-boosted petawatt-class lasers. *Phys. Rev. Lett.*, 127:114801, Sep 2021.

[83] C. Feng, J.-F. Hergott, P.-M. Paul, X. Chen, O. Tcherbakoff, M. Comte, O. Gobert, M. Reduzzi, F. Calegari, C. Manzoni, M. Nisoli, and G. Sansone. Complete analog control of the carrier-envelope-phase of a high-power laser amplifier. *Opt. Express*, 21(21):25248–25256, Oct 2013.

[84] M. Ferray, A. L'Huillier, X. F. Li, L. A. Lompre, G. Mainfray, and C. Manus. Multiple-harmonic conversion of 1064 nm radiation in rare gases. *Journal of Physics B: Atomic, Molecular and Optical Physics*, 21(3):L31–L35, feb 1988.

[85] M. Fibrich, J. Šulc, M. Jelínek, H. Jelínková, and V. Kubeček. Influence of temperature on ti:sapphire spectroscopic and laser characteristics. *Laser Physics*, 28(8), 2018.

[86] A. Flettner, T. Pfeifer, D. Walter, C. Winterfeldt, C. Spielmann, and G. Gerber. High-harmonic generation and plasma radiation from water microdroplets. *Applied Physics B*, 77(8):747–751, Dec 2003.

[87] T. Fordell, M. Miranda, C. L. Arnold, and A. L'Huillier. High-speed carrier-envelope phase drift detection of amplified laser pulses. *Opt. Express*, 19(24):23652–23657, Nov 2011.

[88] T. Fordell, M. Miranda, A. Persson, and A. L'Huillier. Carrier-envelope phase stabilization of a multi-millijoule, regenerative-amplifier-based chirped-pulse amplifier system. *Opt. Express*, 17(23):21091–21097, Nov 2009.

[89] N. Forget, L. Canova, X. Chen, A. Jullien, and R. Lopez-Martens. Closed-loop carrier-envelope phase stabilization with an acousto-optic programmable dispersive filter. *Opt. Lett.*, 34(23):3647–3649, Dec 2009.

[90] N. Forget, V. Crozatier, and P. Tournois. Transmission bragg-grating grisms for pulse compression. *Applied Physics B*, 109(1):121–125, Oct 2012.

[91] D. W. Forslund, J. M. Kindel, K. Lee, E. L. Lindman, and R. L. Morse. Theory and simulation of resonant absorption in a hot plasma. *Phys. Rev. A*, 11:679–683, Feb 1975.

[92] D. Franz, S. Kaassamani, D. Gauthier, R. Nicolas, M. Kholodtsova, L. Douillard, J.-T. Gomes, L. Lavoute, D. Gaponov, N. Ducros, S. Février, J. Biegert, L. Shi, M. Kovacev, W. Boutu, and H. Merdji. All semiconductor enhanced high-harmonic generation from a single nanostructured cone. *Scientific Reports*, 9(1):5663, Apr 2019.

[93] J. P. Freidberg, R. W. Mitchell, R. L. Morse, and L. I. Rudsinski. Resonant absorption of laser light by plasma targets. *Phys. Rev. Lett.*, 28:795–799, Mar 1972.

[94] S. Fritzler, V. Malka, G. Grillon, J. P. Rousseau, F. Burgy, E. Lefebvre, E. d'Humiéres, P. McKenna, and K. W. D. Ledingham. Proton beams generated with high-intensity lasers: Applications to medical isotope production. *Applied Physics Letters*, 83(15):3039–3041, 2003.

[95] J. Gao, B. Li, F. Liu, H. Cai, M. Chen, X. Yuan, X. Ge, L. Chen, Z. Sheng, and J. Zhang. Double optimal density gradients for harmonic generation from relativistically oscillating plasma surfaces. *Physics of Plasmas*, 26(10):103102, 2019.

[96] R. S. Gao, P. S. Gibner, J. H. Newman, K. A. Smith, and R. F. Stebbings. Absolute and angular efficiencies of a microchannel-plate position-sensitive detector. *Review of Scientific Instruments*, 55(11):1756–1759, 1984.

[97] T. Gaumnitz, A. Jain, Y. Pertot, M. Huppert, I. Jordan, F. Ardana-Lamas, and H. J. Worner. Streaking of 43-attosecond soft-x-ray pulses generated by a passively cep-stable mid-infrared driver. *Opt. Express*, 25(22):27506–27518, Oct 2017.

[98] J. P. Geindre, P. Audebert, and R. S. Marjoribanks. Relativistic *ac* gyromagnetic effects in ultraintense laser-matter interaction. *Phys. Rev. Lett.*, 97:085001, Aug 2006.

[99] J. P. Geindre, P. Audebert, A. Rousse, F. Falliès, J. C. Gauthier, A. Mysyrowicz, A. D. Santos, G. Hamoniaux, and A. Antonetti. Frequency-domain interferometer for measuring the phase and amplitude of a femtosecond pulse probing a laser-produced plasma. *Opt. Lett.*, 19(23):1997–1999, Dec 1994.

[100] K. M. George, J. T. Morrison, S. Feister, G. K. Ngirmang, J. R. Smith, A. J. Klim, J. Snyder, D. Austin, W. Erbsen, K. D. Frische, and et al. High-repetition-rate ($\geqslant$ khz) targets and optics from liquid microjets for high-intensity laser-plasma interactions. *High Power Laser Science and Engineering*, 7:e50, 2019.

[101] S. Ghimire, A. D. DiChiara, E. Sistrunk, P. Agostini, L. F. DiMauro, and D. A. Reis. Observation of high-order harmonic generation in a bulk crystal. *Nature Physics*, 7, 2011.

[102] S. Ghimire and D. A. Reis. High-harmonic generation from solids. *Nature Physics*, 15, 2019.

[103] S. Ghimire, B. Shan, C.-Y. Wang, and Z. Chang. High-energy 6.2-fs pulses for attosecond pulse generation. *Laser Physics*, 15:838–842, 06 2005.

[104] P. Gibbon and A. R. Bell. Collisionless absorption in sharp-edged plasmas. *Phys. Rev. Lett.*, 68:1535–1538, Mar 1992.

[105] V. Ginzburg, I. Yakovlev, A. Kochetkov, A. Kuzmin, S. Mironov, I. Shaikin, A. Shaykin, and E. Khazanov. 11 fs, 1.5 pw laser with nonlinear pulse compression. *Opt. Express*, 29(18):28297–28306, Aug 2021.

[106] Y. Glinec, J. Faure, A. Guemnie-Tafo, V. Malka, H. Monard, J. P. Larbre, V. De Waele, J. L. Marignier, and M. Mostafavi. Absolute calibration for a broad range single shot electron spectrometer. *Review of Scientific Instruments*, 77(10):103301, 2006.

[107] A. Golinelli, X. Chen, B. Bussière, E. Gontier, P.-M. Paul, O. Tcherbakoff, P. D'Oliveira, and J.-F. Hergott. Cep-stabilized, sub-18 fs, 10 khz and tw-class 1 khz dual output ti:sa laser with wavelength tunability option. *Opt. Express*, 27(10):13624–13636, May 2019.

[108] A. Gonoskov. Theory of relativistic radiation reflection from plasmas. *Physics of Plasmas*, 25(1):013108, 2018.

[109] A. A. Gonoskov, A. V. Korzhimanov, A. V. Kim, M. Marklund, and A. M. Sergeev. Ultrarelativistic nanoplasmonics as a route towards extreme-intensity attosecond pulses. *Phys. Rev. E*, 84:046403, Oct 2011.

[110] S. Gordienko, A. Pukhov, O. Shorokhov, and T. Baeva. Relativistic doppler effect: Universal spectra and zeptosecond pulses. *Phys. Rev. Lett.*, 93:115002, Sep 2004.

[111] M. Grech, L. Lancia, I. A. Andriyash, P. Audebert, A. BECK, S. Corde, X. Davoine, M. Frotin, A. Grassi, L. Gremillet, S. Le Pape, M. Lobet, A. Leblanc, F. Mathieu, F. Massimo, A. Mercuri-Baron, D. Papadopoulos, F. Pérez, J. Prudent, C. Riconda, L. Romagnani, A. Specka, C. Thaury, K. T. Phuoc, and T. Vinci. Investigating strong-field QED processes in laser-electron beam collisions at Apollon. working paper or preprint, May 2021.

[112] D. Guénot, D. Gustas, A. Vernier, B. Beaurepaire, F. Böhle, M. Bocoum, M. Lozano, A. Jullien, R. Lopez-Martens, A. Lifschitz, and J. Faure. Relativistic electron beams driven by khz single-cycle light pulses. *Nature Photonics*, 11(5):293–296, May 2017.

[113] D. Gustas. *High-repetition-rate relativistic electron acceleration in plasma wakefields driven by few-cycle laser pulses*. PhD thesis, 2018. Thèse de doctorat dirigée par Faure-Vincent, Jérôme Physique des plasmas Université Paris-Saclay (ComUE) 2018.

[114] G. R. Harrison. The production of diffraction gratings: Ii. the design of echelle gratings and spectrographs 1. *J. Opt. Soc. Am.*, 39(7):522–528, Jul 1949.

[115] J. E. Harvey and R. N. Pfisterer. Understanding diffraction grating behavior: including conical diffraction and Rayleigh anomalies from transmission gratings. *Optical Engineering*, 58(8):1 – 21, 2019.

[116] M. T. Hassan, T. T. Luu, A. Moulet, O. Raskazovskaya, P. Zhokhov, M. Garg, N. Karpowicz, A. M. Zheltikov, V. Pervak, F. Krausz, and E. Goulielmakis. Optical attosecond pulses and tracking the nonlinear response of bound electrons. *Nature*, 530(7588):66–70, Feb 2016.

[117] Z.-H. He, B. Hou, V. Lebailly, J. A. Nees, K. Krushelnick, and A. G. R. Thomas. Coherent control of plasma dynamics. *Nature Communications*, 6(1):7156, May 2015.

[118] P. Heissler, R. Hörlein, J. M. Mikhailova, L. Waldecker, P. Tzallas, A. Buck, K. Schmid, C. M. S. Sears, F. Krausz, L. Veisz, M. Zepf, and G. D. Tsakiris. Few-cycle driven relativistically oscillating plasma mirrors: A source of intense isolated attosecond pulses. *Phys. Rev. Lett.*, 108:235003, Jun 2012.

[119] F. W. Helbing, G. Steinmeyer, J. Stenger, H. R. Telle, and U. Keller. Carrier-envelope-offset dynamics and stabilization of femtosecond pulses. *Applied Physics B*, 74(1):s35–s42, Jun 2002.

[120] A. Henig, S. Steinke, M. Schnürer, T. Sokollik, R. Hörlein, D. Kiefer, D. Jung, J. Schreiber, B. M. Hegelich, X. Q. Yan, J. Meyer-ter Vehn, T. Tajima, P. V. Nickles, W. Sandner, and D. Habs. Radiation-pressure acceleration of ion beams driven by circularly polarized laser pulses. *Phys. Rev. Lett.*, 103:245003, Dec 2009.

[121] M. Hentschel, R. Kienberger, C. Spielmann, G. A. Reider, N. Milosevic, T. Brabec, P. Corkum, U. Heinzmann, M. Drescher, and F. Krausz. Attosecond metrology. *Nature*, 414(6863):509–513, Nov 2001.

[122] D. Hoff, F. J. Furch, T. Witting, K. Ruhle, D. Adolph, A. M. Sayler, M. J. J. Vrakking, G. G. Paulus, and C. P. Schulz. Continuous every-single-shot carrier-envelope phase measurement and control at 100 khz. *Opt. Lett.*, 43(16):3850–3853, Aug 2018.

[123] D. Hoff, M. Krüger, L. Maisenbacher, A. Sayler, G. Paulus, and P. Hommelhoff. Tracing the phase of focused broadband laser pulses. *Nature Physics*, 13:947–951, July 2017.

[124] R. Hörlein, S. G. Rykovanov, B. Dromey, Y. Nomura, D. Adams, M. Geissler, M. Zepf, F. Krausz, and G. D. Tsakiris. Controlling the divergence of high harmonics from solid targets: a route toward coherent harmonic focusing. *The European Physical Journal D*, 55(2):475–481, Nov 2009.

[125] B. Hou, J. Nees, J. Easter, J. Davis, G. Petrov, A. Thomas, and K. Krushelnick. Mev proton beams generated by 3 mj ultrafast laser pulses at 0.5 khz. *Applied Physics Letters*, 95(10):101503, 2009.

[126] J. Huijts, I. A. Andriyash, L. Rovige, A. Vernier, and J. Faure. Identifying observable carrier-envelope phase effects in laser wakefield acceleration with near-single-cycle pulses. *Physics of Plasmas*, 28(4):043101, 2021.

[127] J. Huijts, L. Rovige, I. A. Andriyash, A. Vernier, M. Ouillé, J. Kaur, Z. Cheng, R. Lopez-Martens, and J. Faure. Waveform control of relativistic electron dynamics in laser-plasma acceleration. *Phys. Rev. X*, 12:011036, Feb 2022.

[128] O. Jahn, V. E. Leshchenko, P. Tzallas, A. Kessel, M. Krüger, A. Münzer, S. A. Trushin, G. D. Tsakiris, S. Kahaly, D. Kormin, L. Veisz, V. Pervak, F. Krausz, Z. Major, and S. Karsch. Towards intense isolated attosecond pulses from relativistic surface high harmonics. *Optica*, 6(3):280–287, Mar 2019.

[129] A. Jeandet, A. Borot, K. Nakamura, S. W. Jolly, A. J. Gonsalves, C. Tóth, H.-S. Mao, W. P. Leemans, and F. Quéré. Spatio-temporal structure of a petawatt femtosecond laser beam. *Journal of Physics: Photonics*, 1(3):035001, jun 2019.

[130] A. Jeandet, S. W. Jolly, A. Borot, B. Bussière, P. Dumont, J. Gautier, O. Gobert, J.-P. Goddet, A. Gonsalves, A. Irman, W. P. Leemans, R. Lopez-Martens, G. Mennerat, K. Nakamura, M. Ouillé, G. Pariente, M. Pittman, T. Püschel, F. Sanson, F. Sylla, C. Thaury, K. Zeil, and F. Quéré. Survey of spatio-temporal couplings throughout high-power ultrashort lasers. *Opt. Express*, 30(3):3262–3288, Jan 2022.

[131] Y. Jin Woo, G. K. Yeong, W. C. Il, H. S. Jae, W. L. Hwang, K. L. Seong, and H. N. Chang. Realization of laser intensity over 1e23 watt per cm2. *Optica*, 8(5):630–635, May 2021.

[132] S. W. Jolly, O. Gobert, and F. Quéré. Spatio-temporal characterization of ultrashort laser beams: a tutorial. *Journal of Optics*, 22(10):103501, sep 2020.

[133] A. Jullien. *Génération d'impulsions laser ultra brèves et ultra intenses à contraste temporel élevé*. PhD thesis, 2004. Thèse de doctorat dirigée par Chériaux, Gilles Physique Palaiseau, Ecole polytechnique 2004.

[134] A. Jullien, O. Albert, F. Burgy, G. Hamoniaux, J.-P. Rousseau, J.-P. Chambaret, F. Augé-Rochereau, G. Chériaux, J. Etchepare, N. Minkovski, and S. M. Saltiel. 10^{10} temporal contrast for femtosecond ultraintense lasers by cross-polarized wave generation. *Opt. Lett.*, 30(8):920–922, Apr 2005.

[135] A. Jullien, O. Albert, G. Chériaux, J. Etchepare, S. Kourtev, N. Minkovski, and S. M. Saltiel. Two crystal arrangement to fight efficiency saturation in cross-polarized wave generation. *Opt. Express*, 14(7):2760–2769, Apr 2006.

[136] A. Jullien, A. Ricci, F. Böhle, J.-P. Rousseau, S. Grabielle, N. Forget, H. Jacqmin, B. Mercier, and R. Lopez-Martens. Carrier-envelope-phase stable, high-contrast, double chirped-pulse-amplification laser system. *Opt. Lett.*, 39(13):3774–3777, Jul 2014.

[137] S. Kahaly, S. Monchocé, H. Vincenti, T. Dzelzainis, B. Dromey, M. Zepf, P. Martin, and F. Quéré. Direct observation of density-gradient effects in harmonic generation from plasma mirrors. *Phys. Rev. Lett.*, 110:175001, Apr 2013.

[138] M. Kakehata, H. Takada, Y. Kobayashi, K. Torizuka, H. Takamiya, K. Nishijima, T. Homma, H. Takahashi, K. Okubo, S. Nakamura, and Y. Koyamada. Carrier-envelope-phase stabilized chirped-pulse amplification system scalable to higher pulse energies. *Opt. Express*, 12(10):2070–2080, May 2004.

[139] A. Kessel, V. E. Leshchenko, O. Jahn, M. Krüger, A. Münzer, A. Schwarz, V. Pervak, M. Trubetskov, S. A. Trushin, F. Krausz, Z. Major, and S. Karsch. Relativistic few-cycle pulses with high contrast from picosecond-pumped opcpa. *Optica*, 5(4):434–442, Apr 2018.

[140] H. T. Kim, V. B. Pathak, K. Hong Pae, A. Lifschitz, F. Sylla, J. H. Shin, C. Hojbota, S. K. Lee, J. H. Sung, H. W. Lee, E. Guillaume, C. Thaury, K. Nakajima, J. Vieira, L. O. Silva, V. Malka, and C. H. Nam. Stable multi-gev electron accelerator driven by waveform-controlled pw laser pulses. *Scientific Reports*, 7(1):10203, Aug 2017.

[141] T. Kita, T. Harada, N. Nakano, and H. Kuroda. Mechanically ruled aberration-corrected concave gratings for a flat-field grazing-incidence spectrograph. *Appl. Opt.*, 22(4):512–513, Feb 1983.

[142] S. Koke, C. Grebing, H. Frei, A. Anderson, A. Assion, and G. Steinmeyer. Direct frequency comb synthesis with arbitrary offset and shot-noise-limited phase noise. *Nature Photonics*, 4(7):462–465, Jul 2010.

[143] S. Koke, C. Grebing, B. Manschwetus, and G. Steinmeyer. Fast f-to-2f interferometer for a direct measurement of the carrier-envelope phase drift of ultrashort amplified laser pulses. *Opt. Lett.*, 33(21):2545–2547, Nov 2008.

[144] D. Kormin, A. Borot, G. Ma, W. Dallari, B. Bergues, M. Aladi, I. B. Földes, and L. Veisz. Spectral interferometry with waveform-dependent relativistic high-order harmonics from plasma surfaces. *Nature Communications*, 9(1):4992, Nov 2018.

[145] S. Kühn, M. Dumergue, S. Kahaly, S. Mondal, M. FÃ¼le, T. Csizmadia, B. Farkas, B. Major, Z. Várallyay, E. Cormier, M. Kalashnikov, F. Calegari, M. Devetta, F. Frassetto, E. Månsson, L. Poletto, S. Stagira, C. Vozzi, M. Nisoli, P. Rudawski, S. Maclot, F. Campi, H. Wikmark, C. L. Arnold, C. M. Heyl, P. Johnsson, A. L'Huillier, R. Lopez-Martens, S. Haessler, M. Bocoum, F. Böhle, A. Vernier, G. Iaquaniello, E. Skantzakis, N. Papadakis, C. Kalpouzos, P. Tzallas, F. Lépine, D. Charalambidis, K. Varjú, K. Osvay, and G. Sansone. The ELI-ALPS facility: the next generation of attosecond sources. *Journal of Physics B: Atomic, Molecular and Optical Physics*, 50(13):132002, jun 2017.

[146] M. Kurucz, S. Tóth, R. Flender, L. Haizer, B. Kiss, B. Persielle, and E. Cormier. Single-shot cep drift measurement at arbitrary repetition rate based on dispersive fourier transform. *Opt. Express*, 27(9):13387–13399, Apr 2019.

[147] H. G. Kurz, D. S. Steingrube, D. Ristau, M. Lein, U. Morgner, and M. Kovačev. High-order-harmonic generation from dense water microdroplets. *Phys. Rev. A*, 87:063811, Jun 2013.

[148] J. T. Larsen and S. M. Lane. Hyades-a plasma hydrodynamics code for dense plasma studies. *Journal of Quantitative Spectroscopy and Radiative Transfer*, 51(1):179–186, 1994. Special Issue Radiative Properties of Hot Dense Matter.

[149] A. Leblanc. *Miroirs et réseaux plasmas en champs lasers ultra-intenses : génération d'harmoniques d'ordre élevé et de faisceaux d'électrons relativistes.* PhD thesis, 2016. Thèse de doctorat dirigée par Quéré, Fabien Physique Université Paris-Saclay (ComUE) 2016.

[150] A. Leblanc, S. Monchocé, H. Vincenti, S. Kahaly, J.-L. Vay, and F. Quéré. Spatial properties of high-order harmonic beams from plasma mirrors: A ptychographic study. *Phys. Rev. Lett.*, 119:155001, Oct 2017.

[151] H. Lehmeier, W. Leupacher, and A. Penzkofer. Nonresonant third order hyperpolarizability of rare gases and n2 determined by third harmonic generation. *Optics Communications*, 56(1):67–72, 1985.

[152] V. E. Leshchenko, A. Kessel, O. Jahn, M. Krüger, A. Münzer, S. A. Trushin, L. Veisz, Z. Major, and S. Karsch. On-target temporal characterization of optical pulses at relativistic intensity. *Light: Science & Applications*, 8(1):96, Oct 2019.

[153] B. Y. Li, F. Liu, M. Chen, Z. Y. Chen, X. H. Yuan, S. M. Weng, T. Jin, S. G. Rykovanov, J. W. Wang, Z. M. Sheng, and J. Zhang. High-quality high-order harmonic generation through preplasma truncation. *Phys. Rev. E*, 100:053207, Nov 2019.

[154] C. Li, E. Moon, and Z. Chang. Carrier-envelope phase shift caused by variation of grating separation. *Opt. Lett.*, 31(21):3113–3115, Nov 2006.

[155] L. Li, J. C. P. Koliyadu, H. Donnelly, D. Alj, O. Delmas, M. Ruiz-Lopez, O. de La Rochefoucauld, G. Dovillaire, M. Fajardo, C. Zhou, S. Ruan, B. Dromey, M. Zepf, and P. Zeitoun. High numerical aperture hartmann wave front sensor for extreme ultraviolet spectral range. *Opt. Lett.*, 45(15):4248–4251, Aug 2020.

[156] R. Lichters, J. Meyer-ter Vehn, and A. Pukhov. Short-pulse laser harmonics from oscillating plasma surfaces driven at relativistic intensity. *Physics of Plasmas*, 3(9):3425–3437, 1996.

[157] A. F. Lifschitz and V. Malka. Optical phase effects in electron wakefield acceleration using few-cycle laser pulses. *New Journal of Physics*, 14(5):053045, may 2012.

[158] J. Lin, T. Batson, J. Nees, A. G. R. Thomas, and K. Krushelnick. Towards isolated attosecond electron bunches using ultrashort-pulse laser-solid interactions. *Scientific Reports*, 10(1):18354, Oct 2020.

[159] X. Liu, R. Wagner, A. Maksimchuk, E. Goodman, J. Workman, D. Umstadter, and A. Migus. Nonlinear temporal diffraction and frequency shifts resulting from pulse shaping in chirped-pulse amplification systems. *Opt. Lett.*, 20(10):1163–1165, May 1995.

[160] W. Lu, M. Tzoufras, C. Joshi, F. S. Tsung, W. B. Mori, J. Vieira, R. A. Fonseca, and L. O. Silva. Generating multi-gev electron bunches using single stage laser wakefield acceleration in a 3d nonlinear regime. *Phys. Rev. ST Accel. Beams*, 10:061301, Jun 2007.

[161] F. Lücking. *Carrier-envelope phase control for the advancement of attosecond pulse generation*. PhD thesis, July 2014. PhD thesis.

[162] F. Lücking, A. Assion, A. Apolonski, F. Krausz, and G. Steinmeyer. Long-term carrier-envelope-phase-stable few-cycle pulses by use of the feed-forward method. *Opt. Lett.*, 37(11):2076–2078, Jun 2012.

[163] F. Lücking, A. Trabattoni, S. Anumula, G. Sansone, F. Calegari, M. Nisoli, T. Oksenhendler, and G. Tempea. In situ measurement of nonlinear carrier-envelope phase changes in hollow fiber compression. *Opt. Lett.*, 39(8):2302–2305, Apr 2014.

[164] O. Lundh, C. Rechatin, J. Lim, V. Malka, and J. Faure. Experimental measurements of electron-bunch trains in a laser-plasma accelerator. *Phys. Rev. Lett.*, 110:065005, Feb 2013.

[165] F. Lureau, G. Matras, O. Chalus, C. Derycke, T. Morbieu, C. Radier, O. Casagrande, S. Laux, S. Ricaud, G. Rey, and et al. High-energy hybrid femtosecond laser system demonstrating 2 Ã— 10 pw capability. *High Power Laser Science and Engineering*, 8:e43, 2020.

[166] T. T. Luu, Z. Yin, A. Jain, T. Gaumnitz, Y. Pertot, J. Ma, and H. J. Worner. Extreme ultraviolet high harmonic generation in liquids. *Nature Communications*, 9, 2018.

[167] V. Malka. Plasma wake accelerators: Introduction and historical overview. *Proceedings of the 2014 CAS-CERN Accelerator School: Plasma Wake Acceleration*, 1, 02 2016.

[168] A. Malvache. *Optique non-linéaire à haute intensité : Compression d'impulsions laser Interaction laser-plasma*. PhD thesis, 2011. Thèse de doctorat dirigée par Mourou, Gérard Lasers et matière Palaiseau, Ecole polytechnique 2011.

[169] A. Malvache, A. Borot, F. Quéré, and R. Lopez-Martens. Coherent wake emission spectroscopy as a probe of steep plasma density profiles. *Phys. Rev. E*, 87:035101, Mar 2013.

[170] A. Malvache, X. Chen, C. G. Durfee, A. Jullien, and R. Lopez-Martens. Multi-mj pulse compression in hollow fibers using circular polarization. *Applied Physics B*, 104(1):5, Jul 2011.

[171] E. A. J. Marcatili and R. A. Schmeltzer. Hollow metallic and dielectric waveguides for long distance optical transmission and lasers. *Bell System Technical Journal*, 43(4):1783–1809, 1964.

[172] A. McPherson, G. Gibson, H. Jara, U. Johann, T. S. Luk, I. A. McIntyre, K. Boyer, and C. K. Rhodes. Studies of multiphoton production of vacuum-ultraviolet radiation in the rare gases. *J. Opt. Soc. Am. B*, 4(4):595–601, Apr 1987.

[173] J. T. Mendonca and F. Doveil. Stochasticity in plasmas with electromagnetic waves. *Journal of Plasma Physics*, 28(3):485–493, 1982.

[174] J. M. Mikhailova, M. V. Fedorov, N. Karpowicz, P. Gibbon, V. T. Platonenko, A. M. Zheltikov, and F. Krausz. Isolated attosecond pulses from laser-driven synchrotron radiation. *Phys. Rev. Lett.*, 109:245005, Dec 2012.

[175] J. M. Mikhailova, L. Veisz, A. Borot, K. Schmid, C. M. S. Sears, D. Herrmann, R. Tautz, A. Buck, R. Hoerlein, P. Heissler, G. D. Tsakiris, and F. Krausz. Plasma-mirror-cleaned high-contrast few-cycle relativistic-intensity light pulses. In *Conference on Lasers and Electro-Optics 2010*, page JThD5. Optical Society of America, 2010.

[176] M. Miranda, C. L. Arnold, T. Fordell, F. Silva, B. Alonso, R. Weigand, A. L'Huillier, and H. Crespo. Characterization of broadband few-cycle laser pulses with the d-scan technique. *Opt. Express*, 20(17):18732–18743, Aug 2012.

[177] M. Miranda, T. Fordell, C. Arnold, A. L'Huillier, and H. Crespo. Simultaneous compression and characterization of ultrashort laser pulses using chirped mirrors and glass wedges. *Opt. Express*, 20(1):688–697, Jan 2012.

[178] S. K. Mishra, A. Andreev, and M. P. Kalashinikov. Reflection of few cycle laser pulses from an inhomogeneous overdense plasma. *Opt. Express*, 25(10):11637–11651, May 2017.

[179] A. V. Mitrofanov, D. A. Sidorov-Biryukov, P. B. Glek, M. V. Rozhko, E. A. Stepanov, A. D. Shutov, S. V. Ryabchuk, A. A. Voronin, A. B. Fedotov, and A. M. Zheltikov. Chirp-controlled high-harmonic and attosecond-pulse generation via coherent-wake plasma emission driven by mid-infrared laser pulses. *Opt. Lett.*, 45(3):750–753, Feb 2020.

[180] P. Mora. Plasma expansion into a vacuum. *Phys. Rev. Lett.*, 90:185002, May 2003.

[181] A. Moulet, S. Grabielle, C. Cornaggia, N. Forget, and T. Oksenhendler. Single-shot, high-dynamic-range measurement of sub-15 fs pulses by self-referenced spectral interferometry. *Opt. Lett.*, 35(22):3856–3858, Nov 2010.

[182] G. Mourou, N. Naumova, E. Power, V. Yanovsky, and J. Nees. Relativistic optics in the lambda-cubed regime and applications to attosecond physics. In *CLEO/Europe. 2005 Conference on Lasers and Electro-Optics Europe, 2005.*, pages 691–691, 2005.

[183] A. A. Muschet, A. D. Andres, P. Fischer, R. Salh, and L. Veisz. Utilizing the temporal superresolution approach in an optical parametric synthesizer to generate multi-tw sub-4-fs light pulses. *Opt. Express*, 30(3):4374–4380, Jan 2022.

[184] T. Nagy, M. Forster, and P. Simon. Flexible hollow fiber for pulse compressors. *Appl. Opt.*, 47(18):3264–3268, Jun 2008.

[185] T. Nagy, P. Simon, and L. Veisz. High-energy few-cycle pulses: post-compression techniques. *Advances in Physics: X*, 6(1):1845795, 2021.

[186] M. Natile, A. Golinelli, L. Lavenu, F. Guichard, M. Hanna, Y. Zaouter, R. Chiche, X. Chen, J. F. Hergott, W. Boutu, H. Merdji, and P. Georges. Cep-stable high-energy ytterbium-doped fiber amplifier. *Opt. Lett.*, 44(16):3909–3912, Aug 2019.

[187] N. Naumova, G. Mourou, J. Nees, and V. Yanovsky. 'Relativistic λ^3' regime: from relativistic electrons to relativistic ions. In *Conference on Lasers and Electro-Optics/Quantum Electronics and Laser Science Conference*, page CWA30. Optical Society of America, 2003.

[188] N. Naumova, I. Sokolov, J. Nees, A. Maksimchuk, V. Yanovsky, and G. Mourou. Attosecond electron bunches. *Phys. Rev. Lett.*, 93:195003, Nov 2004.

[189] N. M. Naumova, J. A. Nees, I. V. Sokolov, B. Hou, and G. A. Mourou. Relativistic generation of isolated attosecond pulses in a λ^3 focal volume. *Phys. Rev. Lett.*, 92:063902, Feb 2004.

[190] A. Nayak, I. Orfanos, I. Makos, M. Dumergue, S. Kühn, E. Skantzakis, B. Bodi, K. Varju, C. Kalpouzos, H. I. B. Banks, A. Emmanouilidou, D. Charalambidis, and P. Tzallas. Multiple ionization of argon via multi-xuv-photon absorption induced by 20-gw high-order harmonic laser pulses. *Phys. Rev. A*, 98:023426, Aug 2018.

[191] J. Nees, N. Naumova, E. Power, V. Yanovsky, I. Sokolov, A. Maksimchuk, S.-W. Bahk, V. Chvykov, G. Kalintchenko, B. Hou, and G. Mourou. Relativistic generation of isolated attosecond pulses: a different route to extreme intensity. *Journal of Modern Optics*, 52(2-3):305–319, 2005.

[192] E. N. Nerush and I. Y. Kostyukov. Carrier-envelope phase effects in plasma-based electron acceleration with few-cycle laser pulses. *Phys. Rev. Lett.*, 103:035001, Jul 2009.

[193] M. Nisoli, S. De Silvestri, and O. Svelto. Generation of high energy 10 fs pulses by a new pulse compression technique. *Applied Physics Letters*, 68(20):2793–2795, 1996.

[194] M. Nisoli, S. Stagira, S. De Silvestri, O. Svelto, S. Sartania, Z. Cheng, G. Tempea, C. Spielmann, and F. Krausz. Toward a terawatt-scale sub-10-fs laser technology. *IEEE Journal of Selected Topics in Quantum Electronics*, 4(2):414–420, 1998.

[195] Y. Nomura, R. Hörlein, P. Tzallas, B. Dromey, S. Rykovanov, Z. Major, J. Osterhoff, S. Karsch, L. Veisz, M. Zepf, D. Charalambidis, F. Krausz, and G. D. Tsakiris. Attosecond phase locking of harmonics emitted from laser-produced plasmas. *Nature Physics*, 5(2):124–128, Feb 2009.

[196] T. Oksenhendler, S. Coudreau, N. Forget, V. Crozatier, S. Grabielle, R. Herzog, O. Gobert, and D. Kaplan. Self-referenced spectral interferometry. *Applied Physics B*, 99(1):7–12, Apr 2010.

[197] T. Oksenhendler and N. Forget. Pulse-shaping techniques theory and experimental implementations for femtosecond pulses. In M. Grishin, editor, *Advances in Solid State Lasers*, chapter 16. IntechOpen, Rijeka, 2010.

[198] M. Ouillé, A. Vernier, F. Böhle, M. Bocoum, A. Jullien, M. Lozano, J.-P. Rousseau, Z. Cheng, D. Gustas, A. Blumenstein, P. Simon, S. Haessler, J. Faure, T. Nagy, and R. Lopez-Martens. Relativistic-intensity near-single-cycle light waveforms at khz repetition rate. *Light: Science & Applications*, 9(1):47, Mar 2020.

[199] N. A. Papadogiannis, B. Witzel, C. Kalpouzos, and D. Charalambidis. Observation of attosecond light localization in higher order harmonic generation. *Phys. Rev. Lett.*, 83:4289–4292, Nov 1999.

[200] G. Pariente. *Caractérisation spatio-temporelle d'impulsions laser de haute puissance*. PhD thesis, 2017. Thése de doctorat dirigée par Quéré, Fabien Optique et photonique Université Paris-Saclay (ComUE) 2017.

[201] G. Pariente, V. Gallet, A. Borot, O. Gobert, and F. Quéré. Space-time characterization of ultra-intense femtosecond laser beams. *Nature Photonics*, 10(8):547–553, Aug 2016.

[202] S. B. Park, K. Kim, W. Cho, S. I. Hwang, I. Ivanov, C. H. Nam, and K. T. Kim. Direct sampling of a light wave in air. *Optica*, 5(4):402–408, Apr 2018.

[203] P. M. Paul, E. S. Toma, P. Breger, G. Mullot, F. Augé, P. Balcou, H. G. Muller, and P. Agostini. Observation of a train of attosecond pulses from high harmonic generation. *Science*, 292(5522):1689–1692, 2001.

[204] J. Peatross and M. Ware. Physics of light and optics: A free online textbook. In *Frontiers in Optics 2010/Laser Science XXVI*, page JWA64. Optical Society of America, 2010.

[205] C. Pellegrini. The development of xfels. *Nature Reviews Physics*, 2(7):330–331, Jul 2020.

[206] T. Pfeifer, L. Gallmann, M. J. Abel, P. M. Nagel, D. M. Neumark, and S. R. Leone. Heterodyne mixing of laser fields for temporal gating of high-order harmonic generation. *Phys. Rev. Lett.*, 97:163901, Oct 2006.

[207] S. C. Pinault and M. J. Potasek. Frequency broadening by self-phase modulation in optical fibers. *J. Opt. Soc. Am. B*, 2(8):1318–1319, Aug 1985.

[208] F. Planchon. *Solutions globales et comportement asymptotique pour les équations de Navier-Stokes*. PhD thesis, 1996. Thèse de doctorat dirigée par Meyer, Yves Sciences et techniques communes Palaiseau, Ecole polytechnique 1996.

[209] G. Plateau. *Electron bunch diagnostics for laser-plasma accelerators, from THz to X-rays*. Theses, Ecole Polytechnique X, Oct. 2011.

[210] E. Porat, H. Yehuda, I. Cohen, A. Levanon, and I. Pomerantz. Diffraction-limited coherent wake emission. *Phys. Rev. Research*, 3:L032059, Sep 2021.

[211] G. Porat, C. M. Heyl, S. B. Schoun, C. Benko, N. Dörre, K. L. Corwin, and J. Ye. Phase-matched extreme-ultraviolet frequency-comb generation. *Nature Photonics*, 12(7):387–391, Jul 2018.

[212] A. Pukhov and J. Meyer-ter Vehn. Laser wake field acceleration: the highly non-linear broken-wave regime. *Applied Physics B*, 74(4):355–361, Apr 2002.

[213] F. Quéré, C. Thaury, J.-P. Geindre, G. Bonnaud, P. Monot, and P. Martin. Phase properties of laser high-order harmonics generated on plasma mirrors. *Phys. Rev. Lett.*, 100:095004, Mar 2008.

[214] F. Quéré, C. Thaury, P. Monot, S. Dobosz, P. Martin, J.-P. Geindre, and P. Audebert. Coherent wake emission of high-order harmonics from overdense plasmas. *Phys. Rev. Lett.*, 96:125004, Mar 2006.

[215] B. Quesnel and P. Mora. Theory and simulation of the interaction of ultraintense laser pulses with electrons in vacuum. *Phys. Rev. E*, 58:3719–3732, Sep 1998.

[216] N. Raabe, T. Feng, T. Witting, A. Demircan, C. Brée, and G. Steinmeyer. Role of intrapulse coherence in carrier-envelope phase stabilization. *Phys. Rev. Lett.*, 119:123901, Sep 2017.

[217] L. P. Ramirez, D. Papadopoulos, M. Hanna, A. Pellegrina, F. Friebel, P. Georges, and F. Druon. Compact, simple, and robust cross polarized wave generation source of few-cycle, high-contrast pulses for seeding petawatt-class laser systems. *J. Opt. Soc. Am. B*, 30(10):2607–2614, Oct 2013.

[218] A. Ricci. *Développement d'une source laser ultra-brève, stabilisée en phase et à haut contraste, pour l'optique relativiste haute cadence*. Thèses, Ecole Polytechnique X, June 2013.

[219] A. Ricci, A. Jullien, N. Forget, V. Crozatier, P. Tournois, and R. Lopez-Martens. Grism compressor for carrier-envelope phase-stable millijoule-energy chirped pulse amplifier lasers featuring bulk material stretcher. *Opt. Lett.*, 37(7):1196–1198, Apr 2012.

[220] A. Ricci, A. Jullien, J.-P. Rousseau, F. Böhle, S. Grabielle, N. Forget, P. Tournois, and R. Lopez-Martens. High-contrast, cep-controlled double-cpa laser. In *Advanced Solid-State Lasers Congress*, page ATu4A.4. Optical Society of America, 2013.

[221] D. E. Rivas, A. Borot, D. E. Cardenas, G. Marcus, X. Gu, D. Herrmann, J. Xu, J. Tan, D. Kormin, G. Ma, W. Dallari, G. D. Tsakiris, I. B. Földes, S.-w. Chou, M. Weidman, B. Bergues, T. Wittmann, H. Schröder, P. Tzallas, D. Charalambidis, O. Razskazovskaya, V. Pervak, F. Krausz, and L. Veisz. Next generation driver for attosecond and laser-plasma physics. *Scientific Reports*, 7(1):5224, Jul 2017.

[222] C. Rödel, D. an der Brügge, J. Bierbach, M. Yeung, T. Hahn, B. Dromey, S. Herzer, S. Fuchs, A. G. Pour, E. Eckner, M. Behmke, M. Cerchez, O. Jäckel, D. Hemmers, T. Toncian, M. C. Kaluza, A. Belyanin, G. Pretzler, O. Willi, A. Pukhov, M. Zepf, and G. G. Paulus. Harmonic generation from relativistic plasma surfaces in ultrasteep plasma density gradients. *Phys. Rev. Lett.*, 109:125002, Sep 2012.

[223] L. Rovige, J. Huijts, I. Andriyash, A. Vernier, V. Tomkus, V. Girdauskas, G. Raciukaitis, J. Dudutis, V. Stankevic, P. Gecys, M. Ouillé, Z. Cheng, R. Lopez-Martens, and J. Faure. Demonstration of stable long-term operation of a kilohertz laser-plasma accelerator. *Phys. Rev. Accel. Beams*, 23:093401, Sep 2020.

[224] H. A. Rowland. Xxix. on concave gratings for optical purposes. *The London, Edinburgh, and Dublin Philosophical Magazine and Journal of Science*, 16(99):197–210, 1883.

[225] J. Rutledge, A. Catanese, D. D. Hickstein, S. A. Diddams, T. K. Allison, and A. S. Kowligy. Broadband ultraviolet-visible frequency combs from cascaded high-harmonic generation in quasi-phase-matched waveguides. *Journal of the Optical Society of America B*, 38(8):2252, Jul 2021.

[226] M. Salvadori, F. Consoli, C. Verona, M. Cipriani, M. P. Anania, P. L. Andreoli, P. Antici, F. Bisesto, G. Costa, G. Cristofari, R. De Angelis, G. Di Giorgio, M. Ferrario, M. Galletti, D. Giulietti, M. Migliorati, R. Pompili, and A. Zigler. Accurate spectra for high energy ions by advanced time-of-flight diamond-detector schemes in experiments with high energy and intensity lasers. *Scientific Reports*, 11(1):3071, Feb 2021.

[227] G. Sansone, F. Kelkensberg, J. F. Perez-Torres, F. Morales, M. F. Kling, W. Siu, O. Ghafur, P. Johnsson, M. Swoboda, E. Benedetti, F. Ferrari, F. Lepine, J. L. Sanz-Vicario, S. Zherebtsov, I. Znakovskaya, A. L'Huillier, M. Y. Ivanov, M. Nisoli, F. Martin, and M. J. J. Vrakking. Electron localization following attosecond molecular photoionization. *Nature*, 465(7299):763–766, Jun 2010.

[228] S. Sartania, Z. Cheng, M. Lenzner, G. Tempea, C. Spielmann, and F. Krausz. Generation of 0.1-tw 5-fs optical pulses at a 1-khz repetition rate. *Opt. Lett.*, 22(20):1562–1564, Oct 1997.

[229] K. J. Schafer, B. Yang, L. F. DiMauro, and K. C. Kulander. Above threshold ionization beyond the high harmonic cutoff. *Phys. Rev. Lett.*, 70:1599–1602, Mar 1993.

[230] E. Schrödinger. Non-linear optics. *Proc. Roy. Irish Acad. A*, 47:77–117, 1942.

[231] J. Schwinger. On gauge invariance and vacuum polarization. *Phys. Rev.*, 82:664–679, Jun 1951.

[232] Z.-M. Sheng, K. Mima, Y. Sentoku, M. S. Jovanović, T. Taguchi, J. Zhang, and J. Meyer-ter Vehn. Stochastic heating and acceleration of electrons in colliding laser fields in plasma. *Phys. Rev. Lett.*, 88:055004, Jan 2002.

[233] A. D. Shiner, C. Trallero-Herrero, N. Kajumba, H.-C. Bandulet, D. Comtois, F. Légaré, M. Giguère, J.-C. Kieffer, P. B. Corkum, and D. M. Villeneuve. Wavelength scaling of high harmonic generation efficiency. *Phys. Rev. Lett.*, 103:073902, Aug 2009.

[234] M. Sivis, M. Taucer, G. Vampa, K. Johnston, A. Staudte, A. Y. Naumov, D. M. Villeneuve, C. Ropers, and P. B. Corkum. Tailored semiconductors for high-harmonic optoelectronics. *Science*, 357(6348):303–306, 2017.

[235] R. E. Smith, E. White, P. M. Gilmore, B. Dromey, and M. Yeung. Double optical gating of high order harmonics from plasma surfaces. *New Journal of Physics*, 23(9):093010, sep 2021.

[236] J. Stenger and H. R. Telle. Intensity-induced mode shift in a femtosecond laser by a change in the nonlinear index of refraction. *Opt. Lett.*, 25(20):1553–1555, Oct 2000.

[237] D. Strickland and G. Mourou. Compression of amplified chirped optical pulses. *Optics Communications*, 56(3):219–221, 1985.

[238] A. Suda, M. Hatayama, K. Nagasaka, and K. Midorikawa. Generation of sub-10-fs, 5-mj-optical pulses using a hollow fiber with a pressure gradient. *Applied Physics Letters*, 86(11):111116, 2005.

[239] R. Szipöcs, K. Ferencz, C. Spielmann, and F. Krausz. Chirped multilayer coatings for broadband dispersion control in femtosecond lasers. *Opt. Lett.*, 19(3):201–203, Feb 1994.

[240] A. Tajalli, B. Chanteau, M. Kretschmar, H. Kurz, D. Zuber, M. Kovačev, U. Morgner, and T. Nagy. Few-cycle optical pulse characterization via cross-polarized wave generation dispersion scan technique. *Opt. Lett.*, 41(22):5246–5249, Nov 2016.

[241] A. Tajalli, M. Ouillé, A. Vernier, F. Böhle, E. Escoto, S. Kleinert, R. Romero, J. Csontos, U. Morgner, G. Steinmeyer, H. M. Crespo, R. L. Martens, and T. Nagy. Propagation effects in the characterization of 1.5-cycle pulses by xpw dispersion scan. *IEEE Journal of Selected Topics in Quantum Electronics*, 25(4):1–7, 2019.

[242] T. Tajima and J. M. Dawson. Laser electron accelerator. *Phys. Rev. Lett.*, 43:267–270, Jul 1979.

[243] E. J. Takahashi, P. Lan, O. D. Mücke, Y. Nabekawa, and K. Midorikawa. Attosecond nonlinear optics using gigawatt-scale isolated attosecond pulses. *Nature Communications*, 4(1):2691, Oct 2013.

[244] C. Thaury. *Génération d harmoniques d ordres élevés sur miroir plasma.* PhD thesis, 2008. Thèse de doctorat dirigée par Martin, Philippe Physique Paris 11 2008.

[245] C. Thaury, H. George, F. Quéré, R. Loch, J.-P. Geindre, P. Monot, and P. Martin. Coherent dynamics of plasma mirrors. *Nature Physics*, 4(8):631–634, Aug 2008.

[246] C. Thaury and F. Quéré. High-order harmonic and attosecond pulse generation on plasma mirrors: basic mechanisms. *Journal of Physics B: Atomic, Molecular and Optical Physics*, 43(21):213001, oct 2010.

[247] M. Thévenet. *Modeling the interaction between a few-cycle relativistic laser pulse and a plasma mirror: from electron acceleration to harmonic generation.* PhD thesis, 2016. Thèse de doctorat dirigée par Faure, Jérôme Physique des plasmas Université Paris-Saclay (ComUE) 2016.

[248] M. Thévenet, A. Leblanc, S. Kahaly, H. Vincenti, A. Vernier, F. Quéré, and J. Faure. Vacuum laser acceleration of relativistic electrons using plasma mirror injectors. *Nature Physics*, 12(4):355–360, Apr 2016.

[249] M. Thévenet, H. Vincenti, and J. Faure. On the physics of electron ejection from laser-irradiated overdense plasmas. *Physics of Plasmas*, 23(6):063119, 2016.

[250] L. Torrisi, M. Cutroneo, A. Mackova, V. Lavrentiev, M. Pfeifer, and E. Krousky. An unconventional ion implantation method for producing au and si nanostructures using intense laser-generated plasmas. *Plasma Physics and Controlled Fusion*, 58(2):025011, jan 2016.

[251] T. Toshiki and L. Ruxin. Marriage of a 20kev superconducting xfel with a 100pw laser, 2016.

[252] S. Toth, T. Stanislauskas, I. Balciunas, R. Budriunas, J. Adamonis, R. Danilevicius, K. Viskontas, D. Lengvinas, G. Veitas, D. Gadonas, A. Varanavičius, J. Csontos, T. Somoskoi, L. Toth, A. Borzsonyi, and K. Osvay. SYLOS lasers – the frontier of few-cycle, multi-TW, kHz lasers for ultrafast applications at extreme light infrastructure attosecond light pulse source. *Journal of Physics: Photonics*, 2(4):045003, jul 2020.

[253] P. Tournois. Acousto-optic programmable dispersive filter for adaptive compensation of group delay time dispersion in laser systems. *Optics Communications*, 140(4):245–249, 1997.

[254] E. Treacy. Optical pulse compression with diffraction gratings. *IEEE Journal of Quantum Electronics*, 5(9):454–458, 1969.

[255] A. Trisorio. *Développement d'une source laser femtoseconde de quelques cycles optiques pour la génération d'harmoniques sur cible solide.* PhD thesis, 2008. Thèse de doctorat dirigée par Mourou, Gérard et Lopez-Martens, Rodrigo Physique Paris 11 2008.

[256] G. D. Tsakiris, K. Eidmann, J. M. ter Vehn, and F. Krausz. Route to intense single attosecond pulses. *New Journal of Physics*, 8:19–19, jan 2006.

[257] G. Vampa, B. G. Ghamsari, S. Siadat Mousavi, T. J. Hammond, A. Olivieri, E. Lisicka-Skrek, A. Y. Naumov, D. M. Villeneuve, A. Staudte, P. Berini, and P. B. Corkum. Plasmon-enhanced high-harmonic generation from silicon. *Nature Physics*, 13(7):659–662, Jul 2017.

[258] M. Veltcheva, A. Borot, C. Thaury, A. Malvache, E. Lefebvre, A. Flacco, R. Lopez-Martens, and V. Malka. Brunel-dominated proton acceleration with a few-cycle laser pulse. *Phys. Rev. Lett.*, 108:075004, Feb 2012.

[259] H. Vincenti. *Génération d'impulsions attosecondes sur miroir plasma relativiste*. PhD thesis, 2012. Thèse de doctorat dirigée par Bonnaud, Guy Physique Palaiseau, Ecole polytechnique 2012.

[260] H. Vincenti. Achieving extreme light intensities using optically curved relativistic plasma mirrors. *Phys. Rev. Lett.*, 123:105001, Sep 2019.

[261] H. Vincenti, S. Monchocé, S. Kahaly, G. Bonnaud, P. Martin, and F. Quéré. Optical properties of relativistic plasma mirrors. *Nature Communications*, 5(1):3403, Mar 2014.

[262] H. Vincenti and F. Quéré. Attosecond lighthouses: How to use spatiotemporally coupled light fields to generate isolated attosecond pulses. *Phys. Rev. Lett.*, 108:113904, Mar 2012.

[263] C. Vozzi, M. Nisoli, G. Sansone, S. Stagira, and S. De Silvestri. Optimal spectral broadening in hollow-fiber compressor systems. *Appl. Phys. B*, 80:285–289, March 2005.

[264] W. J. Wadsworth, D. W. Coutts, and C. E. Webb. Kilohertz pulse repetition frequency slab Ti:sapphire lasers with high average power (10 w). *Appl. Opt.*, 38(33):6904–6911, Nov 1999.

[265] H. Wang, M. Chini, E. Moon, H. Mashiko, C. Li, and Z. Chang. Coupling between energy and phase in hollow-core fiber based f-to-2f interferometers. *Opt. Express*, 17(14):12082–12089, Jul 2009.

[266] H. Wang, M. Chini, Y. Wu, E. Moon, H. Mashiko, and Z. Chang. Carrier-envelope phase stabilization of 5-fs, 0.5-mj pulses from adaptive phase modulator. *Applied Physics B*, 98(2):291–294, Feb 2010.

[267] P. Welch. The use of fast fourier transform for the estimation of power spectra: A method based on time averaging over short, modified periodograms. *IEEE Transactions on Audio and Electroacoustics*, 15(2):70–73, 1967.

[268] J. A. Wheeler, A. Borot, S. Monchocé, H. Vincenti, A. Ricci, A. Malvache, R. Lopez-Martens, and F. Quéré. Attosecond lighthouses from plasma mirrors. *Nature Photonics*, 6:829–833, 2012.

[269] F. Wiegandt, P. N. Anderson, F. Yu, D. J. Treacher, D. T. Lloyd, P. J. Mosley, S. M. Hooker, and I. A. Walmsley. Quasi-phase-matched high-harmonic generation in gas-filled hollow-core photonic crystal fiber. *Optica*, 6(4):442–447, Apr 2019.

[270] S. Wilks. Simulations of ultraintense laser-plasma interactions. *Physics of Fluids B: Plasma Physics*, 5(7):2603–2608, 1993.

[271] S. C. Wilks, A. B. Langdon, T. E. Cowan, M. Roth, M. Singh, S. Hatchett, M. H. Key, D. Pennington, A. MacKinnon, and R. A. Snavely. Energetic proton generation in ultra-intense laser-solid interactions. *Physics of Plasmas*, 8(2):542–549, 2001.

[272] T. Willemsen, U. Chaulagain, I. Havlíčková, S. Borneis, W. Ebert, H. Ehlers, M. Gauch, T. Groß, D. Kramer, T. Laštovička, J. Nejdl, B. Rus, K. Schrader, T. Tolenis, F. Vaněk, P. K. Velpula, and S. Weber. Large area ion beam sputtered dielectric ultrafast mirrors for petawatt laser beamlines. *Opt. Express*, 30(4):6129–6141, Feb 2022.

[273] R. Withnall. *SPECTROSCOPY / Raman Spectroscopy*, pages 119–134. 12 2005.

[274] T. Witting, F. Frank, C. A. Arrell, W. A. Okell, J. P. Marangos, and J. W. G. Tisch. Characterization of high-intensity sub-4-fs laser pulses using spatially encoded spectral shearing interferometry. *Opt. Lett.*, 36(9):1680–1682, May 2011.

[275] T. Witting, F. Frank, W. A. Okell, C. A. Arrell, J. P. Marangos, and J. W. G. Tisch. Sub-4-fs laser pulse characterization by spatially resolved spectral shearing interferometry and attosecond streaking. *Journal of Physics B: Atomic, Molecular and Optical Physics*, 45(7):074014, mar 2012.

[276] T. Wittman. *Complete characterization of plasma mirrors and development of a single-shot carrier-envelope phase meter*. PhD thesis, 2009. PhD thesis, University of Szeged.

[277] R. Wood. Lxxxv. the echelette grating for the infra-red. *The London, Edinburgh, and Dublin Philosophical Magazine and Journal of Science*, 20(118):770–778, 1910.

[278] A. S. Wyatt, T. Witting, A. Schiavi, D. Fabris, P. Matia-Hernando, I. A. Walmsley, J. P. Marangos, and J. W. G. Tisch. Attosecond sampling of arbitrary optical waveforms. *Optica*, 3(3):303–310, Mar 2016.

[279] X. Xie, K. Doblhoff-Dier, S. Roither, M. S. Schöffler, D. Kartashov, H. Xu, T. Rathje, G. G. Paulus, A. Baltuška, S. Gräfe, and M. Kitzler. Attosecond-recollision-controlled selective fragmentation of polyatomic molecules. *Phys. Rev. Lett.*, 109:243001, Dec 2012.

[280] L. Xu, C. Spielmann, A. Poppe, T. Brabec, F. Krausz, and T. W. Hänsch. Route to phase control of ultrashort light pulses. *Opt. Lett.*, 21(24):2008–2010, Dec 1996.

[281] L. Xu, G. Tempea, A. Poppe, M. Lenzner, C. Spielmann, F. Krausz, A. Stingl, and K. Ferencz. High-power sub-10-fs Ti:sapphire oscillators. *Applied Physics B: Lasers and Optics*, 65(2):151–159, Aug. 1997.

[282] L. Xu, G. Tempea, C. Spielmann, F. Krausz, A. Stingl, K. Ferencz, and S. Takano. Continuous-wave mode-locked ti:sapphire laser focusable to $5 \times 10^{13} w/cm^2$. *Opt. Lett.*, 23(10):789–791, May 1998.

[283] S. Xu, J. Zhang, N. Tang, S. Wang, W. Lu, and Z. Li. Periodic self-injection of electrons in a few-cycle laser driven oscillating plasma wake. *AIP Advances*, 10(9):095310, 2020.

[284] B. Xue, Y. Tamaru, Y. Fu, H. Yuan, P. Lan, O. D. Mücke, A. Suda, K. Midorikawa, and E. J. Takahashi. A custom-tailored multi-tw optical electric field for gigawatt soft-x-ray isolated attosecond pulses. *Ultrafast Science*, 2021:9828026, Aug 2021.

[285] M. Yeung, J. Bierbach, E. Eckner, S. Rykovanov, S. Kuschel, A. Savert, M. Förster, C. Rödel, G. G. Paulus, S. Cousens, M. Coughlan, B. Dromey, and M. Zepf. Noncollinear polarization gating of attosecond pulse trains in the relativistic regime. *Phys. Rev. Lett.*, 115:193903, Nov 2015.

[286] M. Yeung, B. Dromey, D. Adams, S. Cousens, R. Hörlein, Y. Nomura, G. D. Tsakiris, and M. Zepf. Beaming of high-order harmonics generated from laser-plasma interactions. *Phys. Rev. Lett.*, 110:165002, Apr 2013.

[287] M. Yeung, S. Rykovanov, J. Bierbach, L. Li, E. Eckner, S. Kuschel, A. Woldegeorgis, C. Rödel, A. Sävert, G. G. Paulus, M. Coughlan, B. Dromey, and M. Zepf. Experimental observation of attosecond control over relativistic electron bunches with two-colour fields. *Nature Photonics*, 11(1):32–35, Jan 2017.

[288] N. Zaïm. *Modélisation de l'accélération d'électrons par des impulsions lasers relativistes de quelques cycles optiques sur des plasmas surdenses*. Theses, Université Paris Saclay (COmUE), Dec. 2019.

[289] N. Zaïm, F. Böhle, M. Bocoum, A. Vernier, S. Haessler, X. Davoine, L. Videau, J. Faure, and R. Lopez-Martens. Few-cycle laser wakefield acceleration on solid targets with controlled plasma scale length. *Physics of Plasmas*, 26(3):033112, 2019.

[290] N. Zaïm, D. Guénot, L. Chopineau, A. Denoeud, O. Lundh, H. Vincenti, F. Quéré, and J. Faure. Interaction of ultraintense radially-polarized laser pulses with plasma mirrors. *Phys. Rev. X*, 10:041064, Dec 2020.

[291] N. Zaïm, M. Thévenet, A. Lifschitz, and J. Faure. Relativistic acceleration of electrons injected by a plasma mirror into a radially polarized laser beam. *Phys. Rev. Lett.*, 119:094801, Aug 2017.

[292] Y. Zhang, C. L. Zhong, S. P. Zhu, X. T. He, M. Zepf, and B. Qiao. Obtaining intense attosecond pulses in the far field from relativistic laser-plasma interactions. *Phys. Rev. Applied*, 16:024042, Aug 2021.

[293] A. Zhidkov, T. Fujii, and K. Nemoto. Electron self-injection during interaction of tightly focused few-cycle laser pulses with underdense plasma. *Phys. Rev. E*, 78:036406, Sep 2008.

[294] C. Zhou, Y. Bai, L. Song, Y. Zeng, Y. Xu, D. Zhang, X. Lu, Y. Leng, J. Liu, Y. Tian, R. Li, and Z. Xu. Direct mapping of attosecond electron dynamics. *Nature Photonics*, 15(3):216–221, Mar 2021.

List of publications and conference contributions

Publications:

· **Propagation Effects in the Characterization of 1.5-Cycle Pulses by XPW Dispersion Scan**

A. Tajalli, M. Ouillé, A. Vernier, F. Böhle, E. Escoto, S. Kleinert, R. Romero, J. Csontos, U.Morgner, G. Steinmeyer, H.M. Crespo, R. Lopez-Martens, T. Nagy

IEEE Journal of Selected Topics in Quantum Electronics, vol. 25, no. 4, pp. 1-7, (2019), Art no. 5120407

· **Relativistic-intensity near-single-cycle light waveforms at kHz repetition rate**

M. Ouillé, A. Vernier, F. Böhle, M. Bocoum, A. Jullien, M. Lozano, J-P. Rousseau, Z. Cheng, D.Gustas, A. Blumenstein, P. Simon, S. Haessler, J. Faure, T. Nagy and R. Lopez-Martens

Light: Science & Applications, Volume 9, Article number 47 (2020)

· **Demonstration of stable long-term operation of a kilohertz laser-plasma accelerator**

L. Rovige, J. Huijts, I. Andriyash, A. Vernier, V. Tomkus, V. Girdauskas, G. Raciukaitis, J. Dudutis, V. Stankevic, P. Gecys, M. Ouillé, Z. Cheng, R. Lopez-Martens, and J. Faure

Physical Review Accelerators and Beams 23, 093401 (2020)

· **Optimization and stabilization of a kilohertz laser-plasma accelerator**

L. Rovige, J. Huijts, I. A. Andriyash, A. Vernier, M. Ouillé, Z. Cheng, T. Asai, Y. Fukuda, V. Tomkus, V. Girdauskas, G. Raciukaitis, J. Dudutis, V. Stankevic, P. Gecys, R. Lopez-Martens, and J. Faure

Physics of Plasmas 28, 033105 (2021)

· **Survey of Spatio-Temporal Couplings throughout High-Power Ultrashort Lasers**

A. Jeandet, S. W. Jolly, A. Borot, B. Bussière, P. Dumont, J. Gautier, O. Gobert, J-P. Goddet, A. Gonsalves, A. Irman, W. P. Leemans, R. Lopez-Martens, G. Mennerat, K. Nakamura, M. Ouillé, G. Pariente, M. Pittman, T. Püschel, F. Sanson, F. Sylla, C. Thaury, K. Zeil, and F. Quéré

Optics Express 30, 3262-3288 (2022)

· **Waveform control of relativistic electron dynamics in laser-plasma acceleration**

Julius Huijts, Lucas Rovige, Igor A. Andriyash, Aline Vernier, Marie Ouillé, Jaismeen Kaur, Zhao Cheng, Rodrigo Lopez-Martens, and Jérôme Faure

Physical Review X 12, 011036 (2022)

· **Low-divergence MeV-class proton beams from kHz-driven laser-solid interactions**

D. Levy, I. A. Andriyash, S. Haessler, M. Ouillé, J. Kaur, A. Flacco, E. Kroupp, V. Malka, R. Lopez-Martens

Submitted

· **High-Harmonic Generation and Correlated Electron Emission from Relativistic Plasma Mirrors at 1 kHz Repetition Rate**

S. Haessler, M. Ouillé, J. Kaur, M. Bocoum, F. Böhle, D. Levy, L. Daniault, A. Vernier, J. Faure, R. Lopez-Martens

Submitted

Conference contributions (oral presentations)

· **Relativistic-intensity waveform-controlled near-single-cycle pulses from a stretched hollow fiber compressor**

Ultrafast Optics XII

October 2019, Bol, CROATIA

· **Sub-cycle control of relativistic plasma mirror dynamics**

CLEO:QELS-Fundamental Science

May 2021, San Jose, California, USA (online presentation)

· **Sub-light-cycle control of relativistic plasma-mirrors (Best student presentation award)**

EOS Annual Meeting

September 2021, Rome, ITALY

· **High-harmonics and particle beams emission from relativistic plasma mirrors at kHz repetition rate**

Plenary Meeting - GDR Ultrafast Phenomena

November 2021, Paris, FRANCE

· **High-order harmonics and particle beams from relativistic plasma mirrors**

1st International Conference on UltrafastX 2021

April 2022, Xi'an, CHINA (online presentation)

ECOLE
DOCTORALE

Titre : Génération d'impulsions laser proches du cycle optique en durée pour l'interaction laser-matière relativiste à haute cadence

Mots clés : impulsions ultrabrèves ; relativiste ; interaction laser-plasma ; génération d'harmoniques ; cycle optique

Résumé :
Cette thèse expérimentale s'est essentiellement déroulée au Laboratoire d'Optique Appliquée à Palaiseau, sur un système laser capable de générer des impulsions proches du cycle optique en durée avec des énergies de plusieurs mJ à une cadence de 1 kHz : la Salle Noire. Grâce à ce système, nous étudions l'interaction laser-matière en régime relativiste à haute cadence. Nous parvenons, d'une part, dans des jets de gaz, à accélérer des électrons dans le sillage du laser jusqu'à une énergie de quelques MeV ; et d'autre part, par interaction avec des miroirs plasma, à générer des harmoniques d'ordres élevés qui sont associées dans le domaine temporel à des impulsions attosecondes. Malgré la prouesse technique de ces expériences, les propriétés des faisceaux XUV et d'électrons ainsi générés restent encore peu compatibles avec des applications phares en aval. L'objectif du travail de cette thèse a été d'optimiser la source laser afin de maximiser l'intensité sur cible et d'obtenir des faisceaux aux propriétés stables. En stabilisant la phase enveloppe-porteuse des impulsions laser, nous avons ainsi pu générer des impulsions attosecondes uniques en formant une porte temporelle d'intensité relativiste à la surface du miroir plasma, et aussi produire des faisceaux d'électrons stables en énergie et en direction, en localisant l'injection d'électrons dans l'accélérateur laser-plasma.

Title : Generation of near-single-cycle duration pulses for relativistic laser-matter interaction at high repetition rate

Keywords : ultrashort pulses ; relativistic ; laser-plasma interaction ; high-harmonic generation ; optical cycle

Abstract :
This experimental thesis was essentially conducted at Laboratoire d'Optique Appliquée in Palaiseau (FRANCE), on a laser system capable of delivering near-single-cycle duration pulses containing a few mJ of energy at 1kHz repetition rate : the Salle Noire. Using this system, we study laser-matter interaction in the relativistic regime at high repetition rate. We can, on one hand, in gas jets, accelerate electrons in the wakefield of the laser up to several MeV ; and on the other hand, by interacting with plasma mirrors, generate high order harmonics which are associated to attosecond pulses in the time domain. Despite the technological prowess in these experiments, the properties of the XUV and electron beams thus generated remain scarcely compatible with the main applications downstream. The objective of this thesis work was to obtain beams with stable properties. By stabilizing the carrier-envelope phase of the laser pulses, we could generate single attosecond pulses by forming a relativistic-intensity temporal gate at the surface of the plasma mirror, and also produce electron beams exhibiting stable energy and direction, by localizing the electron injection within the plasma accelerator.

Institut Polytechnique de Paris
91120 Palaiseau, France